SPATIAL-TEMPORAL PATTERNS IN EVOLUTIONARY ECOLOGY AND FLUID TURBULENCE

BY

HONG-YAN SHIH

DISSERTATION

Submitted in partial fulfillment of the requirements
for the degree of Doctor of Philosophy in Physics
in the Graduate College of the
University of Illinois at Urbana-Champaign, 2017

Urbana, Illinois

Doctoral Committee:

Professor Karin Dahmen, Chair
Professor Nigel Goldenfeld, Director of Research
Professor Sergei Maslov
Assistant Professor Thomas Kuhlman

Abstract

This thesis explores the turbulence of ecosystems, and the ecology of turbulence. Ecosystems and turbulent fluids are both highly non-equilibrium and exhibit spatio-temporal complexity during the course of their evolution. It might seem that they are too complicated to extract universal properties, even if there are any. Surprisingly, it turns out that each of them can shed light on the other, enabling them both to be solved. In particular, the techniques used to explore ecosystem dynamics turn out to be exactly what is needed to solve the problem of the laminar-turbulent transition in pipes.

Accordingly, this thesis is organized into two parts. Part I discusses what governs the rate of evolution and what are the consequences of the interplay between ecology and evolution at different scales. Three different aspects of these underlying questions are included in this part:

(1) We first study the phenomenon of anomalous population dynamics known as "rapid evolution", in which a fast evolutionary time scale emerges from intense ecological interactions between species. Specific examples are rotifer-algae and bacteria-phage, where the ecosystem is composed of a predator and its prey. However, a sub-population of mutant prey arises from strong environmental pressure, and the trade-off between selection from reproduction and predation is manifested in the patterns of eco-evolutionary dynamics. We discuss how to solve such system with inherent stochasticity by a generic and systematic analytical approach in the spirit of statistical mechanics, using a stochastic individual-level model. We show that this method can naturally capture the universal behavior of the stochastic dynamics from demographic noise without any additional and more biologically detailed assumptions.

(2) Second, we address the question of the role of selection in evolution and its relationship with phenotypic fluctuations. Phenotypic fluctuations have been conjectured to be beneficial characteristics to protect against fluctuating selection from environmental changes. But it is not well-understood how phenotypic fluctuations shape the evolutionary trajectories of organisms. We address these questions in the context of directed evolution experiments on bacterial chemotactic phenotypes. Our stochastic modeling and experiments on the evolution of chemotactic fronts suggest that the strength of selection can determine whether or not phenotypic fluctuations grow or shrink during successive rounds of selection and growth.

(3) The third aspect of the first part focuses on the paradox of coexistent stability in microbial ecosystems that display especially intricate evolutionary phenomena. We propose that horizontal gene transfer, an important evolutionary driving force, is also the driving force that can stabilize microbe-virus ecosystems. The particular biological system for our model is that of the marine cyanobacteria *Prochlorococcus spp.*, one of the most abundant organisms on the planet, and its phage predator. Phylogenetic analysis reveals compelling evidence for horizontal gene transfer of photosynthesis genes between the bacteria and phage. We test our hypothesis by building a spatially-extended stochastic individual-level model and show that the presence of viral-mediated horizontal gene transfer can induce collective coevolution and ecosystem stability, leading to a large pan-genome, an accelerated evolutionary timescale, and the emergence of ecotypes that are adapted to the stratified levels of light transmission as a function of ocean depth.

The goal of Part II is to understand the nature of the transition to turbulence in fluids, which has been a puzzle for more than a century. The novelty of our approach is that we consider transitional turbulence as a non-equilibrium phase transition. Accordingly we attempt to approach this problem by looking for an appropriate long-wavelength effective theory. We report evidence of candidate long-wavelength collective modes in direct numerical simulations of the Navier-Stokes equations in a pipe geometry, where we uncover unexpected spatio-temporal patterns reminiscent of ecological predator-prey dynamics. This finding allows us to construct a minimal Landau theory for transitional turbulence, which resembles a stochastic predator-prey model. This in turn can be mapped into the generic universality class of directed percolation. Stochastic simulations of this spatial-extended individual-level predator-prey model are able to recapitulate the experimentally observed super-exponential dependence of the lifetime of turbulent regions on Reynolds number near the onset of turbulence. We argue that these remarkable scaling phenomena reflect the presence of finite-size effects as the correlation length becomes of order the pipe diameter, leading to a universal finite-size scaling distribution for the velocity fluctuations.

Acknowledgments

My advisor Nigel Goldenfeld is definitely the person who I want to thank more than super-exponentially. I would like to thank Nigel for sharing ideas and giving me opportunities to study hard and challenging problems (what I really mean is thanks for the turbulence deathmarch!). I am also grateful to Nigel for many years support and guidance, especially for his enormous kindness, patience and encouragement that are very important when I was stuck and confused. It would never be possible for me to accomplish the work in this thesis without Nigel. Nigel has influenced and inspired me deeply not only in scientific research but also in many other ways in life. He is eccentric by nature, and always holds positive attitude and is open-minded in research and in life. He looks at science in a critical, but fair and genuine way. Nigel is generous with sharing his ideas and knowledge with everyone, and is devoted to helping junior ones in the community. When we were working together, Nigel is the cheerleader; he would literally jump up and down with excitements whenever a good idea emerged from discussions or when we discovered another subtlety even though it often confused us more. Nigel is also an advisor in life, and is always there for talking, and I am deeply grateful to our friendship.

I also want to thank Nigel for his generosity to provide me opportunities to present our exciting work in public and to visit other research groups. It was a great surprise to me to realize that Osborne Reynolds original pipe apparatus is displayed in Manchester University when I visited there.

Nigel is caring to his students, and has established an inspiring environment in our group, which I have learned and benefited a lot from. Thanks to students and postdocs for great discussions and ideas: Tsung-Lin Hsieh, Maksim Sipos, Luiza Angheluta, Vikyath Rao, Michael Martini, Farshid Jafarpour, Tommaso Biancalani, Nicholas Guttenberg, Chi Xue, Minhui Zhu, Purba Chatterjee, Zhenyu Wang, Michael Assaf, Nicholas Chia, Patricio Jeraldo, Andreas Menzel, Tom Butler, Lanying Zeng, Simon Kit Sang Chu and Qiucen Zhang.

I would like to especially thank Tsung-Lin, who primarily worked on simulations on our turbulence project, for holding up and sticking with it during the turbulence project deathmarch. Thanks to Max in particular for collaborating and discussions when I first started the turbulence project and for his generously

providing his code and helps on directed percolation simulations, as well as helps on computer problems. Max has been a kind and interesting friend who also gave me advices about research and life in my early years in Urbana. Thanks to Luiza for discussions on turbulence and for her kind hospitality when I visited University of Oslo where I gave my first seminar. Thanks to Vikyath, who has always been a very kind officemate and helpful on computer problems, and also helps taking care of my plants when I was traveling. Thanks to Zhenyu for being a kind and caring officemate. Thanks to Nicholas Guttenberg, who provided great help in rendering some of our data for the cover of *Nature Physics*.

I would like to thank Prof. Seppe Kuehn and David Fraebel for collaborations on the chemotaxis project. It was Seppe who shared their research that motivated our work on chemotaxis modeling, which leads to our study on the abstract model. I especially appreciate Seppes kindness and patience about sharing interesting ideas and various discussions and helps on our modeling. Also collaborating with experimentalists has broadened my horizon of research.

I appreciate very much our collaboration with Prof. Björn Hof and Dr. Gregoire Lemoult on the directed percolation project. I am grateful for Prof. Hofs hospitality when I visited his lab. I would also like to thank Prof. Hof and his wife for treating me kindly. I also thank the members of Prof. Hofs group for discussions about their interesting experiments during that time.

I wish to thank Prof. Kunihiko Kaneko and Prof. Masaki Sano for their hospitality and kindness when I visited University of Tokyo. I also appreciated the many discussions on turbulence and biology with Prof. Kaneko and Prof. Sano and their group members, from which I have learned much.

I also would like to express my gratitude to Prof. Frede Thingstad and Dr. Selina Våge for their hospitality and for giving me the chance to participate and to teach NetLogo to ecologists at the Hjort Summer School on Microbial Oceanography in Bergen, Norway.

I would like to thank Prof. Karin Dahmen, Prof. Tom Kuhlman and Prof. Sergei Maslov for being the committee of my dissertation. I would like to thank Prof. Michael Stone for being the committee of preliminary exam.

Special and sincere thanks to Connie Scott in Carl R. Woese Institute for Genomic Biology, who has always provided great and kind helps about traveling and various things.

I also want to express my profound gratitude to Prof. Hsiu-Hau Lin, my master advisor in National Tsing Hua University in Taiwan, without whose guidance, encouragement and helps I would never be able to be here. Hsiu-Hau's positive spirit and incredible enthusiasm has inspired and influenced me deeply.

To my family I owe a lot. I am eternally grateful to them. Thanks to Yi-Ping for unconditional friendship, support and encouragement.

This work was partially supported by the National Science Foundation NSF-DMR-1044901, NASA Astrobiology Institute award NNA13AA91A, the L. S. Edelheit Family Fellowship in Biological Physics (2016) and the Government Scholarship for Study Abroad (2015-2016), Taiwan.

Table of Contents

List of Abbreviations

ILM	Individual-level model
EC	Evolutionary cycle
CC	Cryptic cycle
HGT	Horizontal gene transfer
Re	Reynolds number
DNS	Direct numerical simulation
DP	Directed percolation
i.i.d	Independent and identically distributed
CMP	Coupled map lattice
RG	Renormalization group
BHP	Bramwell-Holdsworth-Pinton

Chapter 1

Introduction

This thesis will explore the turbulence of ecosystems, and the ecology of turbulence. Why should we study turbulence, and what does it have in common with ecology? Turbulence describes the unsteady, fluctuating and unpredictable state of fluids that is prevalent in our daily life; it remains one of the most difficult unsolved problems in physics. Ecosystems are composed of various species and organisms that are coupled by complex interactions and interact with their surrounding fluctuating environment, on scales ranging from microbial communities (e.g. in the human body) to forests and oceans that are constantly driven by energy flows and nutrient cycles. Turbulence and ecosystems both consist of a large number of degrees of freedom, and are highly nonlinear, stochastic and far from equilibrium. Nevertheless, they both exhibit robust scaling laws in many situations. Ecosystems and turbulence are most widely studied in their steady state, well-developed and stable. However, in the last few years, attention has focused on the transitions exhibited by both systems. Fluids are laminar at slow speed (we will define this statement later), but turbulent at high speed [1, 2, 3, 4, 5]. Ecosystems can undergo transitions also, e.g. from flourishing vegetation to desert as an external parameter such as rain fall is varied [6]. Thus, there are immense consequences in both turbulence and ecosystems once they are undergoing phase transitions. In both well-developed and transitional states, turbulence and ecosystems have a wide range of spatial and time scales, leading to universality and scaling laws. Thus we expect that these phenomena can be described by minimal models despite their detailed complexity. An additional question arose unexpectedly during this work: Can the study of ecosystems tell us something about turbulence, or vice versa? Remarkably, I show in this thesis that the answer is yes! There is a precise and exact mapping between certain ecological transitions and the laminar-turbulence transition.

This thesis summarizes various topics that help to address these questions. The first part of this thesis starts with the question: what determines the rate of evolution, under various environmental influences? This is explored by studying predator-prey ecosystems, where the organisms are coupled together through multiscale spatial-temporal interactions, driven far from equilibrium by energy input (e.g. from the sun). Intense interactions in space and time can provide strong selection stress to the ecosystems, driving the system far away from equilibrium. As a result, we can imagine a picture of successive and rapid fixation of

mutant traits. In fact, these systems can develop surprising rapid complex dynamics and also rich patterns in space, in traits and in phase shifts associated with population cycles, where stochasticity plays an important role. Also, the fluctuations in these ecosystems can be characterized by universal scaling in their dynamical power spectra.

These phenomena share similarities with turbulence, a highly non-equilibrium fluid state, characterized by remarkable cascades that arise from an energy flow caused by different length scales. In this sense, an ecosystem can be said to be turbulent.

The second part of this thesis discusses a century-long problem: what is the nature of the onset of turbulence in fluids? Since we seek to understand the universal features that are exhibited in a range of systems, we approach the problem from the aspect of the statistical mechanics of phase transitions. This is different from most studies in the field of fluid dynamics, which focus on nonlinear dynamics and large-scale numerical computation. Remarkably, we found that fluids near the laminar-turbulent transition exhibit a sort of two-fluid model behavior, in which there is coexistence of a coherent state and turbulent fluctuations. More surprisingly, the dynamics of these two fluid modes show characteristics of oscillations in predator-prey ecosystems. This unexpected finding shows the value of studying transitional turbulence as a problem of non-equilibrium phase transitions, from which we can extract universal behavior from the underlying complicated dynamics.

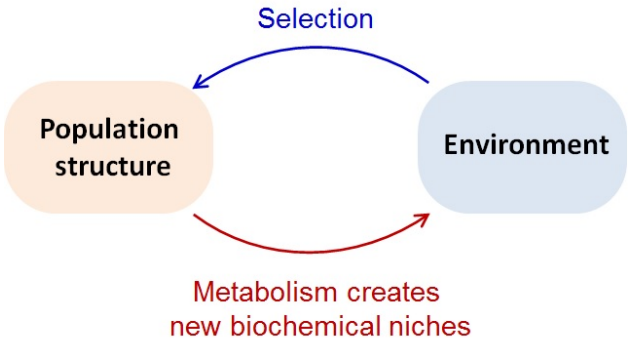

Figure 1.1: **Rapid evolution**.

Part I of this thesis will approach the question of the rate of evolution from three different perspectives. An ecosystem is usually conceived of as a macroscopic ensemble of organisms, with hierarchical trophic levels and foodwebs that are coupled by complex interactions. Yet we may first start by dissecting it into smaller-scaled subsystems in which we consider only relevant interactions between individuals. Arguably the most important relationship is predator-prey interaction. The basic features of the simplest predator-prey system are well-studied by both analytic models and numerical simulations, describing such features

as the persistent global population oscillations in time, the spatial distributions locally of populations, with characteristic phase shifts, and robust power spectra of fluctuations.

It turns out that these population oscillations can only be properly described if the discrete nature of individuals is taken into account. Individuals within a population are created and die by integer amounts. The discreteness is not only important near extinction, where population sizes are small, but even for large populations due to a resonant amplification. This discrete nature of the predator-prey population dynamics leads to an economical description, using quantum field theory. From this path integral approach, we can explore the connection to the universal behavior near phase transitions in statistical physics.

Therefore the predator-prey model can serve as a basic tool to guide our understanding of more complicated ecosystems. In this sense, the predator-prey model for ecosystems is like the Ising model for magnetism, which is a benchmark for understanding phase transitions in condensed matter physics.

Just as the Ising model cannot explain most magnetic phenomena in condensed matter world, real ecosystems surely have much richer biological features than the simplest predator-prey model, due to complexity arising from the various types of multiscale interactions. For example, if the mutation can occur fast enough and thus introduce beneficial or novel species (such as prey that are more adept at avoiding predators), these new species may become well-represented in the ecosystem under intense selection from the surrounding environment (such as ferocious predators or severe nutrient limitation) [7, 8]. If these changes occur within the same order of timescale as an organism's lifetime, then the evolutionary time scale becomes comparable with the ecological time scale. The result is that environment can change the structure of the ecosystem though evolution. Moreover, the new species may introduce innovation, which can, for example, build up new interactions with other organisms or create new metabolic substrates, thereby in turns affecting the environment or the evolutionary pathways. When this process creates new niches in the ecosystem, it is referred to as niche construction [9]. These feedbacks between ecosystems and evolution are generally called "rapid evolution". Chapter 3 and Chapter 4 address the consequences of rapid evolution for a minimal scenario for rapid evolution, where only one mutant prey is considered in a well-mixed predator-prey ecosystem. In this simplest example, the strong pressure from predation induces the rise of mutant prey, leading to dramatic changes in population dynamics of the whole ecosystem.

A main theme in this thesis is the intrinsic stochasticity in natural systems. Since the number of individuals or particles are quantized, population changes during interactions are inherently fluctuating in a discrete manner like shot noise, even in well-mixed systems. Fluctuations due to discreteness are referred to as intrinsic noise, and are important drivers of spatial and temporal structure in ecosystems. In respect to modeling, intrinsic stochasticity in individual-level models can lead to qualitative differences

from conventional deterministic, population models, such as persistent oscillations in population (so-called "quasicycles") and a long-tail scaling in their noise spectrum [10, 11]. This is addressed in Chapter 4 and is the underlying spirit of this thesis.

The trajectories of evolution are shaped by various factors through the selection process. In nature, selection acts on traits or phenotypes of organisms [12]. Phenotypes are determined by the associated genotypes, and the heterogeneity and diversity in phenotypes are attributed to either genetic variations or isogenic fluctuations. The isogenic fluctuations, also called phenotypic fluctuations, arise from different levels of gene expression, which can also reflect environmental fluctuations. Therefore, the relationship between phenotypes and genotypes, and how each adapts to environments and how they are coupled to mutations, along with their response to various sources of selection stress, are the building blocks for basic evolutionary processes and are key to understanding rapid evolution and evolvability of organisms, as described in Chapter 5.

The importance of evolvability and phenotypic plasticity or adaptability has been increasing due to the impact of global climate change [13]. Nevertheless, the complex nature of them complicates studies from extracting reliable causal relationships between each factor. Theoretical models usually require too many assumptions to be tested or proved by real experiments. For example, it has been long hypothesized that organisms can benefit from large phenotypic fluctuations [14]. The idea is that they obtain variety that can sustain populations in changing environments. On the other hand, phenoypic fluctuations can also be detrimental, by destabilizing a well-adapted state of organisms to their environment, leading to a trade-off between evolvability and robustness of evolution. One way to quantify these subtleties is to use techniques of directed evolution. This means, to apply repeated selection on phenotypes or genotypes and observe the population changes, from which we can quantify how the evolutionary trajectory of the ecosystem adapts and develops under these types of selection. However, the dynamics of phenotypes and genotypes is usually difficult to trace in practice.

The second topic for Part I describes collaborative work on a recent directed evolution experiment using a microbial chemotaxis setup, where it is possible to trace phenotypic dynamics under directed evolution [15]. Since chemotaxis is the motility behavior of bacteria as a response to environmental changes, the spatio-temporal patterns developed by microbial colonies reflect the underlying heterogeneity in phenotype composition. Therefore selection in real space, which is straightforward to apply and trace, reflects selection in chemotactic phenotype space. Subsequent mutations with faster and more flexible motility emerge rapidly during the course of repeated selection [15]. Phenotypic fluctuations are observed to decrease as well as the width of the traveling front that presumably reflects the distribution of phenotypes. To understand these

results, Chapter 6 studies a conceptual model that is able to explain and predict the general trends exhibited in directed evolution experiments as a function of selection. In addition, a stochastic individual-level model is built to consider the effect of environments by including realistic physical variables for chemotaxis systems. Interesting, the results predict multiple trends in the evolution of phenotypes. The scope of this chapter is to explore theoretical frameworks including physical factors that are comparable to real experiments and thus provide predictions for further experimental studies.

Another main theme in this thesis is the non-equilibrium nature of ecosystems and turbulence. Predator-prey ecosystems are in general non-equilibrium and break detailed balance. However, studies of the predator-prey model usually focus on the coexistence of predator and prey with a static parametric fixed point. For example, the literature of rapid evolution mainly study how the system changes from one fixed point to another when subjected to mutations or environmental perturbations [7, 6]. In fact, evolution is an on-going process, and ecosystems are open systems subjected to energy flux and species flux with a constant rate. Therefore the fixed point should in general be dynamical, especially when speaking of rapid evolution. Species flux from rapid evolution corresponds to gain or loss of species due to mutation, migration or extinction. As we discussed in the previous paragraphs, in rapid evolution the evolution of prey can constantly induce the evolution of their surrounding predator and then vice versa, leading to coevolution of prey and predator. Coevolution in the context of ecology usually refers to an arms race with antagonistic competition between prey defense and predator aggressiveness [16, 17].

An example where such rapid evolution has entered the public consciousness is antibiotic resistance, which recently has been documented to be emerging rapidly as a result of overtreatment for bacterial infections. Besides mutation, another mechanism that can drive coevolution is horizontal gene transfer (HGT) [18, 19, 20]. HGT is the process of swapping of genetic materials between organisms or species without lineage relations, such as from one bacterial individual to another or even to another species. HGT is prevalent and can play a significant role in evolution, because it provides novel genes to organisms, thereby potentially accelerating the rate of evolution and increasing diversity.

This brings out the third aspect of Part I: collective coevolution. Collective behaviors are common in nature, such as animal swarms, microbial biofilms, cellular differentiation and quorum sensing in microbes, etc. At the scale of genomes, collective effects such as epistasis are important in evolution. One remarkable example that shows a specific and remarkable consequence of collective effects in evolution is the marine cyanobacteria *Prochlorococcus spp.* [21], as introduced in Chapter 7. Cyanobacteria are able to live by processing sunlight. Indeed, chloroplants in plants evolved from an ancient endosymbiosis with cyanobacteria. The first clue to the collective nature of its evolution was that its phage predator contains photosystem

genes. Phylogenetic studies show strong evidence that these genes have been transferred back and forth from bacteria and viruses. Specifically, the genes are transferred via viral infection, and both bacteria and viruses benefit from transferred genes that increase their ability to reproduce. My work, presented in Chapter 8, analyses the dynamics of this ecosystem and shows that such processes are collective, because both directions of transfer are required to form a stable ecosystem to evolve. Therefore, this is an example of a stable coexistence emerging from antagonism between individuals, mediated by horizontal gene transfer.

Part II of this thesis concerns the emergence of turbulence, one of the most intriguing collective non-equilibrium phenomena in physics, which we will introduce in Chapter 9. Turbulence is a phenomenon that involves an extremely high numbers of degrees of freedom. To understand most physical phenomena, we do not need to consider the microscopic structure of the system beyond some level. Any model with large scales or coarse-grained levels is an effective theory. Effective theories are important for understanding physical phenomena, not only because most of the time we cannot quantify the microscopic details at all, but also because these microscopic details are usually not required to understand the macroscopic behavior [22, 23]. Starting from an effective theory that considers reasonable scales, we then keep modifying the model to develop other effective theories at different levels for other physical phenomena. For example, the Ising model is an effective mathematical description for ferromagnetism that neglects the underlying electronic structure. Despite its simplicity, it is not exactly solvable above two dimensions, and even in two dimensions, the external magnetic field must be set to zero. To understand its properties near a phase transition, a Landau theory describing long-wavelength fluctuations of the order parameter, with the same symmetry and dimensionality as the Ising model is used as the next-level effective theory regardless of all other microscopic details of real systems. Based on Landau theory, further analysis such as renormalization group can be applied to calculate critical exponents and then map out the phase diagram and scaling functions [23]. Remarkably, the calculated critical behavior is exact even though multiple levels of coarse-grain approximations have been made.

The power of effective theory explains the notion of universality, and one should be able to follow the same paradigm for phase transitions in non-equilibrium systems such as turbulence. In fluid dynamics, the Navier-Stokes equations are the most well-known starting point and have been applied to many fluid phenomena. However, it is not possible or desirable to understand the laminar-turbulent transition by exactly solving the Navier-Stokes equations. Instead, if it is valid to consider this as a statistical mechanical phase transition, we should seek the corresponding Landau theory. Finding the appropriate long-wavelength modes of the Navier-Stokes equations that enter into a Landau theory is difficult, and we approached this by performing directed numerical simulations (DNS). From our DNS on pipe flow, it turns out that there are

two collective modes dominating the flow near the laminar-turbulent transition. Therefore the corresponding Landau theory becomes a two-fluid model [24]. More surprisingly, the dynamics of these two modes has the same characteristics as a predator-prey ecosystem. From this identification, it is possible to show that the underlying universality class of the laminar-turbulent transition is directed percolation. Chapter 10 describes these studies.

In non-equilibrium phase transitions, directed percolation (DP) plays the role of a basic model system [25], like the Ising model does in magnetism. It is a minimal model that describes the permeability of flow in porous media; depending on the connectedness of pores, there exists a threshold above which the flow always permeates through the system (the wet phase) and below which the flow always terminates in the middle (the dry phase). Such transition is characterized by the existence of an absorbing state, a state that once entered cannot be left. My work strongly suggests that the transition to turbulence is in the same universality class as the extinction-coexistence transition in ecosystems, and is in the universality class of directed percolation. Chapter 11 summarizes several investigations I performed to study the universal statistics of fluctuations near the DP transition. This work may enable future experimental probes to quantify how DP is manifested in real flows near the laminar-turbulent transition.

This high level summary of my thesis shows the close connections between statistical mechanics, turbulence and evolving ecosystems. Now we turn to a more detailed description of the specific projects described in the thesis.

1.1 Emergence of rapid evolution from demographic stochasticity under strong selection in well-mixed ecological systems

The high-level question addressed in this part is how evolutionary timescales interact with ecological timescales. Without mutations, a typical predator-prey ecosystem exhibits characteristic features such as persistent synchronized oscillations and a $\pi/2$ phase difference between the time-dependent prey and predator populations. When rapid evolution occurs, genetic variation in a population can arise so fast as to modify ecosystem dynamics [7, 8]. Such phenomena have been observed in natural predator-prey systems, and characterized in the laboratory where they were first noticed by their unusual phase relationships in population dynamics, specifically a π phase shift between predator and prey (evolutionary cycles) [26] and even undetectable prey oscillations compared to those of the predator (cryptic cycles) [27, 28, 29].

The unusual dynamics turns out to arise from the presence of a new mutant type that has emerged from strong predation pressure, and can be understood by an intuitive illustration. The wild type prey competes with a mutant type of prey that is better defended against the predator (or of low nutritional value to the predator). The defense is usually accomplished at a cost: there is a metabolic compromise in terms of reduction in production (or a negative "selection coefficient"). The trade-off between selection from predation and selection on growth determines the degree of phase anomaly in dynamics. Earlier work attempted to codify this intuition in systems of ordinary differential equations, which required a number of extraneous assumptions in order to reproduce the rapid evolution phenomena [26, 29]. We wanted to model these phenomena without requiring such extraneous assumptions, that are difficult to justify empirically, or fit mathematically. Thus we built a generic individual-level stochastic model of interacting populations that includes a sub-population of lower predation rate and growth rate. Using a master equation formalism, and by mapping to a coherent state path integral solved by a system-size expansion, we showed that evolutionary and cryptic quasicycles can emerge generically from the combination of intrinsic demographic fluctuations and clonal mutations alone, without additional biological mechanisms [30]. The phase diagram of the phase difference in dynamics was calculated as a function of both selection from predation rate and selection on growth rate. This is a simple example of rapid evolution that shows the interplay between ecology and evolution, where strong selection in ecological interactions can accelerate evolutionary timescales.

1.2 Emergence of rapid evolution under strong selection in spatial-extended systems

The overarching goal of this part is to explore how selection influences adaptation of organisms and the evolution of their phenotypic fluctuations, taking the example of chemotaxis in *E. coli.* at scales ranging from the genomic, up through the signaling pathways at the cellular level, ultimately affecting the cells' motility and the behavior of a growing colony. First, we review the detailed experiments that capture the directed evolution of an initially clonal population of *E. coli.* undergoing chemotactically-driven expansion through agar gel [15]. Repeated sampling of the cells at the outer limits of the colony and re-initialization of colony growth results in an evolution of phenotype and genotype. In these experiments, strong bottleneck selection is repeatedly applied over bacteria population, and the nutrient gradient in the environment biases the individuals' motion, whose population changes locally and in turns increases the background gradient. As a result, the population collectively develops a traveling front, which creates a sharp gradient in nutrient and simultaneously behaves as a selection force that leaves the bacteria behind the front to become nutrient-

limited.

In order to interpret the experiments and to isolate the effects of experimentally-related factors such as strength of bottleneck selection, mother-daughter correlation and environmental changes, we construct two types of stochastic individual level models for directed evolution. The first model is purely conceptual and has the lowest level of description, where a single representative phenotype and genotype are considered, and all other details including chemotaxis sensing and updating mechanisms, growth rate dependence (or "fitness landscape") and environmental changes are not explicitly represented but abstracted away into selection strength. Individuals' phenotype and genotype values fluctuate between lineages based on the genotype-phenotype mapping (or epigenetic inheritance) and adapt to selection over repeated rounds. One important feature in this abstract model is the existence of a physical threshold for phenotype and genotype. The main result is that strong selection strength can lead to increase in phenotype variation while weak selection strength can cause reduction in phenotype variation. The reason is that individuals with large phenotype variation are more likely to be selected when their phenotype values are not yet constrained by the physical threshold, but when they evolve near the threshold, phenotype values are degraded due to fluctuations from large variation. This simulation experiment shows that arguments that large phenotype fluctuations under strong selection are a "survival strategy" or "bet-hedging strategy" are overly simplified. One needs to consider the combined effects from selection strength and physical threshold, and the results depend upon their interplay. Another suggestion from our simulation observations is that strong selection may increase evolvability by speeding up evolution before reaching threshold.

The second model I constructed is meant to predict the evolution of specific chemotactic phenotypes for bacteria including run speed and tumble frequency, in order to provide insight into the factors contributing to the main qualitative trends observed experimentally. Thus more realistic environmental influences such as chemotaxis processes, gel structure, spatially-dependent growth rate and selection are considered. In addition, the simulations are able in principle to make predictions about how the adaptation behavior is affected by the strength of the selection and the properties of the medium through which the cells diffuse. Because of the complexity of the phase diagram of this model and the difficulty in establishing a sharp result, this work is not described in the thesis. This project is another example of rapid evolution where individuals adapt to the changing environment.

1.3 Coevolution and stability of marine cyanobacteria

A key question in evolution is to understand the timescale and evolutionary trajectory of the microbial communities that influence the development of the Earth's environment and the biosphere. Here, I focus on the interplay between bacteria and their viruses (often called bacteriophage, or simply phage). In particular, what accounts for the stability, co-evolution and diversity of microbial and viral ecosystems, even though predation and large viral burst size could generically drive such systems to extinction? This part presents a mechanism showing that antagonistic predator-prey dynamics can lead to an emergent mutualistic state, through the interplay between horizontal gene transfer, predation and coevolution. A remarkable example of this collective state, with great significance for the functioning of the planet's global carbon cycle is the world's most abundant organism marine cyanobacteria *Prochlorococcus spp.* and its phages [21]. The hallmark of this collective is that both the cyanobacteria and their phage carry and utilize photosystem II genes, which molecular phylogeny show have been horizontally transferred multiple times between host and phage.

I developed a stochastic, spatially-extended individual-level model of this ecosystem, which I have studied by Monte Carlo simulation. An interesting scenario arises: the photosystem genes evolve more rapidly in the virosphere than in the bacterial pan-genome, and thus bacterial evolution can be accelerated by its interaction with viruses through horizontal gene transfer, albeit at the cost of predation. On the other hand, phage can benefit from the bacterial low mutation rate, and acquire evolved photosynthesis genes that prevent degradation of virus fitness. This positive gene flux through two-way horizontal gene transfer leads to stability, diversity, range expansion and niche stratification of the bacteria-phage ecosystem, and generates a huge pan-genome for the bacteria. This mechanism shows that non-equilibrium spatio-temporal antagonistic interactions between organisms, on scales ranging from genomes to the environment, can drive the emergence of collective stability in predator-prey ecosystems.

1.4 Ecological collapse and the emergence of traveling waves at the onset of shear turbulence

Turbulent flows are complex, stochastic, and unpredictable in detail, but transition at lower velocities to a laminar flow, which is simple, deterministic and predictable. This transition is controlled by the dimensionless parameter known as the Reynolds number, named after Osborne Reynolds whose original observation of intermittent "flashes" of turbulence[31] describes the transition from laminar to turbulent states.

Today, Reynolds' flashes are known as puffs [32], and their behavior has been characterized very precisely through a series of physical and numerical experiments performed during the last decade or so [33, 34, 35, 36] (for a recent review, see [37]) culminating in the *tour de force* observation of a super-exponential functional dependence of the lifetime τ of puffs as a function of Re [38]: $\ln\ln\tau \propto \mathrm{Re}$. For Reynolds numbers based upon pipe diameter D of around 2300, turbulence is sustained longer than the ability to observe its lifetime in finite systems, and the puffs become unstable through a new dynamical processes in which the leading edge breaks away and nucleates the formation of a new puff some distance downstream [39, 40, 41, 42]. The puff-splitting occurs on a characteristic time that decays super-exponentially with increasing Re. Super-exponential scaling behavior near the transition to turbulence has also been reported in plane channel flow [43, 44] and Taylor-Couette flow [45].

The theoretical account of these phenomena has focused primarily on the existence and interactions between nonlinear solutions of the Navier-Stokes equations, particularly periodic orbits [46, 47], traveling waves [48, 3, 49, 50, 51] and the dynamics of long-lived chaotic transients [52]. An alternative line of inquiry has been to characterize the statistical properties of transitional turbulence through *ad hoc* model equations. These have been motivated either by perceptive analogies to excitable media [53] or by phase transition universality arguments that begin with the notion that the laminar state is an absorbing one [54], and show quantitatively how super-exponential decay results from the generic universality class for non-equilibrium absorbing processes [55]: directed percolation (DP) [56]. Both approaches reflect an important aspect of the dynamics, namely that a certain minimum level of energy is required to sustain turbulent puffs [57], leading to a further connection with extreme value statistics [58].

It is the statistical behavior near the transition which concerns us here: how do the various spatial-temporal modes that are excited give rise to such remarkable lifetime statistics? What is the universality class of this transition, in terms of its fluctuation characteristics? Are there simplified effective descriptions that bridge the gap between the underlying fluid dynamics and the large-scale statistical properties? And how do these emerge from the underlying Navier-Stokes equations that govern all hydrodynamic phenomena?

Thus, we sought evidence for dynamical modes of the Navier-Stokes equations which exhibited an interplay between large-scale fluctuations and small-scale dynamics that would be captured by an effective statistical field theory description.

Here we report direct numerical simulations of transitional pipe flow, showing that a zonal flow emerges at large scales, activated by anisotropic turbulent fluctuations; in turn, the zonal flow suppresses the small-scale turbulence leading to stochastic predator-prey dynamics. We show that this "ecological" model of transitional turbulence, which is asymptotically equivalent to DP at the transition [59], reproduces the

lifetime statistics and phenomenology of pipe flow experiments. Our work demonstrates that a fluid on the edge of turbulence exhibits the same transitional scaling behavior as a predator-prey ecosystem on the edge of extinction, and establishes a precise connection with the DP universality class. Finally, we discovered that the super-exponential scaling law with Reynolds number observed in pipe flow has a subtle origin in the interplay between finite-size effects, turbulent fluctuations and extreme value statistics.

1.5 Collaborations

All the work in this thesis was performed in collaboration with my advisor. In addition, the work on chemotaxis was a collaboration with experimentalists Prof. Seppe Kuehn, David Fraebel and Harry Mickalide. The work on cyanobacteria was in collaboration with Dr. Tim Rogers of Bath University, England. The work on turbulence was in collaboration with Tsung-Lin Hsieh, who primarily worked on direct numerical simulations of the Navier-Stokes equations, while I was responsible for the other aspects of the project. The early stages grew out of the thesis work of Maksim Sipos, who kindly provided one of the directed percolation codes I used. We especially appreciated collaborating with Prof. Björn Hof and Dr. Gregoire Lemoult on the finite-size effects of directed percolation.

1.6 Publications

The work in this thesis has already led to three publications (one on rapid evolution, two on turbulence), a draft nearly ready for submission (on chemotaxis), and most likely another two papers (one on finite-size scaling near the laminar-turbulent transition, one or two on cyanobacteria-phage interactions). Specifically these are:

- Hong-Yan Shih and Nigel Goldenfeld, Path-integral calculation for the emergence of rapid evolution from demographic stochasticity. *Phys Rev. E* **90**, 050702(R) (2014).
- Hong-Yan Shih, Tsung-Lin Hsieh and Nigel Goldenfeld, Ecological collapse and the emergence of traveling waves at the onset of shear turbulence. *Nature Physics* **12**, 245 (2016).
- Nigel Goldenfeld and Hong-Yan Shih. Turbulence as a problem in non-equilibrium statistical mechanics. *J. Stat. Phys.* **167**, 575-594 (2017).
- David Fraebel, Hong-Yan Shih, Harry Mickalide, Nigel Goldenfeld, Seppe Kuehn. Evolution of phenotypic fluctuations in the presence of constraints. (manuscript in preparation)

Part I

Rapid Evolution

Chapter 2

Models for predator-prey ecosystems

2.1 Predator-prey dynamics

The basic structure of ecological systems is the trophic relationship between species. The most common direct trophic relation is the predator-prey interaction, wherein a predator (e.g. lynx) hunts prey (e.g. hare) to get energy for growth. Predator-prey interactions can be expected to lead to cyclical population dynamics: The prey population decreases due to predation, and then the predator will be lacking in food and its population will decrease as well. As long as the predation pressure is low enough, the prey can grow back and are hunted by the predator again, and a new cycle begins. The successive dynamics forms oscillating cycles, where in each cycle the population of predator bounces back after the prey resumes the overall growth and before the prey population starts to decline due to excessive numbers of the predator. Therefore the predator dynamics lags the prey within a half cycle of the prey, and thus the phase delay is naively anticipated to be roughly a quarter period. Such population dynamics with a $\pi/2$ phase shift has been well-documented, for example in the famous data for population of lynx and hare [60], as shown in Fig. 2.1. At laboratory scales, experiments on predator-prey ecosystems such as rotifer-algae [26, 29, 62] and

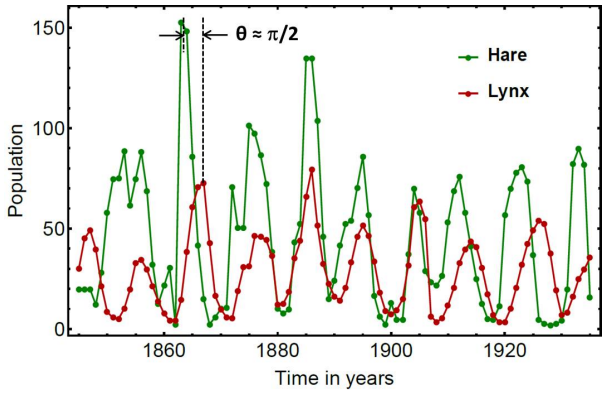

Figure 2.1: **Predator-prey dynamics of lynx-hare ecosystem**. Figure is redrawn from [60], where the original data are in [61].

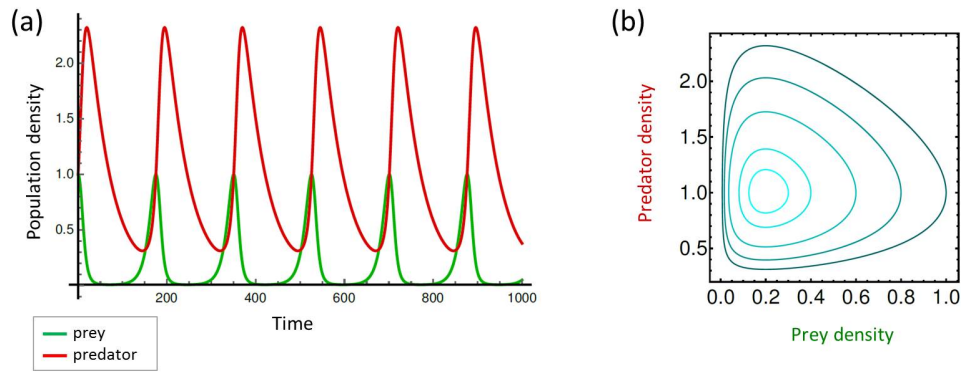

Figure 2.2: **Predator-prey dynamics from Lotka-Volterra model with infinite carrying capacity**. (a) An example when the fixed point is a center. The solutions can be unphysical with infinitesimal population density, which in real world would imply extinction. (b) Phase portrait of solutions with different initial conditions, showing that there is no unified long-time behavior due to the presence of an integral of the motion.

phage-bacteria [27, 28] also exhibit the same characteristics. The pervasiveness of predator-prey dynamics serves itself as a model system upon which we can study more complicated ecosystems.

In this chapter we will review some basic types of mathematical models that are widely used to describe predator-prey ecosystems. In general there are two categories: deterministic population-level based model and stochastic individual-level based models.

2.2 Deterministic models for predator-prey dynamics

2.2.1 Lokta-Volterra model with infinite carrying capacity

The conventional model for predator-prey population dynamics is the set of Lotka-Volterra equations [63, 64], which is a pair of coupled ordinary differential equations for the time-dependence of the spatially averaged densities of the prey u and the predator v. Originally, the Lotka-Volterra equations modeled only the basic processes of birth of the prey, predation and death of predator, leading to:

$$\begin{aligned} \frac{du}{dt} &= bu - puv \ , \\ \frac{dv}{dt} &= puv - \lambda v \ , \end{aligned} \tag{2.1}$$

where b is the prey reproduction rate, λ is the predation rate and d is the predator death rate. In these equations, predation only occurs if a predator encounters a prey, an event that is proportional to the density

of both predator and prey. The fixed points of Eq. (2.1) are

$$(u^*, v^*) = (\frac{\lambda}{p}, \frac{b}{p}) \, , \; (0, 0). \tag{2.2}$$

The Eq. (2.1) can be solved by separation of variables, and the identity established

$$d(b \ln u - pu + \lambda \ln v - pv)/dt = 0. \tag{2.3}$$

This shows that the dynamics is constrained by a conserved quantity that depends on the initial values of u and v, even though the other parameters in the equation are unchanged. The non-zero fixed point in such a case is called a center. The trajectory in the phase portrait is characterized by a closed orbit that depends on initial conditions, as shown in Fig. 2.2, and therefore the dynamics of u and v sustains cycles. The counterclockwise circular trajectory in the phase portrait indicates an approximate phase lag $\pi/2$ of the predator behind the prey. However, these solutions do not describe popuolation cycles, for several reasons. For example, the dynamics do not have a long-term global attractor. This is unphysical, as can be seen in the next section, because of structural instability: the case with large carrying capacity, $K_u = \infty$, is qualitatively different from $K_u \to 0$. A physically correct representation of population cycles should have amplitudes that are independent of initial conditions, i.e. limit cycle solutions, as emphasized by May [65].

2.2.2 Lotka-Volterra model with finite carrying capacity

Without the presence of the predator, the Eqs. (2.1) give unphysical, exponential growth of the prey. To limit the population, one way is to require logistic growth of prey, wherein the growth ceases once the prey population has reached a limiting value K_u. This leads to the equations often known as the Lotka-Volterra equations, even though the history of their development in the present form is somewhat obscure: I was unable to find these equations with the crucially finite carrying capacity term in the standard references to which these equations are attributed [66, 63, 67, 68, 69] (Section 7 Eq. (B) of [68] comes close but then sets the carrying capacity to infinity). We will write the equations as:

$$\begin{aligned} \frac{du}{dt} &= bu(1 - \frac{u}{K_u}) - puv \; , \\ \frac{dv}{dt} &= puv - dv \; , \end{aligned} \tag{2.4}$$

where K_u represents the carrying capacity of the prey and can be interpreted as a death rate proportional to prey density, due to crowdedness or competition for nutrient. The trivial fixed points are $(u^*, v^*) =$

$(K_u, 0), (0, 0)$. In addition, there is a non-trivial coexistence solution

$$(u^*, v^*) = (u_0, v_0). \tag{2.5}$$

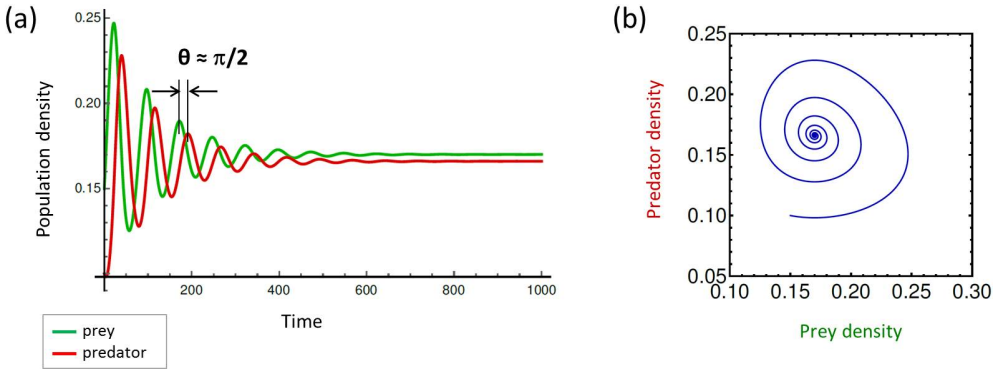

Figure 2.3: **Predator-prey dynamics from Volterra model**. (a) An example of the fixed point being a stable focus into which the solutions converge. (b) Phase portrait shows that trajectory of the solutions spiraling into the fixed point.

Linear stability analysis shows that the coexistence solution of the Volterra equations is a focus; the corresponding eigenvalues are complex, and nearby trajectories in phase portrait will spiral into it. The resultant dynamics also shows a roughly $\pi/2$ phase shift between the predator and the prey but converges to a steady state, which is apparently in disagreement with the real observations (Fig. 2.3).

2.2.3 Satiation model

To recover undamped, persistent oscillations, it is conventional to include additional nonlinearity into the Lotka-Volterra equations. A popular choice for that is to modify the predation interaction to include satiation. The basic idea is that when the prey population vastly outnumber the predators, every predator has no difficulty in finding a prey and so there is a fixed decline of the prey population per unit time, independent of the prey population, but dependent only on the number of predators. This can be captured by the so-called Holling type II functional response, in which the predation term has been modified as shown below:

$$\begin{aligned} \frac{du}{dt} &= bu(1 - \frac{u}{K_u}) - p\frac{uv}{K_s + u}\ , \\ \frac{dv}{dt} &= p\frac{uv}{K_s + u} - dv. \end{aligned} \tag{2.6}$$

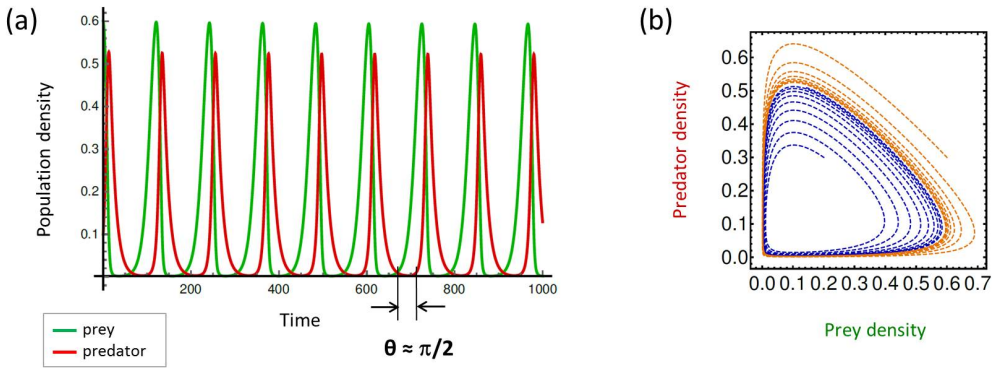

Figure 2.4: **Predator-prey dynamics from the satiation model**. (a) An example shows a solution whose fixed point is a limit cycle, and thus the dynamics sustains persistent oscillations, with a phase shift $\pi/2$ in the predator behind the prey. (b) The trajectory in phase portrait is attracted to the limit cycle. Trajectories in blue and orange show two different initial conditions.

Here the additional constant, K_s, in predation is called the half-satiation constant. This model is also referred to as the Rosenzweig–MacArthur predator-prey model [70]. The coexistence fixed point of the satiation model can be a limit cycle (i.e. a dynamical attractor) depending on the parameter values, with non-negative real part in complex eigenvalues, so that the solutions of Eq. (2.6) reproduce persistent, undamped oscillations with a $\pi/2$ phase shift, as shown in Fig. 2.5. However, as with other deterministic models, the dynamics is smoothly oscillating and is nothing like the very fluctuating experimental data. In addition, the satiation model can be very sensitive to parameter values, especially in describing coexisting state implying that the satiation model is not robust.

Finally, all deterministic differential equation models allow infinitesimally small values for population densities. However, this is a physical impossibility, because in practice an ecosystem would eventually undergo a fluctuation-generated extinction event, as exemplified in Fig. 2.5, when the population size gets to be a small integer number of individuals.

2.3 Stochastic individual-level model

Deterministic models are called population level models, because they focus on population densities. In reality, population dynamics arises from individual processes which stochastically change the number of individuals by integer amount. This implies the need for another approach that includes individual behavior instead of over-averaging it in a mean-field sense. The failure of population-level models to recapitulate population cycles, without adding extra assumptions such as functional response, prompts us to look at a

different level of description.

In addition, strong demographic fluctuations degrade the utility of population-level modeling, rendering it problematic to assess the appropriate scales for ecological modeling [71, 72, 73, 74, 19, 75] and even influencing community assembly on evolutionary time scales. For example, observations of noisy periodicity in time series [60], slowly-decaying correlations [76] and spatiotemporal patterns [77] clearly reflect the stochastic nature of populations [78] and their spatial organization. Moreover, even the simplest predator-prey systems exhibit complex spatial structure. This can arise through a variety of pattern formation processes [79, 80, 81, 82, 83] that include recent results on deterministic [84, 85] and fluctuation-induced Turing instabilites [86, 10, 77], traveling waves [87, 83, 59] and even analogies to the processes of phase separation in binary alloys [88]. In short, collective and stochastic many-body phenomena are ubiquitous in biology, and perhaps nowhere more so than in ecology.

A major conceptual advance was the development of individual-level models, which used statistical mechanics to capture demographic stochasticity and derive population-level dynamics from a microscopic description of organismal interactions for both well-mixed [89, 90, 91] and spatially-extended predator-prey ecosystems [92, 93, 86, 10]. This advance takes explicit account of the discrete nature of individuals in a population, and uses a system-size expansion [94] of the master equation to show how demographic noise acts as a driver of number fluctuations: in a sense, the shot noise persistently drives decaying population fluctuations, whose overall effect is to produce noisy but periodic population dynamics and spatial patterns.

A natural way to formulate these phenomena, especially in a spatially-extended context, is to adapt the annihilation and creation operators of field theory to this classical context [95, 96, 97, 98] (for a review and history, see Ref. ([99])), and thence to derive a path-integral formulation that is especially convenient for calculation[86, 10, 100]. With such techniques, it has been shown, for example that the extinction transition of the predator-prey system can be mapped into Reggeon field theory[59] and thus is in the universality class of directed percolation, which is ubiquitous for non-equilibrium systems with absorbing states [101, 55]. The path-integral formalism applied to an ecological example will be represented later in this chapter. For the moment we introduce commonly used expansion methods to the master equation for the predator-prey model.

2.3.1 Master equation scheme for individual-level model

The individual-level model starts with these processes:

$$\begin{aligned}
&\text{Degradation:} && A \xrightarrow{d_A} \varnothing, \quad B \xrightarrow{d_B} \varnothing, \\
&\text{Predation:} && A + B \xrightarrow{p/V} A + A, \\
&\text{Prey reproduction:} && B \xrightarrow{b} B + B, \\
&\text{Prey carrying capacity:} && B + B \xrightarrow{c/V} B, \\
&\text{(Competitive exclusion)}
\end{aligned} \tag{2.7}$$

where the processes are defined in a well-mixed patch of volume V.

The master equation is the time evolution of the probability of the system being at the state l at time t:

$$\frac{\partial P(l,t)}{\partial t} = \sum_{l' \neq l} T(l|l')P(l',t) - \sum_{l' \neq l} T(l'|n)P(l,t), \tag{2.8}$$

where $T(l|l')$ is the transition rate from state l' to state l. For Eq. (2.7), by denoting the state of the system by the number configuration $\{n_A, n_B\}$, the corresponding master equation is

$$\begin{aligned}
\frac{\partial P(\{n_A,n_B\},t)}{\partial t} &= \{(E_A - 1)T(n_A - 1, n_B|n_A, n_B) \\
&+ (E_B - 1)T(n_A, n_B - 1|n_A, n_B) \\
&+ (E_A^{-1}E_B - 1)T(n_A + 1, n_B - 1|n_A, n_B) \\
&+ (E_B^{-1} - 1)T(n_A, n_B + 1|n_A, n_B)\}P(\{n_A, n_B\}, t)
\end{aligned} \tag{2.9}$$

where the step operators are defined as:

$$E_i^{\pm} f(\{n_i\}) = f(\{n_i \pm 1\}), \tag{2.10}$$

and here $i = A, B$. Specifically, the transition rates for Eq. (2.7) are

$$\begin{aligned}
T(n_A - 1, n_B|n_A, n_B) &= d_A N_A, \\
T(n_A, n_B - 1|n_A, n_B) &= d_B N_B + \frac{c}{V} N_B(N_B - 1), \\
T(n_A + 1, n_B - 1|n_A, n_B) &= \frac{p}{V} N_A N_B, \\
T(n_A, n_B + 1|n_A, n_B) &= bN_B.
\end{aligned} \tag{2.11}$$

2.3.2 van Kampen system size expansion

To solve the master equation, we use expansion techniques. The first is called the Kramers-Moyal expansion [102, 103], and works by expanding the step operators by

$$E_i^{\pm} = \sum_{\nu=0}^{\infty} \frac{(\pm 1)^\nu}{\nu!} \left(\frac{\partial}{\partial n_i} \right)^\nu . \tag{2.12}$$

By taking the first two terms of the expansion, we obtain a Fokker-Planck equation

$$\frac{\partial P}{\partial t} = -\sum_i \frac{\partial}{\partial n_i}(\mathcal{A}_i P) + \frac{1}{2} \sum_{i,j} \frac{\partial^2}{\partial n_i \partial n_j}(\mathcal{B}_{ij} P). \tag{2.13}$$

Note that here the integer variables n_i have been treated as real variables, valid when $n_i \gg 1$. The corresponding Langevin equation in Ito's sense is

$$\frac{d\mathbf{n}}{dt} = \boldsymbol{\mathcal{A}}\mathbf{n} + \boldsymbol{\eta} \tag{2.14}$$

with $\langle \eta_i(t)\eta_j(t') \rangle = \mathcal{B}_{ij}$. However, individual processes are discrete, and thus the derivatives do not make sense for discontinuous transitional rates. A natural way to handle this is to recall that similar problems arise in quantum field theory, and the solution is to map the master equation into the path integral formalism, which we will discuss later.

Another reasonable approach is to write the above equations by treating number variables as densities and considering their incremental changes, leading to $\boldsymbol{\mathcal{A}}$ and $\boldsymbol{\mathcal{B}}$ being functions of the densities $\mathbf{n}/V$.

Van Kampen proposed a systematic expansion in a small parameter $1/\sqrt{\Omega}$, usually called the system size expansion or Ω expansion, to specifically quantify the dynamics of small fluctuations around the mean fields [94, 104]. Unlike the typical Kramers-Moyal expansion with no specific and controllable expansion parameter, in the system size expansion, Ω is an extensive quantity such as the volume of the system or total number of particles, and therefore the solutions converge to mean fields under the limit $\Omega \to \infty$. The zeroth order result of the stochastic theory is the standard set of Lotka-Volterra equations, now seen to be a mean field theory solution. Here we take Ω as some correlation volume, V, in which the dynamics is well-mixed, and the number of species i is expanded around the overall mean-field density, ϕ_i, with perturbation of order of $\sqrt{V}$:

$$n_i(t) = V\phi_i(t) + \sqrt{V}\xi_i(t) + \mathcal{O}(1) + \mathcal{O}(1/\sqrt{V}) + \dots , \tag{2.15}$$

where ξ_i in the first expansion term can be interpreted as the linear fluctuations in the density of i. We may

change variables and then rewrite the master equation as

$$P(\boldsymbol{n}(t)) \equiv \Pi(\boldsymbol{\xi}(t)), \tag{2.16}$$

which satisfies

$$\frac{\partial P}{\partial t} = \frac{\partial \Pi}{\partial t} - \sqrt{V} \sum_i \frac{d\phi_i}{dt} \frac{\partial \Pi}{\partial \xi_i} \,. \tag{2.17}$$

The raising and lowering operators for n_i are expanded as operators for ξ_i as well:

$$E_i^{\pm} = 1 \pm \frac{1}{\sqrt{V}} \frac{\partial}{\partial \xi_i} + \frac{1}{2V} \frac{\partial^2}{\partial \xi_i^2} + ... \tag{2.18}$$

The master equation in Eq. (4.2) can be rewritten in terms of ξ using the above expansion, and the terms of order $1/\sqrt{V}$ collected. To $\mathcal{O}(\sqrt{V})$ we find:

$$\begin{aligned} \frac{d\phi_A(t)}{dt} &= p\phi_A\phi_B - d_A\phi_A, \\ \frac{d\phi_B(t)}{dt} &= b\phi_B(1 - \frac{1}{\kappa}\phi_B) - p\phi_A\phi_B - d_B\phi_B, \end{aligned} \tag{2.19}$$

where $\kappa = \frac{b}{c}$ represents the carrying capacity. Comparing the coefficients of the next order $\mathcal{O}(V^0)$ gives

$$\frac{\partial \Pi(\boldsymbol{\xi}, t)}{\partial t} = -\sum_{i,j} A_{ij} \frac{\partial}{\partial \xi_i} \xi_j \Pi + \frac{1}{2} \sum_{i,j} B_{ij} \frac{\partial^2}{\partial \xi_i \partial \xi_j} \Pi \,, \tag{2.20}$$

where

$$\begin{aligned} A_{11} &= -d_A + p\phi_B, \quad A_{12} = p\phi_A \\ A_{21} &= -p\phi_B, \quad A_{22} = b - d_B - p\phi_A - c\phi_B^2. \end{aligned} \tag{2.21}$$

$$\begin{aligned} B_{11} &= d_A\phi_A + p\phi_A\phi_B, \\ B_{12} &= B_{21} = -p\phi_A\phi_B, \\ B_{22} &= b\phi_B + d_B\phi_B + p\phi_A\phi_B + c\phi_B^2. \end{aligned} \tag{2.22}$$

Eq. (2.20) is the differential equation for the probability of the first order correction $\boldsymbol{\xi}$ to the mean-field equation. This equation is a linear Fokker-Planck equation, i.e. the matrix $\boldsymbol{A}$ and $\boldsymbol{B}$ only depend on the mean-field $\phi_i(t)$ but not the stochastic variables ξ_i. The corresponding Langevin equations from Ito's formula

are

$$\frac{d\boldsymbol{\xi}(t)}{dt} = \boldsymbol{A}\boldsymbol{\xi}(t) + \boldsymbol{\gamma}(t) \ , \tag{2.23}$$

where $\boldsymbol{\gamma}(t)$ is a white noise satisfying

$$\langle \gamma_i(t)\gamma_j(t')\rangle = \boldsymbol{B}_{ij}\delta(t-t') \ . \tag{2.24}$$

Note that in the van Kampen expansion, the Langevin equation at successive orders of $\sqrt{V}$ has an additive noise, but that is because of the linearization step in the expansion. The coefficient of the noise is the field value from the previous order in $\sqrt{V}$. If we had stayed in the Kramers-Moyal expansion, the expansion/linearization step is not taken and the Langevin equation is explicitly with multiplicative noise.

The Langevin equations describe the dynamics of demographic noise. Since the matrices $\boldsymbol{A}$ and $\boldsymbol{B}$ only depend on the mean-field $\phi_i(t)$, the Langevin equations in Eq. (2.23) are linear, but the white noise $\boldsymbol{\gamma}$ is not additive. Thus the solutions for $\boldsymbol{\xi}$ contributed by the linear terms are expected to decay exponentially and converge to mean-field densities $\boldsymbol{\phi}$. However, the white noise plays an important role: whenever it can cancel out the contribution of the eigenvalues of $\boldsymbol{A}$, the dynamics of $\boldsymbol{\xi}$ will be driven away from convergent mean-field densities, i.e. white noise can select the frequency in the deterministic equations. This is interpreted as a resonant effect induced by demographic stochasticity through shot noise with the resonant frequency near the slowest decaying mode in the mean-field solutions [89].

2.3.3 Power spectrum and quasicycles

As described above, the power spectrum of demographic noise is expected to have a resonant frequency corresponding to the deterministic eigenvalue. The power spectrum $P_{ij}(\omega)$ can be calculated by taking the Fourier transform of the Langevin equations:

$$-i\omega\boldsymbol{\xi} = \boldsymbol{A}\boldsymbol{\xi} + \boldsymbol{\gamma}(\omega) \ , \qquad \langle \gamma_i(\omega)\gamma_j(-\omega)\rangle = \boldsymbol{B}_{ij}, \tag{2.25}$$

and thus

$$P_{ij}(\omega) = \langle \widetilde{\xi}_i(\omega)\widetilde{\xi}_j(-\omega)\rangle \ , \tag{2.26}$$

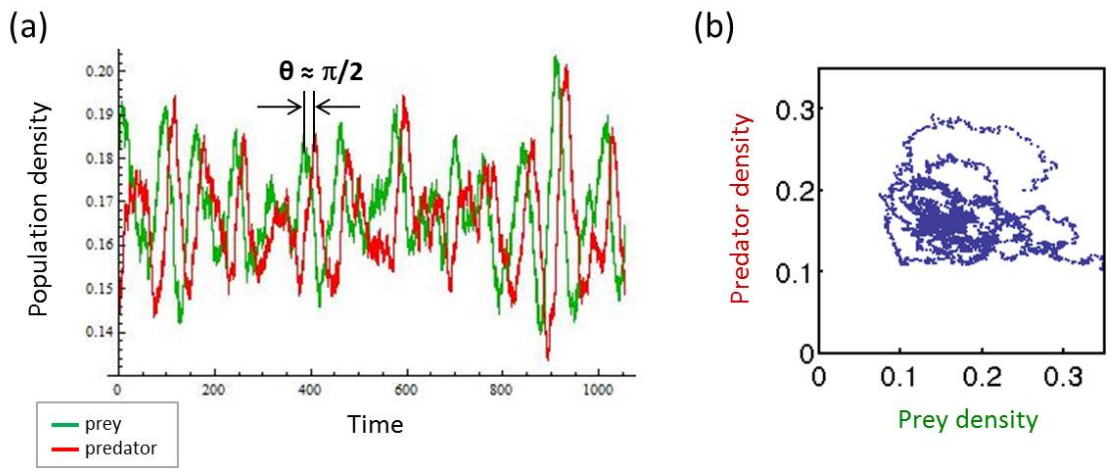

Figure 2.5: **Quasicycles from stochastic individual-level predator-prey model**. (a) Persistent oscillations due to demographic noise, with $\pi/2$ phase shift. (b) Phase portrait shows that whenever the trajectory is drawn to the fixed point in the middle, it is driven out by demographic noise.

whose Fourier transform gives the auto-correlation function. Specifically,

$$P_{11}(\omega) = \frac{\alpha + \beta\omega^2}{(\omega^2 - \Omega^2)^2 + \Gamma^2\omega^2}. \tag{2.27}$$

The form in Eq. (2.27) indicates a resonant spectrum . The peak of the power spectrum represents a characteristic frequency of population oscillations from the demographic noise; such cycles are termed quasicycles. Quasicycles are induced by intrinsic noise due to demographic stochasticity. Contrary to deterministic models such as the satiation model, no additional mechanism is required to reproduce oscillations in population.

The phenomenon of quasicycles has been previously discussed in the literature, some of which had attempted to calculate the spectrum of the oscillations [105, 106, 107, 108, 109, 110, 111, 112, 113]. Nevertheless, the calculations were not generally systematic.

As large ω, the asymptotic form of the spectrum of quasicycles has a long tail with ω^{-2} scaling. In contrast, stochastic oscillations can also come from a dynamical system with limit cycles perturbed by extrinsic noise. In this case, the stochastic limit cycles have a shorter tail with ω^{-4} scaling [10]. This quantitative difference in power spectrum means that fluctuations due to quasicycles have a shorter time scale, and this can be used to distinguish them in real data [10, 76]. In [76], stochastic simulations of "hybrid" individual-level model were performed to test different types of cyclic dynamics. Specifically, through linear stability analysis on the deterministic satiation model in Eq. (2.6), the stable fixed points

and their corresponding eigenvalues can be calculated in terms of parameters. There are three types of fixed points: stable node, stable focus and limit cycles. In the stochastic simulations of this study, the rates of individual processes were adopted from the reaction forms in the deterministic satiation model, and the parameter values were chosen to let the corresponding deterministic fixed point to be each type. The resultant three types of stochastic dynamics are shown in Fig. 2.6. In particular, quasicycles with a stable focus as the deterministic fixed point show an approximately ω^{-2} tail in the noise spectrum, while the noise spectrum of limit cycles displays a shorter tail of an approximately ω^{-4} slope (as shown in the middle colum in Fig. 2.6) [76].

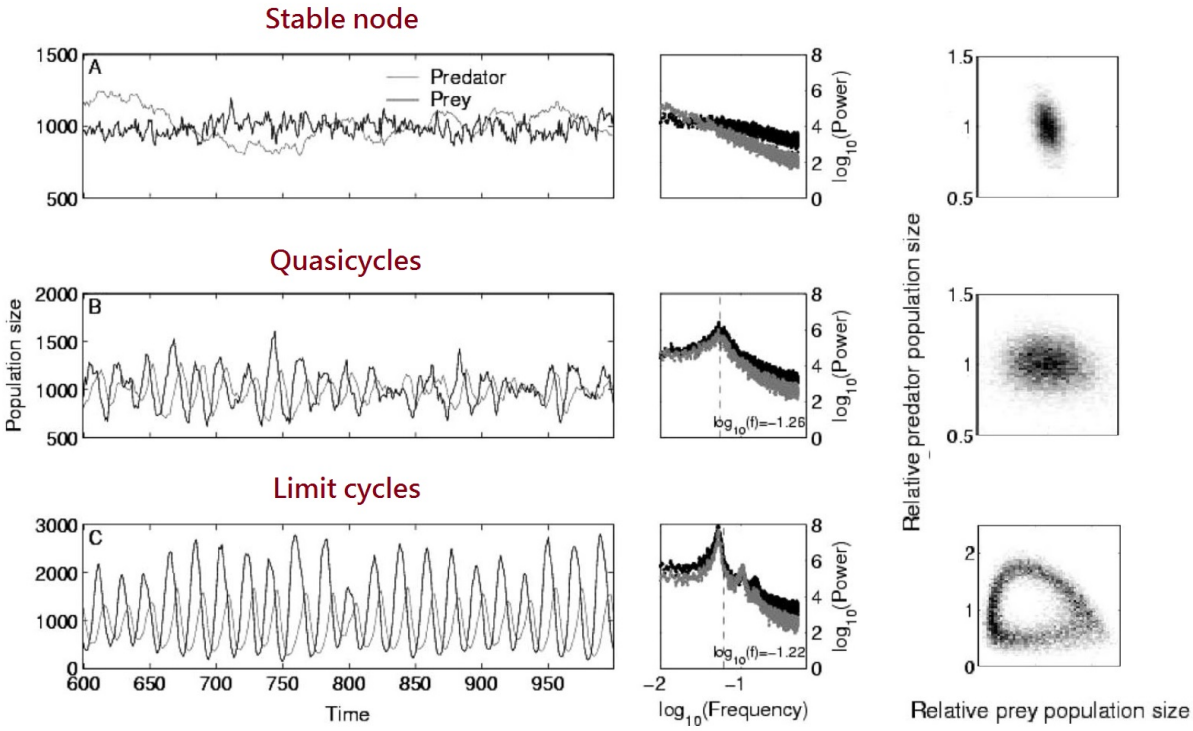

Figure 2.6: **Comparison of different types of cyclic dynamics for predator-prey systems**. The data were generated from "hybrid" stochastic simulations of individual-level model in [76]. Three cases were investigated: The parameters were chosen to make the underlying deterministic fixed point to be one of stable node (top row), stable focus (middle row) and limit cycles (bottom row). Time series of population of each type were shown in the left column. (Middle column) Noise spectrum of quasicycles with a stable focus as the deterministic fixed point shows an approximately ω^{-2} scaling, while the noise spectrum of limit cycles displays a steeper tail of an approximately ω^{-4} scaling. (Right column) Phase portrait of trajectories of each type of dynamics is displayed: For stable node type, random fluctuations without substantial routes, indicating no characteristic cycling behavior; for quasicycles, trajectories fluctuate around, reflecting composition of cycling with a wide range of characteristic period; for limit cycles, trajectories form persistent loops with a main characteristic period and small fluctuations coming from a short range of other periods. Figures are taken from [76].

2.3.4 Validity of well-mixed condition

In Section 2.3.2, the system size expansion method introduced the volume V and $1/\sqrt{V}$ as the small parameter. When $V \to \infty$ the demographic fluctuations average out and the mean field results are obtained. However, the physical meaning of V remains ambiguous. In a large spatially-extended system, the spatial-temporal dynamics should still be observable, because the fluctuations from distant positions would be uncorrelated and therefore the average of demographic fluctuations might not cancel each other. This implies that the meaning of the volume used in the well-mixed system size expansion should relate to the characteristic length of the system, e.g. the correlation length. For instance, if individuals are separated by a distance longer than the correlation length, their behaviors are not correlated and therefore their contributions to the fluctuations will not be suppressed under averaging. The correlation length and the characteristic volume size may be estimated by the parameters of the system [10]. The average time for individuals to diffuse in d dimension in a patch with size $V \sim L^d$ is $t \sim L^2/D$ where D is coarse-grained diffusion coefficient. To regard the patch is well-mixed, the time to have a significant reaction with rate R has to be longer than the diffusive time, i.e. $L^2/D < 1/R$. Thus the size of a well-mixed patch is about $V \sim (D/R)^{d/2}$. Beyond the well-mixed patch, individual behaviors do depend on space, e.g. an individual is hardly affected by another that is distant, and simulations readily exhibit propagating fronts and other spatially-coherent structures [114]. Calculations with consideration of individual diffusion have been done by system size expansion method and bosonic path integral formalism [93, 10, 100], where the results show quasipatterns emerging from demographic stochasticity.

2.3.5 Urn model

An important feature of ecosystem models is the carrying capacity. An alternative way to model this is through a constraint, known as the Urn model. The Urn model is another individual level model, which considers conservation of total individual number N. That is, a new individual can only be created when there is a vacancy E in the system, and a vacancy is regained when any individual is removed. The Urn model version for the predator-prey system was shown in [115, 89]. The individual reactions of a predator-prey system in the Urn model are

$$\begin{aligned} \text{Degradation:} \qquad & A \xrightarrow{d'_{\mathrm{A}}} E, \quad B \xrightarrow{d'_{\mathrm{B}}} E, \\ \text{Predation:} \qquad & A + B \xrightarrow{p'} A + A, \\ \text{Prey reproduction:} \qquad & B + E \xrightarrow{b'} B + B. \end{aligned} \tag{2.28}$$

Note that there is no need to include the competitive exclusion term $B + B \to B$ in Eq. (2.7), because we have the constraint that $\sum_i A_i + \sum_i B_i + \sum_i E_i = N$. Following the technique of master equation and the calculation in Section 2.3.2, the corresponding mean-field equations are

$$\begin{aligned} \frac{d\phi_A(t)}{dt} &= 2p'\phi_A\phi_B - d'_A\phi_A, \\ \frac{d\phi_B(t)}{dt} &= 2b'\phi_B(1-\phi_A-\phi_B) - 2p'\phi_A\phi_B - d'_B\phi_B, \end{aligned} \tag{2.29}$$

which after rearrangement have the same form as Eq. (2.19). Since the Urn model has a constraint on the total number of individuals, its individual-level simulations are in general cheaper.

2.4 Conclusion

In this chapter, we have seen that the modeling of predator-prey interactions is unexpectedly subtle. Mean-field interactions cannot capture the population cycles, which arise due to the effects of demographic stochasticity. Mathematically this is reflected in the presence of multiplicative noise in the governing Langevin equations. The ecological significance is that one does not need to over-model the system to obtain cycles if the proper level of description (the individual level) is used. This means that efforts to fit experimental data need not be so constrained as at present, when satiation effects cannot be fitted independently from the period of population cycles. These considerations apply to spatial variations also, and lead to observable consequences such as stochastic Turing patterns.

The techniques and perspectives introduced here will be used later in this thesis. First we will examine the anomalous population cycles observed when mutations introduce a sub-population into a predator-prey system. Second we will use these techniques to describe interactions in turbulent fluids, which numerical simulations have shown an unexpected predator-prey character. To include space in the description is simplified using quantum field theory techniques to handle the integer-value fields. this leads to a functional integral formulation which can be used to determine the universality class of ecological transitions.

Chapter 3

Anomalous population dynamics arising from rapid evolution

From the previous chapter we have seen that predator-prey ecosystems exhibit characteristic stochastic oscillations arising from demographic stochasticity with $\pi/2$ phase shift, which can be explained from their population dynamics, supported by recorded data. Thence one would naturally expect to observe these features when one conducts experiments on ecosystems composed of prey and predator such as bacteria and their phage. Surprisingly, experimentalists found that it is not always the case; population dynamics characterized by atypical phase relationships have been reported in different predator-prey ecosystems. For example, as shown in Fig. 3.1 (a), the population dynamics between prey (algae) and predator (rotifer) is out of phase (i.e. with π phase difference). In another case shown in Fig. 3.2 (a), at first algae and rotifer showed typical predator-prey oscillations with $\pi/2$ phase difference, but at some point the prey algae population became constant while the predator rotifer population still oscillated, but with a longer period. It was then realized that the anomalous phase relationship reflected the presence of an additional sub-population of prey which arose from mutation, and this mutant strain was impacting the interactions in the ecosystem. Such phenomena are referred to as *rapid evolution*, even though this term is somewhat misleading: mutation rates are not accelerated by predation pressure, but the infiltration of the mutant strain into the population is accelerated, ultimately providing a mechanism for strain diversification.

3.1 Interaction and timescale between ecology and evolution

Evolution is usually thought of as an on-going process involving the combination of genetic variation and selection. Conventionally, the evolutionary time scale is assumed to be much longer than the life time of an individual in the population. This assumption makes sense, since the general impression about evolution is that it has to take millions of years for a "fitter trait" to appear from random mutation, to be selected and to become fixed in the population. Therefore, evolution could hardly matter for ecological events, which come from the interactions between individuals of a system within their life time. However, how exactly the evolutionary process occurs and acts on ecological systems is unknown, and it is not inconceivable to think

that on-going evolution and ecological processes could in principle couple to each other. For this to happen, the evolution time scale must be comparable to the ecological time scale; an example where such rapid evolution has entered the public consciousness is antibiotic resistance, which recently has been documented to be emerging rapidly as a result of the treatment for bacterial infections. In general, rapid evolution can manifest in various changes in traits. The selectable traits are usually referred as phenotypes, whose change sometimes can also reflect genotypic variations [8]. Rapid phenotypic evolution has been reported in many natural ecosystems, of which the evolutionary rate can be extremely high when encountering environmental stress [8].

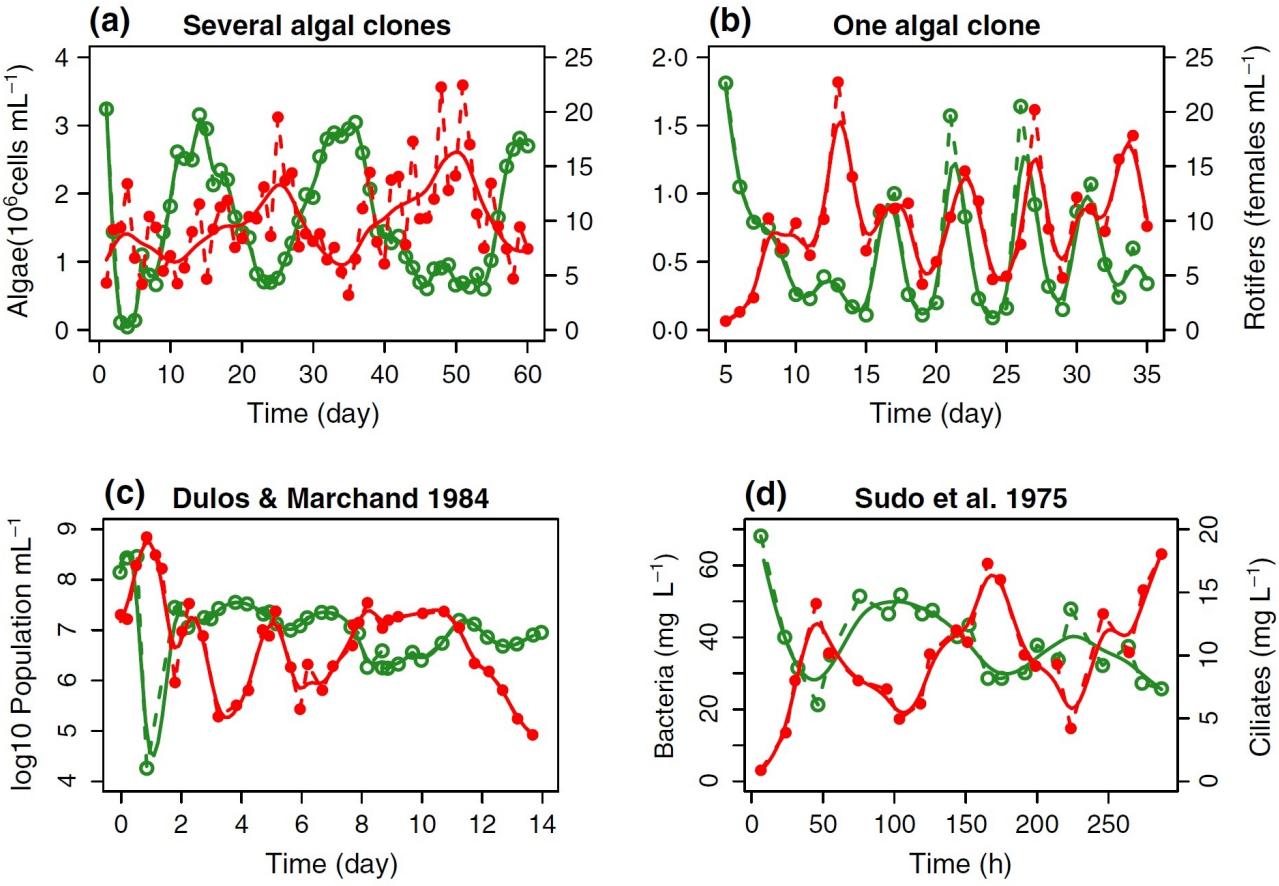

Figure 3.1: **Comparison of normal predator-prey dynamics and evolutionary dynamics**. (a) Evolutionary cycles appear between multiple algae clones (prey, in green) with rotifer (predator, in red). (b) Dyanmics of single algae and rotifer shows typical predator-prey cycles. (c) Evolutionary cycles for *E. coli.* (green) and its phage (red). (d) Evolutionary cycles for bacterial prey (green) and ciliate predator (red). Figures are taken from [7]. Original data in (a)(b) are from [26], data in (c) are from [116] and data in are from [117].

3.2 Experiments on rapid evolution in predator-prey ecosystems

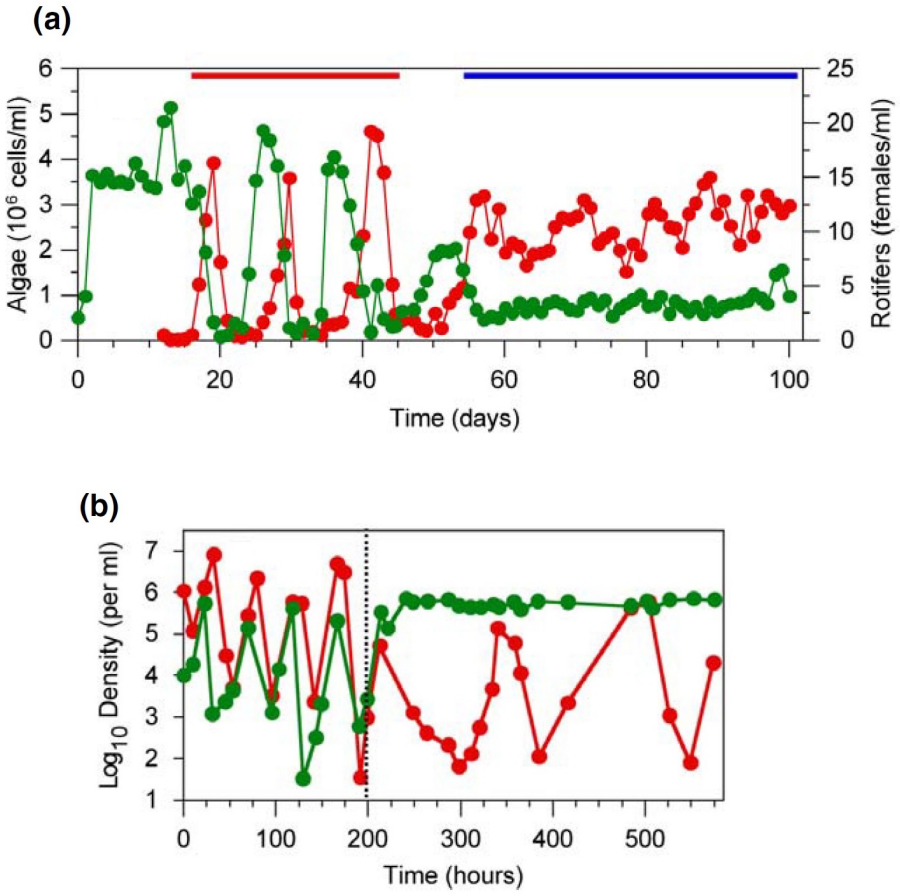

Figure 3.2: **Cryptic cycles in predator-prey dynamics**. (a) Cryptic cycles appear between multiple algae clones (prey, in green) with rotifer (predator, in red). (b) Normal cycles appear first in the dynamics between *E. coli.* (green) and its phage (red), and then cryptic cycles emerge. Figures are taken from [29]; original data in (b) are from [28].

The classical literature on predator-prey systems [118] assumes that evolution occurs on such long time scales that it can be neglected, but it is not obvious that this is always valid [119].

It has been observed that rapid response to strong selection among genetically distinct strains can occur under intense ecological interactions and cause dramatically changes in predator-prey ecosystems in only a few generations [27, 28, 120, 26, 29, 121, 122, 123, 7]. In these examples, anomalous population dynamics appears, potentially as a result of rapid evolution [27, 28, 120, 26, 29, 121, 122, 123, 7]. In such anomalous dynamics, the typical $\pi/2$ phase shift between predator and prey is absent; instead, the dynamics of prey and predator population can be out of phase, *i.e.* with a phase shift of $\pi/2$. The dynamics in these cases is

termed "evolutionary cycles" and has been reported in different predator-prey systems such as rotifer and algae[120, 26], *Bdellovibrio bacteriovorus* and *E. coli* [116] and ciliate and bacteria [117]. It was also found that the dynamics is accompanied by long oscillation periods in the population [26]. More surprisingly, it was also reported that sometimes prey populations remain almost constant while the predator population oscillates. This occurs in rotifer-algae system [29] and phage-*E. coli.* systems [27, 28, 124]. This phenomenon is termed "cryptic cycles".

This anomalous dynamics is attributed to emergent sub-populations in the ecosystems. For example, in the chemostat experiments of the phage-bacteria system studied by Bohannan and Lenski, cryptic cycles occurred once a mutant type of phage-resistant or "inedible" bacteria appeared [27, 28, 124]. It was then postulated that the anomalous phase relationship is a result of dramatic changes in the population structure due to rapid evolution [27, 28, 124, 26, 29]. A similar explanation was also proposed for the rotifer-algae system, where the mutant algae prey is defended against rotifer predator by having low food value or less palatable morphology [26, 29]. The structure change in the population also implies coexistence of both the wild-type and mutant prey; in other words, there should exist some types of trade-offs that prevents the defended mutant prey from overwhelming the ecosystem [27, 28, 124, 26, 29].

3.2.1 Why "rapid" "evolution"?

Why exactly is this dynamics with anomalous phase relationship called "rapid evolution"? Conventionally, ecologists regard this dynamics to be (1)"evolutionary" because the unusual phase relationship is caused by prey sub-populations emerging from a mutation and (2)"rapid" because the dynamics can spread this mutant into a wild-type population on similar time scales as ecological influences. In other words, the mutant prey emerges quickly and coexists with the wild-type prey, and their dynamics is synchronized with the predation.

3.3 Deterministic models in rapid evolution experiments

Such phenomena have been modeled with deterministic differential equations containing empirical satiation as expressed by the Holling type II response function with various hypothesis on the mechanism of species interactions. For example, models include sub-population structures of palatable and defended prey straits with ratio-dependent rates [27], density-dependent or switching predation [125, 120, 126, 26, 127, 29, 121, 62]

3.3.1 Chemostat model

In a basic chemostat model for rapid evolution, densities of nutrient N, defended algae C_1, wild-type algae C_2 and rotifer predator B obey the following equations [120, 126, 26, 128, 127, 121, 62, 129]:

$$\begin{aligned}
\frac{dN}{dt} &= \delta(N_I - N) - \sum_{i=1}^{2} F_c(N, C_i, p_i), \\
\frac{dC_i}{dt} &= \alpha F_c(N, C_i, p_i) - F_b(C_i, B, p_i) - \delta, \\
\frac{dB}{dt} &= \beta \sum_{i=1}^{2} F_b(C_i, B, p_i) - \delta,
\end{aligned} \tag{3.1}$$

where $i = 1, 2$, p_i is palatability by the predator with $p_1 < p_2$, δ is the chemostat dilution rate, N_I is the maximum nutrient concentration, F_c and F_b are saturation function forms for prey's consumption of nutrient and predation respectively with conversion rate α and β. Specifically, the predation response F_b is monotonically increasing with p_i. As a tradeoff, F_c is set to be a function that saturates slower when p_i has lower value, which gives a smaller effective growth rate for algae C_i as a cost. The dimension of such a complicated chemostat model can be reduced by eliminating the nutrient equation after applying an Urn-model-like assumption that the sum of all species density is constant, leading to an effective growth rate, r_i, for the algae species i [121, 29, 62, 130]. Through linear stability analysis on the resultant equations, the relative angle of eigenvectors were investigated for anomalous phase difference in evolutionary cycles and cryptic cycles [121, 29, 62, 130]. The model predicts that when defense of the defended prey is strong (*i.e.* $p_1 \ll p_2$), as the effective growth cost (*i.e.* $r1/r2$) decreases, the dynamics transits from evolutionary cycles to cryptic cycles [125, 131, 29, 121, 62, 130].

3.3.2 Quantitative trait evolution model

Another type of model for rapid evolution is adapted from a quantitative trait evolution model [132]. In this type of model, traits have continuous values that increase with the derivative of fitness of the corresponding trait value at current time. This is interpreted as reflecting phenotypic plasticity or genetic evolution. The prey and predator fitness function forms are given by the reaction functions in the predator-prey model (*e.g.* satiation model) [125, 16, 133, 129, 134, 135, 136, 137, 8, 138]. The coefficients in the interaction terms in the predator-prey model also depend on the trait values at that time. Therefore, by coupling the differential equations of average trait values of prey and predator to the equations of population dynamics in the predator-prey model, the overall dynamics in this type of model is interpreted as feedback between evolution and ecology. The anomalous phase relationship due to rapid adaptation has also been investigated

in these trait evolution models [133, 134, 135, 137, 8, 138].

However, the role of demographic stochasticity, the statistical characteristics and the coherent structures of the systems in rapid evolution are still unknown. In the next chapter, we will use techniques from Chapter 2 to treat the rapid evolution problems stochastically at the individual level.

Chapter 4

Emergence of rapid evolution from demographic stochasticity

The purpose of this chapter is to propose and analyze a minimal model for rapid evolution that includes the effects of demographic stochasticity. Using tools from statistical mechanics, demographic stochasticity has been successfully captured using individual-level models (ILM) in a variety of situations that range from simple well-mixed predator-prey interactions [89, 90, 91] to spatially-extended systems that can exhibit quasi-Turing patterns [59, 92, 86, 93, 10, 100]. Here we propose an ILM for rapid evolution that we solve analytically by techniques of master equation described in Section 2.3, followed by a volume expansion [94] to derive the effective Langevin equation for demographic fluctuations. Accompanied by Gillespie simulation [139] for the model, we show that this simple stochastic model can predict rapid evolution phenomena in well-mixed systems, yielding phase diagrams that are similar to those of more complex deterministic models and in qualitative agreement with available data. Thus key aspects of rapid evolution can be minimally modeled by subpopulation dynamics driven simply by intrinsic demographic stochasticity. We also show a statistical approach by mapping the model into a coherent-state path integral representation [95, 96, 97, 98, 140] (for a review and history, see Ref. ([99])). We will find that the solutions can recover the semi-quantitatively experimental observations with both oscillations and fluctuations, and that the statistical calculation intrinsically includes the deterministic dynamics and the dynamics of the internal demographic fluctuations. It is very important that the internal noise contributing to the undamped fluctuating dynamics is not an additive noise, as is often assumed to be the case in a typical Langevin equation. Demographic stochasticity leads to persistent population cycles called quasicycles. We will see that there is no need to invoke additional dynamical processes, such as predator satiation, to account for the existence of persistent cycles. Our model can serve as a starting point for analyzing spatial distributions and large fluctuations such as extinction.

4.1 Individual-level model for rapid evolution

To model this quantitatively, consider a model for a system composed of nutrients for the prey (N), the vulnerable (wild-type) prey (W), the so-called 'defended' (mutant) prey (D), and the predator (P). The basic individual processes for them are regrowth of nutrients, reproduction of prey, predation by predator, death and migration to the nearest site for all individuals:

$$\begin{aligned} &\varnothing_i \xrightarrow{b} N_i, \quad N_i R_i \xrightarrow{\frac{c_R}{V}} R_i R_i, \quad R_i P_i \xrightarrow{\frac{p_R}{V}} P_i P_i, \\ &S_i \xrightarrow{d_S} \varnothing_i, \quad S_i \xrightarrow[\langle ij \rangle]{\nu_S} S_j \end{aligned} \tag{4.1}$$

where $\varnothing_i$ denotes the empty state at site i, $R = W, D$ is the prey index, S_i represents species $S = N, W, D, P$ at site i, and V is an effective coarse-grained or correlation volume in which there is no significant population spatial variation. In ecology, V is called the patch size, and it acts as a control on the amplitude of demographic fluctuations. Because V is larger than the mean volume per organism, we will make analytical progress by using an expansion in inverse powers of V. The defended prey experiences a smaller predation rate than the wild-type prey, *i.e.* $p_D < p_W$, and also has a smaller reproduction rate or larger degeneration rate due to the metabolic cost for defense, *i.e.* $c_W > c_D$ or $d_W < d_D$. For the nutrients, ν_N and d_N are set to zero. The corresponding master equation that defines the time evolution of the probability distribution of population states is

$$\begin{aligned} \frac{dP(\{n_{S_i}\})}{dt} = &\sum_{\{n_{S_i}\}} \Big\{ b(E_{N_i}^{-1} - 1)(n_{N_i}^{\max} - n_{N_i}) \\ &+ \sum_S d_S (E_{S_i} - 1) n_{S_i} + \sum_R \Big[\frac{c_R}{V} (E_{N_i} E_{R_i}^{-1} - 1) n_{N_i} n_{R_i} \\ &+ \frac{p_R}{V} (E_{R_i} E_{P_i}^{-1} - 1) n_{R_i} n_{P_i} \Big] \Big\} P(\{n_{S_i}\}), \end{aligned} \tag{4.2}$$

where $\{\cdots\}$ denotes the set over all sites and species, the prey index $R = W, D$, and the step operators $E_{S_i}^{\pm}$ are defined as $E_{S_i}^{\pm} f(\{n_{S_i}\}) = f(\{n_{S_i} \pm 1\})$.

4.1.1 Van Kampen's system size expansion

Following van Kampen system size expansion described in Section 2.3.2 [104], the number of species i is expanded around the overall mean-field density, ϕ_i, collecting terms in perturbation theory at different order

of $1/\sqrt{V}$. Specifically, the resultant mean-field equations are

$$\begin{aligned}
\frac{d\phi_N(t)}{dt} &= b\,(\phi_{N,\max} - \phi_N) - c_W\phi_N\phi_W - c_D\phi_N\phi_D, \\
\frac{d\phi_W(t)}{dt} &= c_W\phi_N\phi_W - p_W\phi_D\phi_P - d_W\phi_W, \\
\frac{d\phi_D(t)}{dt} &= c_M\phi_N\phi_D - p_D\phi_D\phi_P - d_D\phi_D, \\
\frac{d\phi_P(t)}{dt} &= p_W\phi_W\phi_P - p_D\phi_D\phi_P - d_P\phi_P\ .
\end{aligned} \tag{4.3}$$

Comparing the coefficients of the next order $\mathcal{O}(V^0)$ gives the Fokker-Planck equation in Eq. (2.20),

$$\frac{\partial\Pi(\boldsymbol{\xi},t)}{\partial t} = -\sum_{i,j} A_{ij}\frac{\partial}{\partial\xi_i}\xi_j\Pi + \frac{1}{2}\sum_{i,j} B_{ij}\frac{\partial^2}{\partial\xi_i\partial\xi_j}\Pi\ ,$$

where coefficient matrices $\boldsymbol{A}$ and $\boldsymbol{B}$ as

$$\begin{aligned}
&A_{11} = -b - c_W\phi_W - c_D\phi_D\ ,\ A_{12} = -c_W\phi_N\ ,\ A_{13} = -c_W\phi_N\ ,\ A_{14} = A_{41} = 0\ , \\
&A_{21} = c_W\phi_W\ ,\ A_{22} = c_W\phi_N - d_W - p_W\phi_P\ ,\ A_{23} = A_{32} = 0\ ,\ A_{24} = -p_W\phi_W\ , \\
&A_{31} = c_D\phi_D, A_{33} = c_D\phi_N - d_D - p_D\phi_P, A_{34} = -p_D\phi_D\ , \\
&A_{42} = p_W\phi_P, A_{43} = p_D\phi_P, A_{44} = p_W\phi_W + p_D\phi_D - d_P\ .
\end{aligned} \tag{4.4}$$

$$\begin{aligned}
&B_{11} = b(\phi_{N,\max} - \phi_N) + c_W\phi_N\phi_W + c_D\phi_N\phi_D\ ,\ B_{12} = B_{21} = -c_W\phi_N\phi_W\ , \\
&B_{13} = B_{31} = -c_D\phi_N\phi_D\ ,\ B_{14} = B_{41} = B_{23} = B_{32} = 0\ , \\
&B_{22} = c_W\phi_N\phi_W + p_W\phi_W\phi_P + d_W\phi_W\ ,\ B_{24} = B_{42} = -p_W\phi_W\phi_P\ , \\
&B_{33} = c_D\phi_N\phi_D + p_D\phi_D\phi_P + d_D\phi_D\ ,\ B_{34} = B_{43} = -p_D\phi_D\phi_P\ , \\
&B_{44} = p_W\phi_W\phi_P + p_D\phi_D\phi_P + d_P\phi_P\ .
\end{aligned} \tag{4.5}$$

4.1.2 Spatial extension

To complete the specification of the model, we need to include particle diffusion, for which the Doi formalism [95] is especially convenient. The resulting spatially-extended model represents a non-perturbative formulation of the model and can be used to study spatial patterns and large demographic fluctuations that are important near the ecosystem extinction transition, where the predator population vanishes [59, 141]. The procedure is to write Eq. (4.2) as a second-quantized Hamiltonian and then express the generating

functional for probabilities and correlations as a path integral [96, 97, 140, 99]. Since the systems in the rotifer-algae experiments are well-mixed, the diffusion terms are neglected in the following calculation and simulation.

4.2 Path integral formalism for rapid evolution

Following the standard procedure, we introduce the probability state vector in the Fock space constructed by different occupation number states

$$|\psi\rangle = \sum_{\{n_{S_i}\}} P(\{n_{S_i}\})|\{n_{S_i}\}\rangle, \tag{4.6}$$

so that the master equation becomes a Liouville equation

$$\partial_t|\psi\rangle = -\hat{H}|\psi\rangle, \tag{4.7}$$

with the Liouvillian $\hat{H} = \sum_i \hat{H}_i$

$$\begin{aligned}\hat{H}_i \quad &= b(1-\hat{a}^\dagger_{N_i})(n^{\max}_{N_i} - \hat{a}^\dagger_{N_i}\hat{a}_{N_i}) + \sum_R \Big[\frac{c_R}{V}(\hat{a}^\dagger_{N_i}\hat{a}_{N_i}\hat{a}^\dagger_R\hat{a}_{R_i} \\ - \quad &\hat{a}_{N_i}\hat{a}^{\dagger 2}_{R_i}\hat{a}_{R_i}) + \frac{p_R}{V}(\hat{a}^\dagger_{R_i}\hat{a}_{R_i}\hat{a}^\dagger_{P_i}\hat{a}_{P_i} - \hat{a}_{R_i}\hat{a}^{\dagger 2}_{P_i}\hat{a}_{P_i})\Big] \\ + \quad &\sum_S \Big[d_S(\hat{a}^\dagger_{S_i}\hat{a}_{S_i} - \hat{a}_{S_i}) + \nu_S \sum_{j\in N.N.}(\hat{a}^\dagger_{S_i} - \hat{a}^\dagger_{S_j})\hat{a}_{S_i}\Big]\end{aligned} \tag{4.8}$$

where $\hat{a}^\dagger_{S_i}$ and $\hat{a}_{S_i}$ are bosonic raising and lowering number operator for species S at site i. Eq. (4.7) and (4.8) are exact and naturally allow the representation of the many-body path integral formalism.

By using the coherent-state representation, the Hamiltonian can be mapped onto the basis of coherent states and becomes a function of α^*_S and α_S which are the left and right eigenstates of $\hat{a}^\dagger_S$ and $\hat{a}_S$ respectively for species $S = N, W, D, P$. Since in general multiple individuals can occupy the same site in spatial extended systems, $\hat{a}^\dagger_S$ and $\hat{a}_S$ are considered to follow the bosonic commutation relation. The effective Lagrangian density in the path integral becomes

$$\mathcal{L} = \sum_i \left[\alpha^*_S\left(\partial_t - \nu_S\nabla^2\right)\alpha_S + H\left(\{\,\alpha^*_S\,\},\{\,\alpha_S\,\}\right)\right] \tag{4.9}$$

where $\nu_N \equiv 0$.

To study the fluctuations about the mean-field densities, it is convenient to map the system from field

variables onto the physical variables by applying the canonical Cole-Hopf transformation [59]

$$\alpha_S^* = e^{\tilde{\rho}_S} \ , \alpha_S = \rho_S e^{-\tilde{\rho}_S} \tag{4.10}$$

where ρ_S are the population variables for species S and $\tilde{\rho}_i$ are analogous to fluctuation variables. The Hamiltonian density under the transformation is obtained as

$$\begin{aligned} H &= b\left(1-d^{\tilde{\rho}_N}\right)\left(n_{N,\max}-\rho_N\right)+\frac{c_R}{V}\left(1-e^{\tilde{\rho}_R-\tilde{\rho}_N}\right) \\ &+ \frac{p_R}{V}\left(1-e^{\tilde{\rho}_P-\tilde{\rho}_R}\right)+d_R\rho_R\left(1-e^{-\tilde{\rho}_R}\right) \\ &+ d_P\rho_P\left(1-e^{-\tilde{\rho}_P}\right). \end{aligned} \tag{4.11}$$

Further we apply the ansatz [93]

$$\tilde{\rho}_S \to \frac{\tilde{\rho}_S}{\sqrt{V}}, \quad \rho_S = V\phi_S + \sqrt{V}\xi_S, \tag{4.12}$$

where $\langle\tilde{\rho}_S\rangle$ are the mean-field population density variables and the deviations around them, ϕ_S, are of order $1/\sqrt{V}$. The patch size V becomes the system size in the well-mixed case. This expansion will lead to a lowest order of fluctuations in Gaussian form. After applying the expansion in Eq. (4.12), the Lagrangian density in Eq. (4.9) can be separated into different orders of $\sqrt{V}$

$$\mathcal{L} = \sqrt{V}\mathcal{L}^{(1)} + \mathcal{L}^{(2)} + ... \tag{4.13}$$

Here

$$\begin{aligned} \mathcal{L}^{(1)} &= \sum_S \tilde{\rho}_S\partial_t\phi_S + b\phi_N\tilde{\rho}_N + \sum_R\big[-\nu_R\tilde{\rho}_R\nabla^2\phi_R \\ &+ c_R\phi_N\phi_R\left(\tilde{\rho}_N-\tilde{\rho}_R\right)+p_R\phi_R\phi_P\left(\tilde{\rho}_R-\tilde{\rho}_P\right) \\ &+ d_R\phi_R\tilde{\rho}_R\big]+d_P\phi_P\tilde{\rho}_P-\nu_P\tilde{\rho}_P\nabla^2\phi_P. \end{aligned} \tag{4.14}$$

The stationary solution from $\frac{\delta\mathcal{L}_1}{\delta\tilde{\rho}_S}=0$ gives the mean-field dynamics:

$$\partial_t\phi_N = b\left(\phi_{N,\max}-\phi_N\right)-c_R\phi_N\phi_R, \tag{4.15}$$

$$\partial_t\phi_R = \nu_R\nabla^2\phi_R + c_R\phi_N\phi_R - p_R\phi_R\phi_P - d_R\phi_R, \tag{4.16}$$

$$\partial_t\phi_P = \nu_P\nabla^2\phi_P + \sum_R p_R\phi_R\phi_P - d_P\phi_P. \tag{4.17}$$

The Lagrangian density in the next order is

$$\mathcal{L}^{(2)} = \tilde{\boldsymbol{\rho}}^T \partial_t \boldsymbol{\xi} - \tilde{\boldsymbol{\rho}}^T \mathbf{A}[\{\phi_S\}]\boldsymbol{\xi} - \frac{1}{2}\tilde{\boldsymbol{\rho}}^T \mathbf{B}[\{\phi_S\}]\boldsymbol{\xi}, \tag{4.18}$$

where $\boldsymbol{\xi} = (\xi_N, \xi_W, \xi_D, \xi_P)$ and $\tilde{\boldsymbol{\rho}} = (\tilde{\rho}_N, \tilde{\rho}_W, \tilde{\rho}_D, \tilde{\rho}_P)$ are the fluctuation field vectors, and

$$\begin{aligned}
&A_{NN} = -b - \sum_R c_R \phi_R, \; A_{NR} = -A_{RN} = -c_R \phi_N, \\
&A_{NP} = A_{PN} = A_{WD} = A_{\nu_R} = 0, \\
&A_{RR} = -\nu_R k^2 + c_R \phi_R - p_R \phi_P - d_R, \\
&A_{RP} = -A_{PR} = -p_R \phi_R, \; A_{PP} = -\nu_P k^2 + p_R \phi_R - d_P,
\end{aligned} \tag{4.19}$$

$$\begin{aligned}
&B_{NN} = b(\phi_N^{\max} - \phi_N) + \sum_R c_R \phi_N \phi_R, \\
&B_{NR} = B_{RN} = -c_R \phi_N \phi_R, \\
&B_{NP} = B_{PN} = B_{WD} = B_{DW} = 0, \\
&B_{RR} = \nu_R \phi_R k^2 + c_R \phi_N \phi_R + p_R \phi_R \phi_P + d_R \phi_R, \\
&B_{RP} = B_{PR} = -p_R \phi_R \phi_P, \\
&B_{PP} = \nu_P \phi_P k^2 + \sum_R p_R \phi_R \phi_P + d_P \phi_P,
\end{aligned} \tag{4.20}$$

where $R = W, D$. The non-diffusive parts of this result agree with the calculation in Eq. (4.4) and (4.5).

Following the Martin-Siggia-Rose response function formalism [142, 143, 144], the next order $\mathcal{L}^{(2)}$ generates a Langevin equation capturing the dynamics with Gaussian fluctuations. However, it is important to emphasize that the Gaussian noise here is intrinsic because these fluctuations originate from the demographic stochasticity of the population at each time step. The outcome is quasicycles induced by a resonant amplification of intrinsic fluctuations [89], which leads to a slowly-decaying tail in the power spectrum that is distinct from the behavior of limit cycles with additive noise [10]. In our calculation, the noise depends on the mean field values because of the linearization step performed as part of the van Kampen volume expansion [94]. However, we emphasize that this is the signature of multiplicative noise within the van Kampen framework. If we had chosen to perform a Kramers-Moyal expansion [102, 103] instead, the noise would have been manifestly multiplicative, and linearization to obtain a systematic calculational procedure would have arrived at the van Kampen expansion results presented here.

Eq. (4.18) is equivalent to the Langevin equations as a function of wavenumber k and time:

$$\begin{aligned} \frac{d\boldsymbol{\xi}}{dt} &= \mathbf{A}\boldsymbol{\xi} + \boldsymbol{\gamma}, \\ \langle \gamma_S(k,t)\gamma_{S'}(k',t')\rangle &= \mathbf{B}_{SS'}(2\pi)^d \delta(k-k')\delta(t-t'). \end{aligned} \tag{4.21}$$

In contrast to deterministic models [120, 26, 29, 121, 122, 123, 27, 7, 126, 127, 133, 134, 129, 134], the dynamics depends not only on the Jacobian $\mathbf{A}[\{\phi_S\}]$ from the mean-field equation but also on the covariance matrix $\mathbf{B}[\{\phi_S\}]$. Since $\mathbf{B}_{RR'}[\{\phi_S\}]$ in Eq. (4.21) is governed by the macroscopic densities, the white noise $\boldsymbol{\gamma}$ that determines the dynamics of fluctuations is effectively non-additive. As mentioned previously, such white noise can select the frequency in the deterministic equations, resulting in periodic and strongly fluctuating population dynamics and spatial patterns as a resonant effect induced by demographic noise [89].

4.3 Predictions

4.3.1 Power spectrum and phase difference spectrum for evolutionary cycles and cryptic cycles

By using the form of power spectrum in Section 2.3.2, *i.e.*

$$P_{ij}(\omega) = \langle \tilde{\xi}_i(\omega)\tilde{\xi}_j(-\omega)\rangle \ ,$$

the phase difference between the fluctuation fields is defined as

$$\theta_{ij}(\omega) = \tan^{-1}\frac{\mathrm{Im}[P_{ij}(\omega)]}{\mathrm{Re}[P_{ij}(\omega)]} \ . \tag{4.22}$$

For example,

$$P_{WW}(\omega) = \frac{\beta_6\omega^6 + \beta_4\omega^4 + \beta_2\omega^2 + \beta_0}{\omega^8 + \alpha_6\omega^6 + \alpha_4\omega^4 + \alpha_2\omega^2 + \alpha_0} \ , \tag{4.23}$$

and the phase difference between total prey and the predator, $\theta_{(W+D)P}$, can be calculated from

$$P_{(W+D)P}(\omega) = \langle (\widetilde{\xi}_W(\omega) + \widetilde{\xi}_D(\omega))\widetilde{\xi}_P(-\omega)\rangle = P_{WP}(\omega) + P_{DP}(\omega) \ . \tag{4.24}$$

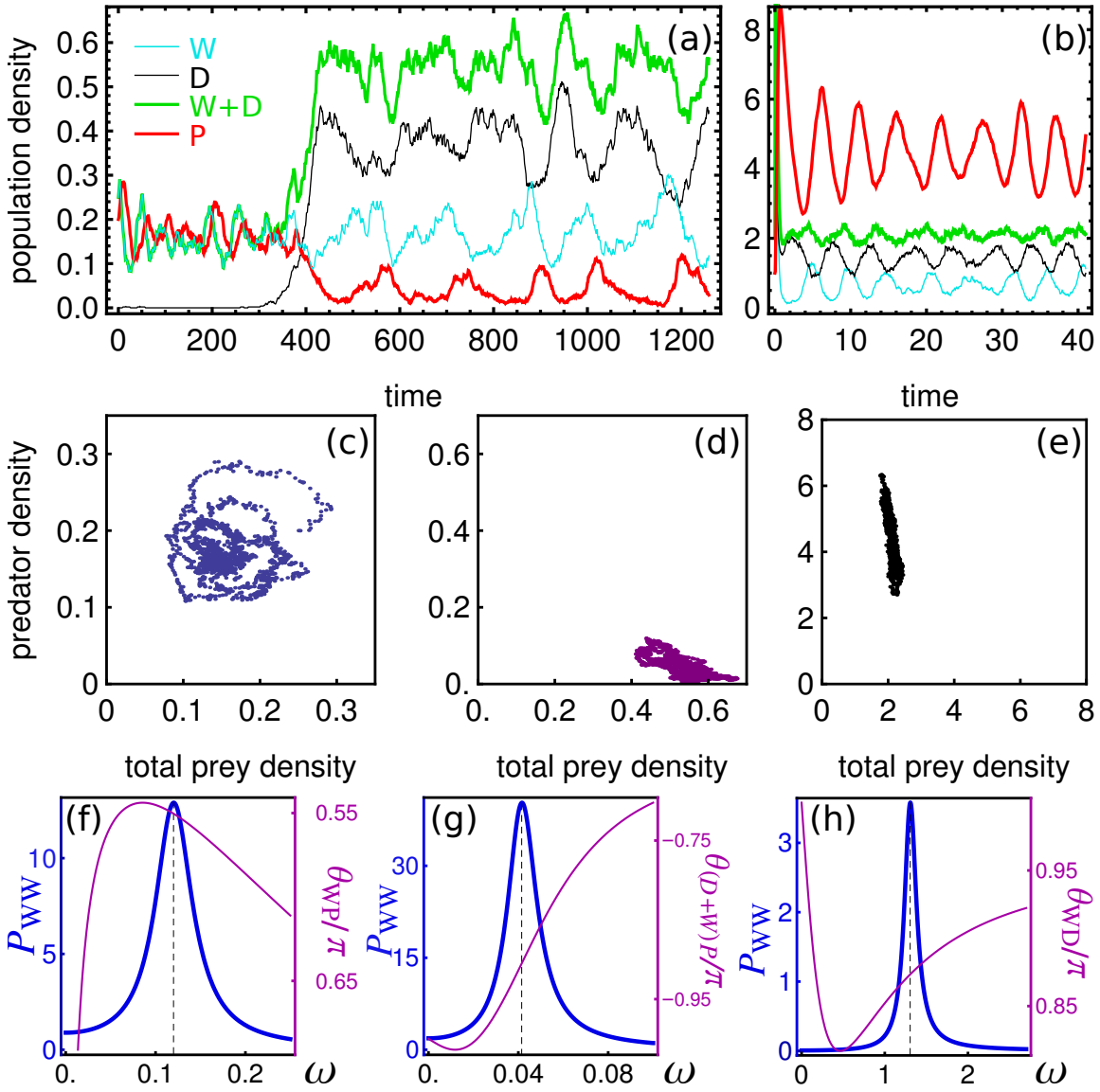

Figure 4.1: **Stochastic simulations for (a) evolutionary cycles emerging from normal cycles due to random mutation and (b) cryptic cycles.** Phase portraits of the steady states of (c) normal cycles and (d) evolutionary cycles from the stochastic simulations show that the phase differences between predator and the total prey population are roughly $\pi/2$ and π, respectively, while for (e) cryptic cycles there is no obvious phase relationship. (f)-(h) Power spectrum of the wild-type prey (thick curve) and phase difference spectrum (thin curve) from analytic calculations based on ILM. The estimated phase differences are -0.55π and 0.905π for (f) normal cycles and (g) evolutionary cycles, and for (h) cryptic cycles the predicted phase difference between the wild-type prey and the defended prey is approximately 0.874π. The parameter values are (a) $V = 1000$, $c_W = 0.3$, $p_W = 0.6$, $c_D/c_W = 0.8$, $p_D/p_W = 0.01$, $d_D/d_W = 1$, $\phi_{N,\max} = 1$, and $b = 0.1$ and (b) $V = 380$, $c_W = 60$, $p_W = 0.92$, $c_D/c_W = 0.95$, $p_D/p_W = 0.001$, $d_D/d_W = 7.5$, $\phi_{N,\max} = 16$, and $b = 0.1$.

Then the spectrum of phase difference between the predator and the total prey can be calculated, which has the form of

$$\theta_{(W+D)P}(\omega) = \frac{\rho_5\omega^5 + \rho_3\omega^3 + \rho_1\omega}{\rho_6\omega^6 + \rho_4\omega^4 + \rho_2\omega^2 + \rho_0} \,. \tag{4.25}$$

The results of analytic calculations and simulations based on Eq. (4.1) are shown in Fig. 4.1. We use the Gillespie algorithm [139] for stochastic simulations and introduce random mutation from the wild-type prey to the defended prey. The mutation is added purely to seed a new sub-population to see the dramatic impact of the fixed sub-population after mutations, but plays no significant role in the subsequent dynamics; thus mutations are neglected in our analytical calculations below. The subsequent anomalous dynamics due to the presence of this sub-population is conventionally called evolution in the ecological literature, because the presence of the additional strain emerges from mutation, and we are interested in following the frequency in the population of the mutant strain. We tried to simulate the experimental results of the rotifer-algae chemostat, where the control parameters are the nutrient concentration in flow media, $\phi_N^{\max}$, and the dilution rate, b. The natural degradation rates of the wild-type prey and predator are assumed to be much slower than the dilution rate, and therefore $b \approx d_P \approx d_W < d_D$ (the defended prey is less healthy). In Fig. 4.1(a), at first there are only the wild-type prey and the predator in the system, and the dynamics exhibits normal cycles where the predator lags behind the prey by $\pi/2$. When predation pressure is high, around $t \sim 400$, a mutation has given rise to a defended prey population that subsequently adapts to dominate the population and cause additional delay in growth of the wild-type prey and the predator, leading to evolutionary cycles with a π phase shift between the total prey and the predator. Fig. 4.1(b) shows an example of cryptic cycles, where the defended prey has a similar reproduction rate as that of the wild-type prey, *i.e.* $c_D \sim c_W$, and the defended prey can advance the wild-type prey by nearly π and thus the total prey population is suppressed. The quasicycle calculations in Fig. 4.1(f)-(h) for the power spectrum and the phase spectrum well predict the simulation results in Fig. 4.1(c)-(e). Besides the expected randomness in the dynamics from the stochastic simulation, Fig. 1(a) and (b) also show similar asymmetric profiles and the longer period after the subpopulation emerges, as in the experimental data in [120, 26, 29, 121, 122, 123, 7].

The phase diagram is usually studied by linear stability analysis of the mean field equations. To reduce the dimension of parameter space, variables are rescaled to be dimensionless: $\bar{t} \equiv bt, \bar{d}_S \equiv d_S/b, \bar{\phi}_S \equiv /\phi_N^{\max}, \bar{c}_S \equiv c_S\phi_N^{\max}/b$ and $\bar{p}_S \equiv p_S\phi_N^{\max}/b$.

However, this rescaling is rather subtle in stochastic calculations. For example, matrices $\mathbf{A}$ and $\mathbf{B}$ from Eq. (4.21) scale with $1/\phi_N^{\max}$ as mean-fields ϕ_S, but γ in Eq. (4.21) rescales with $1/\sqrt{\phi_N^{\max}}$, resulting in

$$\frac{\xi_S}{\phi_S} \sim \frac{1}{\sqrt{\phi_N^{\max}}} \frac{\bar{\xi}_S}{\bar{\phi}_S} \tag{4.26}$$

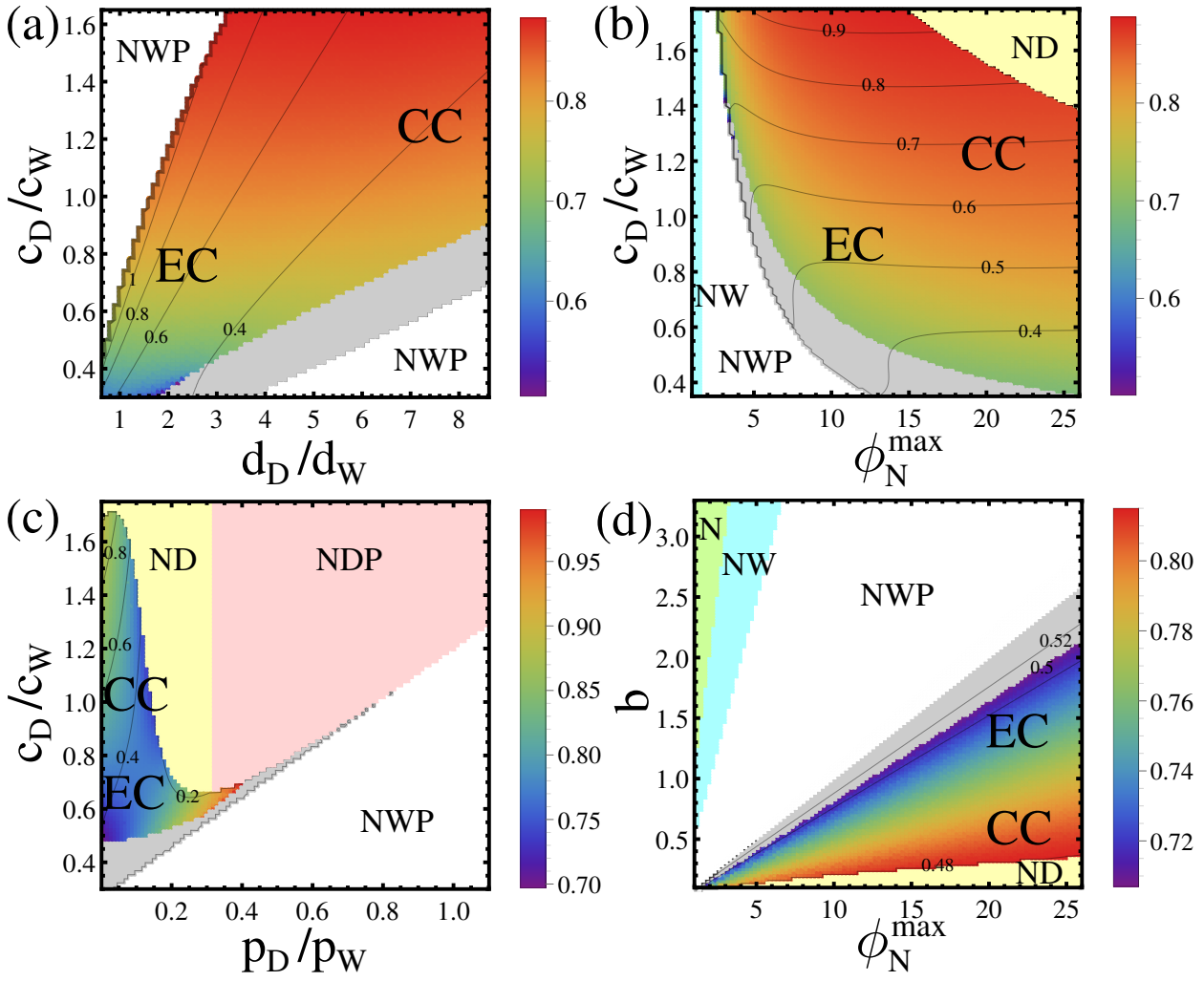

Figure 4.2: **Phase diagrams for evolutionary cycles (EC) and cryptic cycles (CC)**. Phase diagram is calculated from ILM with respect to the ratio of the prey reproduction rate (c_D/c_W), the ratio of the predation rate (p_D/p_W), the maximum nutrient concentration ($\phi_N^{\max}$) and the dilution rate (b). The gradient-colorful region corresponds to the coexistence of all species, and in the other regions the rapid evolution is not stable, with corresponding letters indicating the coexistence of only certain species. The coexistence states are decided by the mean-field densities and their ratio to the fluctuations; when fluctuations are larger than mean-field solutions, the dynamics is under high risk of extinction. The color legend represents the predicted phase difference between the wild-type prey and the defended prey (θ_{WD}) for rapid evolution, in units of π. The contours are the estimated amplitude ratios of wild-type prey to predator, indicating the tendency to be cryptic cycles. In the gray region near transition, the two types of prey start to decouple, leading to degenerate peaks in power spectra, and thus the phase is not well-defined. Except for the axis specified in each diagram, the parameters in the calculations are $V = 300$, $c_W = 1$, $p_W = 1$, $c_D/c_W = 0.8$, $p_D/p_W = 0.01$, $d_D/d_W = 3.5$, $\phi_N^{\max} = 16$, and $b = 0.6$. The predicted phase diagram is consistent with stochastic simulation.

where $\bar{\xi}_S$ are the rescaled demographic noise fields. Therefore, for two stochastic individual-level models with the same mean-field limit after rescaling, demographic fluctuations are more important in the model with smaller nutrient carrying capacity $V\phi_N^{\max}$. Thus neglecting fluctuations as in the conventional rescaling for mean-field equations can potentially cause unphysical predictions for the phase diagram. To avoid this situation, we examine the stability of solutions by comparing the amplitude of the lowest order population fluctuations with their mean fields.

Fig. 4.2 shows the calculated phase diagrams of ILM in Eq. (4.1). In Fig. 4.2(a), due to the cost for defense, the defended prey have inferior reproduction rate ($c_D < c_W$) or are unhealthier than the wild-type prey ($d_D > d_W$), leading to evolutionary cycles (EC). When the cost of reproduction is low, cryptic cycles (CC) can occur, where $\theta_{WD} \approx \pi$. If c_D is moderate, it is possible to have a correspondingly high death rate, and thus the fluctuations of prey are suppressed relative to the wild-type prey, causing the dynamics to be cryptic. In Fig. 4.2(b), under high $\phi_N^{\max}$, the defended prey are more likely to grow and dominate the system, which causes the wild-type prey to experience a greater phase lag than the defended prey, and the dynamics tends towards a completely cryptic cycle. In Fig. 4.2(c), if p_D is low, then higher c_D can lead to more phase delay and thus gives cryptic cycles. When p_D increases, the predator has greater food resource available from the defended prey, yielding a larger population, which then consumes more of the wild-type prey; this in turn reduces the wild-type prey population and leads to the dominance of the defended prey. In such a situation, the wild-type prey experiences a greater phase delay (nearly π) behind the defended prey, but the wild-type prey population is too small to cancel out the fluctuations of the defended prey population, and thus the dynamics cannot be characterized as cryptic. Our result in Fig. 4.2(c) predicts a similar but slightly different phase diagram to Fig. 3 in [29]; the region where all species coexist as predicted by the stochastic model is smaller than the deterministic solutions, because of extinction fluctuations near phase boundaries. In Fig. 4.2(d), under small b, *i.e.* slow supplement of the nutrient and low reduction rate from dilution, although both subpopulations of the prey have low reproduction, the wild-type prey population decreases more due to predation while the defended prey has a greater chance to compete for nutrient; thus the system is more likely to show cryptic cycles.

4.3.2 Comparison between analytic calculation and stochastic simulation

We have computed the power spectra, and compared the results with the stochastic simulation. The power spectrum for species S is calculated analytically by $S_S(\omega) = P_{SS}(\omega) = \langle \tilde{\xi}_S(\omega)\tilde{\xi}_S(-\omega)\rangle$, and from Gillespie

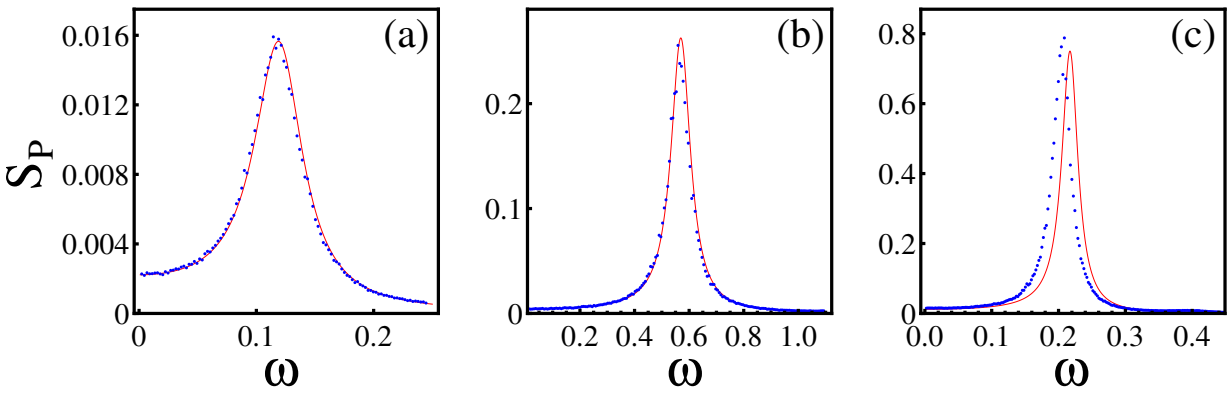

Figure 4.3: **Examples of comparison between analytic calculation and stochastic simulation of noise spectrum in different types of cycles.** Analytic calculation (red curve) and stochastic simulation (blue dots) of power spectrum of population fluctuations of predator for (a) normal cycles, (b) evolutionary cycles and (c) cryptic cycles in individual level model. The parameters in calculations and simulations are (a) $V = 2000$, $b = 0.1$, $c_W = 0.3$, $p_W = 0.6$, $\phi_N^{\max} = 1$, (b) $V = 1600$, $b = 0.6$, $c_W = 1$, $p_W = 1$, $\phi_N^{\max} = 5$, $c_D/c_W = 1.6$, $p_D/p_W = 0.001$, $r_D/r_W = 3.5$ and (c) $V = 1600$, $b = 0.1$, $c_W = 60$, $p_W = 0.92$, $\phi_N^{\max} = 16$, $c_D/c_W = 0.95$, $p_D/p_W = 0.001$, $r_D/r_W = 7.5$.

stochastic simulations of the ILM, using the formula

$$S_S(\omega) = \frac{1}{T}\langle \tilde{\xi'}_S(\omega_m)\tilde{\xi'}_S(-\omega_m)\rangle, \tag{4.27}$$

where T is the duration of total N samplings with discrete time $t_n = (n-1)\Delta t$ and the discrete Fourier transform of ξ is defined as

$$\begin{aligned} \tilde{\xi'}(\omega_m) &= \sum_{n=1}^{N} \xi(t_n) e^{i\omega_m t_n} \Delta t \\ &= \frac{T}{N} \sum_{n=1}^{N} \xi(t_n) e^{i2\pi(m-1)(n-1)/N}. \end{aligned} \tag{4.28}$$

The peaks and magnitudes of the power spectra of calculation and simulation have good agreement when the Gaussian approximation is valid. There are slight deviations when either the wild-type prey or predator has a small population size. In such a case, the dynamics of fluctuations is dominated by the species with smaller population, leading to a skewed and leptokurtic distribution of population fluctuations. Such suppressed fluctuation distribution can explain the deviation of the power spectra of simulation data from the analytic calculation when there is large discrepancy in population sizes between species. Fig. 4.3 shows examples of comparison between analytic calculation and stochastic simulation for normal cycles, evolutionary cycles and cryptic cycles. When population sizes are similar for each species and are not small, analytic

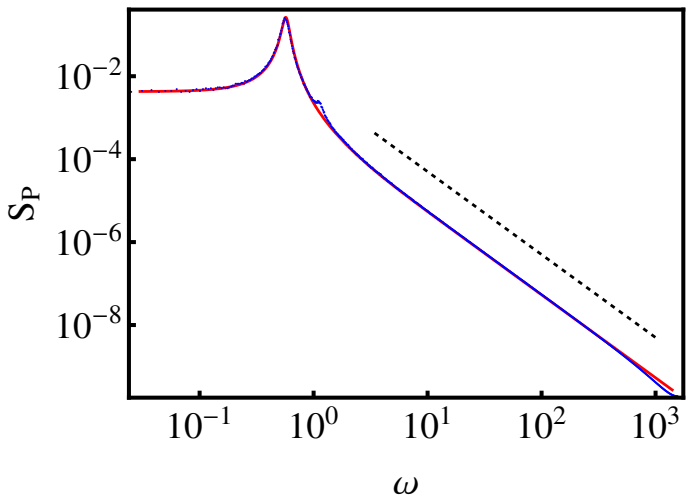

Figure 4.4: **The logarithm scale of comparison of power spectrum between analytic calculation and stochastic simulation**. Data are same as in Fig 4.3(b). The tail with ω^{-2} scaling, indicated by a reference dotted line with slope of -2, is the signature of quasicycles and is predicted by the analytic calculation based on individual level model.

calculation based on Gaussian fluctuations provides good quantitative prediction of characteristic frequency and the shape of power spectrum. Fig. 4.4 shows the ω^{-2} scaling in power spectrum as the signature of quasicycles is also captured by analytic calculation. For cryptic cycles where the oscillations of predator population are relatively larger and the prey population size is usually smaller, the Gaussian approximation is expected to have less quantitative agreement and underestimate the amplitude of fluctuations as shown in Fig. 4.3(c).

4.4 Physical explanation of anomalous predator-prey dynamics

The physical explanation for the anomalous population cycles arises from the interplay between the mutant defended strain, the wild type strain and the predator, and was briefly suggested in [26]. We can understand these anomalous cycles by following the illustrative steps similar to the normal case. In contrast to the $\pi/2$ phase shift of the conventional predator-prey model, evolutionary cycles with a π phase shift can arise because of the existence of a mutant prey population that can defend itself from the predator but which incurs a metabolic cost. The defended prey compete with the wild type for nutrients and thus delay the regrowth of the wild-type prey.

Specifically for evolutionary cycles as shown in Fig. 4.5:

1. Under high predation pressure, the population of the wild-type prey (blue) decreases, while the de-

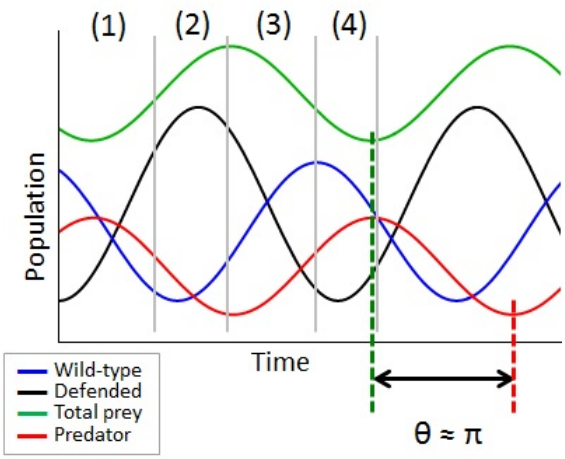

Figure 4.5: **Illustration of evolutionary cycles in rapid evolution**.

fended prey (black) can survive and dominate, consuming most nutrients in the system. The wild-type prey remains at a low level population for a long time, causing the decrease of the predator population (red).

2. Once the predation pressure reduces enough, the healthier wild-type prey can start to grow back and outcompete the defended prey for nutrients.

3. Wild-type prey dominate in the population, and subsequently the predator population will resume.

4. Predation pressure increases again, causing decrease in wild-type prey and regrowth of defended prey; another persistent cycle continues.

The additional defended prey sub-population compete for nutrients and delay the regrowth of the wild-type prey, leading to a phase lag of the wild-type prey behind the defended prey. This phase lag is naively about $\pi/2$ because the wild-type prey can grow back before the population of the defended prey go to the minimum level. Therefore, the predator is delayed by a phase of π behind the total prey (green) where overall the defended prey dominate.

For cryptic cycles, as shown in Fig. 4.6:

1. If the defended prey (black) have very effective defense without much metabolic cost, they can dominate longer and cause more delay of the regrowth of the wild-type prey (blue). Predator (red) decreases due to suppression of wild-type prey.

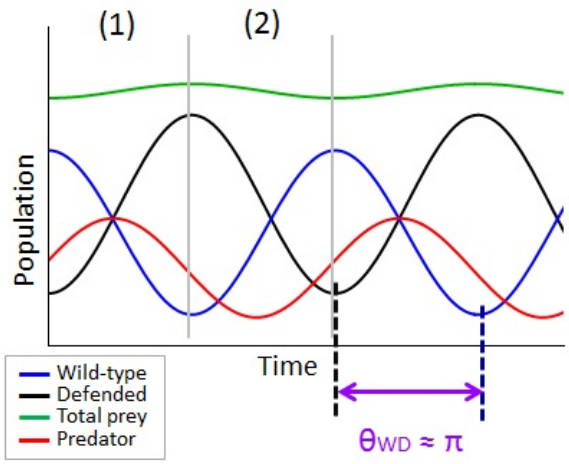

Figure 4.6: **Illustration of cryptic cycles in rapid evolution**.

2. Wild-type prey can regrow only after defended prey decreases and under low predation pressure, leading to substantial phase delay in the wild-type prey behind the defended prey.

If the wild-prey lag the defended prey by π, their fluctuations offset each other, and thus the dynamics of the total prey population (green) appears in aggregate to be suppressed, leading to the phenomenon of cryptic cycles. cycle.

4.5 Conclusion

Our results show that rapid evolution strongly renormalizes the ecosystem time scale, and the prediction of the coexistence region can help estimate the risk of extinction and the impact of the rate of environmental changes (for example, the dilution rate and nutrient concentration in the rotifer-algae system). Our model can also be used to study spatial-extended situations in natural ecosystems or laboratory experiments that are not in a well-mixed chemostat.

In summary, we have shown clearly that a generic stochastic individual-level model can yield rapid evolution phenomena, and that anomalous dynamics can arise without special assumptions or fine tuning, in sharp contrast to existing results in the ecology literature based on deterministic models. We expect this description to be especially useful to study the transition to rapid evolution from normal cycles since before the transition the mutant prey population has low relative abundance and is thus likely to exhibit strong effects of demographic stochasticity and spatiotemporal fluctuations.

Chapter 5

Evolution of phenotypic fluctuations

5.1 Introduction

During the first half of the twentieth century, Wallace and Darwin's theory of natural selection was combined with Mendeleian genetics in the "Modern Synthesis" to form a gene-centric description of evolution, known as population genetics. Population genetics concerns itself with the frequency of alleles, and the way in which their frequencies change under differential reproductive fitness arising from the traits encoded by genes. The genetic variance in a population arises, in this approach, through point mutations, although today we know that there are many other mechanisms of genome plasticity that need to be considered. In the Wallace-Darwin theory of natural selection, the variations which are selected by the environment are today understood as reflecting genetic variations. Indeed, in 1930, Fisher formulated a calculation from which he stated an assertion that the evolutionary rate is proportional to the genetic variance [145]. Although the assertion, known as Fisher's fundamental theorem of natural selection, has been discussed and reexamined since then especially in the context of population genetics, it does not represent a fully general and satisfying account of evolution. One fundamental problem about Fisher's fundamental theorem is the neglect of the role of phenotypic fluctuations. Especially, phenotypic fluctuations are pervasive, and can be important to various scenarios in evolution [146, 147, 14]. In this chapter, we discuss the interplay between phenotypic and genotypic fluctuations, posing the questions explored in the following chapter using a combination of experiment and theoretical modeling.

5.2 Phenotypic fluctuations

Evolution can be said to be the process of selection from heterogeneous phenotypes in a population, so that the ones with greater reproductive success will endure for future generations. Heterogeneity and diversity in phenotypes can be manifested in different ways: for example, in metabolic functions, or organismal morphology that may be better adapted to environments by different degrees. Phenotypic fluctuations

can be classified as stemming either from genetic variations or isogenic fluctuations. Genetic variations can arise from point mutations or other genome rearrangements. Isogenic fluctuations from a clonal genotype are usually thought of as mainly due to stochasticity in gene expression during translation and transcription; but they can also be generated through epigenetic dynamics, different stages of cell physiology or differentiation, etc [146, 147, 14]. At the cellular level, phenotype fluctuations are referred to as cell-to-cell individuality. Needless to say, all these factors can reflect the influence from interactions with the cell's environments. Those phenotypes displaying advantageous or more competitive features, such as higher birth rate or lower degradation rate, will endure in an ecosystem during selection, after long times. One common interpretation for the ubiquity of phenotypic fluctuations is that they provide more flexibility to adapt to environmental changes. The time scale to acquire new traits from mutations and other mechanisms, such as genome rearrangements, are many generations if one is concerned with a global population of an organism such as *E. coli*. On the other hand, phenotypic fluctuations can confer immediate tolerance to a local population against current environmental changes, while still providing flexibility to alter back or change further within a relatively shorter period. The ability to change the phenotype without requiring changes to the genotype is a fast, reversible and locally effective mechanism that gives an advantage to a population to survive in a spatially and temporally fluctuating environment. Such a phenomenon is sometimes referred as the "bet-hedging strategy" [148, 14, 149, 150].

However, more subtleties need to be considered in order to make this commonly accepted argument more than a just-so story. While selecting out particular phenotypes, selection also has the effect of selecting different genotypes that preferentially manifest the favored phenotype. Moreover, in order to benefit from the selective advantages in the long term, the selected phenotypes of individuals need to remain in the population for many generations. That is, selection on genotypes through selecting phenotypes is important to ensure the long-term adaptation of the population and thereby build robustness against environmental changes in future. An obviously crucial factor is the nature of the selection, which comes in various forms, characterized not only by its frequency but also by its strength. How the influence from different types of selection is passed on to genotypes from phenotypes also requires elucidation. This entails discussion of the relationship between phenotype and genotype, or the so-called genotype-phenotype mapping.

5.2.1 Genotype-phenotype mapping

The genotype-phenotype mapping is a probability density function that relates the phenotype of an organism with a given genotype [151]. In general the mapping between genotype and phenotype is a multi-dimensional function that reflects the underlining complex biological features, such as gene regulatory and metabolic

networks. The genotype-phenotype map will in general evolve: a cell's environment exerts a selection pressure on its phenotype, and thus may also influence the genotype-phenotype mapping. Here we are interested in the relevant question of how selection of the phenotype leads to evolution and further selection of the genotype, and what governs the rate of this process

The complete answer to this question lies in more subtleties. In particular, it is worth noticing that phenotypic variation or phenotypic fluctuations should be distinguished from phenotype variability or phenotypic placiticity. Phenotypic variation simply states the variance of the phenotype configuration in the population, whereas phenotypic variability ascribes the propensity to acquire different phenotypes [152, 153, 154, 12]. Similarly, genetic variation is not the same as genetic variability, which represents evolvability. Thus phenotypic variability is closely related to evolvability [152, 153, 154, 12].

Therefore, a more refined version of our question to understand evolution is this: How does selection on phenotype couple to genetic variation and thereafter affect phenotypic variability and evolvability? How do interactions between individuals feedback into environmental selection? The fact that phenotypic fluctuations are selected by the environment, and also feedback onto the environmental dynamics means that the eventual selection of genotypes is influenced by the evolutionary trajectory of the phenotype. In particular, the multiple levels of feedback between phenotype and genotype, and phenotype and environment means the rate of evolution can be determined by the genotype-phenotype map, which itself evolved. If this were not complicated enough, there is an additional layer of complexity and controversy that needs to be addressed, namely the question of whether the organism senses its environment and preferentially presents certain mutations that are adaptive to the environment. This controversial and unsettled topic is known as stress-induced mutagenesis [155, 156].

Specifically, it has been a long-standing debate on whether mutations are purely random events or are induced by selection stress. The Luria-Delbruck experiment on resistance of *E. coli.* to phage has implied the former [157], by showing that the probability density for the size of phage-resistant mutant populations has fat tails, rather than the more narrowly peaked distribution which would be expected in a stress-induced mutagenesis scenario. However, since then further studies of the molecular biology, at the population level have shown evidence that genotype variations can be a rapid response to environmental stress [155, 156]. In other words, the relationship between genotype and phenotype can probably shed light on the interactions between genetic variations and selection stress.

With the development of whole genome sequencing, the relationship between phenotypic fluctuations and genetic variations can be studied quantitatively. Nevertheless, to address the above nuances that are important for evolutionary questions, straightforward and systematical approaches with controllable selection

are required to dissect the intertwined dynamics between phenotypic fluctuations and genotypic variations.

5.3 Directed evolution

One strategy to cope with such complexity in quantitative detail is the technique of directed evolution. Directed evolution describes the process whereby the same selection repeatedly acts on phenotypes or genotypes. The resultant serial changes in the ecosystem reflect the trace of the adaptive response of phenotypes and genotypes to the corresponding selection. Therefore, directed evolution serves as a tool to straightforwardly study how the evolutionary trajectory of the ecosystem is shaped by selection.

Directed evolution has been utilized to study how exactly evolution would process [158, 159, 153, 160, 154, 12]. In particular, artificial experiments of directed evolution were performed designed to explore the dynamics of phenotypic fluctuations, where founder strain *E. coli.* cells were embedded with a fluorescent gene sequence which was engineered to have random deleterious mutations that impacted the fluorescence intensity. [161]. In the directed evolution experiment, the following process was repeated. Individuals with the top 0.2% highest level of fluorescence intensity were selected out, and then the population was amplified to the original size. After the same selection and amplification were applied to the population for few times, a few cells, of which each has a presumably distinct genotype, were randomly chosen, clonally amplified to tested the distribution of phenotypic fluctuations of each clonal strain. It was found that after repeated selection, two types of mutant strains coexist: one type with a high mean value of fluorescence expression level but a narrow distribution range, and another type, with a smaller mean value but a broad distribution. The authors concluded that strong selection may give a preference to large phenotypic variance, which they attributed to transcriptional fluctuations [161]. This experiment gave a different result than an earlier one which used a much less stringent selection on the population, finding that the mean increased but the phenotypic variance decreased. Apparently, with weak selection, there is no special advantage to access the large fluctuations of the tail of the phenotypic distribution.

5.4 Individual adapting to chemical environments: Chemotaxis

The fluorescence experiments yielded interesting but surprisingly contradictory results. We decided to study a richer system where there is an explicit connection to the environment, so that genotype, phenotype and environmental variables could all be probed. We worked with the experimentalists David Fraebel and Seppe Kuehn to use the well understood phenomenon of chemotaxis as a directed evolution system.

In the chemotaxis experiments, we study quantitative traits whose heterogeneity reflects distinct geno-

types under evolution on laboratory time scales. Microbe systems in general, with trackable and manipulatable traits are ideal candidates for this type of study. At the cellular level, one way to change behavior in response to environmental variations is to change motility. Changing motion based on environmental gradients is called taxis; it is crucial to the survival and adaptation for organisms, not only for microbes but also for eukaryotes such as slime molds [162, 163]. Chemotaxis based on sensing gradients of chemicals such as nutrients or toxins is an important mechanism for cellular aggregates, influencing phenomena such as wound repair, immune response, embryo and organ development, biofilm formation and tumor metastasis [163].

Bacterial chemotaxis systems have a wide range of sensitivity to chemical signals [149, 164]. When an extracellular chemical molecule diffuses into a bacterial cell, it combines with the corresponding sensory receptor on the cell membrane, initiating reactions between different types of proteins that drive the chemotactic machinery [165, 162, 146, 166]. The chemotactic proteins are regulated by the bacterial chemotaxis network, which is one of the best studied biochemical networks, and is found to be optimized and robust for bacteria and archaea [149]. In addition, the copy numbers of chemotactic molecules and proteins are of order 100-1000 in the cell, which will lead to substantial demographic noise in gene expression, and thus significant variation in phenotypes [146, 14, 149]. For all these reasons, bacterial chemotaxis and its adaptation to environmental stimuli is an excellent system to study phenotypic evolution and the genotype-phenotype map.

5.4.1 Collective migration emerging from bacterial chemotaxis

Bacterial chemotaxis was discovered in the 1880s by Engelmann and Pfeffer [167, 168, 169, 165, 170], but the first systematical experiments were performed by Adler in 1966 who modified Pfeffer's capillary experiments to investigate the response of the migration of motile *E. coli.* with respect to attractant [171, 172]. In Adler's experiments, the capillary was sealed with agar containing chemoattractant at the end (Fig. 5.1(a)), which created a diffusive gradient of chemoattractant. Cells were found to follow the gradient and accumulated to form a traveling front toward the chemoattractant [171, 172, 173, 174], as shown in Fig. 5.1(b). Similar experiments were tested with chemorepellent, where cells turned out to escape away [174, 169].

To ensure sufficient nutrient supply to cells for observation, Adler also performed experiments in a different assay on plates of semiliquid agarose gel, a porous medium filled with uniform nutrient substrate as chemoattractant [171, 174]. One advantage of the agar-plate assay is that the evolving growth pattern directly reflects an observable chemotaxis response. By consuming nutrient, cells create a spatial gradient of nutrient in the environment, based on which they execute chemotaxis. At the population level, the cell

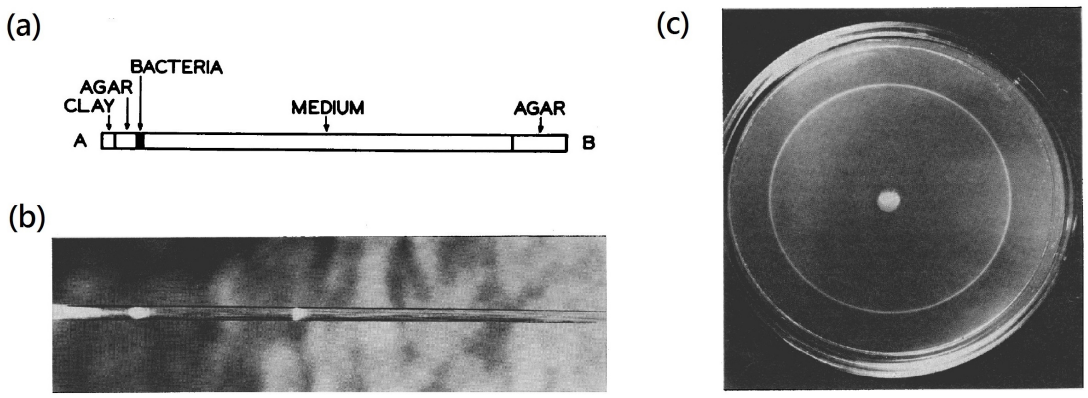

Figure 5.1: **Capillary and agar-plate experiments for bacteria chemotaxis**. (a) Sketch of a capillary experiment: Bacteria cells initially inoculated at the left end swim toward the right end along an increasing gradient of agar concentration. (b) A snapshot of the capillary experiment: Cells formed a high-density traveling front (white part in the center of the capillary) toward the right end. (c) A snapshot of an agar-plate experiment: Cells initially inoculated at the center of a plate of semiliquid gel filled with subtrate formed an outwardly traveling front (white ring) with a high-density population. Figure (a) is taken from [172], and (b) and (c) are taken from [171].

colony is observed to expand outward isotropically with a constant migration speed, forming a circular shape with a high-density ring at the outer limits of the colony [171]. Depending on the composition of agar, different strains might develope several fronts or different patterns [171, 172, 173, 165]. Further experiments by Berg and Brown [175] and other studies [162] identified through tracking individuals that *E. coli.* cells have two swimming modes controlled by the configuration of the cells' flagella: in the "run" mode, motors on flagella rotate counterclockwise, and flagella form into a bundle that propells the cell to move forward; in the "tumble" mode, motors rotate clockwise, and flagella fly apart, making the cell reorient randomly. The change in direction is a broad distribution with a mode around 60 degrees [175, 169, 165, 170, 162].

The run duration was found to follow an exponential-like distribution [175, 148], and for many years it was believed that bacterial chemotaxis follows a random walk. However, recently studies indicated power-law scaling in the distribution of run duration [176, 177], implying that the motion might be a Lévy flight. This has a nice interpretation because a Lévy flight is known to be a type of optimal search strategy [178].

When a cell senses a positive gradient of chemoattractant, the cell prolongs its running in the same direction, resulting in a biased random walk [175, 170, 162], while the cell ignores a negative gradient of chemoattractant [170]. An illustration is shown in Fig. 5.2. It is very interesting to note that the bacteria respond to the change of the logarithm of the chemoattractant concentration [179]. Like many other biological organisms, they obey Weber's law that describes sensory response [179, 180, 181, 182, 149].

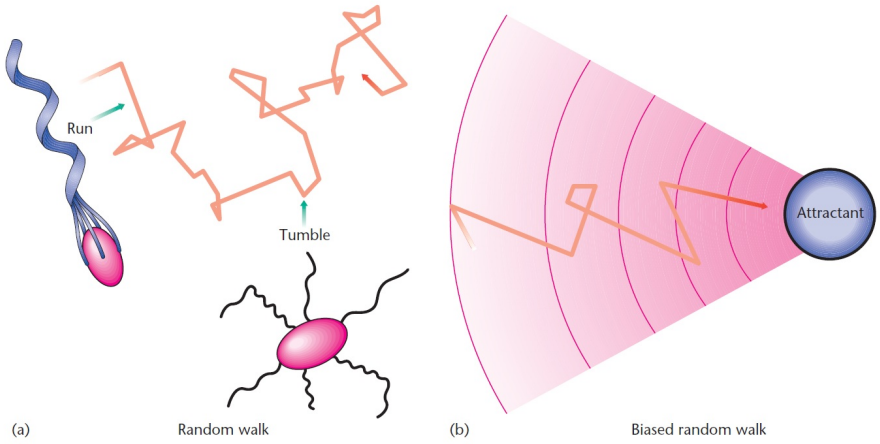

Figure 5.2: **Run and tumble mode in bacterial motion**. (a) Without chemoattractant gradient, consecutive run and tumble segments constitude a random-walk-like motion of a single cell. (b) When encountering a gradient of chemoattractant, the cell biases its motion be reducing the frequency of tumbling. Figure is taken from [162].

A later experiment performed by Wolfe and Berg studied how the individual's running and tumbling leads to group motility [183]. Using the agar-plate technique, the authors compared the growth pattern between the wild type and other strains which always run or tumble with no chemotactic response. Interestingly, cells of these non-chemotactic strains tend to spend most of the time getting trapped or idling in the gel, and a smaller migration speed was observed. It was also found that the migration speed of the strains that both run and tumble freely increases if they tumble more, implying that cells which reorient frequently can move more efficiently through the gel.

5.5 Keller-Segel model for bacterial chemotaxis

In this section, we present an overview of the population level modeling of chemotaxis. Chemotaxis is intrinsically a multiscale phenomenon, and to fully describe the evolution of chemotaxis will requires us to use multiple levels of description. The population level approach to chemotaxis was developed by Keller and Segel in 1971. It is a mean-field model composed of deterministic equations for the spatial-temporal density of cells and a chemoattractant [184, 185]. The goal is to capture cells' dynamics as a balance between chemotaxis, which tries to direct the cells up a concentration gradient, and diffusion, which tends to isotropize the motion. The cells' motion is subjected to a chemotactic flux that is assumed to be the

product of cell density $n(x,t)$ and a coarse-grained drift velocity $\mathbf{v}(\mathbf{x},t)$, i.e.

$$\mathbf{J}_{\text{chemotaxis}}(\mathbf{x},t) = n(\mathbf{x},t)\mathbf{v}(\mathbf{x},t). \tag{5.1}$$

The drift velocity $\mathbf{v}(\mathbf{x},t)$ is assumed to depend on the gradient of the chemoattractant concentration, $C(\mathbf{x},t)$, in the form

$$\mathbf{v} = \chi(C)\nabla C, \tag{5.2}$$

where $\chi(C)$ is a function that corresponds to the sensitivity of a cell to chemoattractant. Usually it is interpreted as the degree of binding between chemotactic receptors of cells and chemotactic ligands, and the commonly used form involves the derivative of Michaelis-Menten kinetics of binding, and the result is

$$\chi(C) \propto \frac{K_C}{(K_C + C)^2}, \tag{5.3}$$

where K_C is the half-saturation constant that represents the limitation of response [186, 187]. In their original paper, Keller and Segel adopted Weber's law with logarithmic response in drift velocity, for which the derived $\chi(C)$ is the derivative of logarithmic response [179]:

$$\chi(C) \propto \frac{1}{C}. \tag{5.4}$$

The continuity equation for the cell density is

$$\frac{\partial n}{\partial t} + \nabla \cdot (\mathbf{J}_{\text{diffusion}} + \mathbf{J}_{\text{chemotaxis}}) = 0, \tag{5.5}$$

with

$$\mathbf{J}_{\text{diffusion}} = -D_n(C)\nabla n, \tag{5.6}$$

where $D_n(C)$ is the effective diffusion coefficient. Thus the motion is a competition between the anisotropic driving from chemotaxis and the isotropic driving from diffusion: chemotaxis causes cells to move along the gradient of environment, and diffusion randomizes the direction of cell motion. The minimal form for the dynamics of $C(\mathbf{x},t)$ includes diffusion with coefficient D_C and basic reactions: (1) cells release chemoattractant with a rate h, and (2) the activity of chemoattractant spontaneously decays with a rate k.

The corresponding Keller-Segel equations become:

$$\frac{\partial n}{\partial t} = \nabla \cdot [D_n(C)\nabla n] - \nabla \cdot [n\chi(C)\nabla n]\,, \tag{5.7}$$

$$\frac{\partial C}{\partial t} = D_C \nabla^2 C + hn - kC. \tag{5.8}$$

The Keller-Segel model captures some of the main characteristics of chemotaxis. For example, analysis and numerical results from simulating the model in one dimension show that the cell density distribution moves in space with time as a traveling front, which is consistent with experimental observations described in the previous section. In a circular geometry the population migrates outwards with the radius $R(t)$ varying linearly in time, rather than the square root of time, as would be the case for pure diffusion.

Despite its success, the Keller-Segel model is for the macroscopic behavior of mean cell density and does not capture the individual run and tumble events. Therefore it is hard to know how the individual behavior and cell-to-cell variation depend on selection and environmental changes. In particular, large fluctuations in tumbling frequency and adaptation time were reported in experiments [148, 176, 149]. Presumably this reflects stochastic gene expression, as evidenced by the relatively small number of chemotactic proteins in each cell [176, 149]. As a result there has been a long-standing interest in individual-level modeling [188, 189] of chemotaxis. For example, there have been studies on chemotaxis with hybrid models that incorporate transitional kernels meant to capture individual run and tumble events and including the dynamics of signaling pathways at microscopic scale. These models can be coarse-grained to reproduce the Keller-Segel model [190, 191, 192]. In our own work, we have used all of these levels of description, as well as an abstract representation of the directed evolution process.

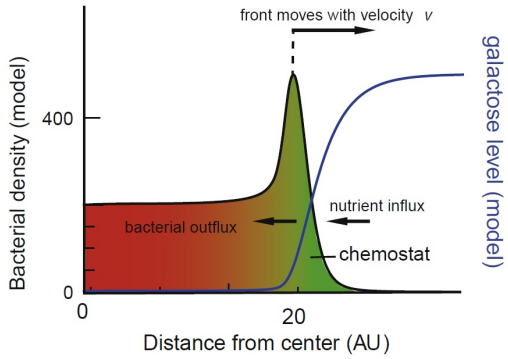

Figure 5.3: **Example of solution of Keller-Segel model**. Figure is taken from [193].

Chapter 6

Emergence of rapid evolution of phenotypic fluctuations in directed evolution

The overarching goal of this project is to explore how a population bottleneck causes adaptation of chemotaxis in E. coli, at scales ranging from the genomic, up through the signaling pathways at the cellular level, ultimately affecting the cells motility and the behavior of a growing colony. In this project, detailed experiments performed by our collaborators capture the directed evolution of an initially clonal population of *E. coli* that undergoes chemotactically-driven expansion through agar gel. Repeated sampling of the cells at the outer limits of the colony and re-initialization of colony growth results in an evolution of phenotype and genotype. We then propose a conceptual model of directed evolution where the biological details are abstracted, and only one coarse-grained effect of phenotypes is present and subjected to selection. The simulations are able to make prediction of the phenotypic variance in population as a function of selection round.

6.1 Experiment on directed evolution of cell-to-cell individuality in bacterial chemotaxis

We now describe an experiment designed to investigate the relationship between phenotypic variation and selection. The experiment was performed on chemotactic bacteria [15], and grew out of earlier work on chemotactic migration on agar gel in [171, 183]. The advantage of adopting the agarose gel assay for phenotypic variation is that the spatial structure directly reflects phenotypic change and thus is easy to observe and measure.

Initially clonal cells of a single *E. coli.* strain were inoculated on an agar gel plate, which is a porous medium with nutrient substrate as the chemoattractant. Similar to [171, 183], the colony developed a circular, outward traveling front. After a certain period of time, a portion of the front population was selected to be inoculated on a new gel plate. Moreover, since cells depleted nutrient behind the front, one would expect that such feedback from cells to the environment will act as a further selective force on cells and presumably will select individuals that are more adept to chemotaxis, either with larger run speed or

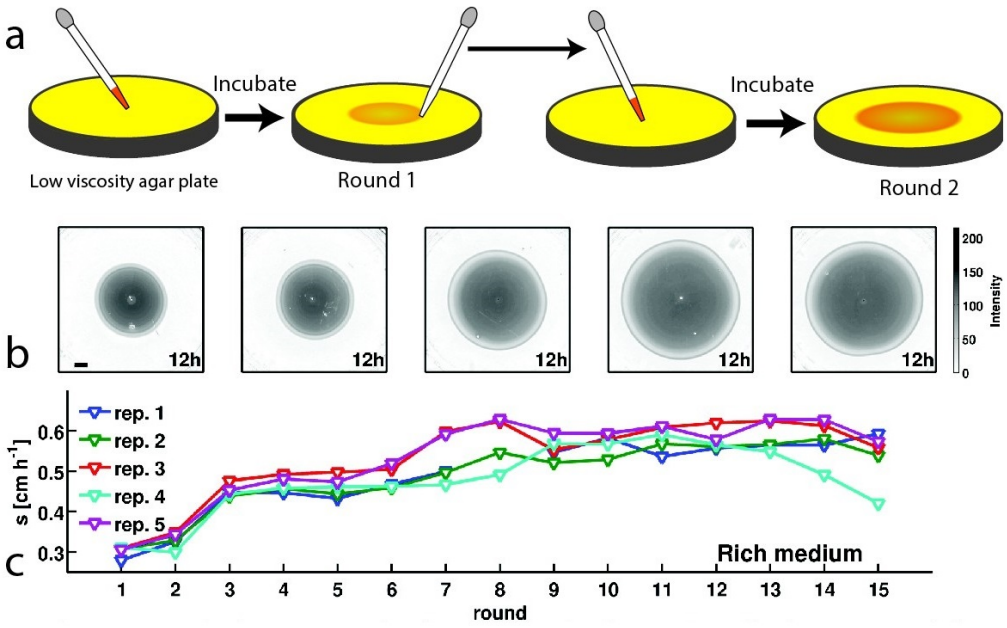

Figure 6.1: **Evolving migration in directed evolution experiment on bacterial chemotaxis**. (a) Selection process (from left to right): Clonal cells were initially inoculated at the center of a low viscosity agar plate. Cells consume nutrient and grow their colony, forming a high-density ring propagating outwards. After every 12 hours, a fraction of cells in the front population is sampled to re-inoculated on another new plate to initiate the next round and same selectin processes are repeated. (b) Snapshots of colonies of sucessive rounds show apparent increase in colony growth after repeated selection. (c) The migration speed is measured by the change of the radius of colony with time, which is constant in each round and increases after each selection. The migration speed increases by twofold after 10 rounds and then saturates, and the trend is reproducible. Figures are taken from [15].

more frequent tumbling rate. By repeating sampling of the cells at the edge after the same period for many times and re-initializing colony growth, cells grew into a larger and larger colony (Fig. 6.1(a)), indicating a higher front propagation speed (Fig. 6.1(b)-(d)).

In order to understand the evolutionary mechanism of the faster migration front, the evolution of chemotactic phenotypes was studied in quantitative detail in another well-mixed environment, without bias from the gel. By single cell tracking individuals in a liquid chamber, trait statistics of individuals sampled from the population after every five selection rounds were measured. At the same time, a portion of each sampled population was sequenced to determine the corresponding genotypes. In a separate liquid chamber, each sampled population replicated for many generations, without any mutation found in its descendants. Therefore the statistics gathered in liquid for each sampled population reflects a truthful amplification with the same composition of the population sampled from the gel experiments. For each sampled population, every

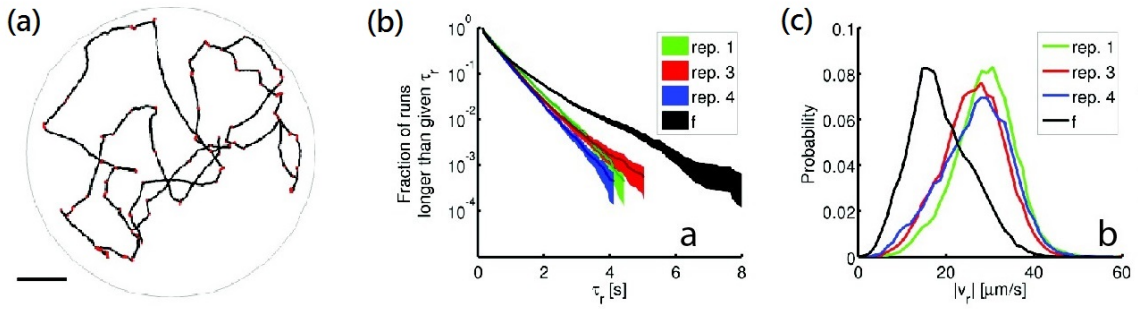

Figure 6.2: **Evolution of phenotypes in directed evolution experiment on bacterial chemotaxis**. (a) The chemotacitc phenotypes were measured in a well-mixed liquid. Cells move freely without chemotaxis, displaying approximately random walks. Run and tumble intervals of each individual were recorded. (b) Comparison of the cumulative distribution of run intervals, τ_r, collected from cells sampled from rounds 5, 10, 15 and 20. The distributions have a roughly exponential tail, indicating a random-walk-like behavior of cells in the well-mixed liquid. The slope of the tail indicates the mean run interval in each round, which increases after selection. (c) The probability density of individual run speed, $|\mathbf{v}_r|$, evolves with selection round. The average run speed increases, and the distribution becomes more left-skewed and weights more at high speed after selection. The distribution is found to be narrower after selection, which reflects the decrease in variance of run speed. Figures are taken from [15].

five selection rounds, the statistics of motility traits including run speed, run duration and tumble duration, etc, was measured.

The results can be summarized as below. A significant increase in run speed and decrease in run duration as a function of selection round were observed. The result indicates that under selection, cells evolved to run faster and tumble more frequently, which is consistent with the expectation. Interesting, cell-to-cell variances in both run speed and run duration decrease, sometimes referred to as a decrease in cell-to-cell individuality. An interpretation would be that under selection cells, evolve to be more specialized at more beneficial traits.

6.2 Abstract model of directed evolution of phenotypic fluctuations

The common interpretation for the utility of phenotypic variation is that it may increase survival probability under environmental changes, by providing variation every generation as opposed to genetic mutation which occurs less frequently. Whether populations are shaped more by phenotypic variation or genotypic variation depends on the degree of phenotypic variation and on the strength and types of environmental selection.

Previous experimental studies on directed evolution have shown that strong selection on the phenotype of GFP fluorescence of *E. coli.* can increase phenotypic variation [161], while in the directed evolution experiments on cell size of *E. coli.* a smaller decrease of variation in strong selection than in weak selection has been reported [194]. Thus, the observed reduction in cell-to-cell variation in our experiments was a surprise. Was this reduction a special feature of the chemotaxis setup, or could it be understood from general principles? To address this, we describe below a simulation model that abstracts away the mechanistic details of our particular experiment. We asked how the process of iterated selection, whereby cells from the tail of a phenotypic distribution are propagated to the next round, alters cell-to-cell variation. Our goal with the simulation was to predict how the evolution of cell-to-cell variation depends on the strength of selection. We also attempted to analyze these phenomena from a more realistic individual-level model, but the results were complex and hard to interpret. Thus they are not presented here.

6.3 Genotype-phenotype map

The genotype-phenotype mapping determines the phenotype of an organism with a given genotype. In general the mapping between genotype and phenotype is a multi-dimensional function that is governed by the underlying complex biological features, such as gene regulatory and metabolic networks. The genotype-phenotype map can in general evolve: a cell's environment exerts a selection pressure on its phenotype, and thus may also influence genotype-phenotype mapping. How phenotype selection is coupled to genetic variation is an important question, whose answer illuminates fundamental questions such as the evolutionary rate and the evolvability of organisms. Therefore, we seek a framework that includes these factors and captures their dynamics during evolution. In real directed evolution experiments, the evolutionary dynamics of a specific phenotype or genotype is generally difficult to trace. Traceable physical quantities, such as the distance moved by a cell, its growth rate and cell size, are represented in a multi-dimensional phenotype space that interacts with a multi-dimensional genotype space. For simplicity, we present a theoretical dynamical model for adaptation of a single effective phenotype and its associated genotype thought of as a projection of a multi-dimensional phenotype/genotype evolving under selection. The idea is related to previous population genetics models [158], but instead of assuming continuous selection due to an assumed fitness landscape, we specify selection through a population bottleneck that is decoupled from the rate of growth. We use this model to calculate the evolution of phenotypic variations under selection. The model is necessarily stochastic in order to capture the dynamics of fluctuations. We do not specify any explicit mechanism for genotype-phenotype mapping or how its function form changes during evolution. Instead, phenotypes are

random numbers generated from a gaussian mapping function whose mean is identified with the genotype, and whose variance reflects fluctuation in the expression of the genotype. The mean and variance change in evolutionary processes such as point mutations.

The abstract model captures key features of a model from a lower-level of discription that would be fulling realistic. Here we focus on experimentally-relevant factors in this abstract model that include strength of bottleneck selection, mother-daughter correlation and environmental changes. The mother-daughter correlation (or epigenetic inheritance) describes the degree of gene expression level that is passed on to descendants, and determines how preserved a phenotype is in subsequent generations. Environmental changes provide selection stress that affects the gene expression and may induce genetic variations. We focus on the effect of the strength of bottleneck selection and assume that the mother-daughter correlation does not evolve. We further assume that the environmentally related elements (including chemotaxis processes) are not explicitly represented but are captured in the process of selection.

6.4 Simulation algorithm for abstract model of directed evolution

In our abstract model, each individual i is represented by a random phenotype value $\chi^{(i)}$ which is determined by the individual's genotype g. $\chi^{(i)}$ is generated from a normal distribution $\widetilde{P}(\chi)$ whose mean is $\mu_\chi(g)$ and whose variance is $s^2_\chi(g)$. We assume that the phenotype does not change within the individual's life cycle. Mutation occurs when the individual reproduces a new individual whose genotype g' is distinct from g and whose phenotype follows another normal distribution with distinct mean $\mu_\chi(g')$ and distinct variance $s^2_\chi(g')$. In our abstract model of directed evolution the phenotypic trait χ is not explicitly stipulated. Instead, our abstract model is intended to explore the dynamics of phenotypic evolution under generic assumptions about how traits are passed between generations and respond to mutations.

Within a clonal population derived from of a single genotype g, the phenotypes of each new generation are generated based on a bivariate gaussian distribution $\mathcal{P}(\chi^{(i)}, \chi^{(i')})$ with correlation coefficient ρ which captures the fact that daughter cells have phenotypes $\chi^{(i')}$ which correlate with those of their mothers' phenotypes $\chi^{(i)}$. Phenotypic correlations between generations in clonal populations can arise from protein copy number fluctuations or non-genetic changes in gene expression [195, 196]. For an individual i', which results from fission of individual i, its phenotype $\chi^{(i')}$ follows the conditional distribution of the variable

$\chi^{(i')}$, given a known value of $\chi^{(i)}$ [197]:

$$\mathcal{P}(\chi^{(i')}|\chi^{(i)}) \sim \mathcal{N}(\mu_\chi(g) + \rho(\chi^{(i)} - \mu_\chi(g)), (1-\rho^2)s_\chi^2(g)), \tag{6.1}$$

where $\mathcal{N}(\mu, \sigma^2)$ is a normal distribution with mean μ variance σ^2. Under evolution with mutation rate ν, the mean and variance of $\widetilde{P}(\chi)$ change correspondingly, because a mutation affects the distribution of a particular trait.

We calculate this dynamics, along with the procedure for directed evolution through selection, as follows:

1. N_s individuals from a single genotype $g = g_0$ are generated from $\widetilde{P}_\chi(\mu_\chi(g_0), \sigma_\chi(g_0)) = \mathcal{N}(\mu_\chi(g_0), s_\chi^2(g_0))$, as illustrated in Fig. 6.3(A). These N_s clonal individuals are defined as the founder strain, which by construction is a population with a distribution of different phenotypes in it.

2. Each individual with phenotype $\chi^{(i)}$ creates a new individual with phenotype $\chi^{(i')}$. The new individual mutates to a new genotype $g = g_1 \neq g_0$ with a rate ν:

   (a) If it mutates, $\chi^{(i')}$ is generated from $\widetilde{P}(\mu_\chi(g_1), s_\chi(g_1)) = \mathcal{N}(\mu_\chi(g_1), s_\chi^2(g_1))$, where $\mu_\chi(g_1)$ and $s_\chi(g_1)$ are generated from $\mathcal{N}(\mu_\chi(g_0), \eta_{\mu_\chi}^2)$ and $\mathcal{N}(s_\chi(g_0), \eta_{s_\chi}^2)$ respectively. The variances of mutation in μ_χ and s_χ are assumed to be constant for all genotypes.

   (b) If the new individual does not mutate, $\chi^{(i')}$ updates based on Eq. (6.1).

   We neglect the degradation of individuals, and thus the population doubles after one generation. Each individual in the doubled population generates a new individual in the next generation following step 2a or 2b with g equal to its current genotype. We assume that the mother-daughter correlation does not mutate. After m generations, selection is applied to the whole population with $N_f = N_s \times 2^m$ individuals. An example of the relationship between different phenotypes in reproduction process is shown in Fig. 6.3(B) and (C).

3. To apply selection, N_r individuals with the largest χ values are chosen from the population. The selection fraction N_r/N_f is defined to be the selection strength. N_s individuals are further randomly selected from the N_r individuals to be the seed population for the next round. N_r is analogous to the outer edge population sampled with a pipette in the experiments, and N_s represents the individuals that are used to inoculate in the new plate. In experiments, $N_f \sim 10^{10}, N_r \sim 10^8$ and $N_s \sim 10^6$.

4. In the new round, step (2) and (3) are repeated for the N_s individuals from the previous round.

5. The phenotypic variance in N_s individuals at the end of each round is measured by amplifying the population to $N_l = N_s \times 2^l$ individuals by repeating step 2b without mutations. This mimics the experimental process of single cell tracking in liquid media, where populations are amplified by growth in well-mixed liquid conditions and presumably mutations can be neglected.

The parameters in the simulations are: $N_s = 20, m = 8, l = 8, \mu_\chi(g_0) = 40, s_\chi(g_0) = 8, \chi_c = 100, \eta_{\mu_\chi} = 5, \eta_{\mu_\chi} = 5, \eta_{s_\chi} = 2, \eta_{\chi_c} = 5$, with $\nu = 0.2$ and 0.5 respectively. Simulations were run over 40 rounds, and χ, μ_χ and s_χ are binned with size $1, 10$ and 1 respectively. The parameters were chosen so that the convergence of values of χ in N_l individuals can be reached in the last 10 rounds in order to compare with the evolving trend in the experiments. The selection process is described in Fig. 6.3(D).

These simulations do not directly stipulate how the phenotypic fluctuations within a given genotype $s_\chi(g)$ evolve – e.g. these can increase or decrease relative to the parent genotype g. This is intended to avoid any bias on phenotypic fluctuations with respect to the evolving mean trait values. For example, we do not explicitly stipulate that $s_\chi(g)$ decreases as $\mu_\chi(g)$ increases. However this could occur in more realistic situations where traits are constrained by trade-offs. For example, there is usually a cost for a trait to deviate very far from the mean, especially when the mean trait values are already very large or deviate from some optimized value for that environment. Second, traits such as run speed cannot physically evolve to infinitely large values and thus should be bounded by a threshold χ_c. The threshold on phenotype represents a limitation of the corresponding cellular machinery, and therefore it fluctuates between cells in general. In our simulations we include thresholds on χ and μ_χ, and the upper thresholds for both are set to be random numbers generated from $\mathcal{N}(\chi_c, \eta^2_{\chi_c})$. We assumed that the evolutionary timescale of the machinery is much longer than that of mutations and set μ_{χ_c} to be a constant value. Since we perform directed evolution on the largest phenotype values, the lower threshold is insignificant. Therefore the value of the phenotype χ for a particular genotype g is distributed with a truncated normal distribution with a random upper bound.

The phenotypic variance in N_s individuals at the end of each round is measured by amplifying the population to $N_l = N_s \times 2^l$ individuals by repeating step 2b without mutations. This mimics the experimental process of single cell tracking in liquid media, where mutations can be neglected. The phenotypic fluctuation (or the cell-to-cell variation), σ_χ, is defined as the variance of χ in the N_l individuals. Fig. 6.4(C)(D) shows the evolution of the distribution of χ of the N_l individuals for different rounds in one simulation experiment, and the standard deviation of χ values of N_l individuals at the end of each round is plotted in Fig. 6.4(E).

We expect that one of the relevant control parameters is the selection strength N_r/N_f. Now we present some intuitive arguments that try to predict the behavior as a function of selection strength. Without any physically-determined threshold on phenotype χ, individuals who evolve higher μ_χ and larger s_χ are

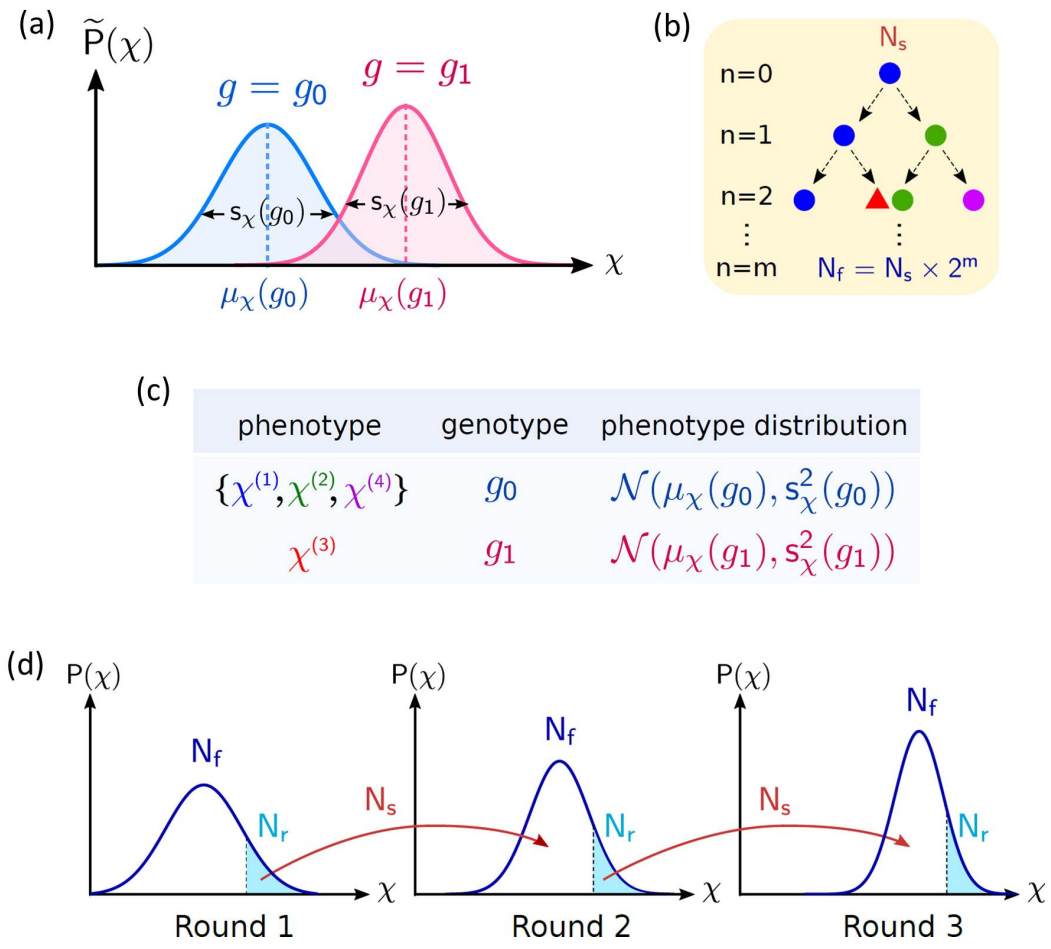

Figure 6.3: **Scheme of the abstract model.** The illustration of procedures (see text for definition of notations): (A) Initially the founder strain with N_s individuals whose phenotype $\chi^{(i)}$ are drawn from $\mathcal{N}(\mu_\chi(g = g_0), s^2_\chi(g = g_0))$ is generated. (B) The N_s individuals reproduce new individuals in the first round with a mutation rate. For example, for one of the initial N_s individuals with the founder genotype g_0 (circle) and a certain phenotype ($\chi^{(1)}$, in blue color), its daughter may have the same genotype but different phenotype ($\chi^{(2)}$, in green color) if it does not mutate. If the daughter mutates, the daughter is assigned a new genotype (triangle) with $\mu_\chi(g_1)$ from $\mathcal{N}(\mu_\chi(g_0), \eta^2_{\mu_\chi})$ and $s_\chi(g_1)$ from $\mathcal{N}(s_\chi(g_0), \eta^2_{s_\chi})$, and its phenotype $\chi^{(3)}$ is drawn from $\mathcal{N}(\mu_\chi(g_1), s^2_\chi(g_1))$ (in red color). All genotype and phenotype values are truncated by a random upper bound χ_c chosen from $\mathcal{N}(\chi_c, \eta^2_{\chi_c})$. After m generations, the population becomes $N_f = N_s \times 2^m$. (C) Table of phenotypes (χ^i) and their corresponding genotypes and phenotype distributions, for individuals in (b). Individuals with the same genotype can have different phenotypes due to phenotypic fluctuations (first row). After m generations of the process shown in (B), the population becomes $N_f = N_s \times 2^m$. (D) The top N_r individuals are selected from N_f individuals, and N_s individuals are randomly sampled from N_r individuals to start the second round. In the next round, N_s individuals repeat reproduction steps in (A) until the population reaches N_f again. At the end of each round, the selected N_s individuals reproduce for l generations without mutations. These $N_l = N_s \times 2^l$ individuals are the population of each round in "liquid media".

expected to preferentially populate the right-most tail of the population trait distribution, and so will have a higher probability of being selected. However, if the distribution is cut off by a threshold χ_c, and when the phenotype value χ approaches the threshold, individuals with larger s_χ will no longer provide a higher trait value. Instead these individuals will have higher weighting at smaller χ values compared with individuals that have the same μ_χ but a smaller s_χ. As a result, once χ_c has been reached, individuals with smaller s_χ will be selected if the selection strength is not too low. On the other hand, if the selection strength is high, the phenotype value χ of the selected N_s individuals are confined to be near χ_c no matter what the s_χ values of their genotype are. The N_l individuals generated from these N_s will contain genotypes with a wide range of s_χ, and thus the overall variance in the measured χ in N_l individuals will increase. In addition, the mutation rate ν determines how rapidly the phenotype distribution will reach its threshold. The higher the mutation rate the shorter the time required to saturate to phenotype threshold eventually. However, a high mutation rate also drives phenotype values away from the threshold afterwards, which leads to smaller mean and larger variance in phenotype. A similar conjecture about the way phenotypic variation might evolve as a function of selection strength was made in [14, 160].

The simulation results are consistent with our prediction. Fig. 6.4(A) shows an example of the evolution of the distribution of phenotype value χ under low selection strength. Before the distribution tail reaches the threshold χ_c, the distribution becomes wider in successive rounds of evolution. Once the distribution tail starts to be cut off by χ_c, the distribution becomes more left-skewed and eventually becomes narrower. Such distribution dynamics is reflected in the measured standard deviation σ_χ, which increases in the first few rounds and then decreases in the later rounds, as shown in Fig. 6.4(B). Fig. 6.4(C) and (D) shows the comparison of the effect of low and high selection strength on evolution of σ_χ and the average phenotype value over population, $\langle\chi\rangle$. If the selection strength is high, the phenotype distribution evolves faster towards larger χ values, and thus cell-to-cell variation increases faster as well. Contrary to the case with low selection strength, σ_χ decreases once the distribution tail reaches the threshold but soon increases again. Fig. 6.4(E) shows that the overall standard deviation at the final round with evolved strains is larger (smaller) than the founder strain if the selection strength is strong (weak). We also observed that if the traits are not bounded by a threshold, *i.e.* $\chi_c \to \infty$, the traits evolve without bound in the simulations, and there is no saturation of trait value after repeated rounds of selection, and there is no decline in the variance in the population.

In conclusion, through the simulations of this minimal abstract model for directed evolution, we have shown that an upper bound of phenotype due to biophysical constraints can lead to finite-time saturation of the evolving phenotype, and to the decrease of phenotypic variation or cell-to-cell variation under temperate selection and with rare mutations. In the case with strong selection and frequent mutations, the decrease of

cell-to-cell variation is not a necessary consequence of directed evolution procedure. Under strong selection, genotypes with larger variance in gene expression stand out as long as they are not constrained by the physical thresholds yet, and the average genotype and phenotype values increase faster (Fig. 6.4(D)). In this sense, strong selection can be regarded as increasing the evolvability. In other words, whether phenotypic variation is advantageous or unfavorable depends on the selection strength and trait limitation.

The reduction in phenotypic variation could also be interpreted as stabilizing selection due to canalization [198], but the mechanism there is different from ours because there is no explicit threshold present. Moreover, even if the attractor assumed in these categories of argument is viewed as the outcome of a physical threshold, it is not clear how the different effects of weak or strong selection would be predicted in this way of viewing the system.

In directed evolution experiments of bacterial chemotaxis, the selection is coupled to the environment: the nutrient gradient caused by consumption by the heterogeneous cell density also applies spatio-temporal selection on population, and there are different types of nutrient. To further understand how the evolutionary dynamics of cellular traits (such as chemotaxis behavior and growth rate) adapt to environmental variations, we need to include space-dependent features.

6.5 Conclusion

From our simulations on the abstract model, we found that the phenotypic fluctuations can both decrease or increase in directed evolution, depending on the strength of selection. This is interesting and even surprising, because one might have expected that "purifying selection" would be operative. In purifying selection, as usually adopted in conventional population genetics with a Mount Fuji fitness landscape, phenotypic fluctuations should always decrease because selection removes mutations that are less than optimal, causing convergence to the fitness peak. However, our abstract model predicts that the form of selection can influence the evolutionary result in opposite ways. This is testable in chemotaxis experiments, for example by enlarging the sample range N_r or even selecting away from the outermost part of the expanding population. The predictive ability of this simple, abstract model for directed evolution can help guide more detailed simulations that capture more of the realism of run-and-tumble, in future theoretical and experimental works.

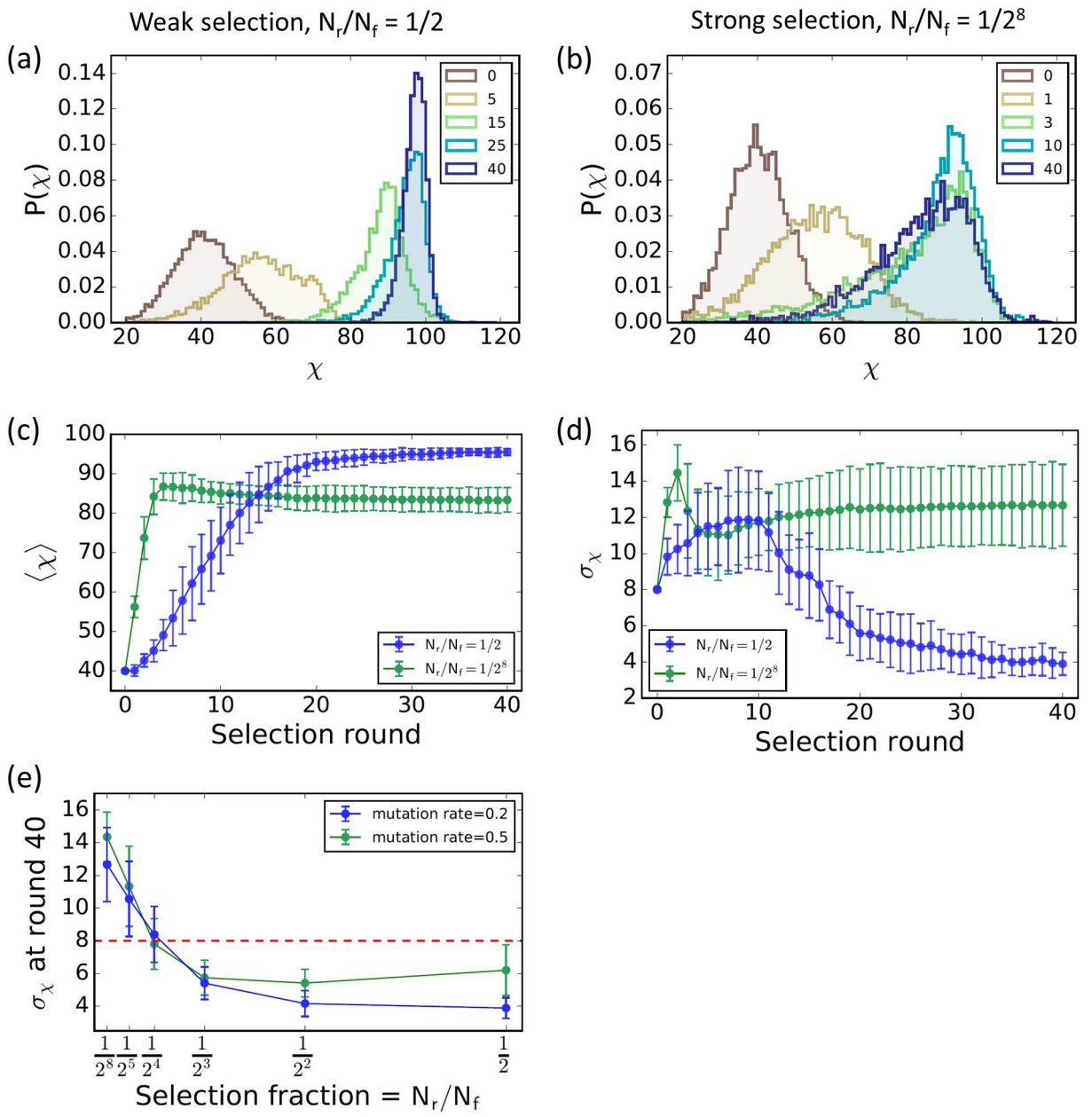

Figure 6.4: **Simulations of the abstract model** (continue from previous page): (A) The distribution of χ of N_l individuals at different rounds under weak selection (e.g. $N_r/N_f = 1/2$): when the distribution $P(\chi)$ is away from χ_c, individuals with larger s_χ are selected, and the overall variance in χ increases. When the tail of distribution $P(\chi)$ starts to reach χ_c (after round 5), $P(\chi)$ becomes tilted, the variance in χ decreases eventually. (B) $P(\chi)$ under strong selection (e.g. $Nr/N_f = 1/2^m$): $P(\chi)$ evolves and hits χ_c faster, and variance in χ first increases (before round 3) and then decreases (round 10). Since individuals with smaller s_χ are not particularly selected under strong selection, $P(\chi)$ eventually relaxes to a wilder shape due to random mutations (round 40). (C)(D) The overall standard deviation and mean of χ measured from (A) and (B) and are averaged over 20 replica. (E) The overall variance in χ as a function of selection strength. The red dashed line represents the standard deviation of χ for the founder strain. Parameters in the above simulations: $N_s = 20, m = 8, l = 8, \mu_\chi(0) = 40, s_\chi(0) = 8, \chi_c = 100, \eta_{\mu_\chi} = 5, \eta_{\mu_\chi} = 5, \eta_{s_\chi} = 2, \eta_{\chi_c} = 5$, and χ, μ_χ and s_χ are binned with size $1, 10$ and 1. In (A)-(D) the mutation rate $\nu = 0.2$.

Chapter 7

Coevolution and marine cyanobacteria

7.1 The "coexistence paradox" in microbe-phage ecosystems

One of the fundamental challenges in understanding microbe-phage communities is the problem of stability: How can such highly diverse systems stay stable? In a nutshell, the problem can easily be posed as follows. Phages are viruses that are parasitic on bacteria, infecting and duplicating inside bacteria cells. After phages duplicate inside cells, the new phages lyse the cell membrane and are released. The number of replicated phage is known as the burst size, and it is typically of order one hundred. Although phages can follow the lysogenic pathway, integrating their genome into the host cell to form a prophage, they can be switched into the lytic state by stress response to UV, starvation and other environmental cues. Lysogeny introduces a time delay into the lytic cycle but does not fundamentally remove the stability problem [199].

One proposed solution for the puzzle is to consider spatial heterogeneity, which dilutes the virulence of phage. By including space, phages resulting from lysis will first infect the neighboring bacteria, leading to a longer survival time for bacteria to recover their population. However the basic instability of the coexistence state does not fundamentally change.

Lysogeny has been interpreted as a non-selfish strategy by phage to promote long-term stability and coexistence in the community [200, 199]. After all, as a parasite whose life wholly depends on its host, a virus should never adopt a strategy to eliminate completely its host bacteria. Both ideas of including space (especially two-dimensional ones) and mild virulence have been tested in Lokta-Volterra type models, and the stability range is found to be less limited [200, 199].

Another point of view is to consider the problem from a more evolutionary perspective, not just within the framework of Lotka-Volterra or reaction-diffusion models. For example, what is the impact of coexistence in microbe-phage communities on their evolutionary trajectories, and what drives the evolution of microbe-phage ecosystems? More specifically, if the coexistence of microbes and phages is ubiquitous, then is there a benefit to microbes (hosts) of viruses (parasites) after all? Is it too simplistic to assign their biological roles based solely on population dynamics, without looking more deeply at other aspects of microbe-phage

interactions, such as the consequences of infection on the genomic level, or other ecological interactions? The answers to these questions should relate to the intricate relationships between microbes and phages, which then brings out the importance of the interplay between ecological interactions and evolution. Microbes also possess many other evolutionary features that make their ecosystems specially intriguing and also display useful information to understand their underlining interactions between ecology and evolution. Fortunately, in the last decade or so, the advent of culture-free sequence-based methods for exploring microbial ecosystems has meant that a detailed study of gene flow can be undertaken in large and important ecosystems, such as oceans, soil and the human gut. In this and following chapters, we will see that marine ecosystems are especially well-suited to framing these questions explicitly, with a hope of being able to make testable hypothesis about ecosystem stability mechanisms.

7.2 Coevolution and horizontal gene transfer

A pitfall of conventional models for microbe-phage ecosystems is that they oversimplify the interactions between them. Phages are usually regarded as the parasite of bacteria and thus become viewed purely as a predator. The traditional approach to study predator-prey systems is the Lotka-Volterra model, where the only interaction between predator and prey population density is predation in an activation-inhibition form. However, the relationship between bacteria and phage is much more complicated. For example, the coevolutionary arms race between antibiotics and pathogenic resistance is well-documented [201, 202]. In microbe-phage ecosystems, genes that encode and regulate the proteins for the conformation of receptors on bacterial cell surface and sequences of phage tail fibers can both continuously mutate after each other, indicating coevolution from microbe-phage interactions [203].

Horizontal gene transfer (HGT) has in the last decade been increasingly realized as a powerful driving force for accelerating evolution. HGT describes genetic materials being transferred between unrelated organisms from different lineages or species, and is especially common in microbes. Recently it has been documented to appear even between microbes and animals [204]. In contrast to vertical evolution, where new genes arise from genome arrangement such as genetic recombination and point mutation from ancestors, HGT provides a shortcut to introduce innovation. HGT was discovered in 1950s [205, 206], but had not been seriously studied for its evolutionary impact until the recent decade [18, 19, 20, 207]. By virtue of being a shortcut to innovation, HGT accelerates evolutionary processes. In particular, HGT has been proposed to be the main cause for the fast emergence of the canonical genetic code [208, 209], and is responsible in part for rapid evolution of antibotic resistance [210, 211]. The diversity of microbial genomes has also been

attributed to HGT [212, 211, 213].

There are three main types of HGT: transduction, conjugation and transformation. Conjugation is the process by which genetic materials are transferred between cells through direct contact. Transformation describes the process by which genes are taken by microbes directly from the environment. In transduction, genetic materials are transferred from one microbial cell to another by viruses following infection; this is the main pathway of HGT between microbes and phages that will concern us in this chapter, and will be elaborated later.

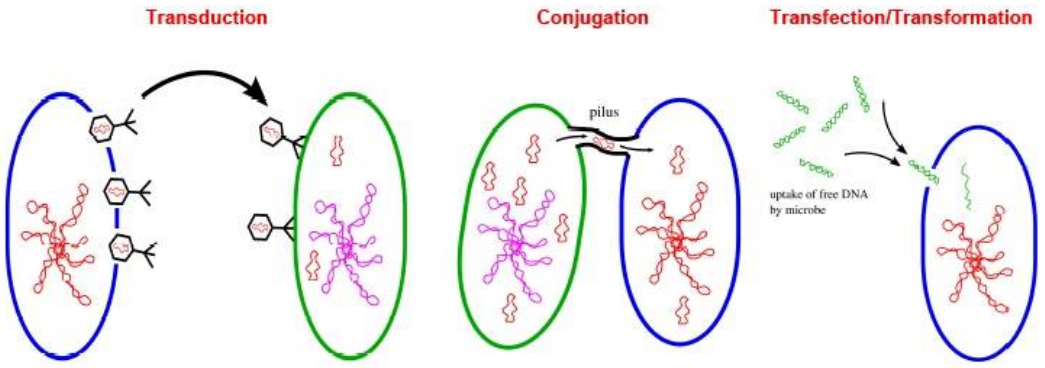

Figure 7.1: **Sketch of three main collective pathways of horizontal gene transfer**. Transduction, considered extensively in this thesis is a viral-mediated pathway, and requires detailed modeling in order to properly account for cyanobacteria-cyanophage interactions. Conjugation requires the bacteria to be in close contact so that plasmids, circular segments of DNA, can pass between the two bacteria. The bacteria are held in position by pili. In transformation, free environmental DNA is absorbed and utilized by a bacterium. This mechanism can be collective in the sense that the DNA source ins typically lysed bacterial cells. Figure courtesy of Nicholas Chia and Nigel Goldenfeld.

7.3 Marine cyanobacteria as a system of collective evolution

To study a concrete bacteria-phage ecosystem, we are going to focus on perhaps the most well-studied example, that of *Prochlorococcus spp.* and its phages. We will see that the special features in bacteria-phage ecosystems suggest an alternative solution to the "coexistence problem", one in which we exploit not only the conventional population dynamics but also the multiscale interplay between ecology and evolution. Therefore, it leads one to reshape the questions for modeling bacteria-phage ecosystems to: How does the multiscale complexity of interactions between bacteria, phages and their genomes influence the evolution, dynamics and stability of their communities? We will see that a model of the collective interactions provides a natural unified description of the features of *Prochlorococcus spp.* system that would otherwise have to be

explained on-by-one as special cases. We now detail these unusual aspects of this system.

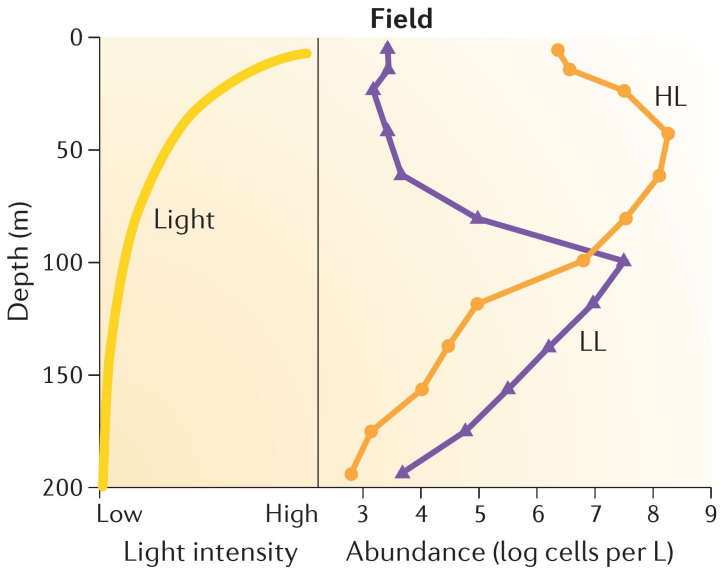

Figure 7.2: **Niche stratification of two ecotypes of *Prochlorococcus*.** Partitioning of the high-light adapted ecotype (HL) and low-light adapted ecotype (LL) which are distributed at different depth of the ocean. Figure is taken from [21].

Prochlorococcus is the most abundant photosynthetic organism on the planet with a total population estimated to be about 10^{27} cells [21]. It fixes the same amount of carbon as all the global croplands. Its genome is highly streamlined with only 1700 genes in 1.65 Mbp [21], which is one of the smallest known. For comparison, *E. coli.* has a genome with 4.6 Mbp and 4377 genes depending on the strain. With such a small genome, *Prochlorococcus* has a small body size that permits increased photosynthesis efficiency, thus allowing it to be free-living in low-nutrient regions of ocean with a dilute density of 10^6 cells/mL [21]. Remarkably, *Prochlorococcus* does not possess any special defense mechanism against phage attack, such as CRISPR, restriction modification or prophages. It seems that their principle means of defense against phage is modification of cell surface molecules that prevent phage attachment. These molecules are expressed from genes that have been rapidly modified through mutations and horizontal gene transfer with other bacteria phyla. These genes reside in genomic islands and constitute the majority of the genetic diversity [21].

Genomic islands indicating horizontal gene transfer: Many genes of the flexible genome are found to cluster in the microbes' chromosomes into a region called a genomic island (GI). Genomic islands usually

contain atypical gene sequence compositions and are flanked by special elements such as insertion sequences, and thus are thought to originate from HGT events, and are regarded as *prima facie* evidence of HGT. Genes contained within genomic islands that encode specific functions such as antibiotic resistance or metabolisms then provide information about the selection pressure during evolution. In *Prochlorococcus spp.*, the genomic islands contain genes associated with the cell surface protein, and have been selected through competition with phage.

Pan-genome and diversity: Indeed, this diversity has made it difficult to apply the biological species concept to microbes. Without going into this complex issue in great depth, in this thesis we will use the 16S rRNA 97% similarity to define operational taxonomic units (OTUs), which we will call "species" for convenience. It is known that bacteria-phage communities are highly diverse. Unlike eukaryotic organisms, bacteria and archaea strains of the same species only share partially the same genes in their genomes. The whole set of genes of the strains from the same microbial species is called a pan-genome. A pan-genome is composed of a core genome and a flexible genome. The core genome contains genes that are present in all strains of the species, and are presumably responsible for the crucial functions, such as translation and replication. The flexible genome is an assembly of genes that differentiate strains such as certain antibiotic resistance genes and metabolic genes. The size of the flexible genome is a measure of the diversity of the pan-genome of a microbial species. The high diversity of pan-genome seemly makes it more difficult to reach stability in microbe-phage communities. With constant gain and lost of genes, the pan-genome of *Prochlorococcus* is still growing today; the estimated size of its pan-genome is huge, with more than 84,000 genes, which is four times larger than the size of the human genome [21].

Ecotypes: Diversity is also manifested in the wide distribution of habitats where different niches have been occupied by *Prochlorococcus* in order to adapt to different light intensity and wavelength for photosynthesis. In particular, on the large scale *Prochlorococcus* exhibits niche stratification with two distinct subgroups: (1) the low-light (LL) adapted ecotype, utilizing shorter wavelength and lower intensity of light occupies the bottom of the euphotic zone; (2) the high-light (HL) adapted ecotype that can live under high intensity light and absorbs longer wavelength is more abundant at the top layers near the surface [21].

Evidence for HGT: Detailed phylogenetic analysis has shown that the high-light adapted ecotype evolved from the low-light adapted ecotype [21]. The specific adaptations, in terms of the evolution of the present day light-harvesting complex of *Prochlorococcus* from its roots in *Synechococcus* about 150 million years ago have been described in [214]. In particular, *Prochlorococcus* uses a chlorophyl light-harvesting complex

where *Synechococcus* uses one based upon Phycobilisomes. These adaptations permit *Prochlorococcus* to exploit variations with depth of sea water absorption spectra, facilitating its expansion from the ancestral range. There is good evidence that this range expansion was facilitated through viral-mediated HGT. We now outline the evidence for this and the way in which viruses benefit from using and even improving their host's photosystem genes.

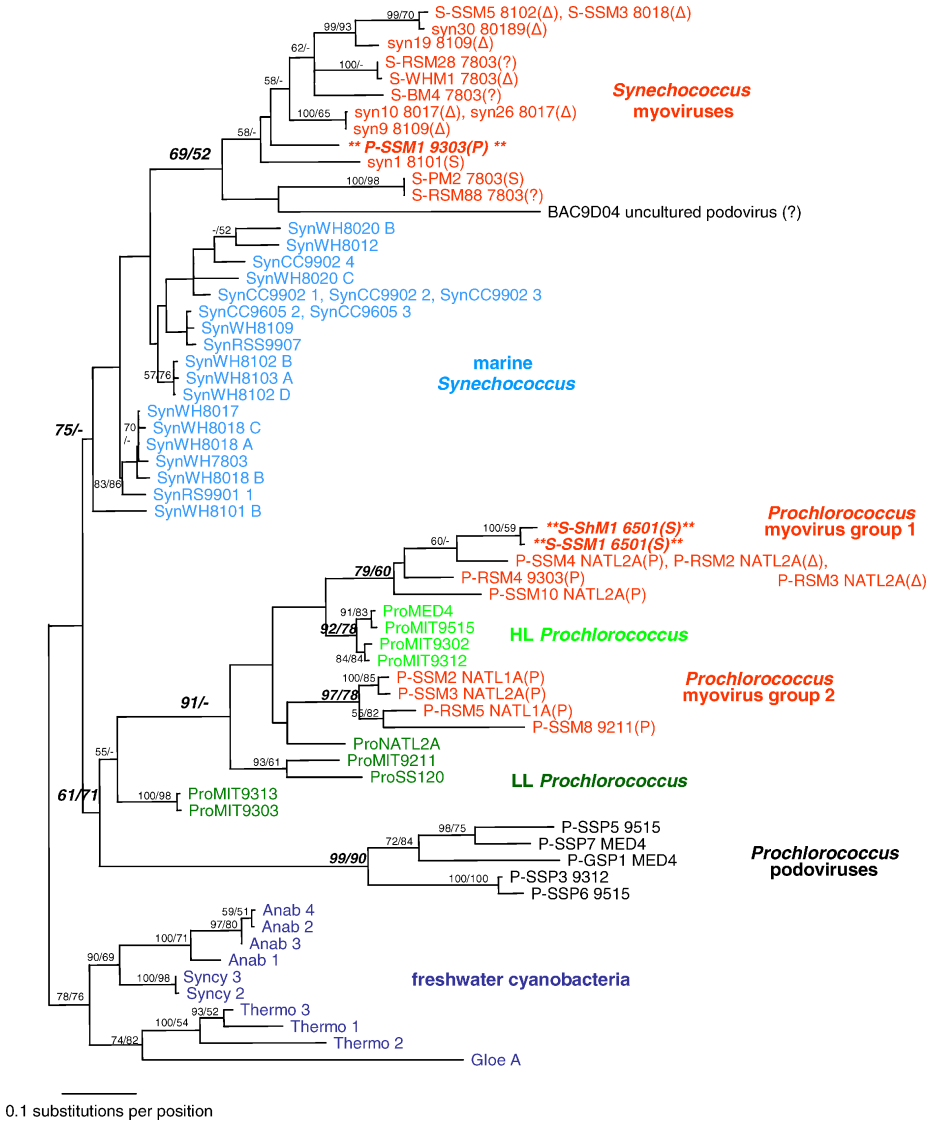

Figure 7.3: **Phylogenetic tree of photosystem II gene** *psbA* **sequences of cyanobacteria and cyanophages.** Four clusters with phage origins that are labeled in red and black color indicate four HGT events. Figure is taken from [215].

Cyanophages: Phages of *Prochlorococcus*, termed cyanophages, are lytic double-stranded DNA tailed phages in T4, T7 and lambdoid groups. However, they contain only partial core genes of these groups, the rest of their payload being Photosystem I and II genes that encode core reaction-center proteins used in photosynthesis [215, 213]. In short, this phylogenetic evidence suggests that cyanophages could have assisted niche stratification of *Prochlorococcus* ecotypes by evolving and distributing high-light-inducible genes that protect the photosynthetic apparatus from sunlight damage and thus can sustain the fitness of cells near the sea surface [216, 217].

One way to decipher the interactions between cyanobacteria and cyanophage is to study the evolutionary trajectories of their shared genes. From phylogenetic analysis of photosystem I and II genes, it appears that these genes had been horizontally transferred first from cyanobacteria to cyanophages and back and forth at least four times [215]. For example, Fig. 7.3 shows the phylogenic tree of sequences of the photosystem II gene *psbA* that is shared between cyanobacteria and cyanophages. If the gene sequences in cyanobacteria and cyanophage were unrelated evolutionarily, they would be located at separate branches of the phylogenetic tree. On the contrary, the analysis showed that they are intertwined together in the phylogenic tree, indicating that the gene had a canonical signature of HGT, in this case between cyanobacteria and cyanophages.

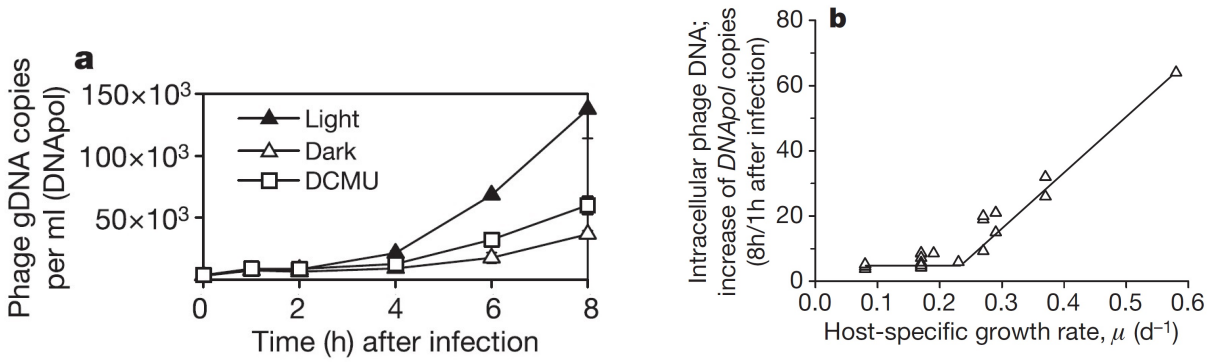

Figure 7.4: **Dependence of cyanophage fitness on hosts' photosynthesis activity and ability.** (a) Copy number of phage DNA, which may be interpreted as related to phage fitness, as a function of time after infection showing the dependence on light intensity. The figure shows that in high light conditions, phage DNA is more abundant, suggesting an increased burst size under such conditions. (b) Cyanophage fitness increases with host-specific growth rate, implying that better photosynthesis performance at best leads to higher phage fitness, presumably between there is more dioxynucleotide triphosphate available to synthesize phage DNA. Figures are taken from [217] and [218] respectively.

Viral utilization of photosynthesis genes: The next specific question is: what is the significance of HGT of the photosystem genes between cyanobacteria and cyanophages, and what are its evolutionary consequences? Experiments showed that both photosystem II genes and high-light-induced genes that were encoded by cyanophages were found to be expressed inside cultured *Prochlorococcus* after infection. This leads to the speculation that these phage genes are utilized to maintain the hosts' photosynthesis capacity during infection [218, 217]. The delay time to lysis (latent time) was also found to become longer when photosystem II genes were expressed [217, 215], suggesting that during infection , the host lifetime is extended by the phage genes, allowing for more replication of phage. At the same time, the resulting copy number of cyanophages increased with host specific growth rate, indicating a positive correlation between phage fitness and the host cell physiology and cell cycle conditions [218, 217], as shown in Fig. 7.4. These data presumably reflect the fact that it is problematic to manufacture enough DNA for the desired number of viruses unless the cellular machinery is available for DNA synthesis. In other words, these experimental results imply that cyanophages benefit in terms of their reproductive fitness when they provide genes to maintain the metabolic function of their hosts.

Summary: In the previous section we have outlined the current understanding of how horizontally-transferred photosystem genes between cyanobacteria and phage coevolve and can produce benefits for both participants. Following the discoveries of HGT evidence in cyanobacteria and cyanophages, Sullivan *et al.* made the following speculative statement [215]:

> "Therefore, mounting evidence indicates that **host-like genes acquired by phages undergo a period of diversification in phage genomes and serve as a genetic reservoir for their hosts**. Thus, a complex picture of overlapping phage and host gene pools emerges, where **genetic exchange across these pools leads to evolutionary change for host and phage**. Fully understanding the mechanisms of microbial and phage coevolution clearly **requires an improvement in our ability to quantify horizontal gene transfer** at the whole and partial gene level and in our ability to accurately estimate the relative fluxes into and out of these pools."
> (Sullivan *et al.* 2006)

That is, microbe-phage interactions, even though apparently mediated antagonistically, resulting in the death of bacteria, can create a global reservoir of genes, which benefits both microbes and phages.

If such an idea is indeed possible to be realized, we should be able to extend our understanding of the process to a fully dynamical description, i.e. to recapitulate similar phenomena in an explicit model. The goal of the model should be to describe specifically how horizontal gene transfer occurs in microbe-phage

ecosystems, leading to a mutualistic coevolution despite the antagonistic predator-prey interaction. Is there a tradeoff between individual sacrifice of bacteria to predation, thus allowing a collective benefit to the whole community? How does the coexisting state evolve spatially from the low-light initial strain of *Synechococcus*? These questions are considered in the next chapter.

Chapter 8

Stochastic individual-level model for cyanobacteria-cyanophage

In this chapter, we present a detailed model for a collective, coevolving state of coexisting cyanobacteria and their phage. We make a deliberately over-simplified model of *Prochlorococcus* to focus on a minimal description of collective mechanism for stability. We will see that many of the idiosyncratic features of the *Prochlorococcus* system emerge naturally from our individual level, minimal model. This suggests that such features would be shared by other ecosystems in which our proposed mechanisms are operative.

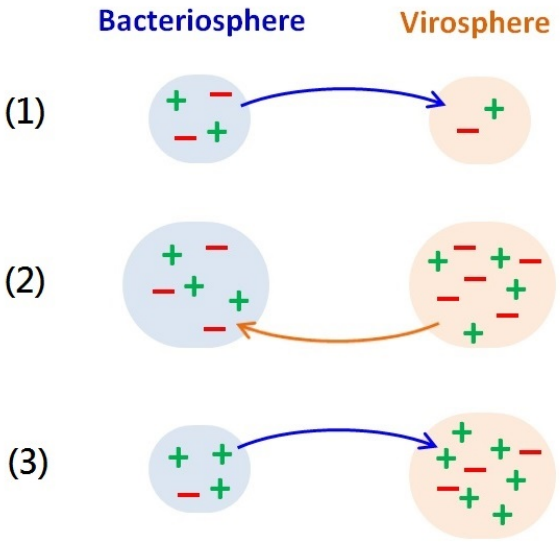

Figure 8.1: **Sketch of collective coevolution through HGT**. (1) Phages first gain genes from bacteria through HGT in terms of generalized transduction. (2) Compared with bacteria replication, phages have higher mutation rate. As a consequence, phages develop larger heterogeneity in their genomes and become a gene pool for bacteria through further HGT. (3) Through HGT from phages to bacteria, bacteria keep beneficial genes following streamlining, and become a beneficial pool for viruses through further HGT.

Our proposed scenario can be sketched in outline as follows (please refer to the cartoon in Fig. 8.1). Consider a phenotype that is assumed to be controlled by a single gene. Here, the green plus sign represents "beneficial genes" for encoding more efficient metabolic functions than those of the wild type, and red minus sign corresponds to the otherwise "inferior genes". We present the argument in three steps.

1. When HGT occurs, genes originally from the bacteriosphere are transferred to viruses.

2. Viruses have a higher mutation rate than bacteria and thus generate novel genes in virosphere. In actuality this step takes place in the cellular environment following infection, but we will discuss as if the mutations occurred within the virosphere. Bacteria acquire these new genes through subsequent HGT from viruses.

3. Since bacteria are under selection pressure to do genome streamlining, the size of their genome remains small, which results in strong selection among strains. Consequently, inferior genes will be filtered out (purifying selection), and the bacteriosphere gradually becomes a pool of beneficial genes relative to the wild type. Thus HGT provides viruses with better genes than before.

In essence, this hypothesis is based on two key points: First, bacteria and phages have distinct evolutionary time scales that make them adept at different situations. Second, two-way HGT compensates for the downside of their evolutionary time scales, through which bacteria and phages benefit from each other. We will explain this in detail below. The consequence is a collective, emergent mutualistic coevolution in the community, despite the cost of individual bacterial sacrifice.

Next we present a sequence of models with different interactions and assumptions to understand qualitative features of phase diagram. These models are caricatures of the following cyanobacteria-phage interactions: (1) predation and evolution of barrier to predation (g_{BP}); (2) HGT dynamics: generalized transduction; (3) phenotypic effect of photosynthesis genes on both bacteria and phage (g_{PS}); (4) consequences of small genome size and deleterious mutations; (5) cyanobacteria and phage in a photon gradient.

8.1 Coevolution of barrier to predation stabilizes bacteria-phage community

In this model, bacteria (B) are assumed to possess a gene that governs the phenotype of defense against the infection by phages (V), and the virulence of phage infection is represented by a phenotype that is determined solely by a phage gene. Of course this is only a crude representation of the complex set of genes and regulatory networks that control phenotypes such as cell surface receptors. Nevertheless our intent is to understand the dynamical interplay between the varied selection pressures acting on the bacteria and the phage. For this purpose, a minimal model is adequate.

The bacterial defense phenotype is quantified by a variable named "bacterial infection barrier", where the value corresponds to the threshold of being infected. The value of the bacterial infection barrier is meant

to mimic the way in which cell surface receptor chemistry is modified by the cell to prevent phage infection Similarly, the variable corresponding to the phage phenotype of virulence, termed "viral infection barrier", is set to be the threshold of a successful infection. This is a simplification of the specific gene sequence that codes for the phage tail that attaches to the bacterial receptors. In general, the virulence of viral infection is related to the phages adsorption properties, such as the diffusivity of phage particles on the bacterial cell membrane before they attach to the receptors. This is also correlated with the density of receptors on the bacterial cell membrane. Virulence is also considered to be related to the delay (or latent time) of lysis after a phage particle attaches to a receptor. Phages with longer delay of lysis are considered to be less virulent.

We must emphasize that the genes that control the bacterial infection barrier and the genes that determine the viral infection barrier are distinct and express different proteins. Nevertheless, to first convey the main idea we simplify the model by assuming that the bacterial infection barrier and the viral infection barrier are controlled by the same gene that can be expressed by both the bacteria and the phage. We model the gene controlling the barrier to infection by its phenotype, whose value is assumed to be a positive real number g_i, which we will call the allele below. Thus B_i would be a bacterium whose gene value is g_i, and V_j would be a virus whose gene value is g_i. The g_i and g_j evolve in time due to the coevolutionary dynamics described below. The competition between bacteria B_i and virus V_j is controlled by the difference $g_i - g_j$, which governs the predation rate in the stochastic individual level model of Section 8.1.2. Under this assumption, a bacterial cell and a phage with the allele of infection barrier value i and a phage with the allele of infection barrier value j can be represented as B_i and V_j respectively. Therefore, a successful infection results from the comparison between the values of the infection barrier of bacteria and phages. The physical interpretation is that when the tail of a phage attaches a receptor on the surface of a bacterium and the value of the phage infection barrier is higher than the value of the bacterial infection barrier, i.e. $i < j$, then with some probability, described in detail below, the phage can successfully insert its genome into the cell. With this scheme, next we study several models under different situations.

8.1.1 Model 1-1: without evolution

We start by considering a minimal model for a system composed of bacteria with certain initial allele $g_i \in \mathbb{R}$ and phages with a single initial allele $g_j > g_i$. There is no evolution of the bacteria or phage,and we simply

consider their well-mixed ecological interactions as follows:

$$\begin{aligned}
&\text{Bacterial reproduction:} && B_i \xrightarrow{b} B_i + B_i \,, \\
&\text{Bacterial competition:} && B_i + B_i \xrightarrow{c} B_i \,, \\
&\text{Bacterial/Viral degradation:} && B_i \xrightarrow{d_{\mathrm{B}}} \varnothing \,, \quad V_j \xrightarrow{d_{\mathrm{V}}} \varnothing \,, \\
&\text{Viral reproduction:} && B_i + V_j \xrightarrow{p} (m+1)V_j \,,
\end{aligned} \tag{8.1}$$

where b is the bacteria birth rate, c is the competition rate between individual bacteria, which determines bacterial carrying capacity, in the mean-field population description. d_{B} and d_{V} are the respective death rates, p is the infection/predation rate and m is the phage burst size.

The population level mean-field equations are:

$$\frac{dB}{dt} = bB - cB^2 - d_{\mathrm{B}} - pBV \tag{8.2}$$

$$\frac{dV}{dt} = mpBV - d_{\mathrm{V}}V, \tag{8.3}$$

and the mean-field fixed point for coexistence is

$$B^* = \frac{d_{\mathrm{V}}}{mp}, \tag{8.4}$$

$$V^* = \frac{b - d_{\mathrm{B}} - cB^*}{p}. \tag{8.5}$$

The phage population would increase quickly due to large burst size, leading to significant decrease of bacteria population. In this case, demographic noise can easily drive the extinction of bacteria, and then phage too. In this sense, although in mean-field theory, the population level model is stable, the individual level model does not exhibit stable coexistence, and undergoes a transition to extinction (Fig. 8.2).

8.1.2 Model 1-2: with coevolution of infection barrier gene

A second important point is that the fixed points of the mean-field population level equation are static. In fact, ecosystems are generally maintained out of equilibrium by energy flux, mutation, co-evolution and HGT, etc. The "steady states" are dynamical, or non-equilibrium steady states that violate detailed balance. Therefore frameworks that consider only static fixed point are in some sense not capturing an important and intrinsic aspect of real ecosystems. Now we will demonstrate that coevolution leads to a non-equilibrium

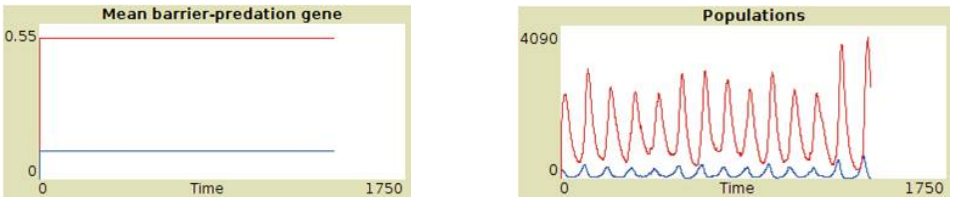

Figure 8.2: **ILM simulations of model without evolution of infection barrier gene.** (Left) Mean gene value for infection barrier for bacteria (blue) and viruses (red) over time. (Right) Bacteria population is driven to extinction due to viral burst size. Allele of bacterial and viral infection barrier are constant $g_i^B(t) = g^B(t=0) = 0.1$ and $g_i^V(t) = g^V(t=0) = 0.5$. Viral burst size $m = 5$, bacterial reproduce rate $b = 0.2$, bacterial and viral degradation rate $d_\mathrm{B} = d_\mathrm{V} = 0.05$ and predation rate $p = 1$.

steady state that has stable coexistence, even though the static, non-evolving system is unstable.

The individual-level model of the previous section is generalized to include mutations of bacteria and phages with arbitrary allele $g_i, g_j \in \mathbb{R}$. Thus the governing reactions become:

$$\begin{aligned}
&\text{Bacterial reproduction:} && B_i \xrightarrow{b\,\mu_\mathrm{B}} B_i + B_i\,, \\
&\text{Bacterial competition:} && B_i + B_j \xrightarrow{c} B_i\,, \\
&\text{Bacterial/Viral degradation:} && B_i \xrightarrow{d_\mathrm{B}} \varnothing\,,\quad V_i \xrightarrow{d_\mathrm{V}} \varnothing\,, \\
&\text{Viral reproduction:} && B_i + V_j \xrightarrow{p_{ij}\,\mu_\mathrm{V}} \sum_{l=1}^{m+1} V_{k_l}\,,
\end{aligned} \tag{8.6}$$

where μ_B and μ_V are the mutation rate for bacteria and phages and p_{ij} the infection rate that depends on alleles g_i, g_j. We take for simplicity $p_{ij} \propto (g_j - g_i)$ When one new bacteria or phage individual is reproduced, its infection barrier gene changes by a normally-distributed amount if mutation occurs. We assume that the rates of birth, competition, death and phage burst size are the same among all bacteria/phage alleles. The predation rate p_{ij} in general is a function of the bacterium allele g_i and phage allele g_j, and the newborn phages can have different allele g_k from the mother phage.

In the literature of co-evolution, several types of interaction kernel between predator and prey have been proposed, describing different biological hypotheses with corresponding different results [16]. The most common assumption for the interaction kernel is the "lock-and-key" mechanism, where a predator allele interacts with a limited range of prey allele [16]. Ideally the predation event only occurs if the predator allele precisely matches that of its target prey. In practice, such extreme host-range specificity is rare, and this delta function interaction is modeled as a Gaussian, or even as a "top hat" function as we do here.

In this model, a co-evolutionary arms race in the infection barrier of bacteria and phage is observed (Fig. 8.3). A bacterium that mutates to a larger value of g_i survives until a virus evolves with a value of g_j that

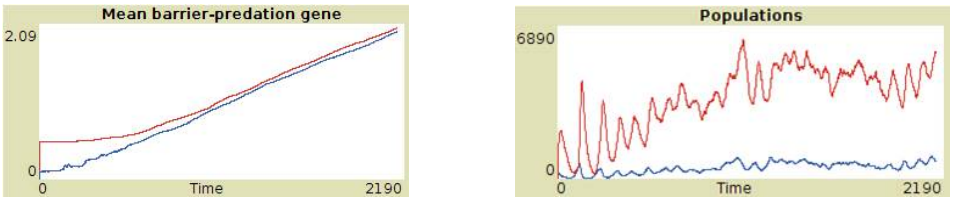

Figure 8.3: **ILM simulations of model with coevolution of infection barrier gene.** (Left) Mean gene value for infection barrier for bacteria (blue) and viruses (red) are evolving over time, showing coevolutionary arms race. (Right) Bacterial and viral population both can sustain through mutation and purifying selection. Initial condition and parameters are same as Fig. 8.2, with bacterial and viral mutation rate for infection barrier $\mu_B = \mu_V = 0.05$, where fluctuations in gene value are Gaussian noise with standard deviation $\sigma = 0.1$

can match g_i. Then the arms race begins another cycle. Mutation ensures a persistent coexisting state by continually providing more competitive genes to both bacteria and phage separately, leaving the bacteria and the phage with the largest infection barrier surviving in the system. The flux of new alleles sustains the system by creating a dynamic steady state of coexistence.

This picture of a coevolutionary arms race changes if there is a significant disparity in mutation rate. Since the mutation rate of phages is in general higher than that of bacteria, we may anticipate that overwhelmingly strong phage alleles arising from rapid mutation will force the bacteria to extinction, as found in simulation (Fig. 8.4). Thus the coevolutionary dynamics only stabilizes the system in a certain range of parameters or time scales, that we have not systematically explored. Nevertheless, the general trend is clearly seen in simulations, but it turns out that the stability can be restored by considering collective effects.

As in the first model with evolution, the large burst size of phage leads to a huge imbalance between the bacteria and phage population numbers. However, this can be alleviated by introducing intraspecies mutations to both bacteria and phages. Similarly, if there is an additional asymmetry due to the higher mutation rate of phages compared to bacteria, the arms race is weighted more on the side of phage. Therefore,

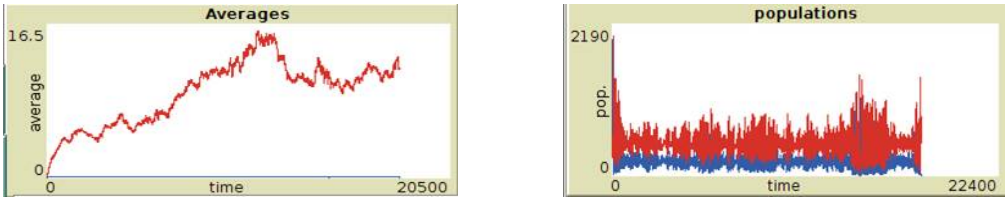

Figure 8.4: **ILM simulations of model with coevolution of infection barrier gene with unequal mutation rate.** (Left) Mean gene value for infection barrier for bacteria (blue) and viruses (red) are evolving over time, where viral mutation rate is faster than bacterial mutation rate. (Right) Bacterial population is driven to extinction due to intense predation by fast mutating viruses. Initial condition and parameters are same as Fig. 8.2, with bacterial and viral mutation rate for infection barrier $\mu_B = 0.05$ and $\mu_V = 0.5$ respectively.

to understand the observed robustness of bacteria-phage systems, we consider an alternative mechanism that uses a collective effect to restore the balance. This mechanism exploits HGT to introduce an interspecies flux of genes, thus stabilizing the system.

To illustrate this effect, we are going to consider next a toy model that is not biologically realistic, but which nevertheless demonstrates the stabilizing influence of HGT. We emphasize that the model is not realistic because we have used a single gene to represent both the bacterial defence phenotype and the viral attack phenotype. In reality they are controlled by different genes. The second level of unrealism is that we will now look at the consequences of horizontal transfer of this gene between virus and bacteria, even though there is no reason to believe that there is a two-way transfer of the genes involved in the coevolutionary arms race. Later we will use this toy model in a situation where it is justified, namely the transfer of photosystem I and II genes between bacteria and phages, as observed in the *Prochlorococcus*-phage system.

8.2 Model 2: Toy model for the stabilizing role of HGT

To include HGT between bacteria and phages in the above minimal model, we need to go into detail about the mechanism of on generalized transduction, which we will model in a coarse-grained way. Generalized

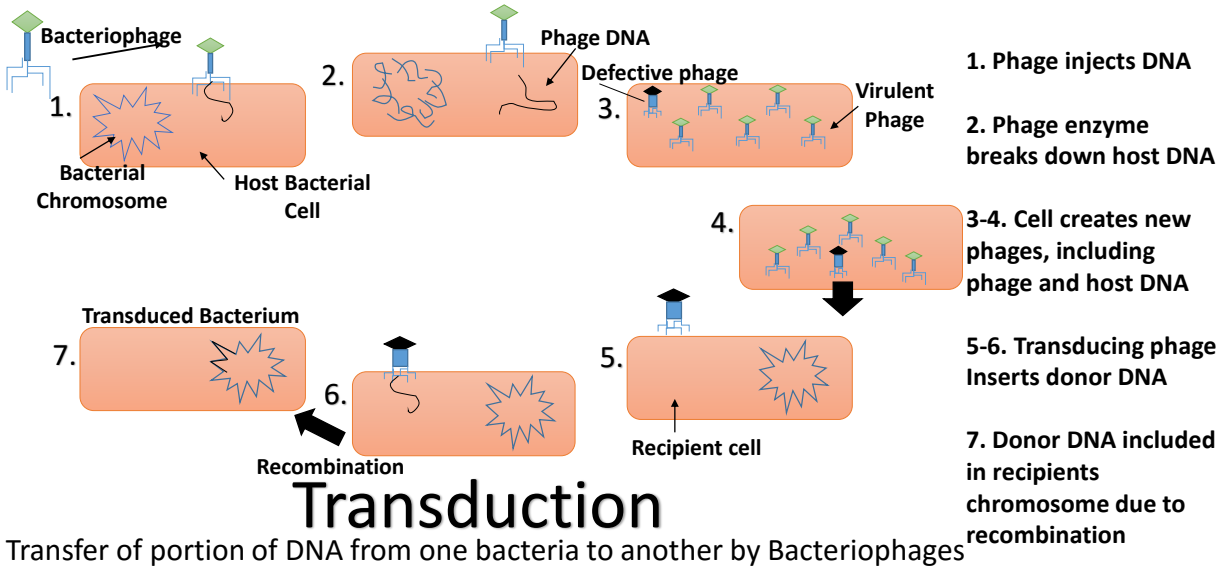

Figure 8.5: **Illustration of generalized transduction.**

transduction involves the following steps, as shown in Fig. 8.5. When a phage that has gene y_j infects a bacterial cell carrying gene x_i, the phage inserts its gene into the cell. Once the infection is successful, the machinery of the host cell with gene x_i is hijacked by the phage gene y_j and thus produces new phages with phage gene y_j. A phage that has gene y_j, and through an assembly error is carrying a bacterial gene x_i, which we refer as a "zombie phage", attaches to another bacterium cell with gene $x_{i'}$, and inserts bacterial gene x_i into the cell. If the infection is successful, the machinery of the host cell with gene $x_{i'}$ is hijacked by the genes from the zombie phage, and the bacterial gene x_i from the another bacterium homologously recombines into the bacterium's genome. Since the cell's machinery is hijacked, only genes from the phage are expressed, but in this case, phage genes are absent. Only the bacteria genes carried by the zombie phage are expressed. Thus, the zombie phage will not initiate lysis and kill the host cell, as other genes from normal phages do. The bacterial gene x_i will be duplicated by the hijacked machinery and carried to descendants when the cell replicates. On the other hand, if the phage with tail gene y_j fails to insert the bacterial gene x_i it carries into the cell, the phage will not be able to survive and the cell remains alive and functions normally. The effective consequence is that the new bacterial cell now carries the genes from the previous bacteria host. This is the way in which viral-mediated HGT works.

In reality, HGT is mediated through the infection process, and a variety of genes can be transferred through generalized transduction. We first focus on HGT of the gene for infection barrier. As mentioned before, we assume that for the moment the gene for bacterial infection barrier and the gene for phage infection barrier are compatible, and thus the alleles can be directly exchanged through generalized transduction in the model. The individual-level model including generalized transduction is modified to:

$$
\begin{aligned}
&\text{Bacterial reproduction:} && B_i \xrightarrow{b\,\mu_{\mathrm{B}}} B_i + B_i\,,\\
&\text{Bacterial competition:} && B_i + B_j \xrightarrow{c} B_i\,,\\
&\text{Bacterial/Viral degradation:} && B_i \xrightarrow{d_{\mathrm{B}}} \varnothing\,,\quad V_i \xrightarrow{d_{\mathrm{V}}} \varnothing\,,\\
&\text{HGT from bacteria to phages:} && B_i + V_j \xrightarrow{p_{ij}\,\mu_{\mathrm{V}}} \sum_{l=1}^{m+1-m_{\mathrm{h}}} V_{k_l} + m_{\mathrm{h}} V_i\,,\\
&\text{HGT from phages to bacteria:} && B_i + V_j \xrightarrow{p_{ij}\,h_{\mathrm{B}}} B_j,
\end{aligned}
\tag{8.7}
$$

where m_{h} is the number of newborn phages that carry the gene from B_i and fail to infect other bacteria. In general m_{h} is stochastic; in our simulation, m_{h} is determined by the horizontal gene transfer rate from bacteria to viruses. We set that each newborn phage among the total burst size adopts the host's gene value at a rate h_{V}. We generally set $h_{\mathrm{V}} = h_{\mathrm{B}}$. These phages are regarded as "zombie phages". Here, since the

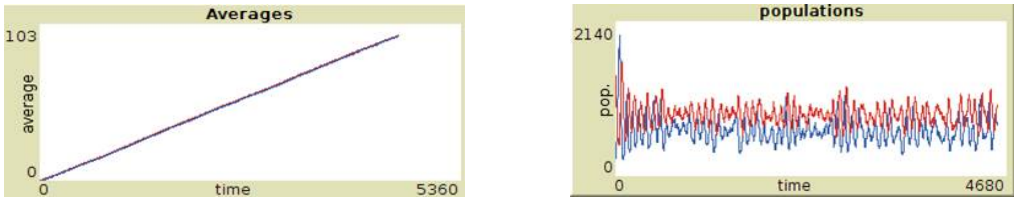

Figure 8.6: **ILM simulations of model with coevolution and horizontal transfer of infection barrier gene.** (Left) Mean gene value for infection barrier for bacteria (blue) and viruses (red) shows coevolutionary arms race again, even though viral mutation rate is faster than bacterial mutation rate. (Right) Bacterial and viral population coexist due to HGT. Initial condition and parameters are same as Fig. 8.2, with bacterial and viral mutation rate for infection barrier $\mu_{\mathrm{B}} = 0.05$ and $\mu_{\mathrm{V}} = 0.5$ respectively and HGT rate $h_{\mathrm{B}} = h_{\mathrm{V}} = 1$.

infection barrier gene of bacteria and the infection barrier gene of phages are assumed to be compatible, they are basically the same variable, so when HGT occurs the bacterium B_i and the phage V_j just exchange their gene value with each other, and with this assumption there is no differentiation between normal and zombie phages. Instead, the effect of individual zombie phages is converted into an average rate h_{B} of "failed" infection for all phage individuals.

When simulated, we found that the bacteria constantly obtain new gene alleles from the phages, whose mutation rate is higher, and thus a coexisting, fluctuating population of bacteria and phage emerges, and is apparently robust over a long time (Fig. 8.6).

8.3 Model 3: Phenotypic effect of photosynthesis genes on both bacteria and phage

In order to complete a description of the self-sustained nature of collective coevolution, we now consider the effect of HGT on fitness. The appropriate genes are those responsible for photosynthesis, which are known to exist and be used in both cyanobacteria and cyanophages. We again focus on a photosynthesis phenotype that is assumed to be governed by a single type of genotype, and a bacterial/phage individual with the allele of photosynthesis gene value i is denoted as B_i/V_i. In particular, the gene affects the bacterial reproduction efficiency which is modeled as a function of the value of the bacterial cell's photosynthesis gene allele. The same gene controls the phage reproduction, i.e. phage burst size, which is also a function of the value of the phage's photosynthesis gene allele. Thus both the bacteria and the phage can benefit from the evolution of the photosynthesis gene.

8.3.1 Model 3-1: Coevolution of photosynthesis genes without HGT

To specifically see the effect of HGT, we start from a model with coevolution but without HGT, in a form similar to Model 1 in Section 8.1.2 for the infection barrier in Eq. (8.6):

$$\begin{aligned}
&\text{Bacterial reproduction:} && B_i \xrightarrow{b_i\,\mu_{\rm B}} B_i + B_i\,, \\
&\text{Bacterial competition:} && B_i + B_j \xrightarrow{c} B_i\,, \\
&\text{Bacterial/Viral degradation:} && B_i \xrightarrow{d_{\rm B}} \varnothing\,,\quad V_i \xrightarrow{d_{\rm V}} \varnothing\,, \\
&\text{Viral reproduction:} && B_i + V_j \xrightarrow{p\,\mu_{\rm V}} \sum_{l=1}^{(m_j+1)} V_{kl}\,,
\end{aligned} \tag{8.8}$$

where both the bacterial reproduction rate b_i and the phage burst size m_j depend on the bacterial/phage individual's allele g_i, g_j respectively. Here we assume that the infection rate is independent of photosynthesis alleles.

Similar to the situation in Section 8.1.2, in the case where the phage mutation rate is much higher than that of bacteria, i.e. $\mu_{\rm V} \gg \mu_{\rm B}$, phages evolve to larger burst size with a speed faster than the evolution in bacterial birth rate, leading to asymmetry in reproduction number again. Thus we observe unstable co-existence leading to extinction of the ecosystem (Fig. 8.7), as in the earlier unrealistic toy model in (Fig. 8.3).

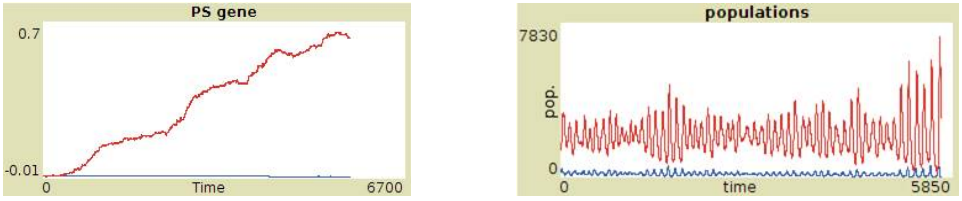

Figure 8.7: **ILM simulations of model with coevolution but without HGT of photothynthesis gene.** (Left) Viral gene (red) evolves faster due to higher viral mutate rate, while bacterial gene (blue) evolves slowly. (Right) This leads to quickly increased viral burst size and thus viral population (red), easily driving bacteria population (blue) to extinction, similar as Fig. 8.4. Initial condition and parameters are same as Fig. 8.2, and the photosynthesis gene values for bacteria and viruses are $g^B_{\rm PS}(t=0) = g^V_{\rm PS}(t=0) = 0$. Bacterial birth rate is set to be linear to photosynthesis gene value, $b_i = b_0 + \lambda_b g_i$, where $b_0 = 0.2$ and $\lambda_b = 1$. Viral burst size is set to be a hyperbolic tangent function and is bounded by a maximum burst size $m_{\rm max} = 10$. Bacterial and viral mutation rate for photosynthesis gene are $\mu_{\rm B} = 0.05$ and $\mu_{\rm V} = 0.5$ respectively.

8.3.2 Model 3-2: Coevolution of photosynthesis genes with HGT

Now we switch on the effects of HGT. The modified individual-level model including generalized transduction as HGT of the photosynthesis gene is:

$$\begin{aligned}
&\text{Bacterial reproduction:} && B_i \xrightarrow{b_i\,\mu_{\rm B}} B_i + B_i\,,\\
&\text{Bacterial competition:} && B_i + B_j \xrightarrow{c} B_i\,,\\
&\text{Bacterial/Viral degradation:} && B_i \xrightarrow{d_{\rm B}} \varnothing\,,\quad V_i \xrightarrow{d_{\rm V}} \varnothing\,,\\
&\text{HGT from bacteria to phages:} && B_i + V_j \xrightarrow{p\,\mu_{\rm V}} \sum_{l=1}^{m_j+1-m_{\rm h}} V_{k_l} + m_{\rm h} V_i\,,\\
&\text{HGT from phages to bacteria:} && B_i + V_j \xrightarrow{p_{ij}\,h_{\rm B}} B_j.
\end{aligned} \tag{8.9}$$

Here HGT rates are defined in the same way as in Section 8.2. As expected, similar to Section 8.2, HGT ensures a persistent coexisting state by continually replenishing competitive photosynthesis genes between bacteria and phage, as shown in Fig. 8.8.

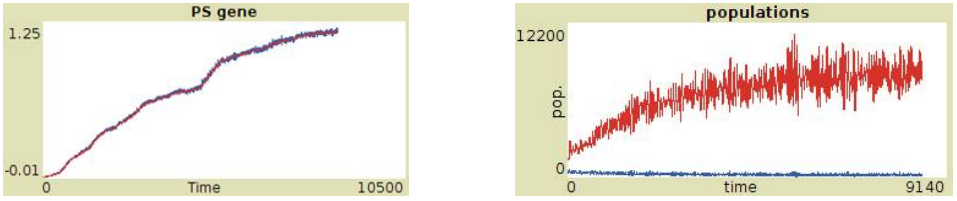

Figure 8.8: **ILM simulations of model with coevolution and HGT of photothynthesis gene.** HGT rates are $h_{\rm B} = h_{\rm V} = 1$. (Left) Through HGT, bacteria obtain new genes created by phages that have high mutation rate, and their gene values improve together in the course of evolution. (Right) In a range of parameter values the bacterial population can be sustained indefinitely.

8.4 Model 4: HGT as a mechanism to avoid mutational meltdown due to deleterious mutations

Up to now, we have seen how the bacteria benefit from HGT and the higher mutation rate of viruses. However, this does not provide a benefit to the viruses. We will now identify the way in which viruses also benefit from the HGT. To do that we need to consider the distribution of fitness of the mutations. For well-adapted species, most mutations are either neutral or deleterious. If mutations are deleterious on average, as shown in Fig. 8.9, the population size will decrease due to degradation in fitness. For a large population, such effect might be infinitesimal. For a small population, however, even under the same mutation rate, the decrease

in population due to deleterious mutations will cause demographic stochasticity to become increasingly important. As a result, degradation in the average fitness of a small population leads to further decline in population. It can be imagined that the accumulation of deleterious genes from mutations will lead to a cascade of successive degradation in average fitness, shrinking the population size, and eventually leading to extinction. This scenario is known as "mutational meltdown" [219].

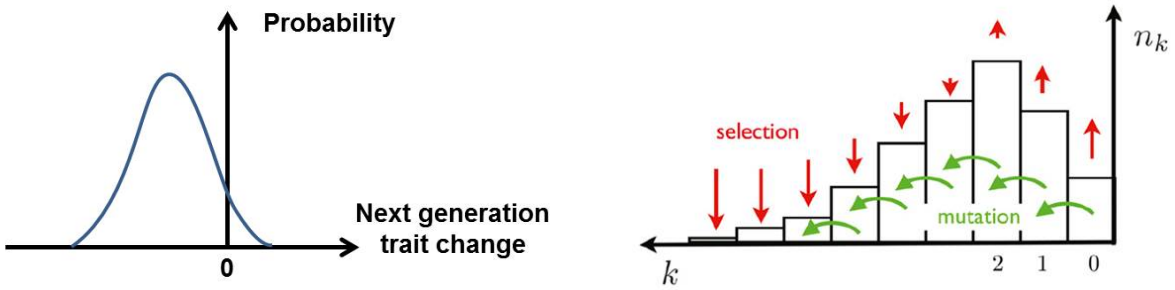

Figure 8.9: **Effect of deleterious mutations.** (Left) Distribution of changes in gene of new generations when mutations are negatively biased. (Right) Illustration of Muller's ratchet (figure is taken from [220]).

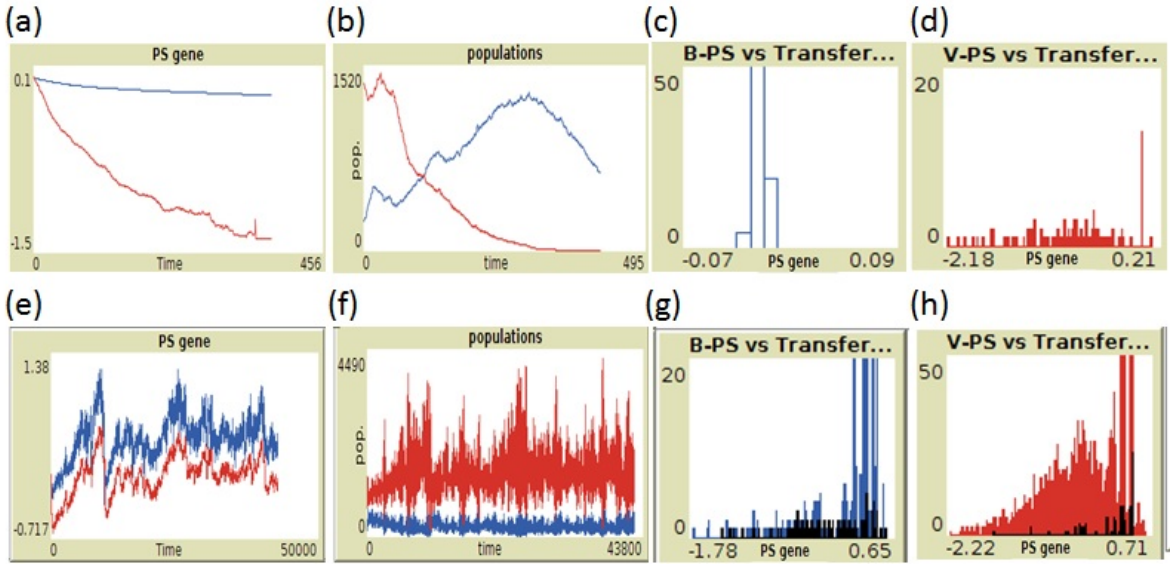

Figure 8.10: **Effect of deleterious mutations in ILM stimulations.** In deleterious mutation, the new gene value has Gaussian fluctuation with negative mean value. The mean values for mutational fluctuations for bacteria and viruses are set to be -0.2 and -1 respectively, indicating that viral mutation tend to deteriorate more. The other parameter values are set to be same as Fig. 8.8. (a)-(d) Without HGT: (a)(b) Deleterious mutations drive phage population to extinction, since new genes generated by phages are biased to negative values as shown in (d). (e)-(h) With HGT, genes transferred from phage to bacteria (black in (g)) and genes transferred from bacteria to phages (black in (h)) are preserved more at high values, and thus both population can avoid collapse from deleterious mutations as shown in (e)(f).

The effect of deleterious mutations is usually regarded to be small for marine microbes since the population size is large globally. However, in a range expansion front,the population size is relatively small, and hence demographic fluctuations are significantly large there, making deleterious mutations more harmful to the evolutionary rate. In particular, since phages have higher mutation rate, these effects are presumably stronger on phages which provide the main drive of generating new genes. Therefore it is natural and appropriate to consider the role of deleterious mutations in the evolutionary dynamics of the *Prochlorococcus*-phage system.

As one might suppose again, the asymmetry in offspring's fitness caused by deleterious mutations would be mitigated by bacteria through HGT. The degradation rate in phage mutations should be proportional to the phage mutation rate and the degree of biased changes in descendants. Bacteria with slower or negligible mutation rate behave like a filter; once detrimental genes are transferred to bacteria, cells with lower fitness will not be competitive and will not survive before they get better genes from the intrinsic genetic drift of bacteria. Thus the overall influence of deleterious mutations mainly depends on the balance between parameters of phage mutation and HGT.

To take deleterious mutations into account, the changes of gene value of new generation are modeled by normally-distributed fluctuations of which the mean value is negative. Fig. 8.10(a)-(d) show an example of simulations without HGT, where the deleterious mutations quickly drive the phage population to extinction. The situation is different when HGT is allowed. In this case, when inferior genes created by phage due to deleterious mutations are transferred to bacteria, they will suffer purifying selection, and only beneficial genes will be retained in bacteria, to be later transferred back to phage. In this case with HGT, the slow evolution of the bacteria saves the virosphere from deteriorating. The result is that bacteria and phage can coexist, as shown in Fig. 8.10(e)-(h).

Evidence has showed that spatially-extended evolutionary trajectories for *Prochlorococcus*, where the high-light adapted ecotype had evolved from the low-light adapted ecotype. During the evolving process, the low-light adapted ecotype had to gradually adapt to a gradient of environmental changes in order to spread its population, forming a traveling front towards lower depth in ocean.

8.5 Why is this a collective state?

We emphasize that, from the above demonstration of models, the emergence of the collective state is essential to coexistence in bacteria-phage ecosystems. This can be better perceived by presenting how many of the transferred genes from HGT (black in Fig. 8.10 (g) and (h)) are present in the population. We may consider

the fraction of viruses with beneficial photosynthesis gene (V_G/V) as the order parameter. This is a function of HGT rate normalized by the phage mutation rate μ_V. As shown in Fig. 8.11, there are in general three regimes in the phase diagram:

1. When the HGT rate is not high enough, beneficial genes cannot be supplied to bacteria and phages in time before they degrade further down.

2. At intermediate HGT rate, beneficial effects by new genes from HGT are able to beat the detrimental effect from deleterious mutations; the flux of beneficial gene and flux of harmful genes strike a balance and form a collective steady state that sustains the ecosystem. In nature there exist limitations in the physical properties such as fitness (bacterial growth rate and phage burst size) which cannot be infinitely large. Once individuals reach the optimal phenotypes, better genes cannot contribute more beneficial effect, and thus the overall effect from deleterious mutations and HGT becomes more neutral as the HGT rate keeps increasing.

3. However, if the HGT rate is too high, all phage and bacterial individuals quickly obtain beneficial genes. Once individuals reach the optimal phenotypes, better genes cannot contribute more beneficial effects, but deleterious genes generated by phages are still frequently swapped to bacteria and start to degrade the average fitness. The consequence is that at some point the accumulating deleterious genes can overwhelm the gene pool of the population and cause collapse of the collective coexistence state.

The coexistence state, despite deleterious mutations, manifests the essence of collective behavior in bacteria-phage ecosystems. In order for coexistence to be robust, HGT in *both* directions is required. In Fig. 8.12, horizontal transferred genes (in black) are the main contribution to the best photosynthesis genes.

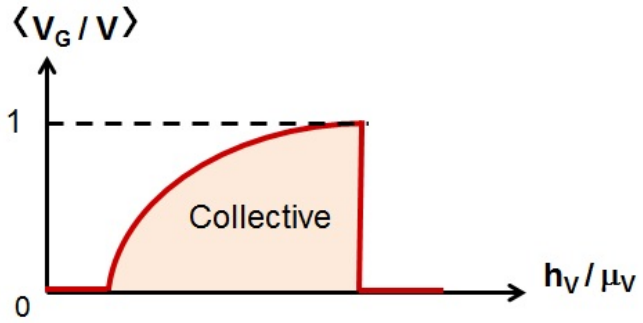

Figure 8.11: **Sketch of phase diagram showing collectiveness:** An illustration of Model 4 with HGT and deleterious mutations.

HGT in both directions is required to maintain the collective state. When both h_V and h_B are comparable and non-zero, the collective state is stable, and the burst-size grows with time. When either one direction of HGT is forbidden, i.e. $h_B = 0$ or $h_V = 0$, the deleterious effect returns. The result is that phage population is driven to extinction again, leading to collapse of coexistence (Fig. 8.12).

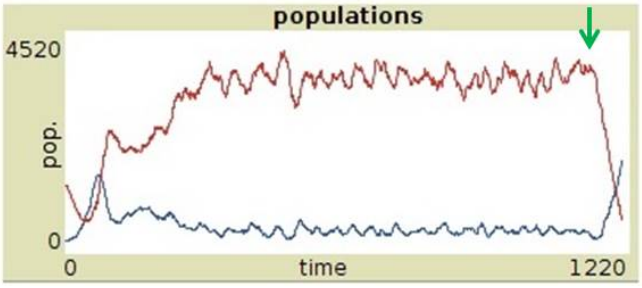

Figure 8.12: **Collective behavior stabilizes the coexistence state.** When one of HGT directions is turned off (green arrow), deleterious mutations can be fatal to phage again and cause phage population (red) to extinction.

8.6 Emergence of niche stratification

After examining the essential physical properties of a minimal well-mixed model for a collectively stabilized coexisting state of bacteria and virues, we now turn to considering the effects of spatial variations. One remarkable aspect of *Prochlorococcus spp.* is niche stratification of ecotypes. To test our model, we extend the simulations to a spatially-extended version but keep all features in the above sections unchanged. The simulations were performed in a two-dimensional system where horizontal and vertical axis represent transversely-spanned sea layers and sea depth l, and bacteria and phage individuals can diffuse randomly. A monotonically decreasing photon density as a function of depth is assigned to mimic the gradient of light intensity under the sea. Since cells near sea level ($l = 0$) are exposed more to high light intensity, we assume that the bacterial death rate is proportional to the light intensity. A threshold in photosynthesis gene value g_c is designated; bacteria with $g_i < g_c$ belongs to the low-light adapted ecotype and otherwise the high-light adapted one. The simulations start with bacteria and phage individuals distributed at the sea floor with assigned photosynthesis gene value $g_0 < g_c$ and raw death rate $d_B(l_0)$ both of which can change when mutation occurs. The parameters were particularly chosen to sustain a marginal coexistence of bacteria and phages.

A qualitative description of simulation results is as follows. If there is no HGT, even with coevolution,

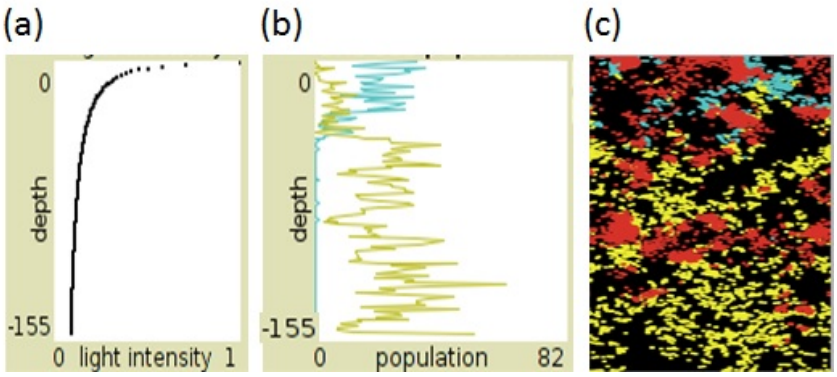

Figure 8.13: **Spatially-extended simulations displays niche stratification.** Light intensity is set to mimic the real distribution in Fig. 7.2. Initially only low-light (LL) adapted bacteria (yellow) and viruses (red) habitat at the bottom of the system. (a) Individuals diffuse freely, but death rate is set to be linearly decreasing with height to mimic the cost due to excess of sunlight. Therefore LL bacteria are forbidden to migrate to the top unless they obtain an improved gene. When HGT is allowed, LL bacteria acquired new gene values from viruses that mutate rapidly, evolving into high-light (HL) adapted bacteria (blue) that can survive near the water surface as shown in (b) that indicates niche stratification. Example of visualization of simulation is shown in (c).

it takes a relatively long time for bacteria to diffuse and move to a higher place and evolve the high-light adapted ecotype with higher photosynthesis gene values. Sometimes the population may go to extinction due to the large demographic noise as phage mutation rate is set to be higher than bacteria. On the other hand, if HGT is allowed, bacteria migrate with phage and adapt to a higher sea level in a relatively rapid time scale. Clusters of bacteria individuals form traveling fronts towards sea level and eventually evolve to the high-light adapted ecotype (Fig. 8.13).

8.7 Discussion

The scheme developed in this chapter should be applicable to a variety of bacteria-phage ecosystems, and not just the *Prochlorococcus* system. We expect that the scheme would explicitly be relevant wherever there is strong selection pressure coupled to spatial gradients. In general, it implies that host genes preserved in phages may be a signature of the selection pressure exerted by the environment for microbes to tolerant to nutrient insufficiency, salt or high temperature [216]. In fact, the genes encoding enzymes that are especially important for microbe sulfur metabolism in deep oceans were found in the deep-sea phage genomes along with their diversity and abundance; it is tempting to speculate that this may be a result of HGT of these chemothythesis genes [221]. Recently a phage of one of the smallest and the most abundant marine bacteria, the $SAR116$ clade, was found to carry genes that may augment its host's metabolism under severe conditions

[222].

A similar situation may arise in eukaryotes: certain type of cyanobacteria, which are usually regarded as parasites of algae, form a biofilm on rocks to supply nutrient or water for the algae layer. This prevents an excess of sunlight and evaporation for the underlying cyanobacteria, implying that they help each to adapt to extreme environments [223, 224]. Accordingly, genes that encode proteins for metabolism in extreme environments were found to be horizontally transferred from bacteria and archaea to algae, presumably helping algae to adapt and evolve [225]. Thus the microbe-algae ecosystem is potentially another example of a collective, mutualistic coevolution.

8.8 Conclusion

In this chapter we developed a minimal model to include horizontal gene transfer as a collective mechanism for stability in *Prochlorococcus*-phage ecosystem. Collective mutualism can emerge even though it is mediated through antagonistic predator-prey interaction between bacteria and phages. From simulation of a series of models, we have shown that bacteria, which have a slow mutation rate compared to that of phage, can benefit from the phage's high mutation rate through horizontal gene transfer, despite the cost of predation.

Horizontal gene transfer works as a collective mechanism for stability. On the other hand, phage with fast mutation rate compared to bacteria will deteriorate by detrimental mutations, but they can benefit from the low mutation rate from bacteria, and in the case of cyanophage of *Prochlorococcus*, acquire evolved photosynthesis genes that prevent degradation of phage fitness and maintain the host's photosynthesis metabolism.

Through spatial-extended simulations, we also show that horizontal gene transfer can accelerate the evolutionary rate to develop different ecotypes of *Prochlorococcus*, leading to increased diversity in both bacteria and phage, range expansion and niche stratification.

Horizontal gene transfer is a driving force to push species away from the current state or static fixed points, along with other mechanisms such as coevolution, mutations and external energy flow. It also plays the role of a collective mechanism for stabilizing ecosystems by providing compensation or benefits from others. However, horizontal gene transfer is not necessarily the only mechanism for stabilizing ecosystems. Nevertheless, horizontal gene transfer in the evolutionary trajectory of marine microbes is an excellent example to show the interplay between ecology and evolution through multiscale interactions in time and space, from the genome to the macroscopic ecosystem.

Part II

Transition to Turbulence in Fluids

Chapter 9

Introduction to Transitional Turbulence

9.1 Introduction to turbulence

Phenomenologically, fluids can be described by two distinct states: steady, streamlined laminar flow and fluctuating, whirling turbulent flow. The onset of turbulence can be triggered by disturbances, and faster flows or less viscous fluids are easier to turn into turbulent states. In general, the steadiness of flows can be characterized by the Reynolds number, Re, a macroscopic dimensionless ratio of the inertia and dissipation. Specifically, the Reynolds number is defined as

$$\mathrm{Re} = UL/\nu, \tag{9.1}$$

where U is the characteristic velocity scale of the fluid, L is the characteristic length scale and ν is the kinematic viscosity of the fluid (defined as the (shear viscosity)/(density)). Re goes up when U and L increases and goes down when ν decreases. Flows are laminar for small Re and become turbulent at large Re.

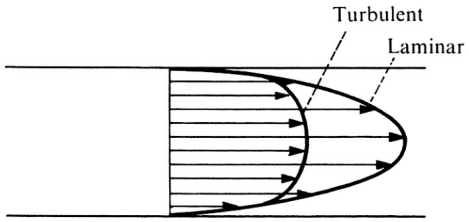

Figure 9.1: **Mean velocity profile of laminar flow and turbulence in pipe flow**. The side view of the velocity field shows the flat profile for turbulence due to the drag it creates, while laminar flow has a parabolic shape. Figure is taken from [226].

Laminar and turbulent states are quantitatively different. One difference is their velocity profile as a function of the distance from the wall. In a pipe, at low Re the Navier-Stokes equation can be solved exactly and the solution is $\mathbf{v} = (v_x(y), 0, 0)$, where x is the streamwise direction, y and z are orthogonal to x and

are sometimes called spanwise, and the function

$$v_x(y) = (R^2 - y^2)\Delta p/4\mu L, \tag{9.2}$$

where pipe radius is R, Δp is pressure difference across pipe length L and μ is the shear viscosity. The velocity profile thus has a parabolic shape for laminar flow. On the other hand, for high Re where the flow is turbulent, the velocity is strongly fluctuating, and the mean velocity profile $\overline{v}_x(y)$ has the form sketched in Fig. 9.1. The irregular fluctuations create a large drag force that resists fluid motion, leading to a wide spread of velocity profile. For a laminar flow the drag force is proportional to velocity, while the drag for a turbulent flow is proportional to the square of the velocity.

9.1.1 Energy spectrum

Another distinction lies in their statistical properties. The statistical properties of turbulence are manifested in the production of coherent structures during energy dissipation. These are emergent, self-organized regions of high vorticity, that are heuristically described as "eddies". The phenomenology was proposed conceptually by Richardson [227], who described turbulence as a self-similar cascade process: Unstable eddies break into smaller and smaller sizes gradually through a Hamiltonian process, until the size reaches the scale of molecular viscosity where energy finally dissipates.

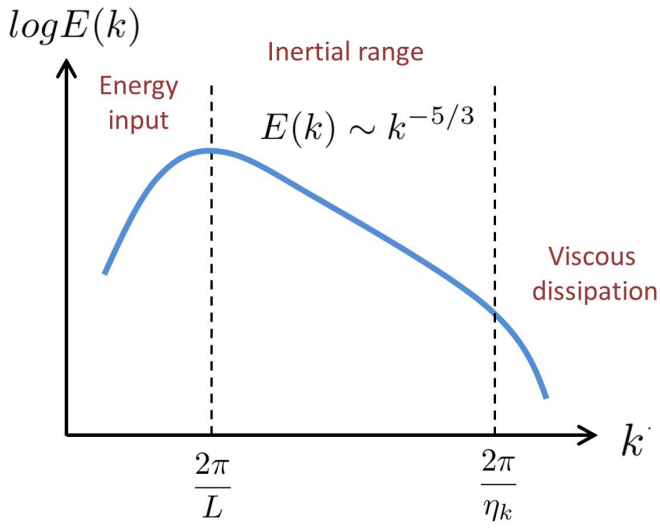

Figure 9.2: **Sketch of energy spectrum of turbulence**. L is the length scale of the driving force, and η_k is the Kolmogorov scale that represents the scale where viscous dissipation dominates. Between the two scale is the inertial range, where energy spectrum scales with a power-law form, as first predicted by Kolmogorov [228].

Richardson's cascade picture was quantified, and the energy spectrum predicted by Kolmogorov [228], as illustrated in Fig. 9.2. The argument is as follows. For an eddy of size r and a characteristic velocity u_r, the energy input rate, ϵ, can be represented as

$$\epsilon \sim \frac{u_r^2}{t_r} \sim \frac{u_r^3}{r}, \tag{9.3}$$

where $t_r \sim r/u_r$ is the time for the eddy to transfer energy to another one with a smaller size without viscous dissipation. The Reynolds number becomes

$$\mathrm{Re}(r) = \frac{u_r r}{\nu} = \frac{(\epsilon r)^{1/3}}{\nu} = \frac{\epsilon^{1/3} r^{4/3}}{\nu}. \tag{9.4}$$

The Kolmogorov scale, η_k, defined as the length scale below which dissipation dominates, is when Re is sufficiently small, e.g. $\mathrm{Re}(r) = 1$, leading to

$$\eta_k = \left(\frac{\nu^3}{\epsilon}\right)^{1/4}. \tag{9.5}$$

Therefore Re can be rewritten as

$$\mathrm{Re}(r) = \left(\frac{r}{\eta_k}\right)^{4/3}. \tag{9.6}$$

In the energy spectrum, the range for self-similar cascade is determined by the macroscopic length scale of the driving force L and the microscopic Kolmogorov scale η_k. From Eq. (9.6), the range in log scale is

$$\frac{L}{\eta_k} = \mathrm{Re}^{3/4}, \tag{9.7}$$

and for $2\pi/L < k < 2\pi/\eta_k$, k is said to be in the *inertial range*. Within the inertial range, the energy spectrum, $E(k)$, was derived by Kolmogorov through dimensional analysis, and the assumption that there is complete similarity in the limit of small viscosity or $\mathrm{Re} \to \infty$ [229, 23]. Specifically, $E(k)$ is defined as the turbulent kinetic energy per unit mass and per wavenumber range, and so is dimensionally of the same form as $[u_r]^2[r]$. From Eq. (9.3) and Eq. (9.5), the dimension of $E(k)$ can be represented in the Kolmogorov scale η_k as

$$[E(k)] = [(\epsilon r)^{2/3} r] = [\epsilon^{2/3} \eta_k^{5/3}] = \left[\nu^2/\eta_k^2\right]. \tag{9.8}$$

Therefore the scaling form becomes

$$E(k) = \frac{\nu^2}{\eta_k} F(k\eta_k) = \epsilon^{2/3} \eta_k^{5/3} F(k\eta_k), \tag{9.9}$$

where $F(k\eta_k)$ is a scaling function that we assume is universal in the inertial range. Eq. (9.9) implies that the turbulent energy has a universal spectrum that only depends on the energy dissipation rate ϵ and the kinematic viscosity ν. This result is known as Kolmogorov's first similarity hypothesis [228].

In the limit $\mathrm{Re} \to \infty$, i.e. $\nu \to 0$ or $\eta_k \to 0$, the energy spectrum $E(k)$, which is expected to be non-zero and finite, is required to be independent of η_k, if we assume complete similarity [229, 23]. Therefore, in this limit, $F(x)$ should have a functional form that can cancel out the dependence of η_k in Eq. (9.9). That is,

$$\lim_{x \to 0} F(x) = x^{-5/3}, \tag{9.10}$$

so that

$$\lim_{\mathrm{Re} \to \infty} E(k) = \epsilon^{2/3} \eta_k^{5/3} \left(k\eta_k\right)^{-5/3} = \epsilon^{2/3} k^{-5/3}. \tag{9.11}$$

This result is known as Kolmogorov's second similarity hypothesis [228]. It makes stronger assumptions than the first similarity hypothesis. The scaling form in Eq. (9.11), known as the Kolmogorov spectrum [228], is regarded as a signature of the cascade in turbulence, and it has been observed in various turbulent systems [230].

It is important to note that, based on Eq. (9.7), the number of degrees of freedom in a three dimensional turbulent box is $(L/\eta_k)^3 = \mathrm{Re}^{9/4}$, which becomes extremely large when $\mathrm{Re} \gg 1$ in the turbulent state. Therefore, the problem of turbulence is a high degree of freedom phenomenon, and this is why it is so hard to simulate it, even on modern supercomputers.

9.1.2 Navier-Stokes equations

The Navier-Stokes equations generally describe the continuous dynamics of an incompressible fluid derived from Newton's law of motion [231]. Specifically, the equations for fluid velocity $\boldsymbol{u}(\boldsymbol{x}, t)$are

$$\frac{\partial \boldsymbol{u}}{\partial t} + (\boldsymbol{u} \cdot \nabla)\boldsymbol{u} = -\frac{1}{\rho} \nabla P + \nu \nabla^2 \boldsymbol{u} + \frac{1}{\rho} \boldsymbol{f}, \tag{9.12}$$

with the incompressibility condition for velocity

$$\nabla \cdot \boldsymbol{u} = 0, \tag{9.13}$$

where ρ is the fluid density, P is the pressure acting on the fluid, ν is the kinetic viscosity and $\boldsymbol{f}$ is the external driving force that can be stochastic. The Navier-Stokes equations have been found to be valid in all fluid systems, from laminar to turbulent flows [231, 232]. Due to the wide applicability, a simulation by numerically solving the Navier-Stokes equations, called direct numerical simulations (DNS), is regarded as a "first principle" approach in fluid dynamics. Other simulation methods are used in engineering to try and get round the fundamental limitation imposed by the $\mathrm{Re}^{9/4}$ scaling of the size of the computational problem. These approaches are unsystematic reductions in the number of degrees of freedom and are not used in this thesis.

Below we briefly introduce some of the common geometries used to explore turbulence in experiments.

9.1.3 Pipe flow and channel flow

Pipe flow is one of the most common systems used to study turbulence and is central to this part of this thesis. It is especially important because turbulence creates much more frictional drag than laminar flow, making transport of oil and other fluids through pipelines expensive and energy intensive [233]. Turbulence in blood vessels are also known to cause aneurysms, near the laminar-turbulent transition [234]. As we will see later, in this regime, alternating regions of laminar and turbulent flow coexist, causing great stress on the blood vessel walls.

A horizontal pipe flow is driven by pressure drop at the ends of the pipe, and the Reynolds number is defined as $\mathrm{Re} = UD/\nu$, where D is the pipe diameter. The laminar flow in pipe geometry is called Hagen-Poiseuille flow or Poiseuille flow. In a pipe, Hagen-Poiseuille flow has a parabolic shape of velocity field, as we saw in Eq. (9.2), while turbulent flow has flat velocity profile (Fig. 9.1). As we will see, even when Re increases, a certain strength of disturbance is required to create turbulence in pipe flow, and the fluid undergoes a series of complicated stages during transition [31, 2, 4], as we will discuss in detail later in this chapter.

The plane version of pipe flow where the fluid in confined within a rectangular container with open ends is called channel flow or plane Poiseuille flow. Channel flow also undergoes a similar transition as pipe flow with different pattern structures due to the symmetry of the system [43, 44, 235]; we will describe it further in Chapter 10.

9.1.4 Taylor-Couette flow

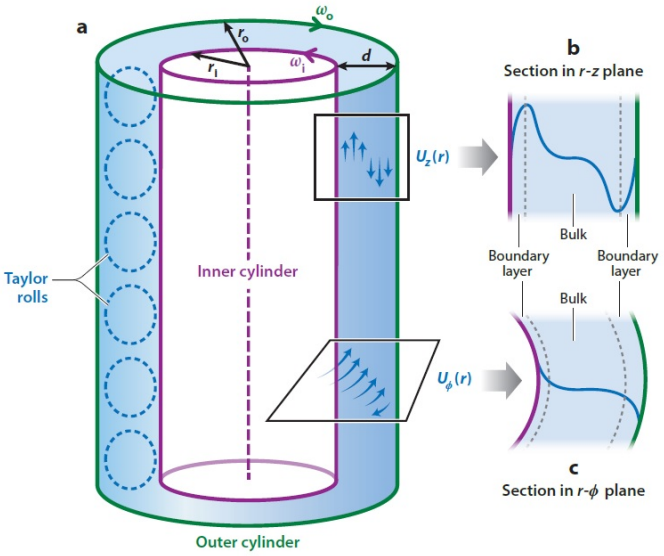

Figure 9.3: **Sketch of Taylor-Couette flow**. (a) Fluid is confined between the inner and outer cylinders that rotate oppositely. When the inner cylinder rotates, various patterns such as Taylor rolls/vortices emerge. (b) Cross section view of the shear on fluid due to cylinder rotation. Figures are taken from [236].

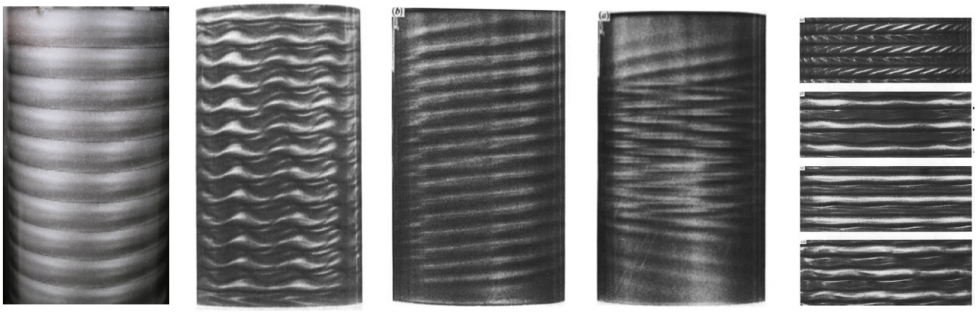

Figure 9.4: **Spiral turbulence in Taylor-Couette flow**. When both inner and outer cylinders rotate, fluid develops rich turbulent patterns. Figures are taken from [237], which were adapted from [238].

Couette flow is the name for a flow that is sheared by two moving walls. When the boundary walls are parallel planes, it is referred to as plane Couette flow, and the transition from the laminar to turbulent state occurs when the wall speed increases [239, 240, 241, 242, 243, 244]. Another commonly studied case is the flow confined between two concentric rotating cylinders, called Taylor-Couette flow, as shown in Fig. 9.3. Taylor-Couette flow has a rich set of instabilities and ordered states. In Taylor-Couette flow, the characteristic velocity and length scale are determined by the angular velocity, the radius of the cylinders and

the aspect ratio. When the inner cylinder rotates, with the outer cylinder static or rotating, as the rotating speed increases, laminar flow undergoes linear instabilities into a sequence of structures such as Taylor vortices and spiral turbulence (Fig. 9.4) [245, 246, 238, 237, 236, 247]. In contrast, when the inner cylinder is static or rotates slowly, the flow is linearly stable at low outer cylinder speed; at large outer cylinder speed, with a sufficiently large external disturbance, the flow transitions to turbulence with fluctuating patterns [45, 237, 236, 247]. Recent advances in studies of transitional turbulence in Taylor-Couette flow will be discussed in Chapter 10.

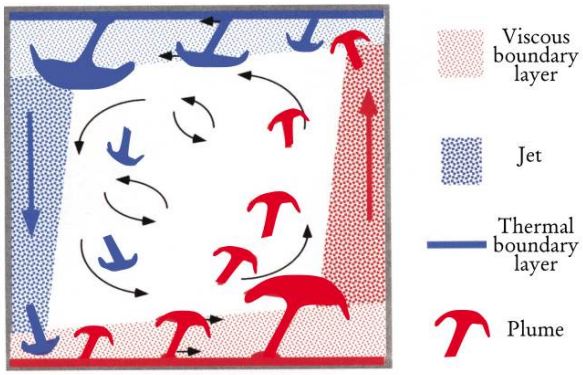

Figure 9.5: **Sketch of Rayleigh-Bénard convection**. Mushroom-shaped thermal plumes emerge from the cold top and hot bottom boundaries. When turbulence arises, plumes spread rapidly, and a large-scale circulation spontaneously emerges. Figure is taken from [248].

9.1.5 Rayleigh-Bénard convection

Rayleigh-Bénard convection is a fluid in a box heated from below, in a gravitation field. The flow is driven by the buoyancy force due to the temperature difference; thermal plumes are generated from the top and bottom boundaries and drift vertically and dissipate, as shown in Fig. 9.5. Turbulence can occur as the temperature gradient increases, and a large-scale circulation can arise in the fluid [249, 248, 250, 251, 252, 253], due to many-body interaction between the plumes. When the aspect ratio is large, so that the horizontal extent is much larger than the height, a zonal flow develops that suppresses the plumes, and as we will discuss in Chapter 10, leads to predator-prey oscillations [254, 255].

9.2 History of transitional turbulence in pipe flows

The first systematic study of the laminar-turbulent transition was performed by Reynolds in 1883 in pipe flows. By inserting a jet of dye into the flow, Reynolds discovered that as Re increases to around 2000, a

flow that was initially in the laminar state starts to appear intermittent patches, which he named "flashes".

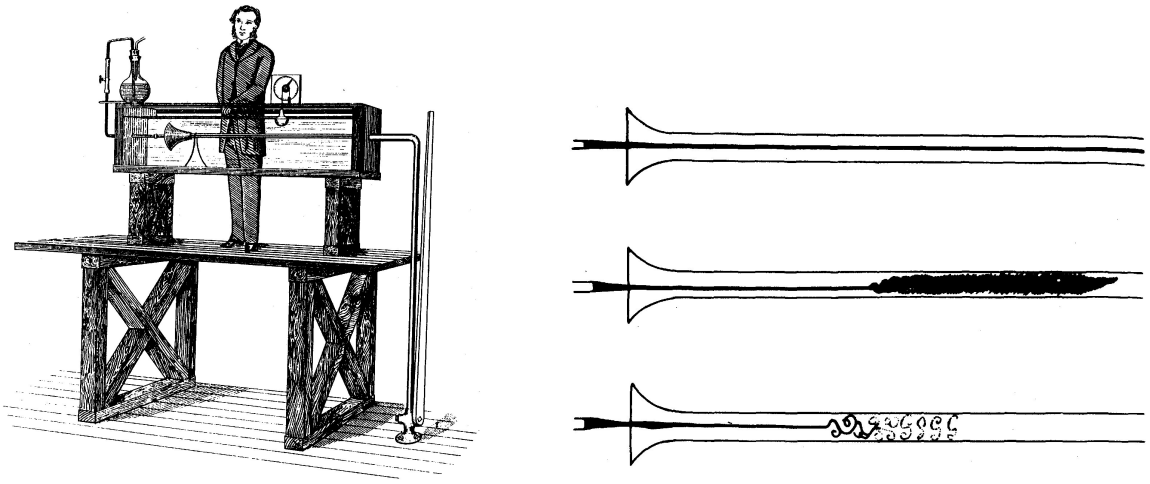

Figure 9.6: Sketches of Reynolds' pipe-flow experiment (left) and his dye observations that show the rise of "flashes" from the laminar state when Re increases from (a) to (c) (right) from [31].

Further experiments on hot wires revealed a more detailed phase diagram [32, 39], confirmed by later experiments in long water pipes [32, 39, 41, 42] and by direct numerical simulations (DNS) on the Navier-Stokes equation [40]. The transitions have the following dependence as Re increases from around 1500 to 2200 or so:

1. Under a disturbance, Reynolds' flashes, known today as metastable "puffs", occur in an intermittent way, first forming from the laminar flow and then decaying after a lifetime τ_d.

2. When Re $\sim$ 2040, the puffs become unstable through a new dynamical process in which the leading edge breaks away and nucleates the formation of a new puff some distance downstream. This is called "puff splitting".

3. As Re increases to around 2300, turbulence is sustained for so long that it is virtually impossible to observe its decay in finite systems. Intermittent and splitting puffs can, at higher Re, develop into so-called "turbulent slugs" which grow when traveling downstream. For Re $>$ 2500, slugs can uniformly expand along laminar flows.

The question of whether there is a unique onset of turbulence is not at all clear, as this transition range is broad. Furthermore, it is not clear how to even define such a sharp onset, givven the complex, spatially heterogeneous nature of transitional phenomena.

Another difficulty that makes it difficult to define a unique transition point is that there are sub-critical and hysteretic phenomena. In order to excite turbulence in the above experiments, a finite amplitude

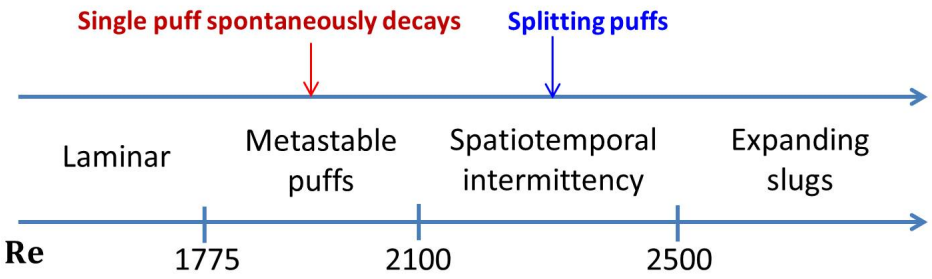

Figure 9.7: **Sketch of phase diagram in pipe flow.**

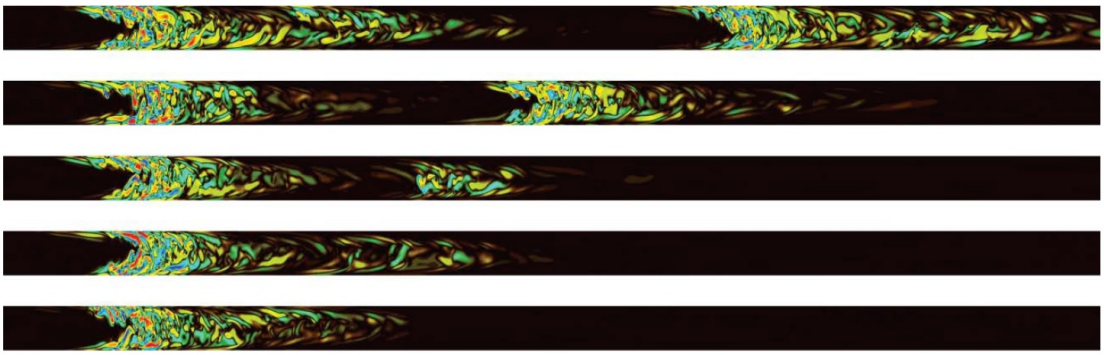

Figure 9.8: **Turbulent puff splittings in pipe flow simulations.** At Re=2250, time increases from bottom to top, and the flow is to the right. Red and blue color represent positive and negative streamwise vorticity the reflects turbulent density. Figure is taken from [41].

perturbation is required to trigger the turbulence [32]. With very careful experiments, it was found that under infinitesimal perturbations, pipe flow can remain laminar at least up to Re $\sim 10^5$ in experiments [256] and up to Re $\sim 10^7$ in numerical simulations [257]. Theoretical studies on transitional turbulence in pipe flow have been devoted to searching theories from various aspects that can explain the problem of linear stability, but today there is still no satisfactory theory.

Experimental research on the spatiotemporal intermittency regime has mostly focused on identifying special unstable, localized or traveling wave flow configurations that can be the basis of a description in the language of deterministic dynamical theory [46, 50, 48, 51, 47, 3, 37, 49]. Although this large body of work has been impressively developed during the past decade, explanatory power for the main statistical features of the laminar-turbulent transition has been lacking. Indeed, it is the statistical features which are most striking, and thus the focus of this thesis research.

Fluctuations and their statistical properties during transition had not been addressed much until the experiments by Bottin *et al.* late 1990s [241, 242]. In their experimental studies of transitional plane Couette flow, they measured the turbulent decay time and observed an exponential decay of its complementary

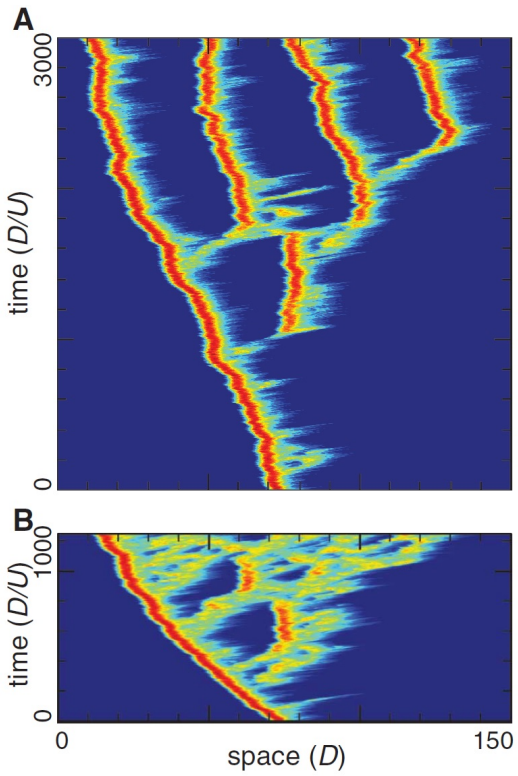

Figure 9.9: **Space-time plot shows turbulent puff splittings in pipe flow simulations.** Red and blue color represent positive and negative streamwise vorticity the reflects turbulent density. (a) At Re=2300, a puff splits around t=1000, followed by multiple splitting events later. (b) At Re=4500, the initial puff becomes unstable more rapidly. Splitting is not clear, and the puff soon expands into a growing cluster. Figures are taken from [41].

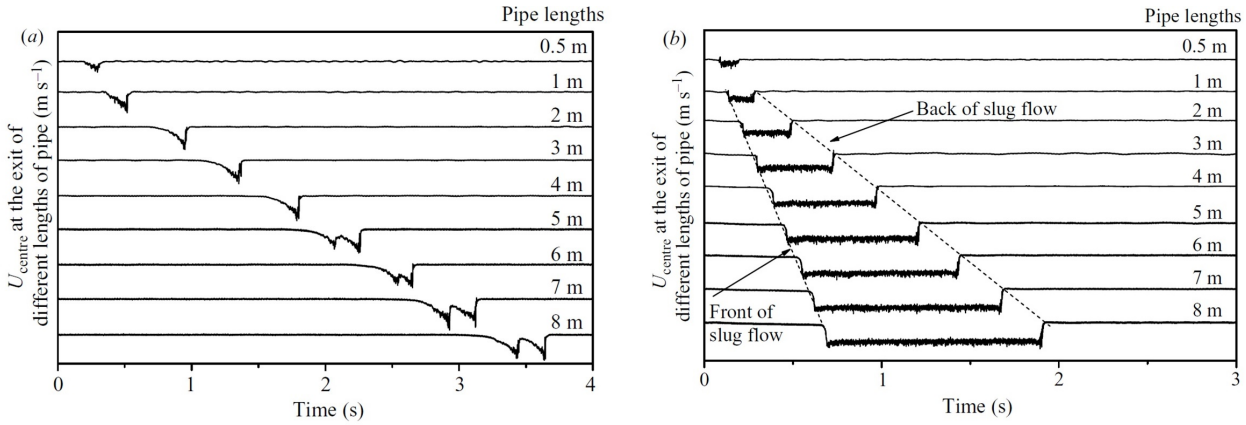

Figure 9.10: **Experiments in hot-wire anemometers**. Measurements of the centerline velocity as a function of time for pipes of varying length. These data show (a) a puff splitting at Re = 2495 and (b) an expanding slug at Re = 8230 [42].

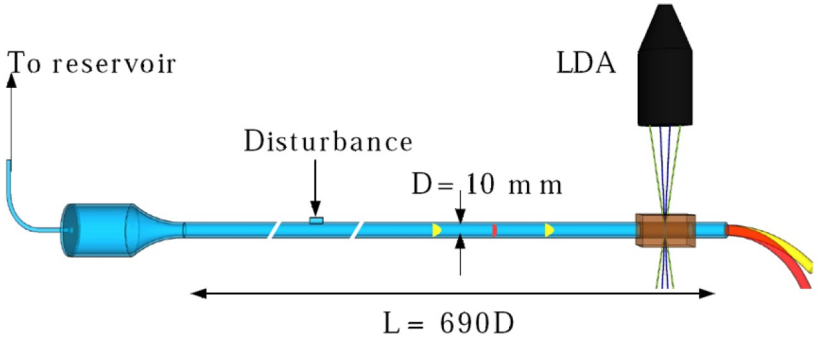

Figure 9.11: **Experiments in thin pipes of water flow**. (a) Sketch of experimental setup. The flow is driven by gravity, and initially a puff is created by the disturbance. The outflow will bend more if the puff remains to the end (red), due to turbulent drag, or will be smoother if the puff has decayed by the time it would have reached the outflow (yellow). The outflow angle is measured at the end. Image is taken from [258].

cumulative distribution. Since the inverse of the slope of an exponential distribution can be interpreted as the decay rate, they proposed that measuring the slope of the distribution can be a better estimation of mean lifetime [241].

The tasks of obtaining the statistics of turbulent puff lifetimes, and further determining the critical Re, are very challenging in pipe flow, because the puff lifetime rapidly grows near the transition region, and so it becomes more and more unlikely to observe the puff making the transition back to laminar flow in a pipe with finite length.

For this reason, pipes whose length is much larger than their diameter are required. In order to perform experiments in extremely thin pipes to measure puff lifetimes that are long in dimensionless units of D/U, Hof *et al.* developed a method to determine the fluid state inside thin pipes [35]. The scheme is as follows and illustrated in Fig. 9.11: The flow of water in a pipe is driven by gravity, and a turbulent puff is created by a disturbance. If the puff does not decay when the fluid reaches the end of the pipe, the outflow will be slower and so bend downward due to turbulent drag (red trajectory in Fig. 9.11). If the puff becomes laminarized, the angle of the outflow trajectory will be smaller (yellow trajectory in Fig. 9.12). By observing the angle, i.e. whether the puff lives or decays, and knowing the speed of advection U, the probability of decay in the time LD/U, where L is the distance between the disturbance injection point and the outflow, can be measured. To do this requires multiple repetitions and a highly stable apparatus. In particular, the viscosity of water is temperature dependent, and this then affects the Reynolds number, potentially. Thus temperature control was one of the many novel aspects of the *tour de force* experiment by Hof's group.

Following Bottin *et al.*'s idea, the complementary cumulative distribution of puff lifetime, or the survival probability of turbulent puffs, was fitted by

$$P(t) = e^{-(t-t_0)/\tau_d}, \tag{9.14}$$

where τ_d is defined as the mean lifetime and a timescale $t_0 \ll \tau_d$ is interpreted as a delay time for the initial formation of a turbulent state [35]. Due to such an exponential-like tail in the survival probability, decay of turbulent states is interpreted as memoryless processes [258].

Hof *et al.*'s results turned out to be surprising and disagreed with previous studies by Bottin *et al.* and others. Hof *et al.* found that the mean lifetime τ_d from both experiments and DNS in pipe flow has an exponential dependence on Re over three decades of lifetime with the form

$$\ln \tau \propto \mathrm{Re}. \tag{9.15}$$

This result is surprising because of two reasons. First, as mentioned previously, the field of transitional turbulence had been influenced by dynamical system theory and had been regarded as instability of chaotic dynamics in low dimensions which predicts that the time to be attracted by the fixed point should diverge as a power law near a critical value of the control parameter. For example, it could be $\tau_d \sim (\epsilon - \epsilon_c)^{-\sigma}$, where σ is a positive exponent, ϵ is the control parameter and ϵ_c is a critical value, above which a state with different order in dynamics arises. This expectation had been supported by an earlier experiment in pipe flow measured at Re between 1580 and 1740, and Re_c was estimated to be 1750 ± 10 [259]. Second, as there is no critical Re in Eq. (9.15), Hof *et al.* made the interpretation that turbulence in pipe flow is just a transient state whose decay time is always finite for any finite Re. In other words, turbulence is a long-lived metastable state and not a true phase transition. This conclusion is not only contradictory to the known phase diagram, but also disagrees with the fact that the functional form of the scaling of the friction factor measured in pipe flow experiments [260] has the behavior expected using Komogorov's theory for the spectrum of fully-developed turbulence [261, 262], for Re above several thousand. This interpretation of this result, obtained using non-equilibrium critical scaling ideas from statistical mechanics is that turbulence is a phenomenon distinct from laminar flow.

Further experiments by Hof *et al.* managed to measure the lifetime up to a range of of 8 decades in time, and found that τ_d actually scales super-exponentially with a specific "double exponential" form [258, 41, 263],

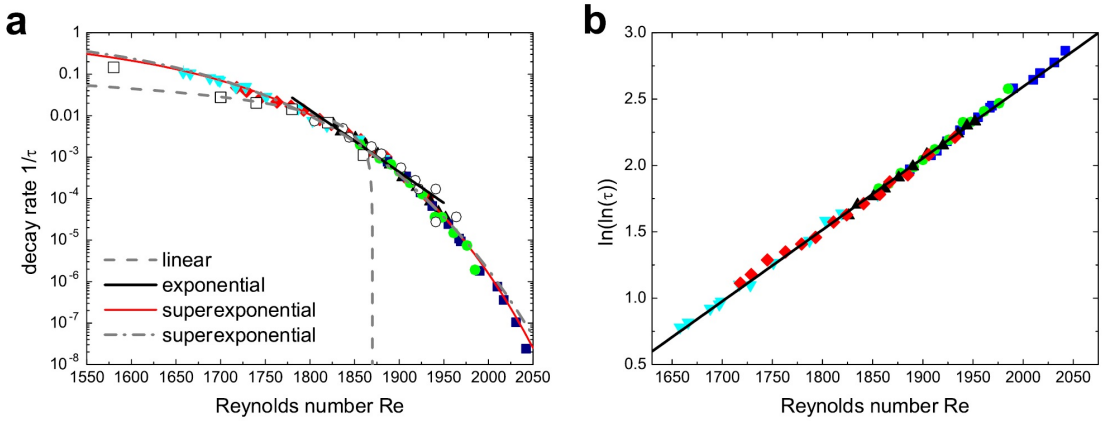

Figure 9.12: **Superexponential scaling of mean lifetime in pipe flow**. (a) The decay rate $1/\tau_d$ of the survival probability in Eq. (9.14) plotted in semi-log scale decreases faster than exponential, indicating that the mean lifetime τ increases faster than exponential with increasing Re. (b) Plot of double-log of τ_d shows that the mean lifetime scales super-exponentially with $\ln\ln\tau \propto \mathrm{Re}$. Figures are taken from [258].

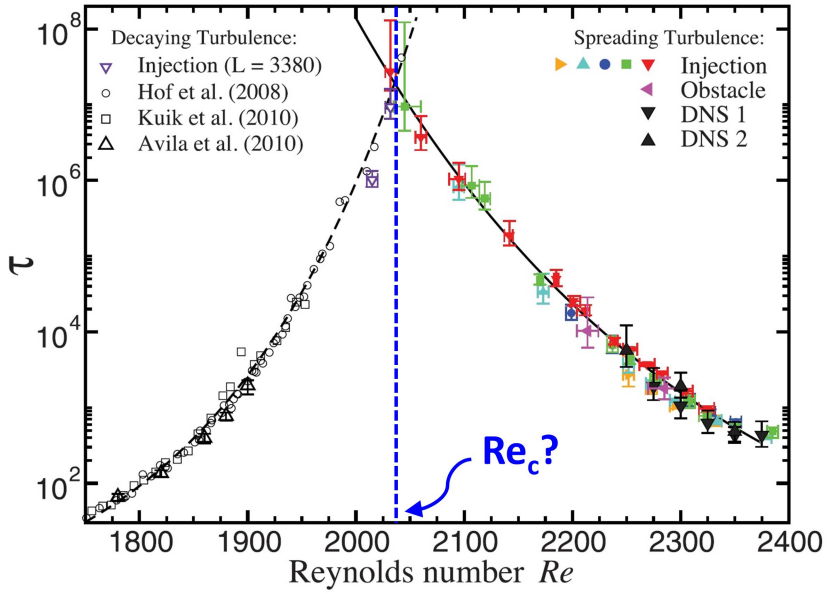

Figure 9.13: **Superexponential scaling of mean lifetime and mean splitting time in pipe flow**. Both time scales grows/decays faster than an exponential form. Figure is taken from [41]. The putative critical Re is given by the intersection of the two super-exponential curves. The solid lines are fits to functions of the form $\tau/\tau_0 = \exp(\exp(A + B\mathrm{Re}))$.

i.e.

$$\ln\ln\tau \propto \mathrm{Re}. \tag{9.16}$$

as shown in Fig. 9.12. In later work, Avila *et al.* calculated the probability of non-splitting, $1 - P(t)$, by identifying the time before a single puff splits in both pipe flow experiments and DNS [41]. The inverse of the decay slope in $1 - P(t)$ is defined as the mean splitting time, and this too was found to follow the super-exponential scaling. By plotting together the measured mean lifetime and mean splitting time, Avila *et al.* suggested that the critical Re can be regarded as the intersection of the two scaling curves (Fig. 9.13). The reasoning is that above this point, there will always be some turbulence in the pipe at long times, if the pipe is long enough; below this point the long time state of the pipe would be laminar, since all puffs generated by noise would have died away, in the limit of vanishing noise. The goal of the program of research which includes the work completed in this thesis is to understand and if possible, derive from first principles, the strange and contradicting phenomena uncovered by the Hof experiments. As we will see, we can make some definite progress towards this goal, but of course open questions remain.

9.3 Models for transitions to turbulence

9.3.1 Supercritical and subcritical bifurcation from Landau equation

The theoretical description of the transition to turbulence has presented a challenge for many decades. The difficulty in studying the transition in pipe flow from the Navier-Stokes equations is that the laminar state is linearly stable.

As it is very hard to develop a theory for nonlinear perturbations, Landau proposed a heuristic argument to investigate the onset of instability by considering nonlinear terms in the linear perturbation [264, 265]

$$\mathbf{v}_1 = \mathbf{v} - \mathbf{v}_{\text{laminar}}, \tag{9.17}$$

where $\mathbf{v}_{\text{laminar}}$ is the laminar velocity. The argument starts with the stability of one mode for $\mathbf{v}_1$ and considers only the time dynamics of the mode. The dynamics is assumed to be separable into two timescales. One is long and associated with the envelope of the mode. The other is short and associated with a finite wavenumber instability that is postulated as the transition. Neglecting the spatial structure for simplicity, we can write that the change in amplitude is of the form

$$\mathbf{v}_1 = A(t)e^{-\Omega t} = A(t)e^{i\gamma t - \omega t}. \tag{9.18}$$

During the onset of an unstable mode, the linear growth rate $\gamma \sim (\text{Re} - \text{Re}_c) \ll \omega$, and thus significant dynamics occurs after averaging over a time scale of $2\pi/\gamma$ since oscillations from ω are negligible. Similarly,

from analyticity, only even terms of $|A|^2$ are important. With the next lowest term, the dynamical equation of $|A|^2$ is

$$\overline{\frac{d|A|^2}{dt}} = \gamma|A|^2 - \alpha|A|^4, \tag{9.19}$$

where the "$\overline{\quad}$" indicates time averaging over the fast mode. To avoid a nontrivial solution becoming unstable, the coefficient of the nonlinear term, α, has to be positive. The nontrivial solution then becomes

$$|A| \propto \sqrt{\mathrm{Re} - \mathrm{Re}_c}, \tag{9.20}$$

and $|A|$ undergoes a continuous change from the laminar state ($|A| = 0$) to a non-trivial state ($|A| > 0$) when Re increases as shown in Fig. 9.14. This behavior has been reported in a variety of experimental geometries, including inner cylinder rotating Taylor-Couette flow [237, 236, 247] and Rayleigh-Bénard convection [249, 250, 251]. This type of bifurcation is called supercritical in the language of nonlinear dynamics, and is analogous to a second-order phase transition in a mean-field sense.

To get a different type of transition, higher order nonlinear terms must be considered. The simplest modification is:

$$\overline{\frac{d|A|^2}{dt}} = \gamma A^2 - \alpha|A|^4 - \beta|A|^6, \tag{9.21}$$

where $\alpha < 0$ and $\beta > 0$. The non-trivial solution $|A| > 0$ turns out to be discontinuous from $|A| = 0$ when Re increases as shown in Fig. 9.14. In the range $\mathrm{Re}_c' < \mathrm{Re} < \mathrm{Re}_c$, coexistence of two stable solutions indicates that a finite perturbation can drive the system from the laminar state to the non-trivial one. This case is an example of a subcritical bifurcation, and the coexistence of two stable phases is reminiscent of the notion of a first-order or discontinuous phase transition, and has been reported in pipe flow [2], channel flow [43, 44], outer cylinder rotating Taylor-Couette flow [237, 236, 247] and plane Couette flow [240, 241, 242, 244]. In principle, when Re increases, more and more modes contribute to the dynamics. Neverthess, the picture of subcritical bifurcation is considered to be the underlying explanation for why pipe flow may become turbulent at finite $\mathrm{Re} \ll \mathrm{Re}_c$ and has become central to studies of transitional turbulence in pipe flow.

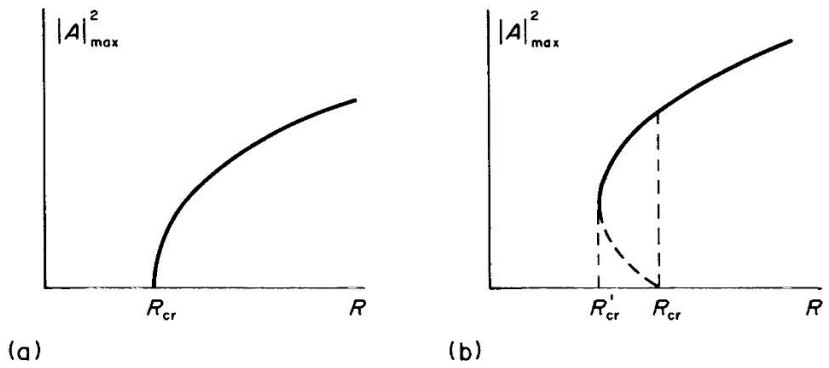

Figure 9.14: **Supercritical and subcritical bifurcation in Landau equation**. (a) In supercitical bifurcation, amplitude increases continuously when control parameter Reincreases, while (b) amplitude jumps discontinuously in subcritical bifurcation. Figures are taken from [265].

9.3.2 Pomeau's directed percolation picture for transitional turbulence in pipe flows

In Pomeau's conceptually important paper of 1986 [54], he used Landau's subcritical bifurcation picture for the laminar-turbulent transitions in pipe flow, but including diffusion of turbulent energy in the amplitude equation. Pomeau described the transition in terms of the propagation of the interface between laminar and turbulent states. He pointed out that turbulent fluctuations at the front may not be ignored and intuitively depicted their effect as a microscopic "contamination" process, where a turbulent region can excite its laminar neighborhood or decay spontaneously if its energy is below the excitation threshold. Relating this intermittent process to directed percolation (as described below), he proposed that critical power-law scaling should be able to be observed in experiments. Pomeau's conjecture has brought into the research field of turbulence an important insight, regarding transitions to turbulence as critical phenomena in statistical mechanics, whereas previous studies mainly focused on deterministic differential equations and low-dimensional dynamical system models.

However, Pomeau's argument may seemingly lead to a contradiction: If the laminar-turbulent transition can be described as a subcritical bifurcation, which is like a first-order phase transition, and has been supported by experiments [2, 43, 44, 240, 241, 242, 244, 237, 236, 247] how could it also belong to the directed percolation universality class, whose transition is second-order?

To answer this subtle point, we need to consider more carefully what is an appropriate order parameter for the laminar-turbulent transition. It is not the amplitude A, as is assumed in the Landau picture. It is worth commenting that discontinuities arise in other examples of continuous transitions, perhaps most famously in the Kosterlitz-Thouless transition of two-dimensional superfluids where the superfluid density

jumps discontinuously at the transition.

9.3.3 Introduction to directed percolation

Directed percolation (DP) is a dynamical model first introduced for the process of fluids spreading through a porous media [266]. DP is a type of discrete contact process on a lattice that describes movement and splitting/merging of nearby particles, biased by gravity and thus directed downwards as time evolves. Therefore the vertical direction plays the role of time direction. In nature, how far a fluid can penetrate a porous medium is determined by its compactness. In DP models, the permeability is conceptually described by the connectivity between neighboring sites with an overall spreading rate. This rate is denoted by the so-called percolation probability p, and the density on each site is either 1 if it is occupied or 0 otherwise. In bond directed percolation, at time t the bonds between nearest sites are turned on with probability p, and for an active site i with occupancy $x_i(t) \equiv 1$, the occupancy of its neighbors at the next time, $x_j(t+1)$, becomes 1 if the bond between i and j is turned on. The order parameter $\rho(t)$ is defined as the density of active sites, and the state of a DP configuration is said to be active if $\rho > 0$ as $t \to \infty$ or inactive if $\rho = 0$. An empty lattice in the inactive phase is also termed an absorbing state, a state that once you enter can never be escaped from. The final state depends on the percolating probability p: When p is below the critical value p_c, configurations always go to the absorbing state within finite time. As p approaches p_c, the cluster of active sites branches out, and the time it takes for the trajectories to terminate becomes longer and longer. Around $p \sim p_c$, the active sites form a spatiotemporal intermittent pattern. By intermittency, what is usually meant is a bursty pattern of fluctuations in either space, time or both. Intermittency can be described using Liapunov exponents, multifractals, or other techniques, but such quantitative refinements are not added in the present discussion. Spatio-temporal intermittency is characterized by correlation lengths in time and spatial directions, and the order parameter ρ exhibiting power-law scaling forms near the transition:

$$\xi_{\parallel} \sim |p - p_c|^{\nu_{\parallel}}, \tag{9.22}$$

$$\xi_{\perp} \sim |p - p_c|^{\nu_{\perp}}, \tag{9.23}$$

$$\rho_{\text{stationary}} \equiv \lim_{t \to \infty} \rho(t) \sim (p - p_c)^{\beta}, \tag{9.24}$$

where $\nu_{\parallel}$, $\nu_{\perp}$ and β are critical exponents that only depend on dimension. Here $\xi_{\parallel}$ is the correlation length in the time-like direction, and $\xi_{\perp}$ is the correlation length in the space-like directions. When $p > p_c$, the cluster size grows, and the trajectories become unlimited. At this stage, eventually a non-zero fraction of the lattice sites become occupied, and the configuration is at an active state with non-zero of $\rho_{\text{stationary}}$.

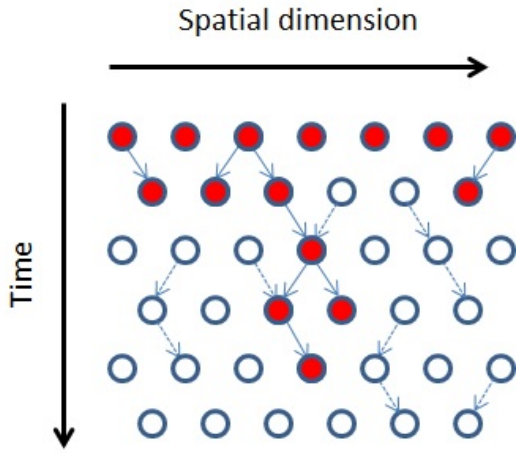

Figure 9.15: **An example of directed percolation configuration in $1+1$ dimension.** All lattice sites are active (red) in the initial configuration. Arrows are permeable bonds that are randomly assigned between sites with percolating probability p. The allowed paths are shown with solid arrows. In this case the sites in the final configuration are all empty, so the system is in an absorbing state, such as with $p < p_c$.

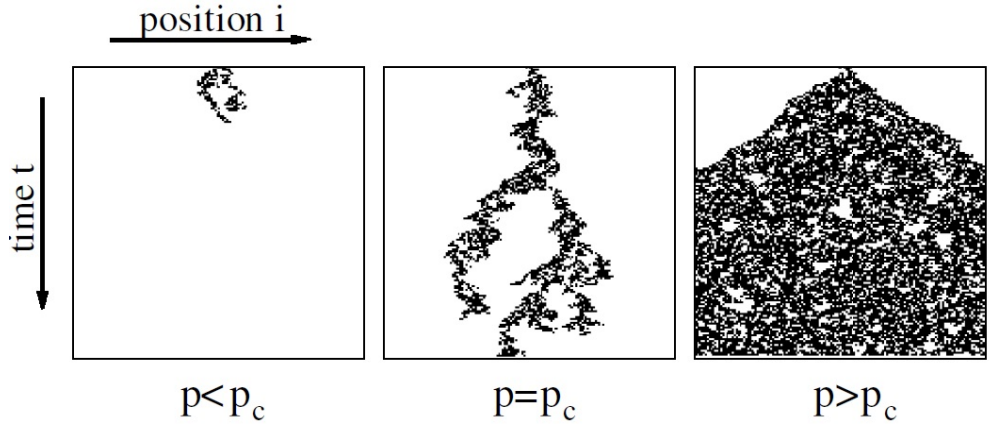

Figure 9.16: **An illustration of the configurations and phase diagram for directed percolation:** An example of (1+1)-dimensional DP with a single active seed as the initial condition. When the percolating probability p is below the critical value p_c, trajectories always terminate within finite time. Around p_c, active sites form a spatiotemporal intermittent cluster, and trajectories become unlimited. The cluster spreads and eventually fills a non-zero fraction of the lattice when $p > p_c$. The figure is taken from [25].

DP is a non-equilibrium process and breaks detailed balance. It is widely believed to be the generic universality class for non-equilibrium critical dynamical systems with absorbing states [55, 267]. The field theory corresponding to the universality class of DP is Reggeon field theory, a model for hadron scattering and decay that was developed phenomenologically in the 1970's [55]. Reggeon field theory has a non-Hermitian Hamiltonian, because it involves decay processes. Despite its original purpose of describing

natural percolating phenomena, and its conjectured wide applicability to non-equilibrium processes with absorbing states in various models, it was not convincingly observed in real life or realized in experiments until only a decade ago, using an ingenious setup containing two different types of fluctuating liquid crystal domains [268]. We will discuss recent progress in identifying natural examples of DP in Section 10.10.

9.3.4 Coupled map lattices

Around the same period of time as Pomeau's work, much attention was devoted to another theoretical model called coupled map lattices (CMLs), which exhibit spatiotemporal intermittency and chaotic properties. CMLs were introduced by Kaneko in 1983 to construct a phenomenological, dynamical system model that shows low-dimensional spatiotemporal chaos [269]. In CMLs, the discrete time evolution of each lattice site update is based on the coupling with its neighbors through a specified nonlinear mapping function such as the logistic map. A one-dimensional CML with diffusive coupling type has the general form [270]:

$$x_i^{n+1} = (1-\epsilon) f(x_i^n) + \frac{\epsilon}{2}\left[f(x_{i+1}^n + f(x_{i-1}^n)\right], \tag{9.25}$$

where x_i^n is a continuous field on lattice site i at discrete time step n, $0 < \epsilon < 1$ is the coupling strength and f is a nonlinear mapping function.

The spatiotemporal intermittency in CMLs was early on recognized as being analogous to turbulence [269, 270, 52]. The time for a CML to converge to the steady state was found to scale faster with system size than exponential (denoted as supertransient in chaos); the intermittent state was also conjectured be analogous to the long-lived turbulent state near transition, even though in CMLs the scaling is with respect to the system size [52, 271], not Re. These early results have stimulated recent studies that apply CMLs to model transitional turbulence [242, 241], and also the search for DP universality in CMLs with absorbing state [272]. However, discrepancies were found as to whether the transition in CMLs is discontinuous or continuous, and the critical exponents in CMLs seemingly disagreed with those in DP [272, 273]. In fact, in contrast to DP, CMLs are purely deterministic, and the spatiotemporal patterns they generate strongly rely on the specific mapping rule and the random initial condition [273]. It is now clear that the origin of the discrepancy about whether or not the transition in CML is first or second order depends on the system size. For large system, it is a continuous transition [274].

Another issue in the above models is that there is no clear way to connect them to fluid equations such as the Navier-Stokes equations, which show transitions from laminar to turbulent states in their numerical solutions. Even though spatiotemporal intermittency is exhibited in some of the above models, DP had not

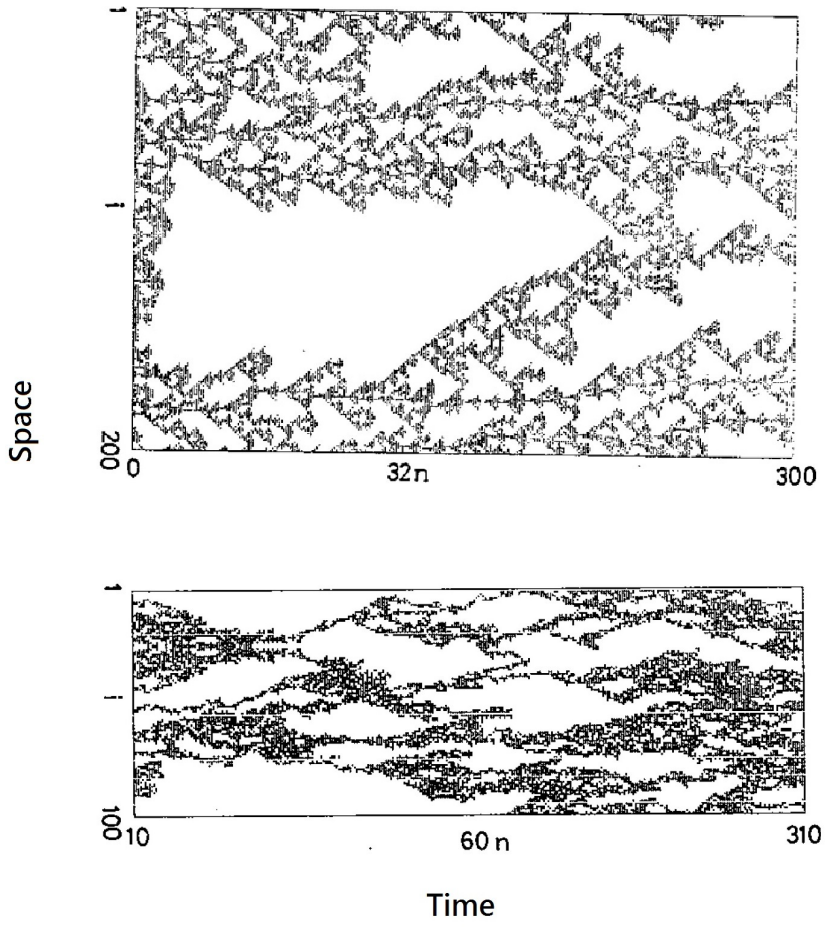

Figure 9.17: **Spatiotemporal intermittency from coupled map lattice models.** Simulations are generated by a logistic map function in Eq. (9.25) with different coupling strength and mapping cycles. Images are taken from [270].

been found in experiments or simulations of fluid systems until the last year, as we will see. Hence further theoretical studies that connect simple CMLs to the underlying physics are needed.

9.3.5 Unstable exact solutions of the Navier-Stokes equations

Another theoretical attempt to understand transitions to turbulence, using the picture of low-dimensional chaos and dynamical systems, is to search for unstable exact solutions of Navier-Stokes equations, using numerical simulation. This approach focuses on looking for a finite number of dynamical modes, and projects their dynamics on phase space. The instability of these modes from their interactions in the phase space has been interpreted as a signature of the transition to turbulence. These modes have been proposed and visualized in numerical simulations of confined flows, such as periodic orbits, streamwise vortices and

streaks, traveling waves and edge states [46, 50, 48, 51, 47, 3, 37, 49]. Nevertheless, turbulence is usually not confined in small spaces, and in general contains a high number of degrees of freedom. Thus a large number of these solutions would be required to fully capture transitional flows, and this poses an operational difficulty that has not yet been overcome. In this thesis, I take the perspective that the most appropriate way to capture the statistics of transitional turbulence is to use an approach rooted in non-equilibrium statistical mechanics and phase transition theory. Thus to serve the needs of studying non-equilibrium phase transition and critical phenomena, different approaches in the style of statistical mechanics would be preferred.

9.3.6 Extreme value statistics

Since the mean decay rate, τ_d, from the statistics of fluctuating turbulence exhibits super-exponential scaling in at least two different transitional turbulent systems (pipe flow [258, 41] and Taylor-Couette flow [45]), it seems that it might result from a generic, statistical property of turbulence. An interpretation that puts aside all detailed interactions and structures of specific fluid systems, and regards puff decay from the view point of rare events was proposed by Goldenfeld *et al.* [58]. The hypothesis is that turbulence decays if the energy at every place in a puff falls below some sustaining threshold that is Re-dependent. Numerical experiments clearly show the existence of this sort of threshold in pipe flow [56]. Therefore, when the largest energy of the coarse grained patches in the system fails to reach the threshold, the turbulent flow becomes laminarized. In this argument, one may imagine a turbulent fluid as a set of coarse-grained patches whose energy fluctuates with time. The probability for the maximum energy to fluctuate below the threshold should be related to an extremal distribution of the largest value, a problem well-studied in the mathematical literature. For independent identically distributed (i.i.d.) random variables whose distribution decays exponentially or faster, the distribution of their mean value is normal according to the central limit theorem. By contrast, the distribution of their largest or smallest value obeys the first type out of three of the Fisher-Tippett distributions [275]. Specifically, the cumulative form of the so-called Type I Fisher-Tippett distribution, or sometimes known as the Gumbel distribution [276, 277], for the maximum value $x_{\max}$ is

$$\widetilde{p}(x) = \exp\left(-e^{-(x-\mu)/\beta}\right), \tag{9.26}$$

where μ represents the location and β sets the scale. In the context of turbulence, both parameters would depend on Re. Eq. (9.26) thus represents the decay probability for turbulence as a function of decay threshold x which presumably decreases with Re. Suppose that $\widetilde{p}$ is the decay probability over a correlated

time interval τ_0 outside which events are independent; then the probability that a fluid sustains its turbulence after time duration t from t_0 is given by

$$P(t) = (1 - \widetilde{p})^{(t-t_0)/\tau_0}. \tag{9.27}$$

This leads to a survival probability, with an exponential tail of the form in Eq. 9.14, with

$$\ln P(t) = -\frac{t - t_0}{\tau_d} = \frac{t - t_0}{\tau_0} \ln(1 - \widetilde{p}), \tag{9.28}$$

$$\tau_d = \frac{\tau_0}{\ln(1 - \widetilde{p})}. \tag{9.29}$$

From Eq. (9.26), and performing a Taylor expansion of μ and β with respect to Re then leads to a super-exponential dependence of τ_d on Re with the form [58]:

$$\tau = \tau_0 \exp\left\{\exp\left(a\,\mathrm{Re} + b + \text{higher orders}\right)\right\}. \tag{9.30}$$

Another way to see how extreme value statistics may enter the distribution of turbulence lifetimes is to note that the lifetime is the time that the last turbulent patch becomes laminarized, i.e. the longest over several independent patches. In the directed percolation picture, this can be interpreted as the longest percolation trajectory in the time direction.

There are some caveats to consider when applying this argument of extreme value statistics to transitional turbulence. Near the transition, turbulent patches are more and more correlated if there really is a continuous phase transition, and the assumption of independent and identically distributed variables may not be valid. Nevertheless, it has been found that in isotropic percolation, this correlation does not affect the super-exponential scaling on the size distribution of percolation clusters [278]. The issue will be elaborated more in Chapter 11.

9.4 Theoretical models for transitional turbulence in pipe flows

9.4.1 DP transition in the pipe geometry

A quantitative test of Pomeau's analogy between DP and the laminar-turbulent transition in pipe flow was demonstrated by Sipos and Goldenfeld [56]. The idea is that if transitional pipe flow belongs to the DP universality class, then near the transition, the DP process as a minimal model would be expected to show the same critical behavior as measured in Hof *et al.*'s experiments, regardless of the specific details

in a real pipe flow. The authors performed simulations of bond directed percolation in a pipe geometry of 3+1 dimension, where an occupied (or active/wet) lattice site is the analogy of a coarse-grained region of turbulence and an empty (or inactive/dry) site represents a laminar region. The percolating probability p plays the role of the Reynolds number, and in the critical region it is expected that $(p - p_c) \propto (\mathrm{Re} - \mathrm{Re}_c)$. The initial condition was set to be a cluster of occupied sites to mimic a puff initiated in a pipe flow, and the dynamics of this active cluster was simulated in the puff's moving frame. In fact, an active cluster is more like a coarse-grained expression of a puff and thus it is not necessary to have the same structure as a real puff. Each lattice site updates based on the rule in Section 9.3.3. By analogy to pipe flow, for example, an active site contaminating its neighbors with a probability p is like a fluctuating turbulent patch randomly transmitting energy to nearby laminar regions. As lattice sites update, the internal structure of the active cluster may become patchy and fluctuating. This should not be a concern for studying universality, not only because the order parameter is a global quantity–the system is in the active state as long as any site remains active, but also the critical behavior is defined by the statistics of fluctuations over ensembles. Examples of simulation realizations are shown in Fig. 9.18. The simulation can reproduce the phase diagram observed in pipe flow experiments: When $p < p_c$, all lattice sites will eventually become empty, meaning that the initial turbulent puff decays and the flow becomes laminarized. As p increases, the active cluster branches out, showing similar spatiotemporal intermittency like splitting puffs. When $p > p_c$, the active cluster expands like a slug spreading in a pipe, and finally all lattice sites are occupied. In the critical region, when the correlation length is larger than the pipe diameter, the universality class crosses over to 1+1 DP.

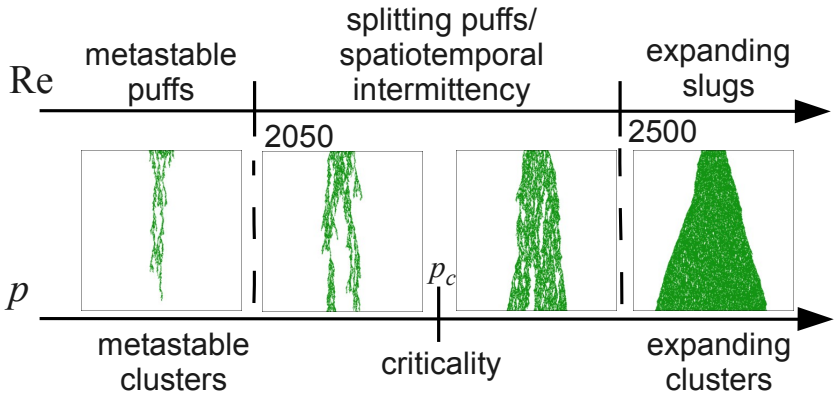

Figure 9.18: **Comparison of phase diagram of pipe flow and directed percolation.** The figure is taken from [56].

As already stressed, the system stays active until the last occupied site becomes inactive. Hence the length of the longest percolation trajectory spanned in the space-time domain is the lifetime of an initial

active cluster. To measure the characteristic lifetime τ_d, the same steps as in Hof *et al.* 's experiments were performed to calculate the survival probability over a large number of simulation realizations at different p. It turns out that τ in DP simulations also exhibits a super-exponential scaling versus p. Moreover, for $p > p_c$, the propagating velocity of the percolation front, defined as $G = \xi_\perp/\xi_\parallel \sim (p - p_c)^{\nu_\parallel - \nu_\perp}$ is found to scale as $(p - p_c)^\gamma$, where $\gamma \sim 0.58$ is close to the theoretical value for 3+1 DP and agrees with early experimental observations in pipe flows [279, 280]. These are the first results that support the conjecture that the laminar-turbulent transition in pipe flow is in the DP universality class in a quantitative, as well as a qualitative way.

Despite these successes, open questions remained. Splitting events were not quantified in this work, and the finite size effect on the statistics of mean puff lifetime was not specifically investigated. The connection of DP to the underlying hydrodynamics equations was also left open. Addressing this question is the main goal of Part II of this thesis.

9.4.2 Barkley's Excitable media model

One of the interesting aspects of the transition to turbulence problem is the diversity of approaches and methodologies that have been applied to tackle this challenging problem. In particular, there is the issue of what type of theory is deemed to be an explanation of the empirical facts, and this forces us to consider the distinction between "model" and "theory". Actually this question arose earlier in phase transition physics, when the development of the renormalization group forced researchers in high-energy physics to realize that the standard description of so-called fundamental interactions is an effective field theory model (with over 20 adjustable parameters) [281, 282].

In the case of turbulence, one would like a description that as much as possible can be seen to connect to the underlying Navier-Stokes equations, and at the same time makes clear and useful predictions about the phenomenology. A less ambitious goal is to take as input some of the empirical findings, and write down *ad hoc* mathematical models that reproduce some other aspect of the observations.

Such models can frequently be constructed by analogy, and can be iteratively improved with input from experiment. This sort of model has, arguably, a different goal and level of explanatory power than a full theory. The latter is able to make widely generalizable predictions beyond the initial system analyzed, using a perspective that is constructive and leads to new testable predictions. In a sense, theory is extrapolation, while modeling is interpolation.

Excitable media are models of reaction-diffusion processes that describe the propagation of fields that can be locally increased (e.g. excited by a stimulus or through interactions) and subsequently decrease after

a transient time, such as neuron dynamics, wildfire and traveling waves in embryo development [53, 283, 2]. For example, a typical description of neuron dynamics is illustrated in Fig. 9.19 An excitable field (e.g. a cell membrane voltage) is excited if its increment at the beginning is above a threshold; otherwise it decays back to the rest state. Then the excitable field in the excited state is relaxed through inhibition, and will eventually reach the rest state, forming a transient peak (e.g. an action potential). A typical model for excitable media is the FitzHugh-Nagumo model, whose form without spatial dependence is:

$$\frac{dV}{dt} = V - \frac{V^3}{3} - W + I, \tag{9.31}$$

$$\frac{dW}{dt} = a(V + bW + c), \tag{9.32}$$

where V represents the excitable field and W is the recovery field that inhibits V. As shown in Fig. 9.19, V is driven by the nonlinearity and converges back to the stable fixed point or the recovery state.

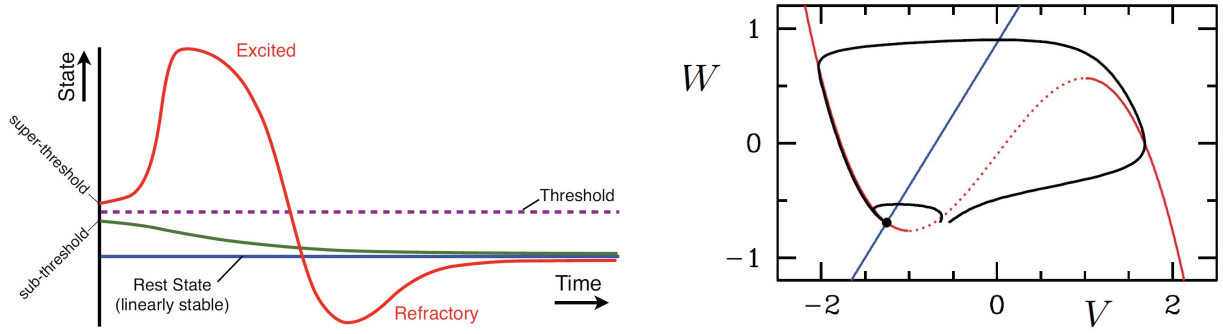

Figure 9.19: **Examples of excitable media.** (Left) A typical illustration for an excitable medium that can be described by FitzHugh-Nagumo model in Eq. (9.31). An action potential (red) can be created in the excited state if the initial condition of the excited field reaches above the threshold, or the field is unexcited (green) and decays to the rest state (blue). The action then falls and returns to the rest state. (Right) The phase portrait with nullclines $W = 0$ (red line) and $V = 0$ (blue line) and the trajectories (black lines) of an excited state and an unexcited states from different initial conditions corresponding to the left figure. Images are taken from [283].

The transient growth of V, and the required threshold for excitation are reminiscent of the dynamics of metastable puffs in experiments [284, 42] and the subcritical bifurcation picture. By analogy, Barkley proposed equations for an excitable field q that represents turbulent intensity, and that is coupled to a recovery field u which corresponds to the streamwise centerline velocity in pipe flow:

$$\begin{aligned}(\partial_t + U\partial_x)q &= q\left(u + r - 1 - (r+\delta)(q-1)^2\right) + \partial_{xx}q,\\ (\partial_t + U\partial_x)u &= \epsilon_1(1-u) - \epsilon_2 uq - \partial_x u,\end{aligned} \tag{9.33}$$

where q is a measure of turbulent intensity and u is the streamwise centerline velocity that converts energy to turbulence. Also r is the main control parameter that represents the Reynolds number, ϵ_1 is the rate for streamwise flow to relax back to laminar flow, ϵ_2 describes the rate of energy conversion from the streamwise flow to turbulent fluctuations and U is the mean flow velocity that advects the flows downstream. The dynamics of q and u are shown in Fig. 9.20. At small r, the equations have a linearly stable fixed point $(q = 0, u = 1)$, so after being excited the turbulence field returns back to the recovery state (see Fig. 9.20(a)). This describes a metastable puff that eventually relaminarizes (Fig. 9.20(c)). By increasing r, the equations exhibit an additional nonlinearly stable fixed point $(q > 0, u > 0)$ (Fig. 9.20(b)), by which turbulence can develop into a slug (Fig. 9.20(d)).

In order to recapitulate the detailed structure observed in experiments, the model needs to somehow represent turbulence itself, and this is done by introducing a local CML rule with spatio-temporal intermittency for discrete updating of $q(x,t)$, now represented by q_i^n for the turbulent intensity at site i and time n:

$$\begin{aligned} q_i^{n+1} &= F\left[q_i^n + d\left(q_{i-1}^n - 2q_i^n + q_{i+1}^n\right), R, u_i^n\right] \\ u_i^{n+1} &= u_i^n + \epsilon_1(1 - u_i^n) - \epsilon_2 u_i^n q_i^n - c(u_i^n - u_{i-1}^n). \end{aligned} \tag{9.34}$$

Here F is a complicated mapping function determined by a rescaled Reynolds number R and three other parameters, and c describes the downstream advection of the streamwise flow. The specific mapping function chosen is shown in Fig. 9.21(b). By changing parameters in the mapping function, the CML rule can lead to transient dynamics for metastable puffs, persistent splitting puffs or slugs. Thorough descriptions of Barkley's model can be found in [53, 283, 2].

By construction, the refractory state of a nerve means that Barkley's model represents the fact that two puffs cannot be too close to coexist [283], as found in experimental observations [285]. The mean lifetime and splitting time measured from the survival probability in simulations of Barkley's model also showed super-exponential scaling as a function of r [283]. Moreover, the turbulent fraction in simulation scales as $F_t \sim (r - r_c)^\beta$, where β agrees with the critical exponent for (1+1)-dimensional DP. Thus, Barkley's model is, by construction, in the DP universality class because it has an absorbing state and a chaotic dynamics that represent stochastic non-equilibrium dynamics.

Barkley's model is specifically constructed from empirical observations and makes no explicit connection to the equations of fluid dynamics, along with earlier *ad hoc* but well-motivated CMLs. Barkley's model is also specific for pipe flows where it is limited to centerline flow, and does not explain transitional phenomena

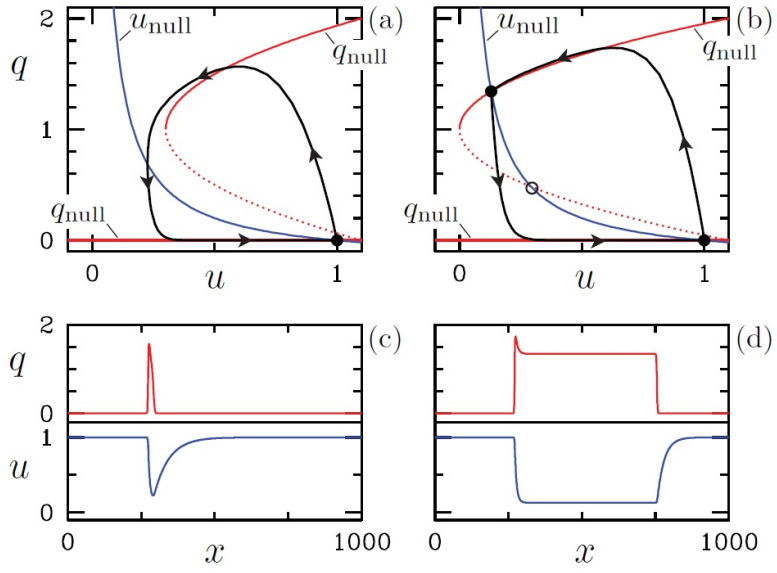

Figure 9.20: **Barkley's excitable media model for transitional pipe flows:** (a) Eq. (9.34) has one linearly stable fixed point in phase plane when Re -like control parameter $r = 0.7$, corresponding to a metastable puff in (c). (b) An additional nonlinearly stable fixed point appears when $r = 1$, corresponding to a sustained slug in (d) [283].

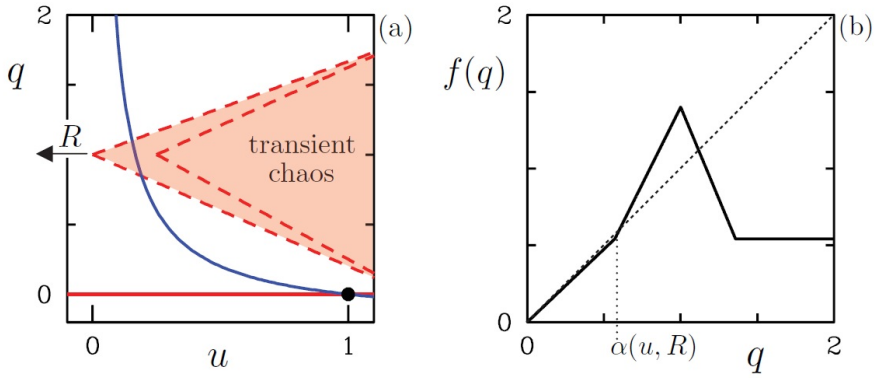

Figure 9.21: **Discrete version of Barkley's excitable media model:** (a) An example shows that the turbulent field q for a puff has "transient chaotic dynamics" based on the control parameter R. R is the rescaled r to be comparable with the real Re value. (b) The chosen CML rule $f(q)$ for discrete updating of Eq. (9.34) enables puff splitting in the model [53].

in other types of turbulent flows.

9.5 Laminar-turbulent transitions in other fluid systems

The onset to turbulent modes and spatio-temporal intermittency in other fluid systems have been studied. Specifically, super-exponential scaling in mean lifetime was also found in laminar-turbulent transitions in

channel flow [44] and Taylor-Couette flow [45], suggesting that the super-exponential behavior is generic and that these transitional turbulent systems are in the same universality class (presumably DP).

To this end, after decades of long-winding investigations, studies have now shown some convincing signs connecting the laminar-turbulent transition to DP universality class, but the route to a basic understanding to resolve confusions and nuances has just began. Interestingly, after our work and later experimental observations, even Pomeau later suggested that the laminar-turbulent transition might still be outside of the DP universality class [286]. Thus, at the time of writing, this field is in a state of flux, with a growing acceptance of the importance of directed percolation and statistical physics in transitional turbulence [287].

Chapter 10

Ecological model of transitional turbulence

10.1 Introduction

In this chapter, we will present a theory for the laminar-turbulent transition that approaches the problem from the perspective of statistical mechanics. We will begin by reminding the reader about the standard textbook approach to this topic based on Landau theory. It is important to be explicit about the logic because even in condensed matter physics, it is not possible to go from the most microscopic formulation of the problem to the detailed calculation of critical exponents and phase diagram. This is understood and now accepted in condensed matter physics. In fluid dynamics, however, the gold standard of calculation is to proceed directly from the Navier-Stokes equations, and so the phase transition approach based on symmetry, phenomenology and renormalization group arguments might seem incomplete. We will try to explain why this is not the case, and in particular, we will use direct numerical simulation (DNS) of the Navier-Stokes equations to avoid having to make unsystematic approximations that are sometimes necessary in strongly-interacting condensed matter problems where there is no small parameter in which to do perturbation theory. The phase transition problem indeed is generally one without a small parameter, and this is the case in the laminar-turbulent transition also. Sometimes it is thought that the distance from the critical point $((T - T_c)/T_c$ or $(\mathrm{Re} - \mathrm{Re}_c)/\mathrm{Re}_c$, where T and Re denote temperature and Reynolds number and c denotes the critical value) serves as a small parameter, but it turns out that it gets scaled away and enters into an effective coupling constant that diverges near the phase transition (see Chapter 7 of [23]).

10.2 Landau theory for laminar-turbulent transition

A statistical mechanics framework that has been widely adopted in order to describe phase transitions was developed by Landau in 1937 [22]. Landau theory was developed to understand phase transitions in magnetization, superconductivity, superfluidity, etc. Landau theory is now understood to be a mean-field description that regards a transition between thermodynamic phases as manifested in the change in the order

parameter. The sudden changes in the order parameter near the transition control the thermodynamics and correlations of the system. The order parameter is identified as the coarse-grained value of a physical variable of interest and depends on control parameters such as temperature, Reynolds number and space. In a Landau theory for a physical system, the free energy is assumed to be analytically expanded to symmetry-allowed powers of the order parameters. For example, a Landau theory for a uniform magnetic system is represented by an appropriate free energy written in terms of the average magnetization. As long as the symmetry and dimensionality are consistent with the physical system of interest, a Landau theory and its renormalization group extension can provide essentially exact predictions for universal physical characteristics near the transition. It is remarkable that an approximate model can give a precise description; this is the power of renormalization group. Therefore a Landau theory is an effective theory for phase transitions, and it is the phenomenon of universality near criticality that is responsible for the general effectiveness of Landau theory. However, although Landau theory is meant to explain phase transitions, it can break down exactly when systems are near criticality. Near a phase transition, the growing correlation length means that fluctuations on a wide range of scales are correlated, and hence the mean-field description is no longer valid there. It requires the extension using renormalization group (RG) methods, which exploits scale invariance, to obtain a quantitative description of the phenomena and study the obtain universality class. Nevertheless, Landau theory still recapitulates the qualitative features of phase transitions and serves as the first-step in the protocol to identify the potentially relevant physics.

The most counter-intuitve aspect of Landau theory is that it seems like you get something from nothing. A naive perspective would suggest that one starts with a Hamiltonian for a physical problem and somehow calculate the thermodynamics by evaluating the partition function. In Landau's approach to phase transitions (and RG extension), it is neither necessary nor desirable to derive the coarse-grained effective theory from a microscopic description, because any such derivation would need a small parameter and would thus only have limited validity due to the analytical approximations made. A familiar example of this situation is that even though the Navier-Stokes equations can be derived from Boltzmann's kinetic equations for gases, such a derivation would imply that the Navier-Stokes equation is only valid for dilute gases. In fact, the Navier-Stokes equations are an excellent description for dense liquids as well, and can be obtained by perfectly satisfactory phenomenological and symmetry arguments. The derivation from Boltzmann's kinetic theory is inherently limited by the regime of validity of the kinetic theory—low density—and this leads to an unnecessarily restrictive derivation of the equations of fluid dynamics. Returning to phase transitions, the reason why an analytical derivation of the coarse-grained theory is unnecessary is that even if the coefficients of the terms could be computed in the order parameter expansion of the Landau theory, they do

not come into the exponents or scaling functions anyway, and thus they do not affect the critical behavior. In the case of the transition to turbulence, the strategy then is to construct an effective theory that is valid near the transition. This effective theory would be an exact representation of the critical behavior of the laminar-turbulent transition, and as is often the case, could potentially be mapped into one of the canonical representatives of a known universality class. That universality class turns out to be directed percolation (DP).

10.3 Collective modes in the Navier-Stokes equations

In order to build an effective theory for the transitional turbulence problem, we need to identify the symmetry-allowed collective and long-wavelength modes. Constructing such modes from analytical methods is difficult. To avoid approximations which can be non-systematic and are hard to justify systematically, we applied direct numerical simulation (DNS) of the Navier-Stokes equations in a pipe to identify the important collective modes. As elaborated in the rest of this chapter, from simulations we found that at the onset of turbulence there are two important modes: a large-scale flow mode and small-scale turbulent fluctuations, and their interplay exhibits interesting dynamics [24] that echoes the perspective of statistical mechanics described described above. From these numerical discoveries, we proposed a physical interpretation of the interplay between these collective modes, which has been tested in simulations too. Based on this numerical evidence, we thence write down the corresponding minimal stochastic model in the spirit of the Landau theory of phase transitions [24, 288]. Furthermore, our findings suggest a heuristic derivation, from which we can motivate how such a minimal model can be related to the Navier-Stokes equations.

10.4 Direct numerical simulations of the Navier-Stokes equations

We performed direct numerical simulations (DNS) of the Navier-Stokes equations in a pipe, using the open-source code "*Openpipeflow*" [289, 290]. The equations were solved using a pseudo-spectral method in cylindrical coordinates [289, 290]. The pseudo-spectral method is a numerical scheme that aims to efficiently solve differential equations containing both local terms and non-local spatial derivatives. The basic idea is to calculate spatial non-local derivatives in Fourier space where they are local; this especially simplifies linear terms such as the incompressibility condition, $\nabla \cdot \mathbf{u} = 0$, and the viscous term, $\nu \nabla^2 \mathbf{u}$. The price is that non-linear derivative terms in space will result in many non-local terms that make calculation very expensive. This comment applies to the advective term, $(\mathbf{u} \cdot \nabla)\mathbf{u}$, which is complicated in k-space, but much simpler to calculate in real space. Thus we calculate this term in real space and then transform back to

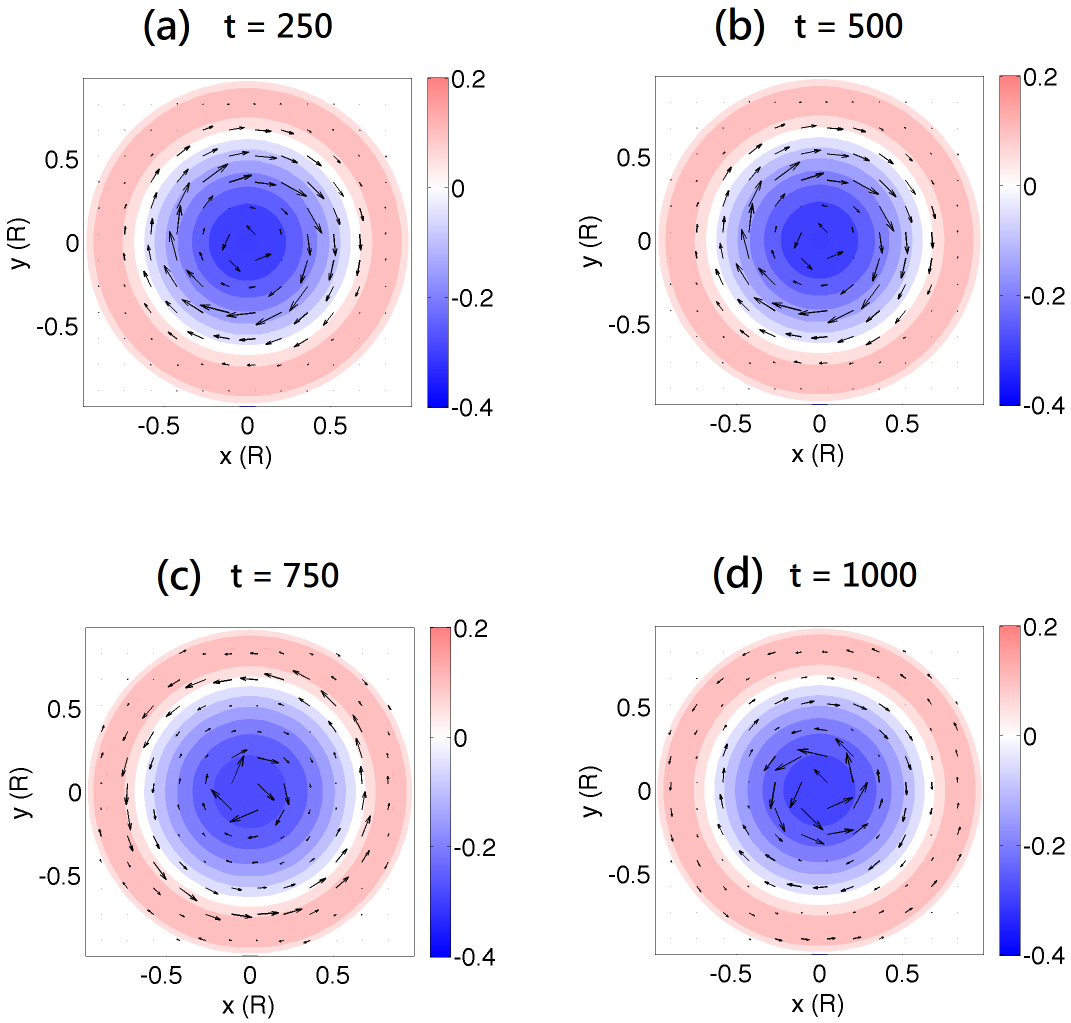

Figure 10.1: **Velocity field configuration of the zonal flow and its time evolution.** Snapshots of the zonal flow mode $\vec{\overline{u}}$ in cross section view taken from directed numerical simulations of the Navier-Stokes equations. The color bar indicates the value of $\overline{u}_z$. The direction and the size of arrows show the direction and the relative magnitude of local $\overline{u}_\theta(r)$ compared with the maximum $\overline{u}_\theta$ at that time. Note that both the direction and the magnitude of the zonal flow are changing with time; especially, the direction of $\overline{u}_\theta(r)$ reverses over time through (a) to (d), indicating oscillation behavior of the zonal flow. Time is shown in the unit R/U.

Fourier space to calculate the next time step of the field $\mathbf{u}(\mathbf{r}, t)$ In *Openpipeflow*, with the symmetry of the pipe geometry, θ and z components are decomposed in Fourier space, and the radial direction is represented in Chebyshev polynomial basis [290, 291], has the advantage that it focuses grid points near the pipe walls where there are rapidly varying boundary layers that mush be resolved.

In our simulations, there are 60 grid points in the radial (r) direction, 32 Fourier modes in the azimuthal (θ) direction and 128 modes in the axial (z) direction. Such a model is of course a reduced description of reality, but the main features can be well captured, with a slight renormalization of the Re needed to compare with experiment [289]. For the accuracy required in our study, we used 32 modes in the azimuthal direction, typical of most studies in the literature, although we note that useful, semi-quantitative results have been obtained with as few as 2 modes [289]. The spatial resolutions were chosen such that the resolvable power spectra span over six orders of magnitude. The pipe length L is 20 times its radius R, with periodic boundary conditions in the z direction [289]. With this resolution, the transition to turbulence occurs in a range of Re numbers between 2200 and 3000, and moves to smaller Re at still higher resolution. We report here measurements at Re = 2600, slightly above the transition [41]. The mass flux and Re = 2600 were held constant in time [289]. The laminar flow is the Hagen–Poiseuille flow, which was independent of time as the mass flux was held constant [289]. Because we were interested in transitional behavior, we applied a decomposition of different modes by first substracting the laminar part (in pipe flow known as the Hagen–Poiseuille flow), denoted the time-dependent velocity deviation by $\mathbf{u}(z, \theta, r) = (u_z, u_\theta, u_r)$ [292, 40, 293, 43, 44]. We specifically looked for large-scale modes that would indicate some form of collective behavior, as well as small-scale modes that would be representative of turbulent dynamics that would be representative of turbulent dynamics. In particular, we found a type of large-scale mode with characteristic dynamics. This mode is defined as $\mathbf{u} = (\overline{u}_z, \overline{u}_\theta, \overline{u}_r)$, where the bar denotes average over z and θ. Interestingly, this mode is purely azimuthal, *i.e.* $\overline{u}_r = 0$. In Fourier space, this mode is given by $\tilde{\overline{u}}(k = 0, m = 0, r)$, where k is the axial wavenumber and m is the azimuthal wavenumber, r is the real space radial coordinate and the tilde denotes Fourier transform in the θ and z directions only.

The flow configuration for this mode is shown in Fig. 10.1, and consists of a series of azimuthally symmetric modes with direction reversals as a function of radius r. We refer to this as the zonal flow (ZF) after the reminiscence of the large-scale jet flow in the atmosphere. Such banded shear flows are of special significance in plasma physics, astrophysical and geophysical flows, owing to their role in regulating turbulence [294]. In our simulation, the purely azimuthal component of the zonal flow, denoted by $\overline{u}_\theta(r)$ is spatially uniform in z. It is crucial to emphasize that the lack of a radial component means that it is not driven by pressure gradients, in contrast to the mean flow. Thus it can only exist due to nonlinear

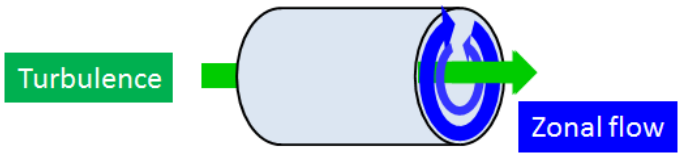

Figure 10.2: **Sketch of the zonal flow and turbulent fluctuations**. The zonal flow (green) is the composition of layers of the azimuthal flows with alternating directions that change with time as well as their magnitude. The turbulence mode is the remaining part with smaller scales of fluctuations whose overall propagation is longitudinal.

interactions with other modes such as turbulent fluctuations. In this sense, it is a collective mode emerging from self-organized fluid behavior and hence shall have special significance for transitional turbulence [24].

10.5 Observation of predator-prey dynamics in the Navier-Stokes equations

Apart from the zonal flow, turbulence was represented by short-wavelength modes, whose energy is $E_T(t) \equiv \frac{1}{2}\sum_{|k|\geq 1,|m|\geq 1}\int |\tilde{u}(k,m,r)|^2\,\mathrm{d}V$. We found that turbulence and the zonal flow exhibit remarkable features in their energy dynamics. Shown in Fig. 10.3 (a) is a time series for the energy $E_{ZF}(t)$ of the zonal flow, compared with the energy $E_T(t)$ of the turbulent energy. The curves display clear persistent oscillatory behavior, modulated by long-wavelength stochasticity. The phase portrait in Fig. 10.3 (b) shows a circular-like trajectory, indicating an approximate $\pi/2$ phase shift between turbulence energy and the zonal flow energy. We have calculated the phase shift between the turbulence and zonal flows, by using $\theta(\omega) = \tan^{-1}\left(Im[\tilde{C}(\omega)]/Re[\tilde{C}(\omega)]\right)$, where $\tilde{C}(\omega)$ is the Fourier transform of the correlation function between the turbulence and the zonal flow in time series in Fig. 10.3 (a). The resultant phase difference is shifted to be positive and plotted in In Fig. 10.3 (c), where the turbulent energy leads the zonal flow energy by $\sim \pi/2$. This suggests that these oscillations can be interpreted as a time-series resulting from activator-inhibitor dynamics, such as occurs in a predator-prey ecosystem [24].

10.5.1 What drives the zonal flow?

Why does such predator-prey dynamics exist in turbulence? And how can such a purely azimuthal long-wavelength mode emerge from and be sustained in randomly fluctuating turbulence anyway? The answer is rooted in the predator-prey-like dynamics between the zonal flow energy and turbulence energy. As described in previous chapters, predator-prey ecosystems are characterized by the following behavior: the

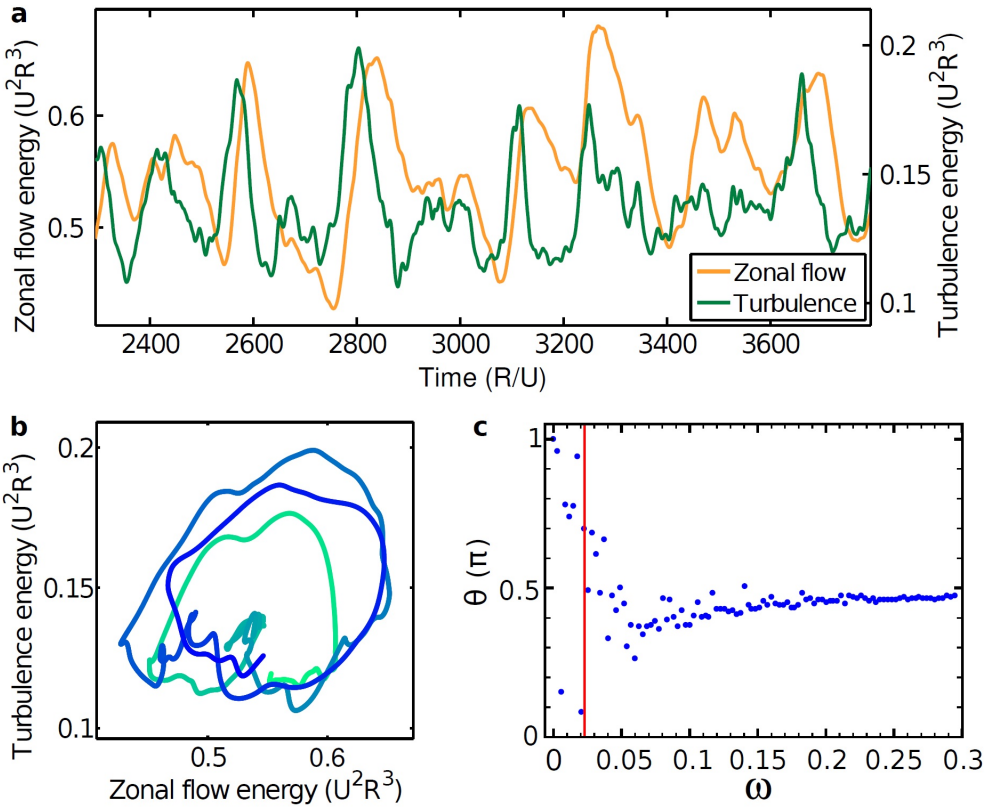

Figure 10.3: Predator-prey oscillations in transitional turbulent pipe flow. (a) Energy vs. time for the zonal flow (orange) and turbulent modes (green). (b) Phase portrait of the zonal flow and turbulent modes as a function of time, with color indicating the earliest time in dark blue progressing to the latest time in light green. (c) Phase shift between the turbulent and zonal flow modes as a function of frequency, showing that the turbulence leads the zonal flow by $\pi/2$ consistent with predator-prey dynamics. The phase shift $\theta(\omega) = \tan^{-1}\left(Im[\tilde{C}(\omega)]/Re[\tilde{C}(\omega)]\right)$ and is shifted to be positive, where $\tilde{C}(\omega)$ is the Fourier transform of the correlation function between the turbulence and the zonal flow in (a). The red line corresponds to the dominant frequency in the power spectrum. The phase shift near small ω is scatter due to the finite time duration of the time series. Figures are taken from [24].

"prey" mode activates the "predator" mode, which then grows in abundance. At the same time, the growing predator mode begins to inhibit the prey mode. The inhibition of the prey mode starves the predator mode, and it too becomes inhibited. The inhibition of the predator mode allows the prey mode to re-activate, and the population cycle begins again. We thence look for similar activation-inhibition couplings in pipe flow. The simplest way for such an azimuthal shear flow to couple to turbulent fluctuations is through the Reynolds stress τ: however, a uniform Reynolds stress cannot drive a shear flow, so the first symmetry-allowed possibility is the radial gradient of the Reynolds stress [294], as expressed in the Reynolds momentum equation. Specifically, the dynamics of the zonal flow velocity field obeys

$$\partial_t \overline{u}_\theta(r) \propto -\partial_r \langle \tilde{v_r} \tilde{v_\theta} \rangle, \tag{10.1}$$

Thus, to probe the dynamics that govern the emergence of the zonal flow, we have calculated the time-averaged radial gradient of the instantaneous Reynolds stress, $\tau \equiv u'_\theta \cdot u'_r$, where $\vec{u'}(z, \theta, r) \equiv \vec{u} - \vec{\overline{u}}$, and show in Fig. 10.4 (b) the 4.5-time-unit-running-mean time series of $-\partial_t \overline{u}_\theta$ and the radial gradient $\partial_r \tau$. Both quantities have been averaged over $0 \leq z \leq L$, $0 \leq \theta \leq 2\pi$ and $R_0 \leq r < R$, where $R_0 = 0.641R$, and the resulting time series are clearly highly correlated [24].

Fig. 10.4 shows the evidence of the high correlation between the turbulent fluctuations and the zonal flow: The radial shear of mean Reynolds stress and the temporal changes in the azimuthal component of the zonal flow keep in pace with each other in both space and time. This implies that the rise and fall of the zonal flow and turbulence are strongly tied to each other. The mean Reynolds stress in radial direction represents the radial anisotropy; the former is zero when the overall fluctuations is isotropic in radial direction.

This is consistent with the phenomenological explanation for the predator-prey-like dynamics in the energy of the zonal flow and turbulent fluctuations: When the zonal flow is originally seeded from turbulence, probably from some singular instability, energy from the anisotropic fluctuations of turbulence is transferred to the zonal flow. Since the zonal flow is isotropic in the radial direction, the mode shears the turbulence and thus has the effect of reducing the anisotropy of the turbulent fluctuations. From Eq. 10.1 and our measurements, the decrease in anisotropy of turbulent fluctuations reduces the source of the azimuthal velocity which will decline as well. Once the zonal flow has diminished, the turbulence is no longer sheared so strongly and so is less suppressed than before. As a result the energy in the turbulent modes increases, and the flow become anisotropic again, which fuels the zonal flow and leads to another cycle of their interplay [24]. In summary, the zonal flow is generated by turbulence but also regulates turbulence.

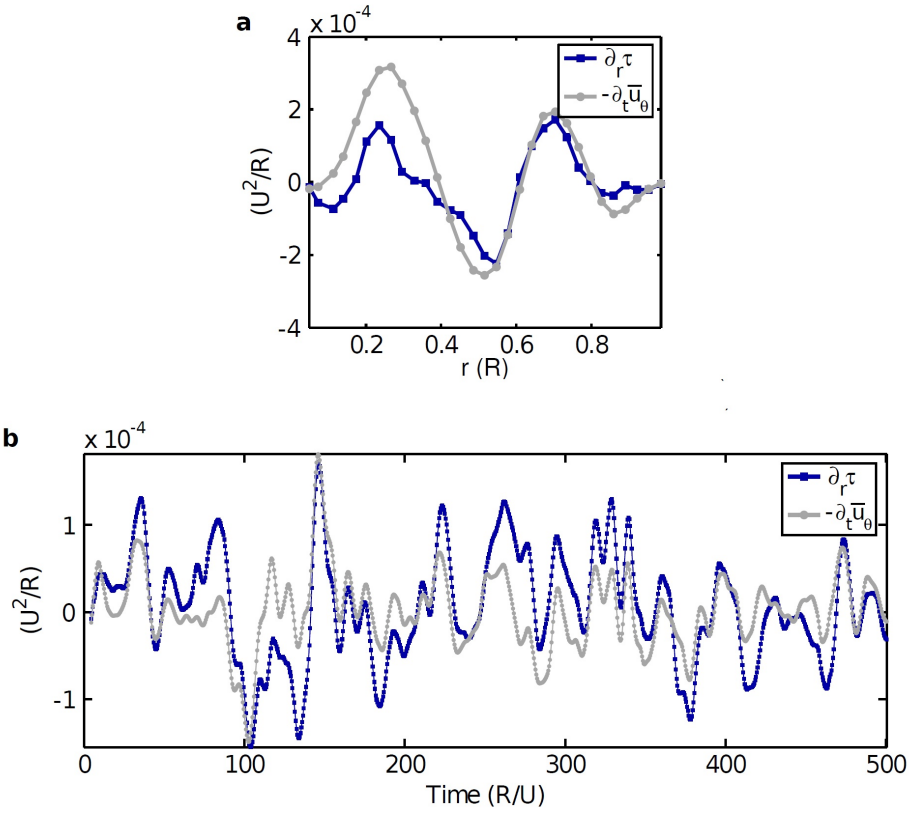

Figure 10.4: (a) Snapshot of the Reynolds stress gradient and zonal flow time-derivative as functions of r. (b) Reynolds stress gradient and zonal flow time derivative as functions of time. The evident proportionality shows that zonal flow dynamics is driven by the radial gradient of the Reynolds stress. Figures are taken from [24].

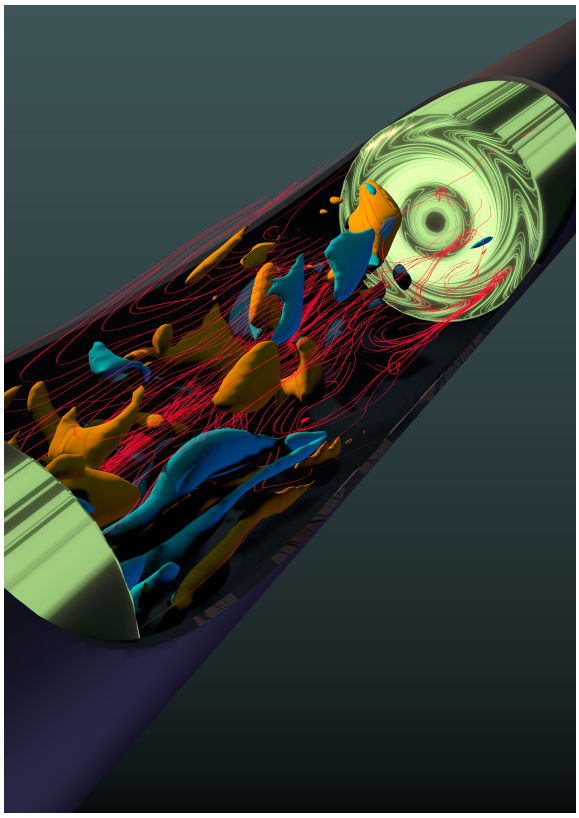

Figure 10.5: **Cutaway view of DNS for pipe flow near the transition to turbulence**. Zonal flow (green), isosurfaces of Reynolds stress (blue and orange) and streamlines (red) are shown. Their definition is described in Section 10.4 and 10.5 of this chapter. Figure is taken from [24].

10.6 Lotka-Volterra equations in transitional turbulence

Combining our numerical results with general considerations from phase transition theory [23] would suggest that the emergence of a long-wavelength zonal flow collective mode would dominate the non-equilibrium transition of pipe flow from the laminar to the turbulent state, through the predator-prey interaction with the small scale velocity fluctuations. Such a "two fluid" effective field description of transitional turbulence implies that stochastic predator-prey populations should undergo spatiotemporal fluctuations whose functional form matches precisely the observations for the lifetime and splitting time of turbulent puffs in a pipe, close to the laminar-turbulent transition. In this section, we will delve into this in great detail.

10.6.1 Stochastic predator-prey model for transitional turbulence

These considerations are significant for the interactions between turbulence and zonal flows, as stochasticity, in effect, arises due to the microscopic interactions between localized unstable modes of the fluid flow. The predator-prey nature of the interactions shows that turbulence is the prey, whereas the zonal flow is the predator. In order to construct a Landau theory for the laminar-turbulence transition, it is necessary to write down all possible interactions between the turbulence and the zonal flow. These are summarized in Fig. (10.6), and displayed in the language of stochastic predator-prey processes.

The narrative of the activation-inhibition interplay between the zonal flow and turbulent fluctuations parallels that which occurs in predator-prey ecosystems. A predator-prey ecosystem is typically modeled at mean-field level by the Lotka-Volterra equations [69, 64, 295] for the population of predator A and prey B:

$$\dot{A} = pAB - d_{\mathrm{A}} A \tag{10.2}$$

$$\dot{B} = bB(1 - B/\kappa) - pAB - d_{\mathrm{B}} B, \tag{10.3}$$

where time derivative is denoted by a dot, p is predation rate, d_{A} and d_{B} are predator and prey death rate respectively, b is prey birth rate and κ is the carrying capacity. As described in Chapter 2, the prey carrying capacity represents the maximum amount of prey that the ecosystem nutrient supply can support. If κ is taken to infinity, the equations simplify somewhat, but exhibit unphysical behavior. Specifically there is a constant of the motion and the trajectories in the (A, B) phase space are cycles that form a center, whose radius depends on initial conditions. These cycles are sometimes confused with limit cycles but there is a big difference. Limit cycles are attractors for a wide range of llimited conditions, whereas the center orbits are structurally unstable and the solution changes depending on the initial conditions. In fact, the real reason for population cycles in Lotka-Volterra equation is demographic stochasticity, as explained in Chapter 2.

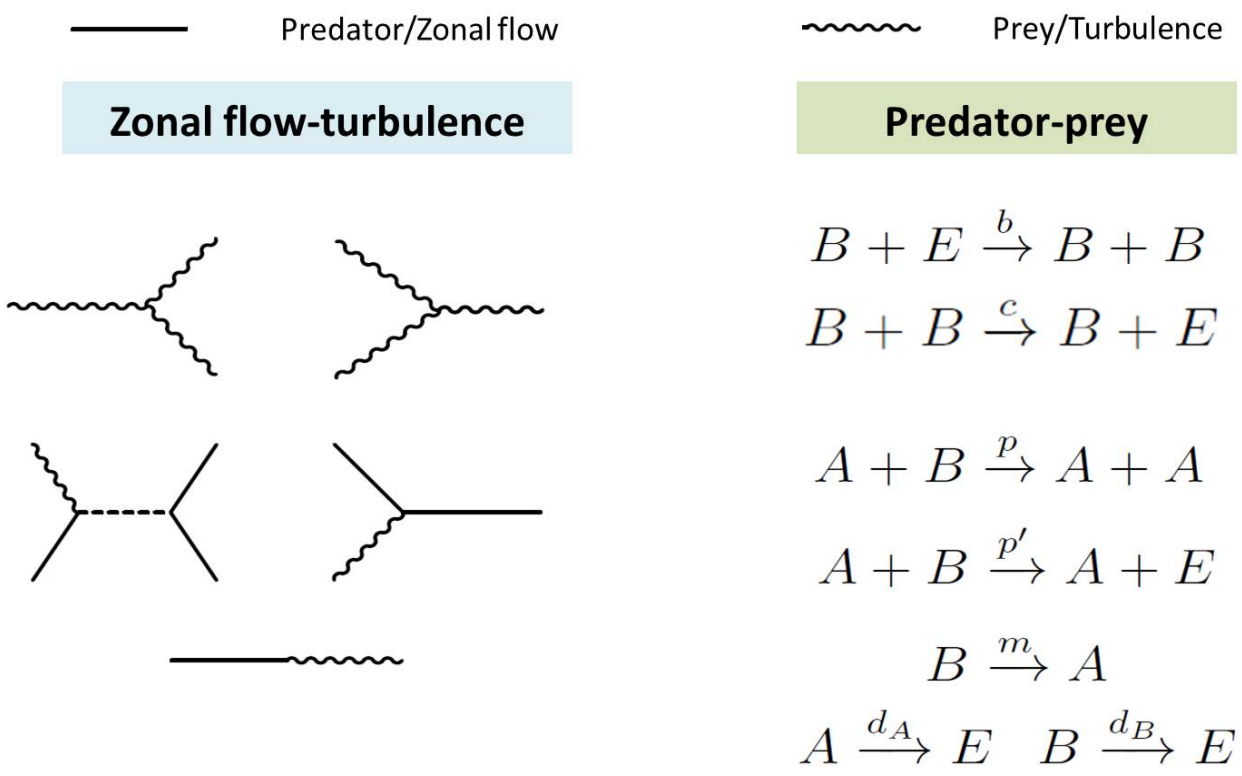

Figure 10.6: Effective theory for interactions between small-scale turbulence and large-scale zonal flow. The allowed interactions between turbulence modes (prey B, wiggly lines) and zonal flow (predator A, straight lines) are shown, together with their interpretation as processes describing birth, death and predatory activity. An allowed process at the lowest order corresponds to the conversion between prey and predator with rate m, something that does not have a direct realization in most biological systems. The symbol E denotes the third trophic level in the ecosystem of turbulence, namely the food that sustains the prey, which in the fluid dynamics picture is simply the laminar flow state itself. The symbols above the arrows denote rate constants. The definition of predator-prey processes is described in the text. In the right column the predation process with rate p' is not included in our model since it only renormalizes the predation coefficient in the prey equation in Eq. (10.3).

Thus the genuine origin of population cycles requires analysis beyond mean-field theory.

Remarkably, stochastic simulations of this predator-prey model, in a 2D strip intended to represent the 3D pipe geometry of the original turbulence experiments, reproduce the main features of the laminar-turbulence transition as we describe below. In this case, the control parameter turns out to be the birth rate b of the prey, and this is the analogue of Re [24]. We will now demonstrate three main claims:

1. First of all the phase diagram is reproduced as a function of the birth rate b of the prey, which plays the role of Re. In particular there is a phase where no prey survive; then at higher b, a phase where the prey and predator co-exist, but localized regions of prey decay; then at still higher values of b, a region where localized regions of prey split, so that the dynamics exhibits the strong intermittency in space and time seen in the turbulence simulations and experiments.

2. Furthermore, it is found that there is a super-exponential variation of decay and splitting lifetimes on the prey lifetime b [24].

3. In addition to recapitulating the phenomenology of the laminar-turbulence transition in pipes, the stochastic predator-prey model Eq. (10.4) can be mapped exactly into Reggeon field theory [59, 100] and this field theory itself has long been known to be in the DP universality class [101, 55]. As mentioned in the previous chapter, (1+1)-dimensional DP simulation displays super-exponential scaling in the longest percolation path. Does the predator-prey ecosystem, whose dynamics is shown in transitional pipe flow simulations, also have the same characteristic time scaling like pipe flow and DP?

To test this idea, we have performed simulations of a spatially-extended stochastic predator-prey ecosystem, in a quasi-one-dimensional geometry to mimic the pipe environment. The specific system has three trophic levels: nutrient (E), Prey (B) and Predator (A), which correspond in the fluid system to laminar flow, turbulence and zonal flow respectively. The interactions between individual representatives of these levels are given by the following rate equations

$$\begin{aligned}
&A_i \xrightarrow{d_A} E_i, \qquad B_i \xrightarrow{d_B} E_i, \qquad A_i + B_j \xrightarrow[\langle ij \rangle]{p} A_i + A_j, \\
&B_i + E_j \xrightarrow[\langle ij \rangle]{b} B_i + B_j, \qquad B_i \xrightarrow{m} A_i, \\
&A_i + E_j \xrightarrow[\langle ij \rangle]{D} E_i + A_j, \quad B_i + E_j \xrightarrow[\langle ij \rangle]{D} E_i + B_j.
\end{aligned} \tag{10.4}$$

where d_A and d_B are the death rates of A and B, p is the predation rate, b is the prey birth rate due to consumption of nutrient, $\langle ij \rangle$ denotes hopping to nearest neighbor sites, D is the nearest-neighbor hopping rate, and m is the point mutation rate from prey to predator, which models the induction of the zonal flow

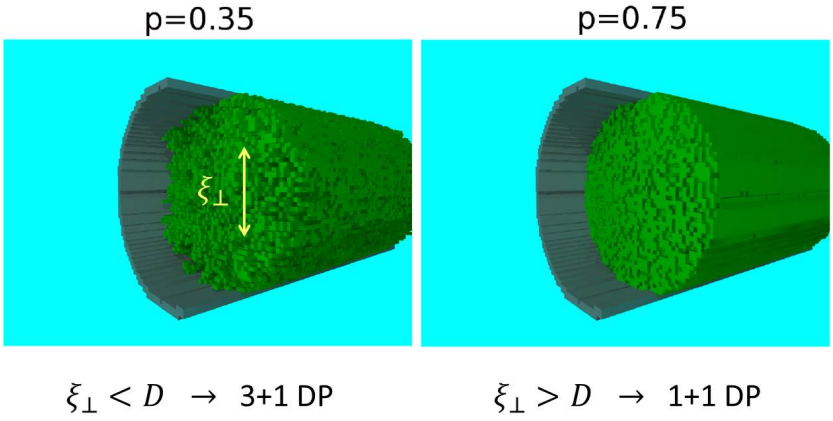

Figure 10.7: **Finite-size effect in directed percolation.** Visualization of (3+1)-dimensional directed percolation simulation in a pipe geometry: When $|p - p_c| \ll 1$, radial correlation length is finite; as $p \sim p_c$, radial correlation length becomes comparable to pipe diameter, resulting (1+1)-dimensional DP dynamics. Figures are taken from [56].

from the turbulence degrees of freedom.

We are primarily interested in long-wavelength properties of the system, at least in the vicinity of the turbulence transition, where we expect the transverse correlation length to be larger than the pipe diameter, implying that the behavior is in fact quasi-one-dimensional. The crossover phenomena associated with this have been discussed previously [56], and thus our quasi-one-dimensional model should be appropriate and quantitatively correct near the transition.

We will return to the dimensional crossover between (3+1)- and (1+1)-dimensional DP when we discuss our analysis of finite size scaling later in Chapter 11, as there is a remarkable subtlety which we discovered near the end of this thesis work.

10.6.2 Stochastic simulations of predator-prey dynamics.

The specific system has three trophic levels: nutrient (E), Prey (B) and Predator (A), which correspond in the fluid system to laminar flow, turbulence and zonal flow respectively. Such a system can be naively modeled by the Lotka-Volterra ordinary differential equations [69, 64, 295] which in the case of ecosystems with finite resources becomes Eq. (10.3). However, as stated in Chapter 2, Eq. (10.3) do not permit long-time persistent oscillatory solutions, unless additional biological details such as functional response are included. In fact, it is necessary to include the dynamics of individual birth-death events, and when this is done correctly, it is found that the number fluctuations drive the population oscillations [89] through resonant amplification. Thus, we use a stochastic model at the outset.

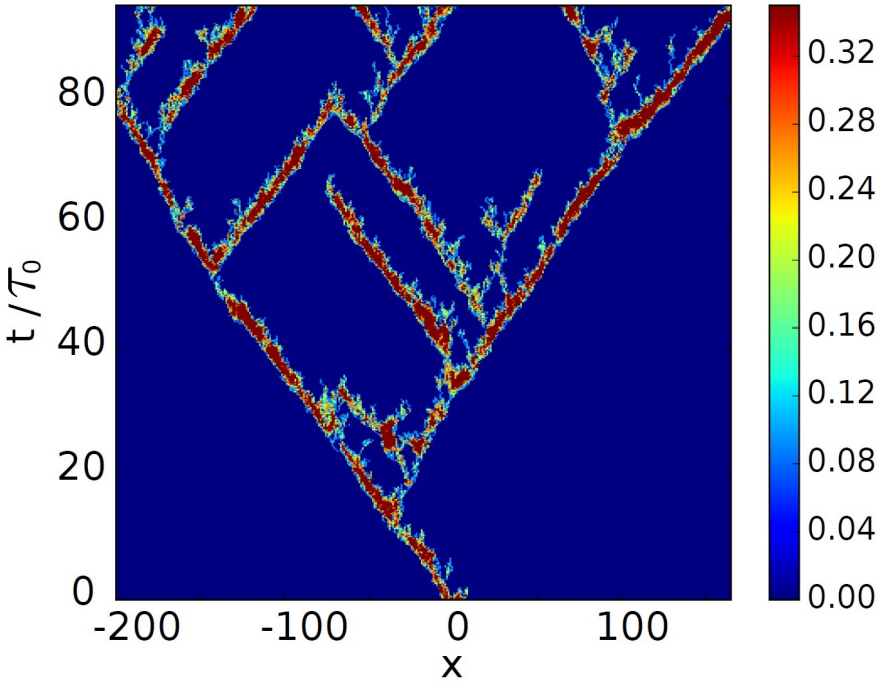

Figure 10.8: Stochastic predator-prey model reproduces similar space-time plot of the transitional pipe turbulence. To compare with the experiments [38], predator-prey dynamics are performed in two-dimensional pipe geometry as described in the text. World line of clusters of prey splitting to form predator-prey traveling waves. The color measures the local density of prey, corresponding to intensity of turbulence in pipe flow. In the simulation, the dimensionless parameters are $D = 0.1$, $b = 0.1$, $p = 0.2$, $d_A = 0.01$, $d_B = 0.01$ and $m = 0.001$. In the model simulated, diffusion is isotropic, not biased as would be the case corresponding to a mean flow, where the clusters will accumulate at large times with a well-defined separation set by the depletion zone of nutrient behind each predator-prey traveling wave.

The interactions between individual representatives of these levels are given by Eq. 10.4. We simulated these equations on a 401×11 lattice in two dimensions, intended to emulate the pipe geometry. Lattice sites were only allowed to be occupied by one of E, A or B. The predator (A) and prey (B) are additionally allowed to diffuse via random walk on the lattice with diffusion coefficient 0.1 in units of the square of the lattice spacing divided by the time step (set equal to unity). The initial conditions for the simulations were a random population of prey and predator, occupying with probability $4/5$ and $1/5$ respectively on the lattice sites between $x \in [-15, 15]$ and $y \in [-5, 5]$ where x labels the direction along the axis of the ecosystem (pipe) and y labels the transverse direction. The predator-prey dynamics in Eq. 10.4 was implemented by the following algorithm: at each time step, a site i is randomly chosen, a random number s, is generated from the uniform distribution between zero and one. The behavior on the site is decided by the random number: (1) if $s < 1/6$ and the site i is occupied by any individual, and if a randomly chosen neighbor site is empty, then that individual diffuses to the random neighboring site with rate $\mu = 0.01$ (i.e. this reaction happens if another uniformly distributed random number is less than $1 - \exp \mu$); (2) if $1/6 \leq s < 1/3$ and the site i is occupied by a prey individual, and if a randomly chosen neighbor site, j, is empty, then one prey individual is born on the site j with rate b; (3) if $1/3 \leq s < 1/2$ and the site i is occupied by a predator individual, and if a randomly chosen neighbor site, j, is occupied by a prey individual, then the prey individual is replaced by a new-born predator individual with rate p; (4) if $1/2 \leq s < 2/3$ and the site i is occupied by a predator individual, that predator individual dies with rate d_A; (5) if $2/3 \leq s < 5/6$ and the site i is occupied by a prey individual, that prey individual dies with rate d_B; (6) if $5/6 \leq s < 1$ and the site i is occupied by a prey individual, then the prey individual is replaced by a predator individual with rate m. Then within the same time step, the above processes are repeated 401×11 times so that on average one reaction takes place at each lattice site in the system.

In our simulation, the control parameter is the prey birth rate b. When b is small enough, the population is metastable, and cannot sustain itself: all individuals, both predator and prey, eventually die within a finite lifetime $\tau^d(b)$. As b increases, the lifetime of the population increases rapidly: in particular the prey lifetime increases rapidly with b. At large enough values of b, the decay of the initial population is not observed, but instead the initially localized population proliferates, spreading outwards and spontaneously splitting into multiple clusters. An example of space-time plot of clusters of prey in simulations is shown in Fig. 10.8. The splitting of trajectories indicates the formation of predator-prey traveling waves. The color measures the local density of prey, corresponding to intensity of turbulence in pipe flow. The clusters will accumulate at large times with a well-defined separation set by the depletion zone of nutrient behind each predator-prey traveling wave.

To quantify these observations, we have measured both the lifetime of population clusters in the metastable region and their splitting time using a procedure directly following that of the turbulence experiments and simulations [41], and described below in details. We comment that both timescales involve implicitly measurements of quantities that exceed a given threshold, and thus it is natural that the results are found to conform to extreme value statistics [58, 56].

10.6.3 Measurement of decay and splitting lifetimes.

We measured both the lifetime of population clusters in the metastable region and their splitting time using a procedure directly following that of the turbulence experiments and simulations [41]. To this end, we monitor the coarse-grained prey population density $\tilde{n}_B(i) = \sum_{j=-J}^{j=J} \sum_{l=-H/2}^{l=H/2} n_B(i+j,l)/(H+1)/(2J+1) - 0.25$, where H is the height of the system (11 lattice units) and $J = 3$. The lifetime of prey clusters is defined as the time it takes for the last prey individual to die. The cluster splitting time is defined as the first time that the distance between the edges of two coarse-grained prey clusters exceed 25 unit sites. We comment that both timescales involve implicitly measurements of quantities that exceed a given threshold, and thus it might be natural that the results are found to conform to extreme value statistics [58, 56]. We will discuss more about this point in the next chapter.

In Figure 10.9 we show the phenomenology of the dynamics of initial clusters of prey, corresponding to the predator-prey analogue for the experiments in pipe flow which followed the dynamics of an initial puff of turbulence injected into the flow [38]. Depending upon the prey birth rate, the cluster decays either homogeneously or by splitting, precisely mimicking the behavior of turbulent puffs as a function of Reynolds number. Figure 10.9 (A) and (B) show that the decay has an exponential-like tail. Figure 10.9 (C) and (D) show that the survival probability is a sigmoidal curve, whose inverse lifetime as a function of prey birth rate is plotted in a log scale in Figure 10.9 (E). If the lifetime were an exponential function, this curve would be a straight line with negative slope. The downward curvature is a manifestation of super-exponential behavior. These figures indicate a remarkable similarity to the corresponding plots obtained for transitional pipe turbulence in both experiments [38] and direct numerical simulations [41], and demonstrate conclusively that experimental observations are well captured by an effective two-fluid model of pipe flow turbulence with predator-prey interactions between the zonal flow and the small scale turbulence.

In Fig. 10.10 is shown the semi-log plot of lifetime for both decay and splitting as a function of prey birth rate, the upward curvature indicative of super-exponential behavior. The inset to Fig. 10.10 shows a double exponential plot of puff lifetime and splitting time vs. prey birth rate, the straight line being the fit to the functional form indicated in the caption. These figures indicate a remarkable similarity to the corresponding

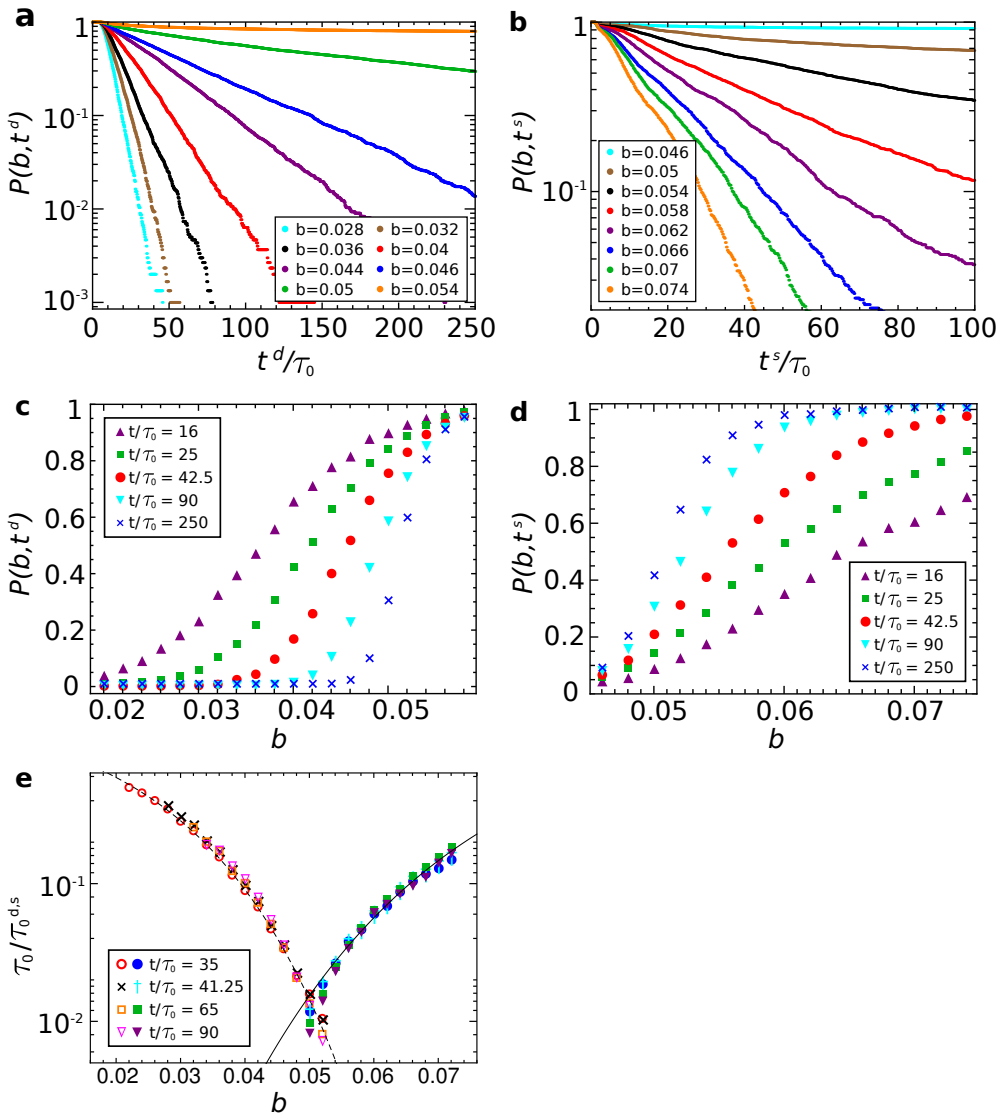

Figure 10.9: Stochastic predator-prey model reproduces the phenomenology of transitional pipe turbulence. Decay lifetime, τ^d, and splitting time, τ^s, of clusters of prey are memoryless processes and obey super-exponential statistics as a function of prey birth rate. To compare with the experiments [38], predator-prey dynamics are performed in two-dimensional pipe geometry as described in the text. The dimensionless parameters in the simulation are $D = 0.01$, $p = 0.1$, $d_A = 0.015$, $d_B = 0.025$ and $m = 0.001$. (A) Log survival probability of prey cluster vs. time during homogeneous decay to extinction. Here the characteristic time scale that is estimated by $\tau_0 \sim 200$. (B) Log survival probability of prey cluster vs. time during decay to splitting. (C) Survival probability of prey cluster as a function of prey birth rate during homogeneous decay to extinction. (D) Survival probability of prey cluster as a function of prey birth rate during decay to splitting. (E) Log inverse lifetime of prey cluster, as a function of prey birth rate during homogeneous decay to extinction (left curve, τ^d) and during decay to splitting (right curve, τ^s). The dashed curve is given by $\tau_0/\tau^d = 1/\exp(\exp(46.539b - 0.731))$, and the solid curve is given by $\tau_0/\tau^s = 1/\exp(\exp(-31.148b - 3.141))$.

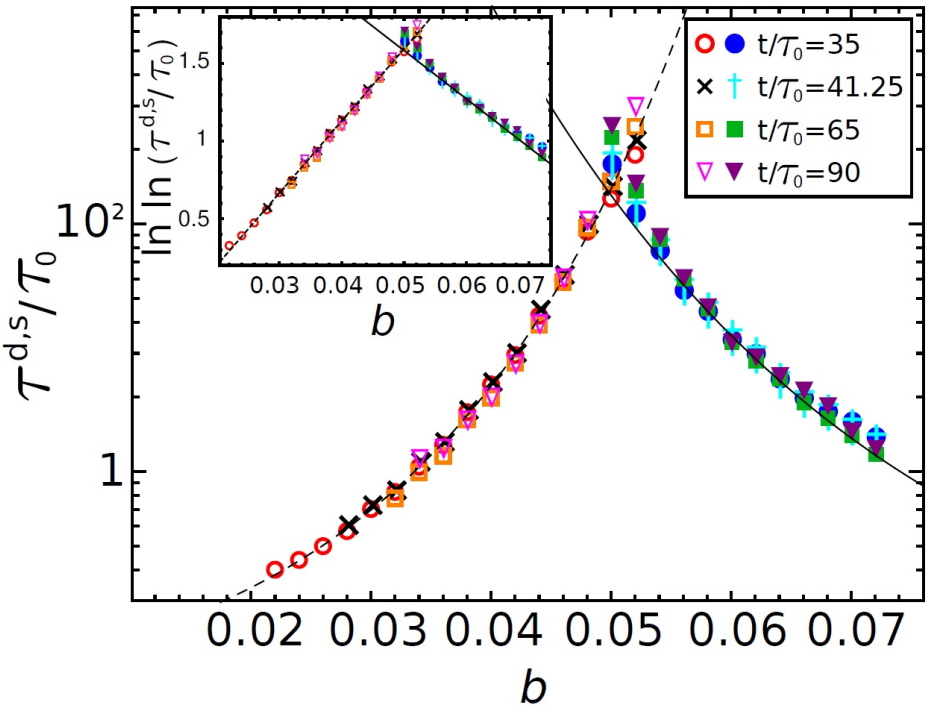

Figure 10.10: Log decay lifetime of prey cluster and splitting time as a function of prey birth rate. The upward curvature signifies super-exponential behavior. The parameters are $D = 0.01$, $p = 0.1$, $d_A = 0.015$, $d_B = 0.025$ and $m = 0.001$. Inset: Double log lifetime vs prey birth rate, showing the fit to the following functional forms: the dashed curve is given by $\tau^d/\tau_0 = \exp(\exp(46.539b - 0.731))$, and the solid curve is given by $\tau^s/\tau_0 = \exp(\exp(-31.148b - 3.141))$.

plots obtained for transitional pipe turbulence in both experiments [38] and direct numerical simulations [41], and demonstrate conclusively that experimental observations are well captured by an effective two-fluid model of pipe flow turbulence with predator-prey interactions between the zonal flow and the small scale turbulence.

10.7 Universality class of the laminar-turbulence transition in pipes

The two-fluid predator-prey model expressed by Eq. (10.4) exhibits a rich phase diagram that captures the main features observed in transitional turbulence in pipes. The transition to puff-splitting can be identified with a change of stability of the spatially-uniform mean-field predator-prey coexistence point, where a stable node becomes a stable focus or spiral with increasing birth rate. In the language of predator-prey systems, this corresponds to the breakdown of spatially homogeneous prey domains into periodic traveling wave states. The phase diagram is sketched in Figure 10.12, along with the corresponding phase diagram for transitional pipe turbulence as determined by experiment. The phenomenology of the predator-prey system mirrors that of turbulent pipe flow.

In order to determine the universality class of the non-equilibrium phase transition from laminar to turbulent flow, we use the two-fluid predator-prey mode in Eq. (10.4). Near the transition to prey extinction, the prey population is very small and no predator can survive, and thus Eq. (10.4) simplify to

$$\begin{aligned} B_i &\xrightarrow{d_B} E_i, \\ B_i + E_j &\xrightarrow[\langle ij \rangle]{b} B_i + B_j, \\ B_i + E_j &\xrightarrow[\langle ij \rangle]{D} E_i + B_j, \\ B_i + B_j &\xrightarrow[\langle ij \rangle]{c} B_i + E_j. \end{aligned} \tag{10.5}$$

If we think of B_i as representing the site i being occupied and E_i as representing the site i being empty, then these equations have the diagramatic representation the asme as for DP, as shown in Fig. 10.11. These equations are exactly those of the reaction-diffusion model for directed percolation [296], as illustrated in Fig. 10.11.

A more detailed and systematic way to reach this conclusion is to represent Eq. 10.4 exactly in path integral form [95, 96, 97, 98, 99, 296], as described in Chapter 4. The resulting action simplifies near the transition to that of Reggeon field theory [59, 100], which has been shown to be in the universality class of

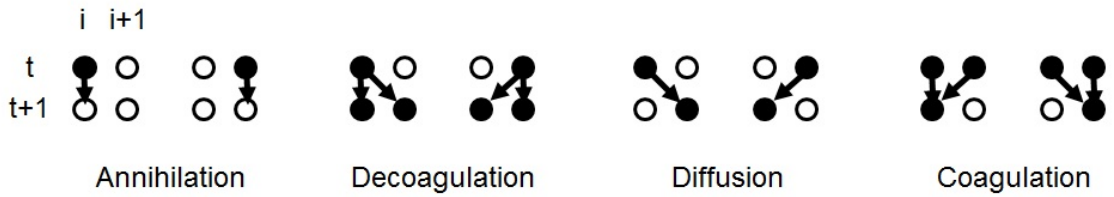

Figure 10.11: **Basic rules for directed percolation**. Horizontal axis is space, and i is lattice index. The basic rules of directed percolation imply that on a space-time lattice, the updating of the configuration of the lattice from time t to time $t+1$ can be represented as arising from four fundamental processes, shown here. Each rule can be represented as each process in Eq. (10.5) from predator-prey system near predator extinction.

directed percolation [101, 55]. Numerical simulations of 3+1 directed percolation in a pipe geometry have reproduced the statistics and behavior of turbulent puffs and slugs in pipe flow [56, 297], and a detailed comparison between theory and experiment has been presented [298]. Specifically, the reaction Hamiltonian that corresponds to Eq. (10.4) can be represented in Fock space as:

$$H_{\text{reaction}} = -\Sigma \left[d(1-\hat{\alpha}_i^\dagger)\hat{\alpha}_i + b(\hat{\beta}_i^\dagger - 1)\hat{\beta}_i^\dagger \hat{\beta}_i + p(\hat{\alpha}_i^\dagger - \hat{\beta}_i^\dagger)\hat{\alpha}_i^\dagger \hat{\alpha}_i \hat{\beta}_i \right], \tag{10.6}$$

where $\hat{\alpha}_i^\dagger$ and $\hat{\alpha}_i$ are bosonic raising and lowering number operator for predator at site i and $\hat{\beta}_i^\dagger$ and $\hat{\beta}_i$ are number operators for prey respectively. The reaction Hamiltonian can be mapped onto the basis of coherent states in terms of α^* and α, which are the left and right eigenstate of $\hat{\alpha}^\dagger$ and $\hat{\alpha}$, and β^* and β, which are left and right eigenstate of $\hat{\beta}^\dagger$ and $\hat{\beta}$. With diffusion terms, the corresponding coherent state path integral representation becomes:

$$S_{\text{reaction}} = \int d^d x \int dt \left[\alpha^* \left(\frac{\partial}{\partial t} - D_{\text{A}} \nabla^2 \right) \alpha + \beta^* \left(\frac{\partial}{\partial t} - D_{\text{B}} \nabla^2 \right) \beta + H_{\text{reaction}}(\alpha^*, \alpha, \beta^*, \beta) \right]. \tag{10.7}$$

Near the transition to extinction of predator, by changing the fields to fluctuations respect to the fixed point $(\alpha = 0, \beta = \kappa)$, after change of variables, the action becomes [59, 100]:

$$S_{\text{reaction}} = \int d^d x \int dt \left[\tilde{\psi} \left(\frac{\partial}{\partial t} + D_{\text{A}}(\lambda_1 - \nabla^2) \right) \psi - \lambda_2 \tilde{\psi}(\tilde{\psi} - \psi)\psi + \lambda_3 \tilde{\psi}^2 \psi^2 \right], \tag{10.8}$$

where $\tilde{\psi}, \psi$ are the fields after change of variables. Eq. (10.8) is in the same form as Reggeon field theory which is also known to be in DP universality class [101, 55, 267]. The super-exponential behavior of DP might seem to contradict the expectation based upon the known critical behavior which is usually manifested in power-law scalings. This turns out to be subtle and will be discussed in Chapter 11.

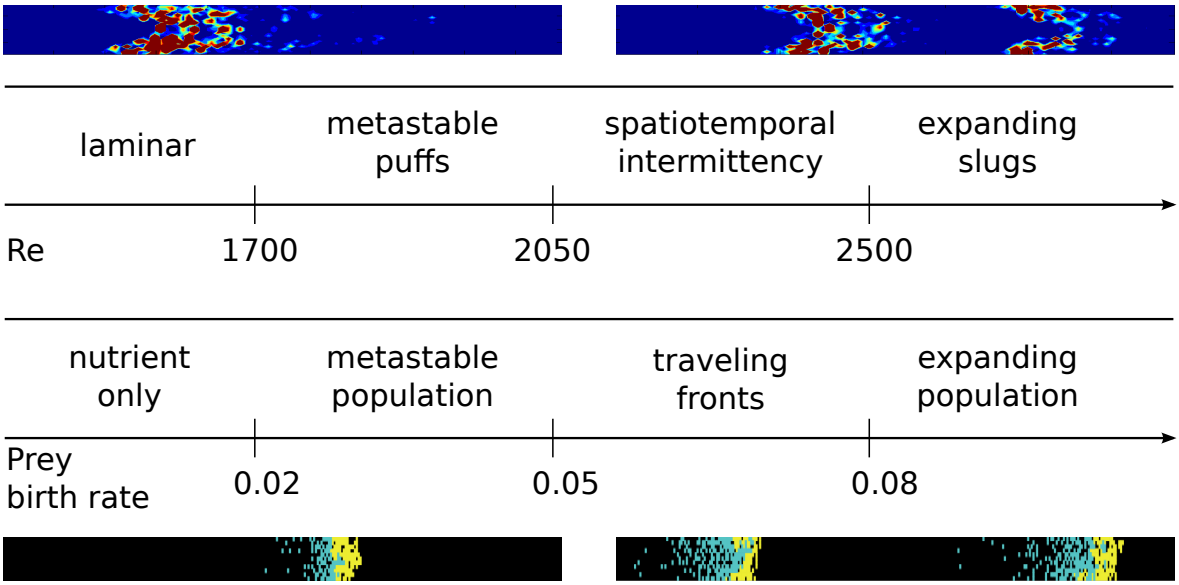

Figure 10.12: Schematic phase diagram for transitional pipe turbulence as a function of Reynolds number compared with the phase diagram for predator-prey dynamics as a function of prey birth rate. Above each phase is shown a typical flow or predator-prey configuration, indicating the similarity between the turbulent pipe and ecosystem dynamics.

10.7.1 Lotka-Volterra equations in transitional turbulence

An outline of how to derive the predator-prey equations in pipe transitional turbulence is as follows, modeled after efforts to obtain such equations heuristically in tokamak physics [294]. We start by sketching the form of an equation describing the time variation of the energy of turbulent modes, due to local instabilities and the likely interaction with the zonal flow. The basic premise is that there is a primary instability generating turbulence at small scales, probably arising from the interaction of localized unstable modes such as periodic orbits. The energy of turbulent fluctuations E at the relevant wavenumber or range of wavenumbers will have three main contributions to dE/dt. The first is the primary linear instability of the form $\propto E$. The second term will be of higher order, describing eddy interactions through some sort of non-local scattering kernel or triad processes. We will make the usual ansatz that near a phase transition, it is permissible to replace the non-local kernel by local terms describing eddy damping, of the form $\propto -E^2$. Finally, from the numerics we know that turbulent fluctuations are suppressed by interaction with the zonal flow. What should be the form of this interaction? The zonal flow is a collective shear mode; the azimuthal velocity component u_θ experiences shear in the radial direction r, and will be denoted by $\Omega \equiv \partial\langle\overline{u}_\theta(r)\rangle/\partial r$. Here θ is the azimuthal direction, and $\overline{u}_\theta(r)$ represents the purely azimuthal component of the zonal flow that is spatially uniform in the longitudinal direction, indicating it it not driven by pressure gradients in pipe flows. The damping should occur through interaction between the Reynolds stress and Ω, but should be

independent of the direction of the shear. Thus, the most generic coupling between the turbulence and Ω should be proportional to both E and $U \equiv \Omega^2$.

These considerations suggest that

$$\frac{dE}{dt} = \gamma_0 E - \alpha_1 E^2 - \alpha_2 EU \tag{10.9}$$

where γ_0, α_1 and α_2 are constants.

Next we sketch an outline of how one can obtain a description of the zonal flow equation of motion. The starting point in the Reynolds momentum balance equation, which we will write in the approximate form for the zonal flow velocity field:

$$\frac{\partial \overline{u}_\theta(r)}{\partial t} = -\frac{\partial \langle \tilde{v_r} \tilde{v_\theta} \rangle}{\partial r} - \mu \langle \overline{u}_\theta(r) \rangle \tag{10.10}$$

where μ is some damping coefficient, the tilde denotes fluctuation component and $\langle \tilde{v_r} \tilde{v_\theta} \rangle$ is the Reynolds stress in the azimuthal direction. In Eq. 10.10, we have omitted terms that are in principle present from the Reynolds equation, but either vanish due to the azimuthal average or are small compared to the terms retained. We do not have a fully systematic derivation of this equation. However, we have measured the right and left hand terms of this equation in the DNS and the results show that these terms do indeed track one another [24], as shown in Section 10.5. Taking the radial derivative of Eq. 10.10 leads to

$$\partial_t \Omega = -\partial_r^2 \langle \tilde{v_r} \tilde{v_\theta} \rangle - \mu \Omega \tag{10.11}$$

This equation is not closed of course, but we can make progress with scaling arguments. We conjecture that $\langle \tilde{v_r} \tilde{v_\theta} \rangle$ is quadratic in velocity fluctuations and therefore should be proportional to E. Note that the term $\langle \tilde{v_r} \tilde{v_\theta} \rangle$ vanishes by symmetry in an isotropic flow, but is non-zero when the turbulent fluctuations are anisotropic and coupled to the zonal flow which provides a local directionality to the velocity fluctuations. This suggests that $-\partial_r^2 \langle \tilde{v_r} \tilde{v_\theta} \rangle \propto +\Omega + O(\Omega^2)$ where it is important to note that the $+$ sign means that the Reynolds stress anisotropy is exciting the zonal flow, and not damping it, corresponding to the DNS results. Putting these scaling arguments together and multiplying through by Ω suggests that

$$\partial_t U = \alpha_3 EU - 2\mu U \tag{10.12}$$

where α_3 is another phenomenological constant. The equation argued for above is basically a scalar equation, but a full understanding of the interaction of mean flows or zonal flows with turbulence anisotropy requires a detailed consideration of the full tensor Reynolds equation, the spatial variation of the eigenvectors of the

Turbulence-zonal flow dynamics	Prey-predator dynamics
$\frac{dE}{dt} = \gamma_0 E - \alpha_1 E^2 - \alpha_2 EU$	$\dot{B} = bB(1 - B/\kappa) - pAB$
$\partial_t U = \alpha_3 EU - 2\mu U$	$\dot{A} = pAB - dA$

Figure 10.13: **Comparison between turbulence-zonal flow mean-field equation and Lotka-Volterra equations for the prey-predator system.**

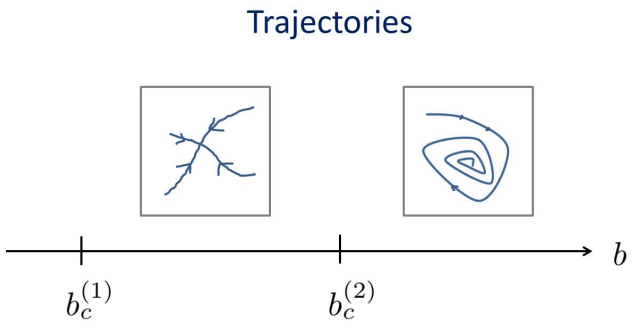

Figure 10.14: **Instability in Lokta-Voterra model as a splitting mechanism.** Sketch of phase portrait of Eq. (10.3) as a function of prey birth rate b.

stress tensor etc. The heuristic derivation described here can be checked by direct numerical computations, in principle, and we hope to do this in the future. The immediate consequence of Eq. (10.9) and Eq. (10.12) is that they have the form of the mean field Lotka-Volterra equations Eq. (10.3), and thus would be expected to predict (at the mean field level) the existence of predator-prey oscillations.

Unfortunately, as explained in Chapter 2 before, the mean field Lotka-Volterra equations do not predict population oscillations at all, and an individual-level model that includes carrying capacity is the most satisfying solution as the way we demonstrated in Section 10.6.3.

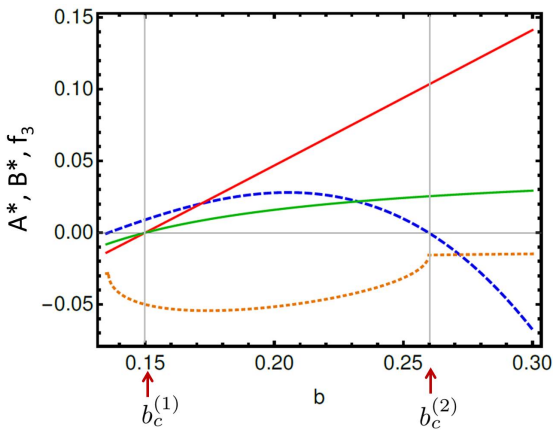

Figure 10.15: **Example of coexistence solution and its linear stablity analysis in the Lokta-Volterra equations**. The plot shows the coexistence fixed point of Eq. (10.3) with $A^* > 0$ (predator, red line) and $B^* > 0$ (prey, green line), as functions of prey birth rate b. In this case, at $b = b_c^{(1)} = 0.15$, the stable fixed point changes from extinction ($A^* = 0, B^* = 0$) to coexistence ($A^* > 0, B^* > 0$). The function f_3 in Eq. (10.13) (dashed blue line, rescaled by multiplying with 0.1) shows a sign change from positive to negative, indicating that the eigenvalues corresponding to the stable coexistence fixed point change from real to imaginary values across $b = b_c^{(2)} = 0.26$. The real part of the eigenvalues s is also shown (dotted orange line). The values of the parameters are $p = 1, \kappa = 1$ and $d_A = d_B = 0.4$.

10.8 Splitting mechanism from the Lokta-Volterra equations

In general, it is the case that zonal flows are driven by statistical anisotropy in turbulence, but are themselves an isotropizing influence on the turbulence through their coupling to the Reynolds stress [299, 300, 301]. The general way to investigate the pattern of predator-prey dynamics is to consider spatially-extended systems where stochasticity locally drives instabilities, leading to fluctuation-induced Turing patterns or traveling waves if there are appropriate sources of nonlinearity [86, 302]. Here we will show the linear stability analysis of the Lotka-Volterra equation, Eq. (10.3). We argue that in order to have instability in the partial differential equations of predator-prey systems, there needs to be an instability in the ordinary differential equations as well. Therefore, we have a heuristic way to see how splitting may arise from the mean-field equations in Eq. (10.3). We solve for the steady states by setting the time derivatives equal to zero and seek coexistence fixed points where $A^* > 0, B^* > 0$. There are other fixed points, such as total extinction ($A^* = 0, B^* = 0$), but they are not our present interest. We find a transition in the fixed points of Eq. (10.3) occurs at $b = b_c^{(1)}$ where the fixed point changes from the extinction solution ($A^* = 0, B^* = 0$) to the coexistence solution ($A^* > 0, B^* > 0$). The linear stability analysis with respect to the coexistence fixed point leads to eigenvalues in the form of

$$s = f_1 \pm f_2 \sqrt{f_3}, \tag{10.13}$$

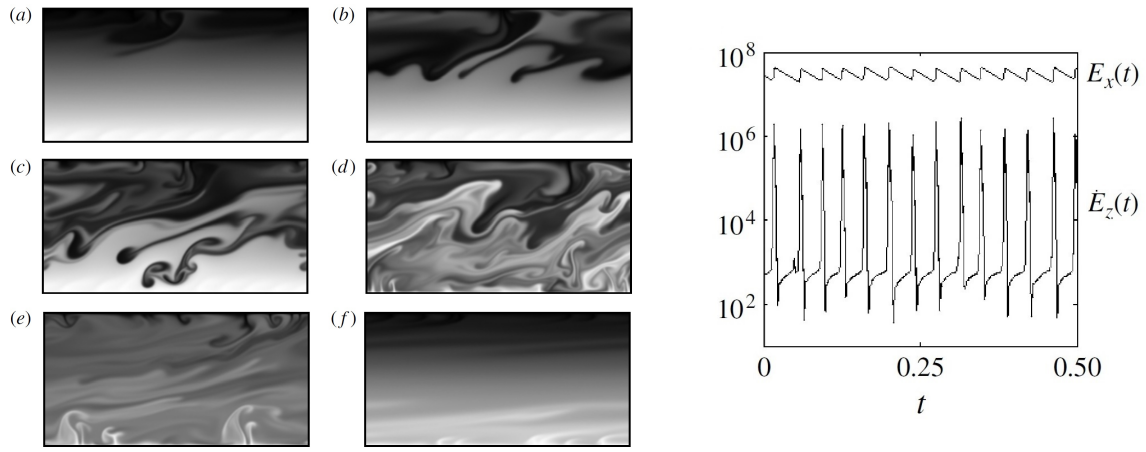

Figure 10.16: **Predator-prey oscillations in thermal convection**. The left panel shows that in the 2-dimensional Rayleigh Bénard convection simulations, from (a) to (f) the decrease of the transverse zonal flow (predator) along the top and bottom is followed by the rise of the vertical turbulent plumes (prey), and thence the zonal flow arises again. The dynamics of the energy of the zonal flow (E_x) and turbulent plumes (E_z) is shown in the right panel, where the zonal flow energy is behind the turbulent plume energy by $\pi/2$. Figures are taken from [254].

where f_1, f_2 and f_3 are real functions of parameters in Eq. (10.3). It turns out that there is a second transition at $b = b_c^{(2)} > b_c^{(1)}$. For $b_c^{(1)} < b < b_c^{(2)}$ the eigenvalues s are real and for $b > b_c^{(2)}$ the eigenvalues s become complex (*i.e.* $f_3 < 0$). The complex eigenvalues indicate that the stable fixed point is a stable focus: trajectories spiral into the fixed point on the phase portrait. Fig. 10.15 shows an example of the coexistence fixed point and the corresponding eigenvalues.

10.9 Predator-prey dynamics in other turbulent systems

The most obvious prediction of our theory is that transitional turbulence involves predator-prey dynamics. Interestingly, there is experimental and numerical support for this idea in other transitional flows. We briefly describe these phenomena in this section.

10.9.1 Predator-prey dynamics in thermal convection

The interplay between zonal flow suppression of turbulence and turbulence initiation of zonal flow has been reported in thermal convection in a variety of geometries by Goluskin *et al.* [254, 255]. In two-dimensional numerical simulations of Rayleigh Bérnard convection, vertical heat transport due to temperature difference between the top and bottom boundaries creates heat transport [254]. For small enough temperature difference, small-scale thermal plumes generated from the top and bottom boundaries drift vertically and

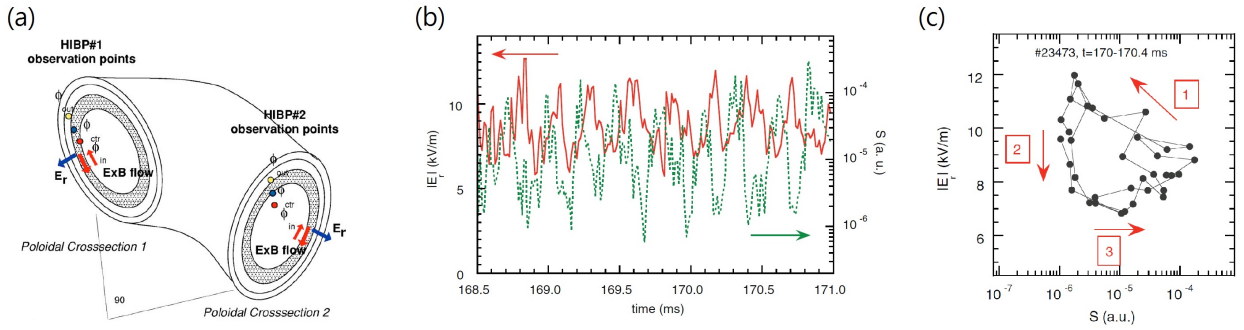

Figure 10.17: **Predator-prey oscillations in turbulent plasma**. (a) A cross-section view of tokamak. (b) Predator-prey dynamics of the radial electronic field $|E_r|$ (red, predator) that shears the zonal flow and the plasma density fluctuations (green, prey). (c) Phase portrait of trajectory indicates a $\pi/2$ phase delay of $|E_r|$ behind density fluctuations. Figure (a) is taken from [303], and figure (b) and (c) are taken from [304].

dissipate. As heat transport becomes large, described by an increased temperature difference, plumes driven by buoyancy force become turbulent, and a large-scale zonal flow emerges from shearing at the top and bottom boundaries traveling rightward and leftward respectively in the transverse direction. The plumes transfer energy to the zonal flow and are drifted away, and the flow exhibits "sustained shearing convection" [254, 255]. When viscous dissipation is reduced, characterized by a small Prandtl number, the plumes become more turbulent and their nonlinear interactions with the zonal flow becomes strong. This leads to dramatic oscillations between turbulent plumes and the zonal flow, forming "bursting shearing convection" where the zonal flow energy and plume energy show predator-prey oscillations, as shown in Fig. 10.16 [254, 255]. Just as with the zonal flow in pipe flow, in this case, the zonal flow is orthogonal to the heat transport and thus is not driven by the buoyancy force that generates the normal convection [254, 255].

10.9.2 Predator-prey in turbulent plasma

Predator-prey behavior in turbulent systems was first proposed in magnetohydrodynamics by Diamond and collaborators [294, 305, 303] many years ago in the context of the interaction between drift-wave turbulence and zonal flows in tokomaks.

To enhance nuclear fusion, particles need to be highly confined under reactions. In magnetic confinement fusion plasma in a tokamak (toroidal chamber with axial magnetic field), plasma flows are induced and confined by magnetic fields along the toroidal direction and have drift transport along the center of the toroid. Small-scale fluctuating drift waves nonlinearly generate poloidal $E_r \times B$ mesoscopic flows, called zonal flows [303]. Zonal flows cause radial shears and thus damp drift waves. The decline of turbulent drift

waves will suppress the driving force behind the zonal flows, which then makes the turbulent drift waves regain their amplitude. Zonal flows also dissipate due to damping effect [303]. At the transition from low confinement mode to high confinement mode (L-H transition), zonal flows are found to steadily coexist with turbulent drift waves [304, 306]. The growth and decay process between turbulent drift waves and zonal flows provides a self-regulating picture of predator-prey dynamics: zonal flows behave as the predator, growing by consuming turbulent drift waves (which are analogous to the prey) and decreasing after turbulent drift waves decline. Experiments measure the time-dependent density fluctuations of turbulent plasma drift waves and the radial electric field E_r that contributes zonal flows. The magnitudes of radial electric potential and the envelope modulation of turbulent densities are found to have predator-prey dynamics as shown in Fig. 10.17 [304, 306].

Theoretical models [294, 307] originally proposed the idea of predator-prey interactions to explain the self-regulating coexistence of turbulent drift waves and zonal flows at the L-H transition. Diamond *et al.* [307] heuristically proposed a set of Lotka-Volterra equations derived from complicated nonlinear magnetohydrodynamics mechanisms with various uncontrolled but physically well-motivated approximations. Other models consider modified forms of the commonly adopted Lotka-Volterra equations by phenomenologically including magnetohydrodynamics effects in terms of predator satiation as described in Chapter 2. In these deterministic models, the fluctuating randomness in dynamics shown in experiments is not explained. Also, an anomalous π phase shift has been found in experiments when the equilibrium shear flows plays an additional role intermediate between turbulent drift waves and zonal flows [306], and this phenomenon would arise from predator-prey dynamics analogous to that of rapid evolution driven by demographic stochasticity.

10.9.3 Predator-prey dynamics in electroconvection

Another magnetohydrodynamics system that exhibits transitional turbulence was reported by Bardóczi *et al.* in table-top electroconvection [300]. The experiment was implemented in a thin layer ionic fluid on top of randomly oriented magnets applied with a electric field. Initially the random $\mathbf{E} \times \mathbf{B}$ force induced localized vortices, and gradually the flow developed a large-scale zonal flow in the azimuthal direction (Fig. 10.18 (a)). The energy of the zonal flow and the turbulent fluctuations were found to display predator-prey dynamics (Fig. 10.18 (b)). The turbulent Reynolds stress and the radial shear were also measured and shown to evolve together (Fig. 10.18 (b)).

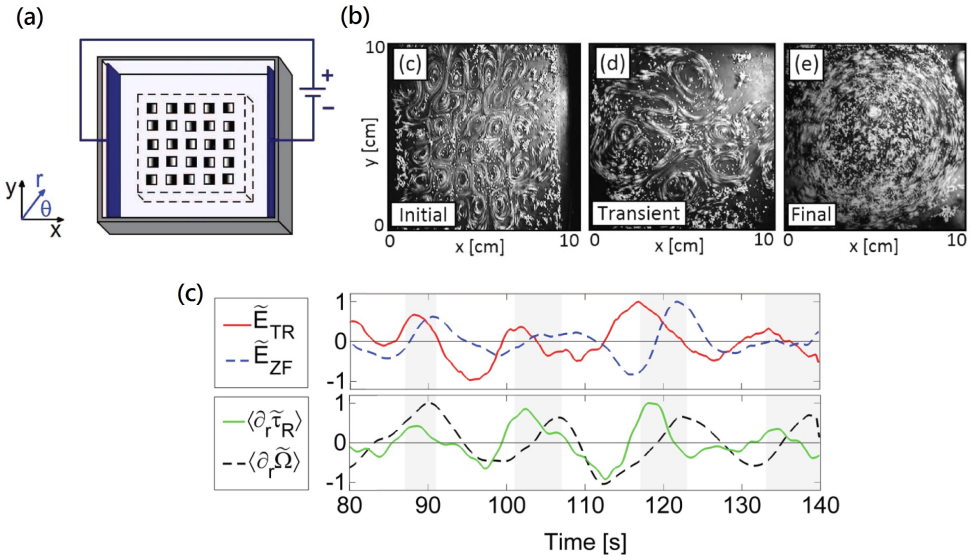

Figure 10.18: **Zonal flow and Predator-prey dynamics in the electroconvection experiment**. (a) Sketch of the experimental setup. Ionic fluid placed above randomly-oriented magnets is driven by an electric field. (b) Snapshots at sequential time show the emergence of the zonal flow. (c) The dynamics of the zonal flow energy and the turbulence energy shows predator-prey oscillations with a $\pi/2$ phase shift of the zonal flow behind turbulence, indicating that the zonal flow behaves as the "predator" of turbulence. Radial gradient of Reynolds stress and the shear fluctuations are also in accordance with this interpretation. Figures are taken from [300].

10.10 Directed percolation in other turbulent systems

The predator-prey dynamics uncovered here at the onset of turbulence is in the universality class of directed percolation (DP). Predator-prey dynamics requires interactions between long-wavelength zonal flows and small scale turbulence. Wherever these fluids can co-exit, the conditions are appropriate for transitional behavior in the DP universality class. In the section, we briefly review those experimental geometries other than pipe where zonal flow/turbulence can arise, and where there is evidence for the DP universality class.

10.10.1 DP in Taylor-Couette flow

Recently, Lemoult *et al.* performed an experiment in quenched Couette flow with large aspect ratio that was designed to observe critical dynamics at much smaller Re than in pipe flow [308]. The experiment was performed in a Taylor-Couette flow with static inner cylinder and rotating outer cylinder. Taylor-Couette systems have a rich phase diagram as a function of the inner and outer cylinder rotation rate. The most relevant phase for the purposes of this work is the state where the inner cylinder is stationary and only the outer cylinder rotates. In this situation the laminar solid body flow, known as Couette flow, is linearly

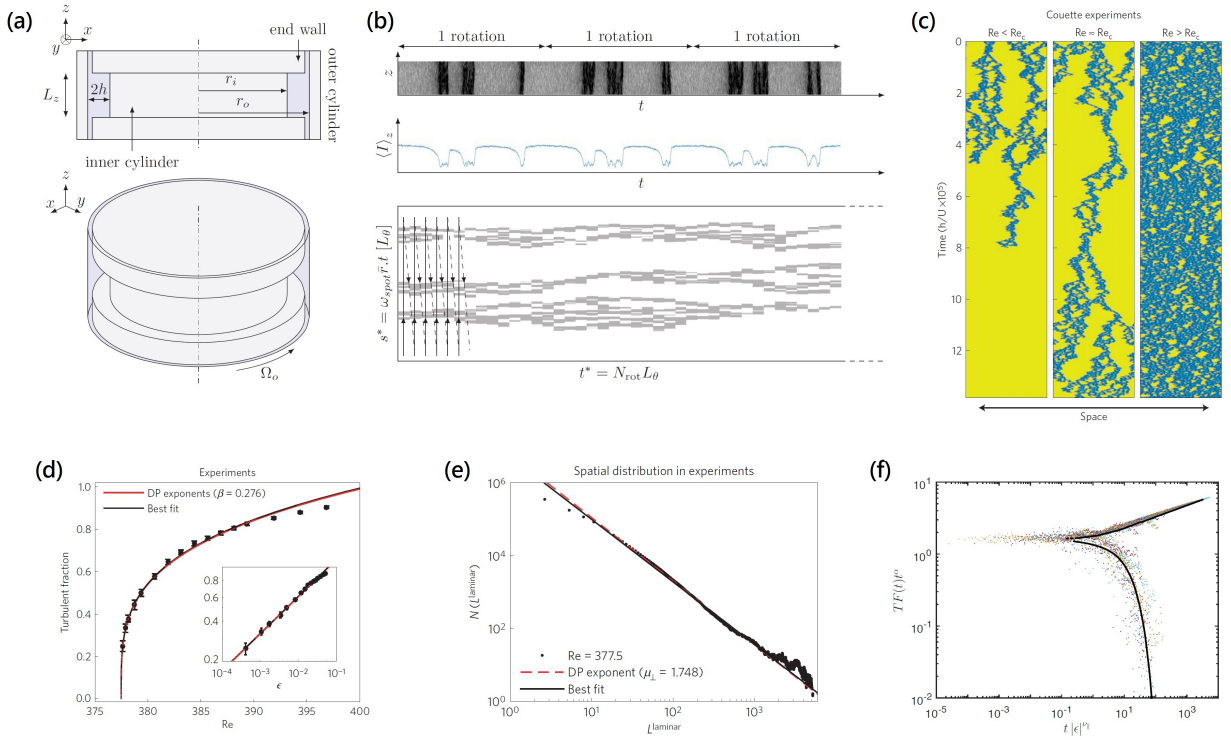

Figure 10.19: **Directed percolation in turbulent Taylor-Couette flow**. (a) Experimental apparautus with ultra-narrow large aspect ratio Taylor-Couette flow. (b) Turbulent patches extend and branch when the outer cylinder rotates, forming DP-like trajectories. (c) Time evolution of turbulent patches show transitional patterns like DP when Re changes. At Re $\gtrsim$ Re$_c$, (d) scaling of the measured turbulent fraction in (c) as a function of Re is comparable with DP scaling, and (e) the distribution of the laminar length interval can be fitted with 1+1 DP prediction. (f) Data collapse of the dynamical scaling of turbulent fraction indicates the DP universality class. Figures are taken from [308].

stable, analogous to the Hagen-Poiseuille flow in pipes. In this geometry, then, Taylor vortices (spanwise vortex rolls)are suppressed, and a zonal flow can develop in the plane defined by the cylinder axis and the radial direction. The experimental setup has extremely large aspect ratio with ultra-narrow gap between the inner and out cylinder, effectively making the fluid into a quasi-one dimensional long band flow (Fig. 10.19 (a)). To measure the transitional behavior, the experiment started with fully-developed turbulence at high Re which was later reduced down to near Re$_c$ to quench the turbulence. This protocol prevents hysteresis associated with the subcritical bifurcation to turbulence. The flow forms vertical turbulent patches that extend between the top and bottom of the cylinders and may branch. The recorded flow pattern at different times were stacked together to recover the whole configuration, which displays percolation-like trajectories as shown in Fig. 10.19 (b). For comparison, we show a similar graph made with our strip geometry predator-prey system.

The turbulent fraction and the distribution of laminar length intervals at $\mathrm{Re} \gtrsim \mathrm{Re}_c$ were found to scale as power-laws with (1+1)-dimensional DP critical exponents as in Fig. 10.19 (d) and (e). In addition, the dynamical scaling of turbulent fraction was found to agree with DP scaling and even exhibits data collapse when fitted with the known DP universal scaling function (Fig. 10.19 (f)). The authors also found consistency with direct numerical simulations [308].

This experiment on Taylor-Couette flow and another recent experiment on channel flow which we introduce below are the first realization of DP in "natural systems". Previously DP had been documented only in laboratory systems specially designed to mimic the DP dynamics in an analogue form [268, 309].

10.10.2 DP in channel flow

Another recent experiment on transitional turbulence was presented by Sano and Tamai in channel flow [235]. As shown in Fig. 10.20, the authors observed transitions to turbulence when Re becomes larger than an estimated $\mathrm{Re}_c = 830$. When Re increases, the flow forms localized turbulent spots, that are the analogy of puffs in pipe flow, traveling downstream. At $\mathrm{Re} < \mathrm{Re}_c$, turbulent spots decay eventually. When $\mathrm{Re} > \mathrm{Re}_c$, turbulent spots split and extend, and the flow develops patterns with spatiotemporal intermittency. As Re becomes larger, the turbulent cluster spreads and sustains (Fig. 10.20 (b)). The scaling of turbulent fraction and the distribution of laminar length intervals were found to be fitted to 2+1 DP scaling within some range (Fig. 10.20 (c) and (d)). The universal scaling function of the cumulative distribution of laminar length intervals exhibits data collapse, which is a sign of universality [235]. Concerns have been raised (B. Hof *et al.*, private communication) that (1) it seems that it is possible to get turbulence below the value of Re_c reported in this experiment (down to $\mathrm{Re} \sim 750$); (2) the scaling ranges in turbulent fraction and laminar intervals seem to be relatively short, which is probably due to (1). Nevertheless, the universal scaling function appears to span two decades of scaling, so it is possible that the correct universal scaling function can be obtained in terms of $(\mathrm{Re} - \mathrm{Re}_c)/\mathrm{Re}_c$, despite the fact that Re_c is not accurately placed. The cause of the elevated value of Re_c is likely to be the injection method.

10.10.3 DP in the Navier-Stokes equations

Given the remarkable claim that the Navier-Stokes equations can exhibit behavior characteristic of interacting particles on a lattice, it is important to have a direct observation from DNS. To this end, a shear plane flow with slip-free boundaries was specifically designed to reach a huge system size in order to search for DP scaling [287]. The calculation was a mode truncated shear flow with slip-free boundary condition, known as Waleffe flow. The simulation showed a longer range of (1+1)-dimensional DP scaling compared

with [308] and universal data collapse in the large system domain [287]. Moreover, they showed that in a small system size the scaling is broken, and the transition becomes discontinuous, as reported in an earlier smaller simulation study on plane Couette flow [310]. The authors also separately performed a simulation on a coupled map lattice model and found that at small system sizes, a continuous DP transition appears artifactually to exhibit a discontinuous transition.

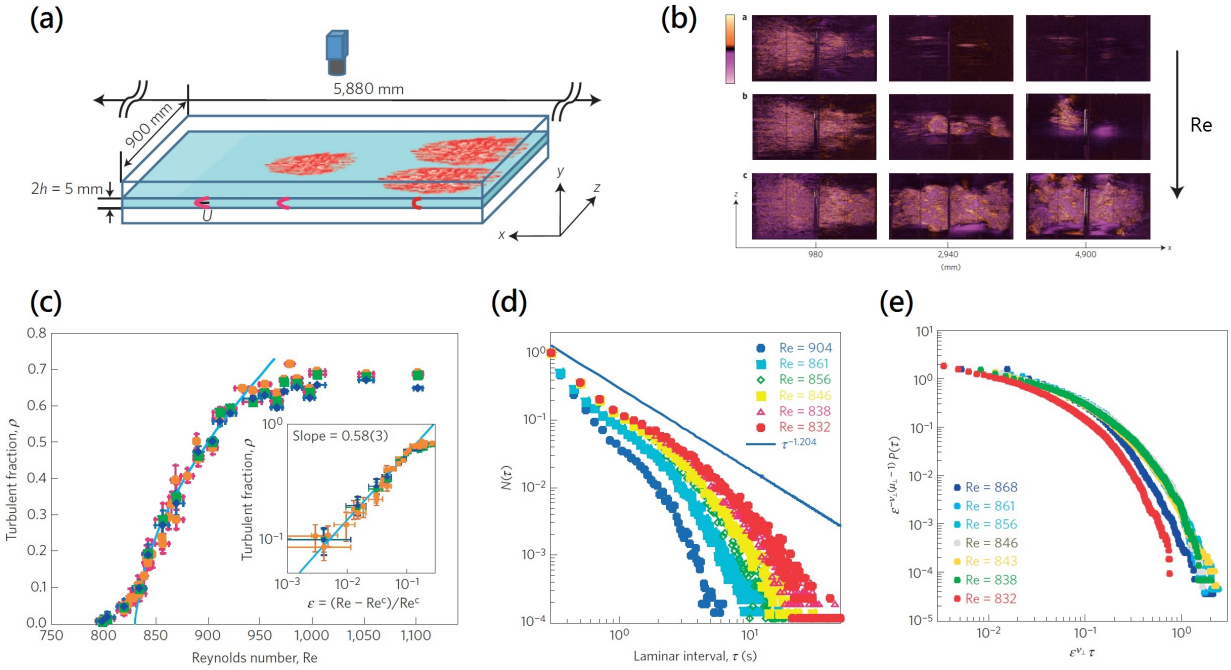

Figure 10.20: **Directed percolation in channel flow**. (a) Experimental setup for channel flow. The flow is disturbed constantly at the origin $x = 0$. (b) Time evolution (left to right) of normalized density of flow configuration at small to large Re (top to bottom row). When Re is small (top row, Re=798), the flow develps into separated spots which propagate but eventually decay; when Re $>$ Re$_c$ $=$ 830 (middle row, Re=842), spots split and extend, and the flow becomes turbulent and displays spatiotemporal intermittency. At larger Re (bottom row, Re=1005), the turbulent state always sustains. (c) Scaling of the measured turbulent fraction as a function of Re at different position x. The inset shows log-log plot fitted with the (2+1)-dimensional DP exponent. (d) Distribution of laminar length intervals at different Re and fitted with the (2+1)-dimensional DP exponent. (e) The universal scaling function of the cumulative distribution of the laminar length interval show data collapse that indicates DP universality class. Figures are taken from [235].

10.11 Discussion

10.11.1 "Turbulence" in decaying puffs

Our work on pipe flow, and the above studies in various transitional turbulence systems, show evidence of predator-prey dynamics from the activation-inhibition interactions between an emergent large-scale zonal flow and small-scale turbulent fluctuations. In these systems, the onset of the coexisting laminar and turbulent flows corresponds to the coexistence between prey and predator. This occurs when the predation rate or prey birth rate are large enough to prevent extinction. Since the transition in predator-prey belongs to the DP universality class through a mathematical mapping to Reggeon theory, the laminar-turbulent transition will also be, in general, in the DP universality class, which supports Pomeau's original conjecture on the pipe flow transition first observed in Reynolds' 1883 experiments.

Nevertheless, there is still a debate about whether the DP transition, with such simple structure, can apply to metastable puffs. Especially, Pomeau himself recently suggested an alternative to his original insight; he speculated that the transitions observed in experiments might not be described by DP, because the flow there is not unstable enough to be classified as turbulence, and hence might just bifurcate from laminar flow into a stable, non-turbulent wave state [286]. If true, this would imply that since fully-developed turbulence definitely occurs as $\mathrm{Re} \to \infty$, the transitions to metastable puffs and spatiotemporal intermittency at relatively low Re would not be the real phase transition to turbulence. It would also mean that another transition or crossover could occur as $\mathrm{Re} \to \infty$, perhaps with fully-developed turbulence.

A recent experiment in pipe flow provided an interesting clue that might clarify this debate. Cerbus *et al.* have measured the friction factor and energy spectra of metastable puffs and slugs in pipe flow [311]. Interestingly, it was found that the energy spectrum can be collapsed following Kolmogorov's first similarity hypothesis [228] even with $\mathrm{Re} \sim 800$, onto the same universal scaling curve associated with high Re turbulence. Moreover, the friction factor is always a composition of laminar and turbulent sector contributions [311]. This implies that the transitional turbulence discussed in this thesis is statistically the same as fully-developed turbulence [311].

10.11.2 Zonal flows, mean flows and self-sustaining cycles: What's the difference?

Even though the zonal flow is a large-scale long-wavelength mode, it is distinct from the mean flow. As described earlier in this chapter, the zonal flow is an emergent mode in the azimuthal direction and is not generated by pressure. In contrast, the mean flow is driven by pressure and propagates longitudinally.

Other studies have paid attention to longitudinal modes such as the mean flow, since they are contributed by pressure driving and thus have dominant magnitude. Indeed, a Kelvin-Helmoholtz instability near the wall is responsible for feeding energy into the turbulent puffs in pipe flow [312].

Another activation-inhibition type of model is the self-sustaining cycle [313, 312]. The self-sustaining cycle also considers nonlinear interactions between streamwise vortices, streaks and fluctuations [313, 312]. The model has been regarded as an explanation for the traveling wave found in simulations of pipe flow [314]. One question may arise: Since the interactions between turbulence and longitudinal modes have larger magnitude than the interaction between turbulence and the zonal flow, should the former dominate the transitional behavior at the onset of turbulence?

One loophole is that this argument has an implicit assumption that small perturbations always behave regularly. However, even if a perturbation is small, it can lead to significant changes when it is a singular perturbation. We claim that the emergence of the zonal flow and its interactions with turbulence give rise to the singularities associated mathematically with the phase transition of predator-prey dynamics and the accompanying divergences of DP, even though other dynamical modes contribute more to the total energy.

This is analogous to the situation in condensed matter systems, such as superconductors, where the singular part of the heat capacity is due to electron-electron interaction, and may be a very small fraction of the total heat capacity arising from phonon and electron contributions [315].

10.12 Further experimental predictions

The theoretical work described in this thesis makes a number of predictions in addition to detailed critical behavior. in particular, our work associates the transition with the emergence in the transitional region of zonal flows that interact with the nascent small-scale turbulence. These are observable in some systems, and have specific consequences, which we briefly outline here.

10.12.1 Rotating pipe flow

One special configuration that might be a candidate to test the effect of zonal flow is a rotating pipe. By rotating the pipe flow, turbulent fluctuations should be forced to be more aligned due to the centrifugal force. Therefore the "predation pressure" from the zonal flow on turbulence may be more intense. The effect can also depend on the condition of the flow. Rotation can initiate perturbations on laminar flow. Once the turbulent fluctuations appear, they can be suppressed more by the rotating shear. The net effect is that we would expect the transitional Re would be increased due to this effect. Indeed experiments on

axially-rotating pipes [316] are consistent with this prediction. A recent study on pipe flow designed with boundary perturbations that inhibit turbulence generation, which has similar effect as the zonal flow, also showed relaminarization effect on turbulence [317].

Another interesting setup is the annular pipe flow, where fluid flows between two uniaxial pipes with tunable radius ratio [318, 319]. With additional shear from boundaries, the effect of the zonal flow is expected to be enhanced.

10.12.2 Zonal flow in channel flow

As mentioned previously, the turbulent spots observed in channel flow [43, 44, 235] and plane Couette flow [244] are the analogy of puffs in pipe flow. This naturally leads us to ask whether and how to observe the corresponding zonal flow in these systems. In particular, an experiment in channel flow studied by Lemoult *et al.* [43, 44] reported large-scale flows around turbulent spots, whose span-wise and wall-normal component may be a candidate of the zonal flow. Since the plane setup is not as symmetric as a pipe, zonal flows in plane flows will have components in streamwise direction, and the associated Landau theory will be more complicated than the one outlined here for pipe flow.

10.13 Conclusion

In summary, we used DNS to identify the important collective modes at the onset of turbulence—the predator-prey modes—and then wrote down the simplest minimal stochastic model to account for these observations. This model *predicts* without using the Navier-Stokes equations the puff lifetime and splitting behavior observed in experiment. This approach is a precise parallel to that used in the conventional theory of phase transitions, where one builds a Landau theory, a coarse-grained (or effective) theory, using symmetry principles (see Fig. 10.21). This intermediate level description can then be used as a starting point for renormalization group analysis to compute the critical behavior. In this case, however, the statistical description arises from non-equilibrium statistical mechanics, as the predator-prey equations do not obey detailed balance.

We have shown that directed percolation arises in transitional turbulence due to the appearance of collective modes near criticality, whose fluctuations exhibit the characteristics of stochastic predator-prey dynamics near the collapse of an ecosystem from its coexistent state. Signs of directed percolation in recent experimental and numerical studies in various geometries support our results. We also showed that both turbulence and predator-prey ecosystem criticality manifest super-exponential scaling laws that are probably

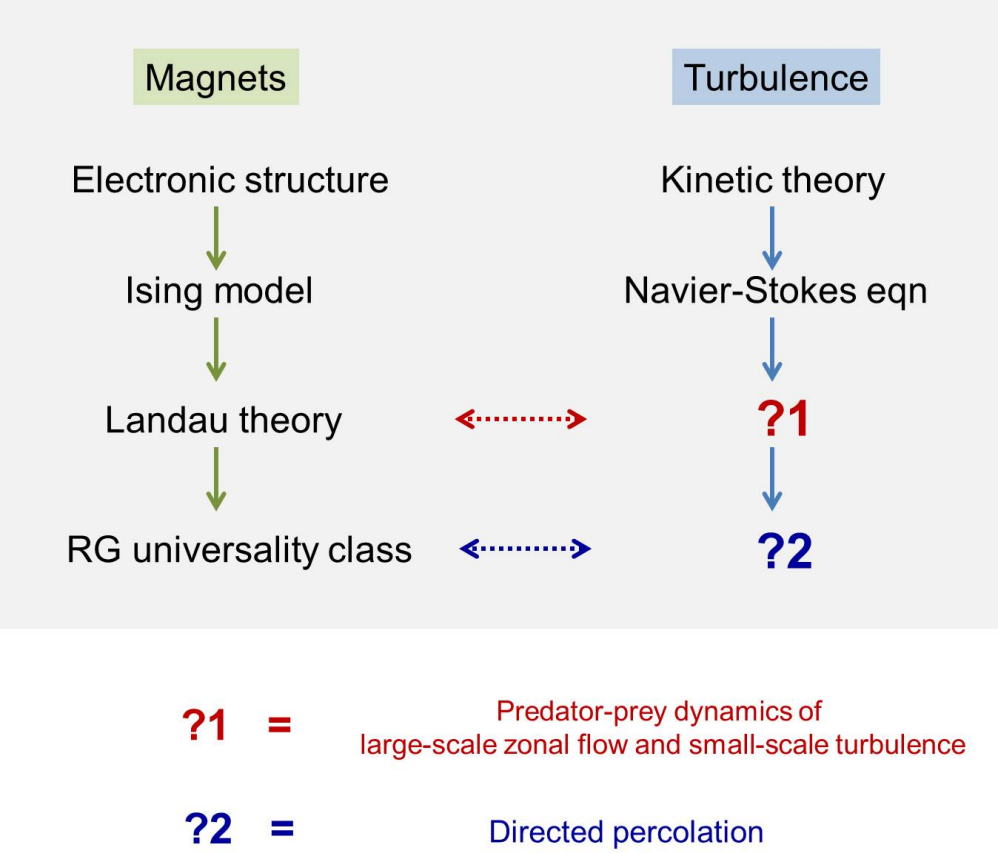

Figure 10.21: **Summary of the logic of modeling the laminar-turbulent phase transition.** Compared with the corresponding steps for the conventional ferromagnetic transition of an Ising model.

related to extreme value statistics, and such generic scaling may reflect an unprecedented connection between transitions involving absorbing states, predator-prey extinction, directed percolation and extreme value statistics. Our approach is thus a precise parallel to the way in which phase transitions are understood in condensed matter physics, and shows that concepts of universality and effective theories are applicable to the laminar-turbulence transition.

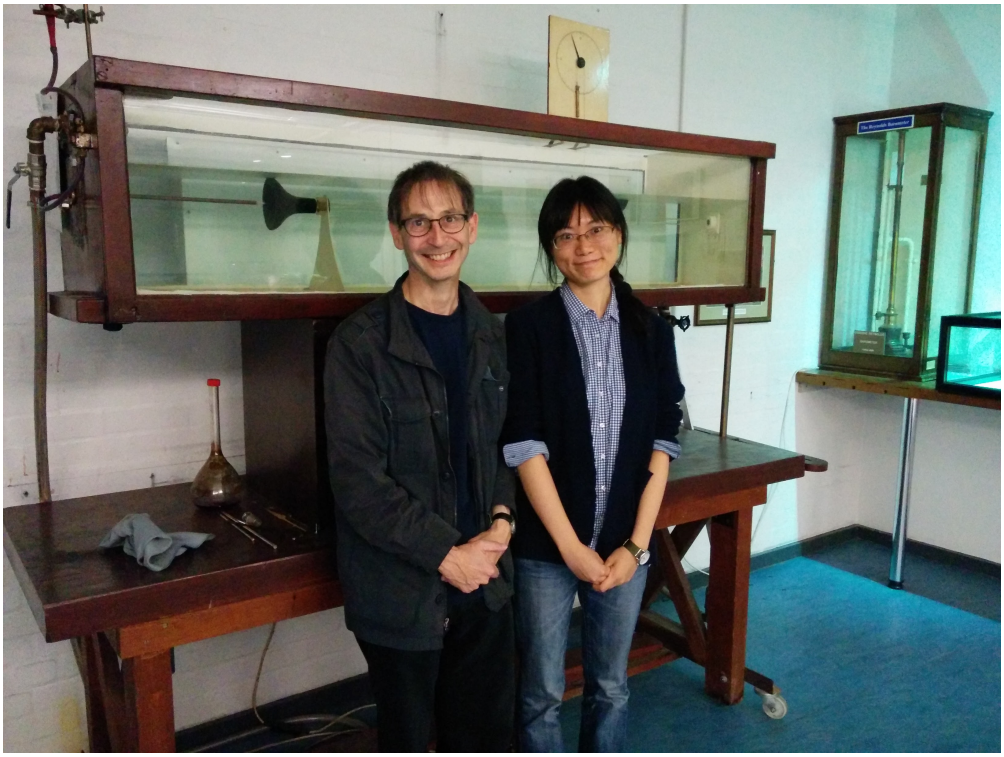

Figure 10.22: **Reynolds' original apparatus on the display in Manchester University.**

Chapter 11

Universal finite size scaling in transitional turbulence and directed percolation

11.1 Overview

Experiments on transitional turbulence in pipe flow have been interpreted as revealing that turbulence is a transient metastable state since the measured mean lifetime of turbulence puffs does not diverge asymptotically at a critical Reynolds number [35]. Instead, exquisitely sensitive measurements reveal that the lifetime scales with Reynolds number in a super-exponential way that is reminiscent of extreme value statistics [258, 41]. On the other hand, simulations and experiments in Taylor-Couette flow [308] and channel flow [235] exhibit directed percolation type scaling phenomena near a well-defined transition. Theoretically, this universality class arises from the interplay between small-scale turbulence and a large-scale collective zonal flow, which exhibit predator-prey behavior [24]. Nevertheless, it still remains a paradox as to why asymptotically divergent behavior is not observed, even though phase transition properties such as directed percolation are present in turbulence. Using directed percolation as a model system, we investigate the relation between power law critical behavior and extreme value statistics, and show that the paradox may be resolved by considering crossover from the directed percolation critical fixed point to the Fisher-Tippett-Gumbel fixed point, describing extreme value statistics arising from finite-size effects. Nevertheless, another contradiction emerges in this argument: the condition of identical and independently distributed random variables, a necessary but not sufficient condition for the applicability of standard extreme value statistics corresponding to Fisher-Tippett-Gumbel fixed point breaks down near the DP critical point, because the spatial correlation length must become of order the pipe radius, and the transverse fluctuations will become highly correlated, not independent. What happens to the statistics in this case? It turns out that in the limit where the correlation length saturates the system size, there is a crossover to a strongly correlated fixed point, for which a variety of exact and asymptotic results are known. Remarkably, the distribution of the sum of correlated random variables is captured by a universal finite-size scaling function or generalized extreme value statistics, originally identified by Bramwell, Holdsworth and Pinton (BHP) in the context of the fluctuations in the 2D XY model, in the spin wave approximation [320].

We will show that our simulations of 1+1 dimensional DP show clear evidence for the presence of the BHP distribution, and point to a picture of the decay of turbulence proceeding through nucleation phenomena in the strongly-correlated regime.

We also verify these phenomena in stochastic individual-level simulations of the minimal predator-prey ecosystem, which recapitulate the scaling behavior of the pipe flow laminar-turbulence transition and predicts the directed percolation universality class [24]. We discuss how our argument can be testified in experiments and apply similar considerations to a broader class of transitional turbulent systems.

The discovery of the universal finite-size scaling regime in our models of turbulence, DP and even predator-prey dynamics, prompts us to revisit the argument originally made for the explanation of the super-exponential behavior in pipe flow as being a manifestation of the Fisher-Tippett-Gumbel extreme value universality class [58]. Revising that argument to take into account the strongly-correlated BHP fixed point turns out to not change anything essential about the result, but puts it on a logically consistent basis. In summary, this work explains how it is that power-law and super-exponential behavior can coexist in the same datasets.

11.2 Is turbulence a long-lived metastable state?

It has been a long-stand debate about whether the turbulent state is transient or not, based on the measurements of its lifetime near transition. It has been reported in pipe flow experiments and direct numerical simulations that the mean lifetime of turbulent puffs scales as an exponential function of Re [35]; later refinements of the experimental technique, and the extension to the puff-splitting regime showed that decay and splitting timescales could be well-described by a super-exponential function of Re [258, 41] (although other functional forms such as stretched exponential could not be ruled out). In other words, the data taken at face value indicate that the lifetime never diverges asymptotically as a particular critical Reynolds number is approached, as would be the case in typical phase transition phenomena. Therefore turbulence could be argued to be a long-lived metastable state [35], with a pragmatic critical Re identified as the crossing of the decay and splitting lifetime curves.

On the other hand, a different point of view regards turbulence as a non-equilibrium phase transition problem. This aspect is consistent with Pomeau's suggestion [54], followed by further model studies showing quantitatively that the laminar-turbulence transition in pipes is similar to directed percolation (DP), the well-known universality class of non-equilibrium systems with an absorbing state [53, 56]. An analytic approach to deriving this mapping was attempted by using numerical simulations to identify the important

modes of turbulence near the transition; the simplified Landau-style description thus obtained exhibited activation/inhibition behavior analogous to that in a predator-prey ecosystem, which is known to be in the DP universality class [24, 288]. At the same time, DP scaling behavior was reported for Taylor-Couette flows [308] and channel flows [235]. Thus, at varying levels of precision and resolution, there is good evidence that the laminar-turbulence transition in several geometries is a non-equilibrium phase transition in the DP universality class.

A third perspective is that the super-exponential scaling of the puff decay and splitting lifetimes arises from the Fisher-Tippett distribution [275] (sometimes known as the Gumbel distribution [276, 277]), describing extreme value statistics. It is sometimes known as the Fisher-Tippett-Gumbel distribution, or Gumbel distribution for short. Extreme value statistics enters into the problem as a reflection of a threshold for energy fluctuations, which when exceeded, causes the turbulent puff to decay [58]. In the context of DP, extreme value statistics arises because the extinction of turbulence corresponds to the lifetime of the longest percolation path.

Nevertheless, it still remains a paradox as to why asymptotically divergent behavior is apparently missing from the decay and splitting timescale variation with Reynolds number, while other phase transition properties characteristic of a sharp DP transition are exhibited in turbulence data.

The goal of this chapter is to resolve this paradox, by showing how both extreme value statistics and conventional dynamic critical scaling can be exhibited at the same time in directed percolation, predator-prey models, and experiments on turbulent systems.

11.3 Extreme value statistics

Let us briefly recall some basic results from the statistics of extreme values.

Suppose N independent, identically-distributed (i.i.d.) random numbers, $\{x_1, x_2, ..., x_i, ..., x_N\}$ are generated from some commonly encountered distribution, such as the normal distribution, which decays faster than exponential at infinity. The probability density of the largest random number, $x_{\max}$, follows the Fisher-Tippet Type I (or so-called Gumbel) distribution:

$$P(x_{\max}) = \frac{1}{\beta} e^{-(x-\mu)/\beta} e^{-e^{-(x-\mu)/\beta}}, \tag{11.1}$$

where μ and β are parameters, often referred to as the location and scale respectively, that can be calculated

in terms of the means and standard deviations of the x_i. The cumulative distribution is simply

$$G(y) = Prob(x_{\max} < y) = \int_{-\infty}^{y} P(x_{\max}) dx_{\max} = e^{-e^{-(y-\mu)/\beta}}. \tag{11.2}$$

which has an exponential-like tail at large x. Therefore, the cumulative distribution can be approximately presented as

$$G(y) \sim 1 - e^{-y/\zeta}, \tag{11.3}$$

where ζ will be referred to as the correlation scale.

11.4 Survival probability and extreme value statistics in DP

In DP when the percolating probability $p < p_c$, the percolation clusters terminate within a finite time. For example, in $(1+1)$-dimensional bond DP, the percolation path is in the $t-$direction (defined as the parallel direction), and the longest path is analogous to the largest random number above. Therefore, the statistics of the longest path/decay time in DP, $t_{\rm d}$, is expected to follow the Fisher-Tippet distribution. Then the probability that the longest percolation path survives at time t is the complementary cumulative distribution function of Eq. (11.2):

$$P(t_{\rm d} > t) = 1 - P(t_{\rm d} < t) = 1 - e^{-e^{-(t-\mu_{\rm d})/\beta_{\rm d}}}, \tag{11.4}$$

which also has an exponential-like tail. It is important to emphasize that in reaching this conclusion, we assumed that different percolation trees, descending down from an initial random configuration of sites, were independent.

The survival probability in turbulence measurements is usually fitted by an exponential form:

$$P(t_{\rm d} > t) \equiv e^{-(t-t_0)/\tau_{\rm d}}, \tag{11.5}$$

where $\tau_{\rm d}$ is defined as the decay rate or the so-called *mean lifetime*. Fig. 11.1 shows the comparison for i.i.d. random variables satisfying the Fisher-Tippett distribution between the exact form of the survival probability in Eq. (11.4) and an assumed exponential form Eq. (11.5). Apart from a small region near the origin, the exponential decay fits extremely well, and is for practical purposes indistinguishable from the actual super-exponential behavior plotted. The key point is that, if the actual lifetime statistics were indeed

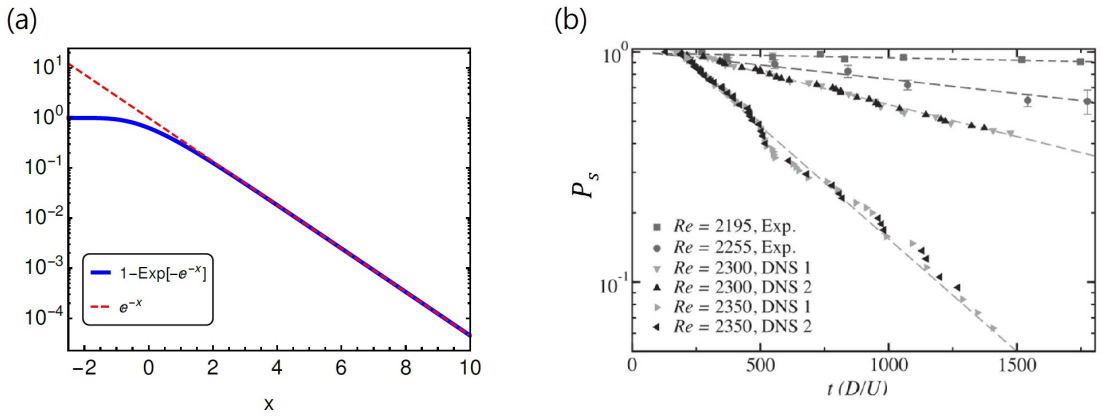

Figure 11.1: **Survival probability as the extreme value distribution**. (a) Comparison between the complementary cumulative distribution for the maximum value given by the Fisher-Tippett distribution in Eq. (11.4) and the exponential form. The two functions are similar at the tail. (b) The survival probability of a single puff in the pipe flow experiments. Note the plateau at small time is reminiscent of the extreme value distribution in (a). Figure (b) is taken from [308].

governed by DP, and thus followed Eq. (11.4), the data would be interpreted as being a simple exponential decay Eq. (11.5) characteristic of a memoryless process [258, 41].

11.5 Non-splitting probability and extreme value statistics in DP

To explain how extreme value statistics enter into the description of the puff-splitting regime, we need to identify a quantity whose properties are analogous to independent random numbers and which reflect the physical aspects of splitting. When $p > p_c$, DP clusters are dense, with fluctuations that can be thought of as holes. Near p_c, these fluctuations are correlated, and the hole dimensions scale with the correlation lengths $\xi_\parallel$ and $\xi_\perp$ respectively in the space-like and time-like directions. If we make a particle-hole transformation on the DP clusters, we obtain the inverse picture, in which the DP clusters are the spatial background on which is superimposed a dilute gas of holes, which we will regard as independent, at least as long as the correlation lengths are smaller than the mean distance between the clusters, a condition that will be valid not too close to p_c, but for $p > p_c$.

Splitting events in transitional pipe flows are defined to have occurred only when the split puff has attained a certain threshold distance from the original puff, so that the two are considered independent. Splitting events in DP clusters are similarly defined by two branches being considered to have attained a certain threshold distance from each other, which means that the size of the hole bounded by those two branches should on average be larger than the threshold.

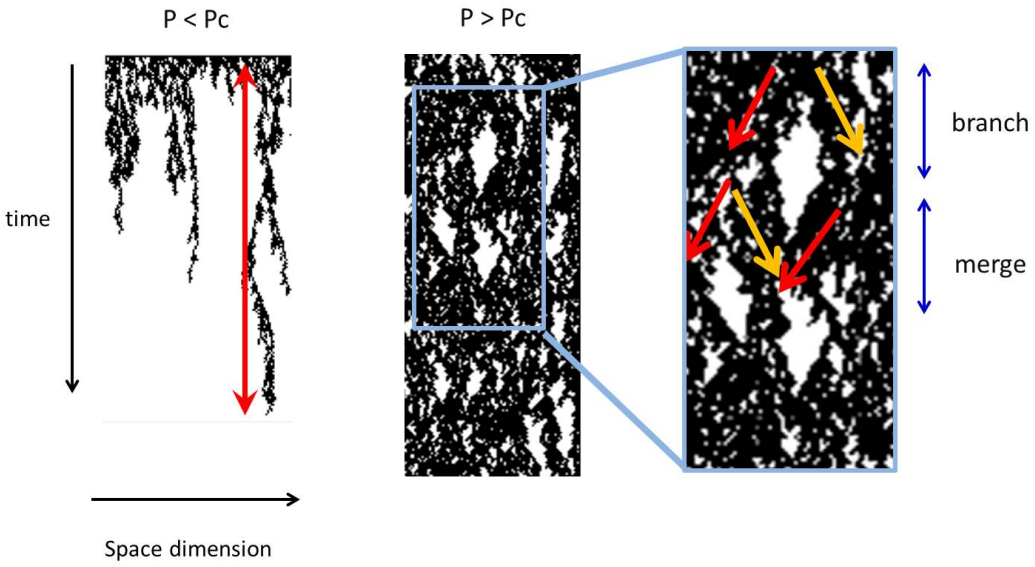

Figure 11.2: Bond directed percolation in $1+1$ dimension, with time running horizontally. The width $L_x = 100$ and $p = 0.67$ (i.e. $p > p_c$). The holes occur on a range of length scales, but are well-defined with the main cluster splitting events and subsequent merging of clusters occurring around the largest holes. The small holes correspond to very short-lived puff-splitting and re-merging and do not fulfill the requirement that the puffs separate beyond a certain threshold distance.

In DP (and also in turbulence in fact), holes are formed by two processes: first a branching and secondly a subsequent merging event between two cluster branches, i.e. one cluster divides outwards and the two branches percolate inward to coagulate. Since the right branch of a merging event is also the left branch of another splitting event on its right side, the average time it takes (i.e. the average length in time direction) for one cluster to split into two branches is roughly the same as the time for two branches to merge. Therefore, the splitting time t_{split} is roughly half the size of the holes in the time-like direction, ℓ_t. In DP the size of holes fluctuate in time and space, with a power law probability distribution near the critical point. Small holes correspond to puff-splitting events that very quickly anneal and reform. Only large holes correspond to puffs that split and separate far enough that they can be considered independent puffs, as shown in Fig. (11.2). Thus, for a puff-splitting event that exceeds the threshold by which the event is defined, the corresponding hole must also be above a certain threshold. Conversely, the probability that the maximum hole size in the time-like direction ℓ_{max} does not exceed a critical threshold ℓ_c is analogous to the probability that a splitting event has not yet occurred (in the context of turbulent pipe flows). In other words, the survival probability $P_s(t)$ measured in experiments/numerical simulations [41] that a puff has not yet split up to time t is equal to the probability that the time-like dimension of the largest holes is greater than t.

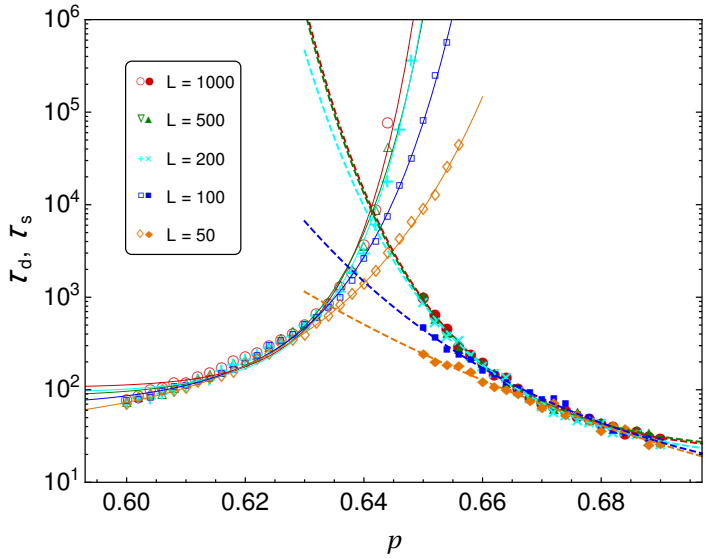

Figure 11.3: Bond directed percolation in 1+1 dimensions. Measurements of the decay time τ_d and splitting time τ_s versus percolation probability p for various transverse system sizes L. The fitted curves are of the form $\exp[\exp(ap+b)+c]$.

This is just one minus the cumulative probability distribution for the largest holes:

$$P(\ell_{\max} > t) = 1 - e^{-e^{-(t-\mu_s)/\beta_s}} \tag{11.6}$$

where μ_s and β_s are the location and scale of the extreme value distribution for the splitting events. Again, this probability is found to resemble a pure exponential in the experimental measurements, and thus we measured the splitting rate for the exponential decay function, in the same way as the decay rate in the decay case. The summary of these results from simulations of (1+1)-dimensional bond DP is shown in Fig. (11.3), where the decay time and splitting time exhibit super-exponential behavior, for a range of system sizes.

11.6 Finite-size effect in the scaling of decay rate

With this figure, we have shown how DP recapitulates the main stylized facts of decaying and splitting in the laminar-turbulence transition, as they were known until very recently. Nevertheless, when $p \sim p_c$, DP clusters will survive for a long time and probably will not have decayed when our simulations reach their maximum time, even though if they could be run indefinitely, the system would eventually go to the absorbing state as $t \to \infty$. In addition, the assumption that we can apply extreme value statistics in previous

sections cannot generally be true, because the stochastic process of DP has a natural correlation length in the transverse (space-like) direction. Far from the critical region, this correlation length would be expected to be a few lattice sites or so. However, near the critical point, the transverse correlation length $\xi_\perp$ diverges, and thus the sites become highly correlated. As a result, there is a reduction in the number of effective degrees of freedom, represented by $L_x/\xi_\perp$, where L_x is the system size. When $p \to p_c$, $L_x/\xi_\perp \to 0$ and the clusters become correlated. In this limit, the extreme value theorem does not apply, and the lifetime is not well captured by extreme value statistics. Moreover, since clusters become more correlated due to finite size effects, we expect that $p_c = p_c(L_x)$ is a decreasing function of L_x, and for finite system size $p_c(L_x) > p_c^\infty \equiv p_c(L_x \to \infty)$, and the critical scaling regime will be obscured, due to finite-size effects.

11.6.1 Scaling of decay rate in different system size

With these considerations, to test the validity of extreme value statistics in the lifetime statistics near the DP transition, we performed (1+1)-dimensional DP simulations in large system sizes (up to 10^4 sites in the x-direction) for very long times. Unless otherwise stated below, we allowed all simulations to run until extinction occurred. The statistics of lifetimes was recorded, and the decay rate τ_d as a function of control parameter p was calculated by fitting the survival probability with Eq. (11.5). The simulation results for system sizes $L_x = 10000, 1000, 100$ are shown in Fig. 11.4, Fig. 11.5 and Fig. 11.6 respectively.

We found that for the largest system sizes ($L_x = 10000$ and 1000), τ_d diverges in a form that is very well-captured as a power-law form (Fig. 11.4 (a)), when plotted in several different ways. This stands in contrast to what we observed at smaller system size ($L_x = 100$, Fig. 11.6 (a)). To check if the scaling behavior shows critical scaling like DP, τ_d was replotted by rescaling with the (1+1)-dimensional DP critical exponent $\nu_\parallel$, as shown in the inset in Fig. 11.4 (a), Fig. 11.5 (a) and Fig. 11.6 (a). For τ_d in $L_x = 10000$ and 1000, the data show good agreement with DP scaling, remarkably even down to small p. However, for $L_x = 100$, the power-law scaling only fits better below p_c^∞, while τ_d scales more like a super-exponential near and even above p_c^∞. We note that since the system is finite, the effective p_c depends on L_x and so it is possible for $p > p_c^\infty$.

11.6.2 Survival probability in different system size

How is this behavior related to the assumed underlying extreme value statistics in lifetime statistics, discussed above? As mentioned earlier, extreme value statistics should break down as the correlation length $\xi_\perp \geq L_x$. Therefore, the larger is the system, the smaller is the range of p that shows the violation of the i.i.d. condition for the applicability of extreme value statistics. To see this explicitly, we zoom in near p_c, as shown in Fig.

11.4 (b) and Fig. 11.5 (b); it can be seen that $\tau_{\rm d}$ asymptotically fits super-exponential form when $p \to p_c$, and deviates from the power-law functional form that is seen for smaller p.

We specifically checked the distribution of lifetimes in different system sizes at different p. The distributions of lifetime $P(t_{\rm d})$ in the case where p is well away from p_c, e.g. $p = 0.58$ are shown in Fig. 11.4 (c) and Fig. 11.5 (c), and the corresponding complementary cumulative distributions (survival probabilities), $P_{\rm s}(t_{\rm d})$, are plotted in log scale in the inset respectively. As expected, the functional form of extreme value statistics agrees with the data. However, Fig. 11.4 (d), Fig. 11.5 (d) and 11.6 (d) show that at large p the numerical data significantly deviate from the super-exponential scaling in Eq. (11.1) and Eq. (11.2), and the functional form of extreme value statistics poorly fit the data.

It was the decade-long evidence for super-exponential scaling in the experimental observations of decay rate that seemed reminiscent of extreme value statistics [58]. So it is paradoxical that the extreme value statistics only correctly describe the probability distribution of lifetimes when the decay rate shows power-law critical scaling at intermediate p, yet fails when the decay rate display super-exponential scaling as $p \to p_c$! The argument of ref. [58] attributes the super-exponential scaling in the decay-rate to a super-exponential distribution in the probability distribution of lifetimes. Yet, the data show that the super-exponential scaling of the decay rate occurs near the critical point where the Fisher-Tippett-Gumbel distribution does not apply, and our measurements confirm that it does not apply there. This is the paradox that we address in the following sections. Specifically, we need to examine carefully how the universal Fisher-Tippett-Gumbel distribution can break down. We'll see first that there are two important, related considerations. First, near the critical point, the number of effective degrees of freedom is not infinite or large, but is of order unity. Second, this arises because the degrees of freedom become strongly correlated.

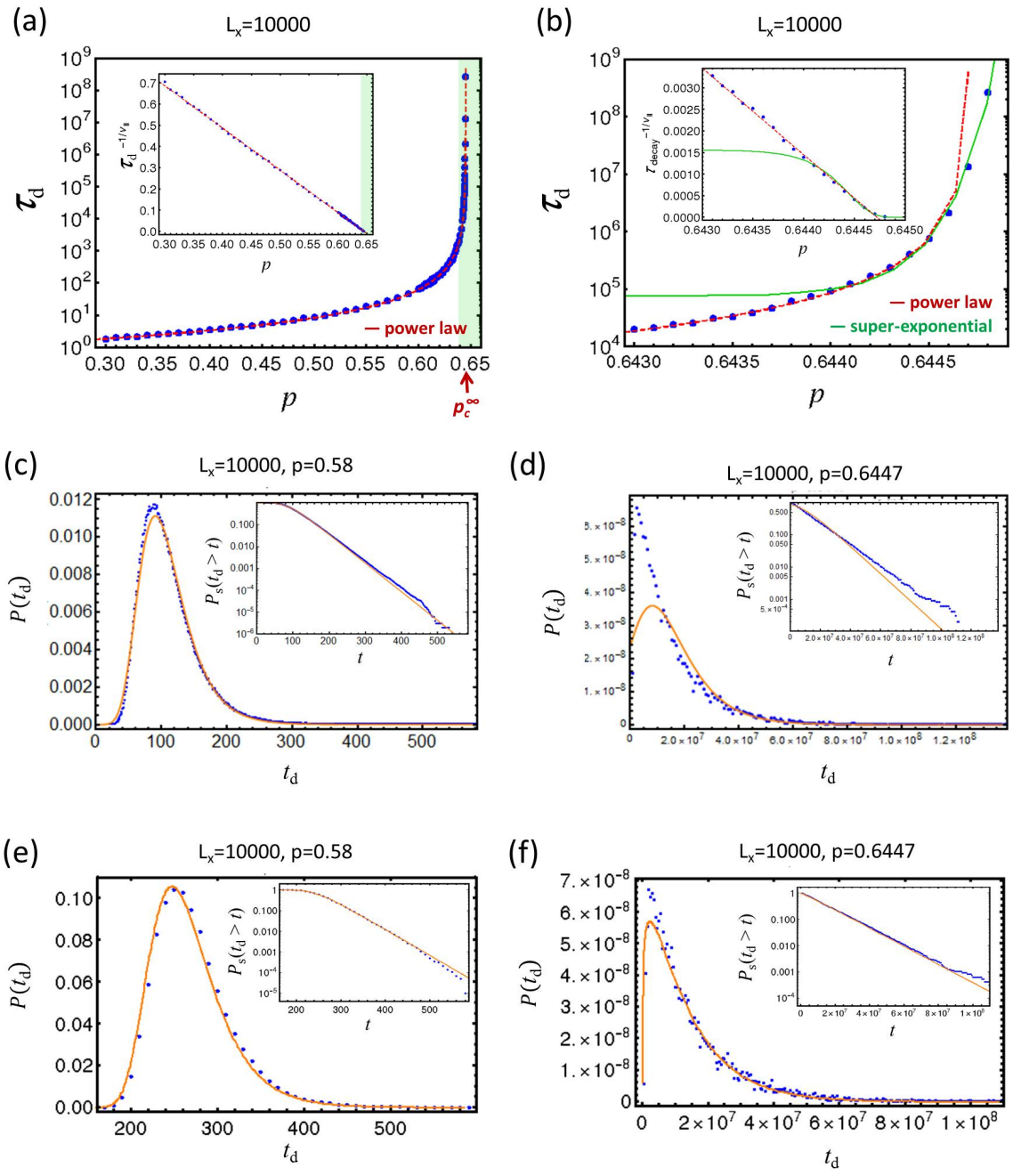

Figure 11.4: **(1+1)-dimensional directed percolation with L_x=10000**. (a) The decay rate $\tau_{\rm d}$ as a function of the percolation probability p. The inset plot shows the rescaled $\tau_{\rm d}$ with the DP critical exponent $\nu_\parallel$ follows a straight line, indicating that $\tau_{\rm d}$ has the power-law critical scaling of DP. The red arrow corresponds to the theoretical $p_c^\infty \approx 0.6447$ at infinite system size. (b) However, the zoom-in of green area in (a) shows that very near p_c, $\tau_{\rm d}$ does not diverge, and it can be fitted with a super-exponential function. (c) The distribution of lifetime $t_{\rm d}$ from DP simulations (blue dots) when p is far away from p_c ($p = 0.58$), which can be fitted by using Eq. (11.4) (orange). The inset shows the complementary cumulative distribution in log scale, which is interpreted as survival probability $P_{\rm s}$. (d) When $p \sim p_c$ ($p = 0.6447$), percolation clusters are correlated, and the data do not agree with the extreme value function. (e)(f) Same data as in (c)(d) but with a modified fitting with the finite-size extreme value statistics by using Eq. (11.10). The fitted parameters are $N \approx 1200$ and $\zeta = 34.8$ in (e) and $N = 1.18$ and $\zeta = 1.25 \times 10^7$ in (f), which is consistent with the prediction. See description in Section 11.6.

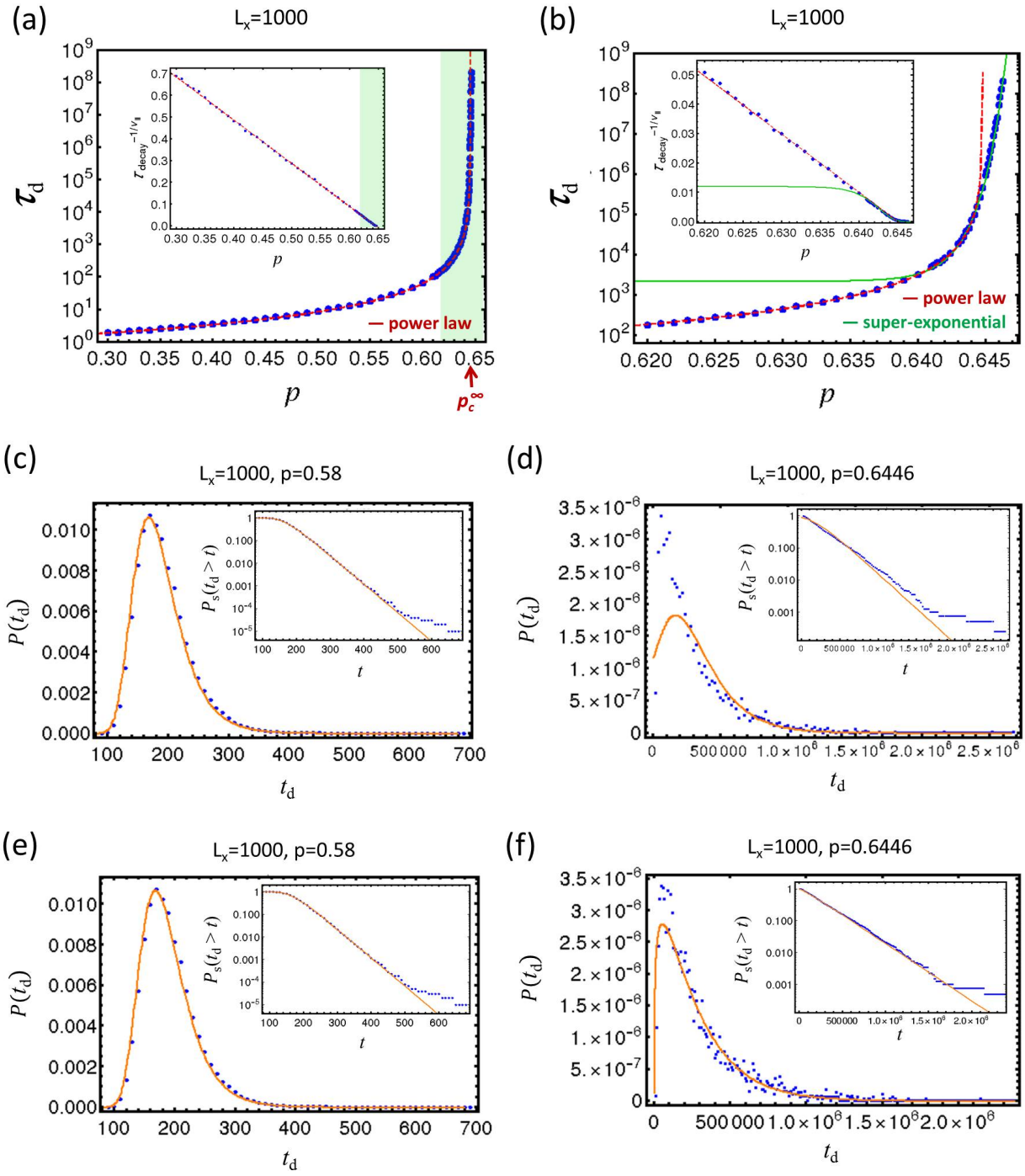

Figure 11.5: **(1+1)-dimensional directed percolation with L_x=1000**. The description is same as Fig. 11.4. The fitted parameters are $N \approx 120$ and $\zeta = 34.6$ in (e) and $N = 1.24$ and $\zeta = 2.41 \times 10^5$ in (f).

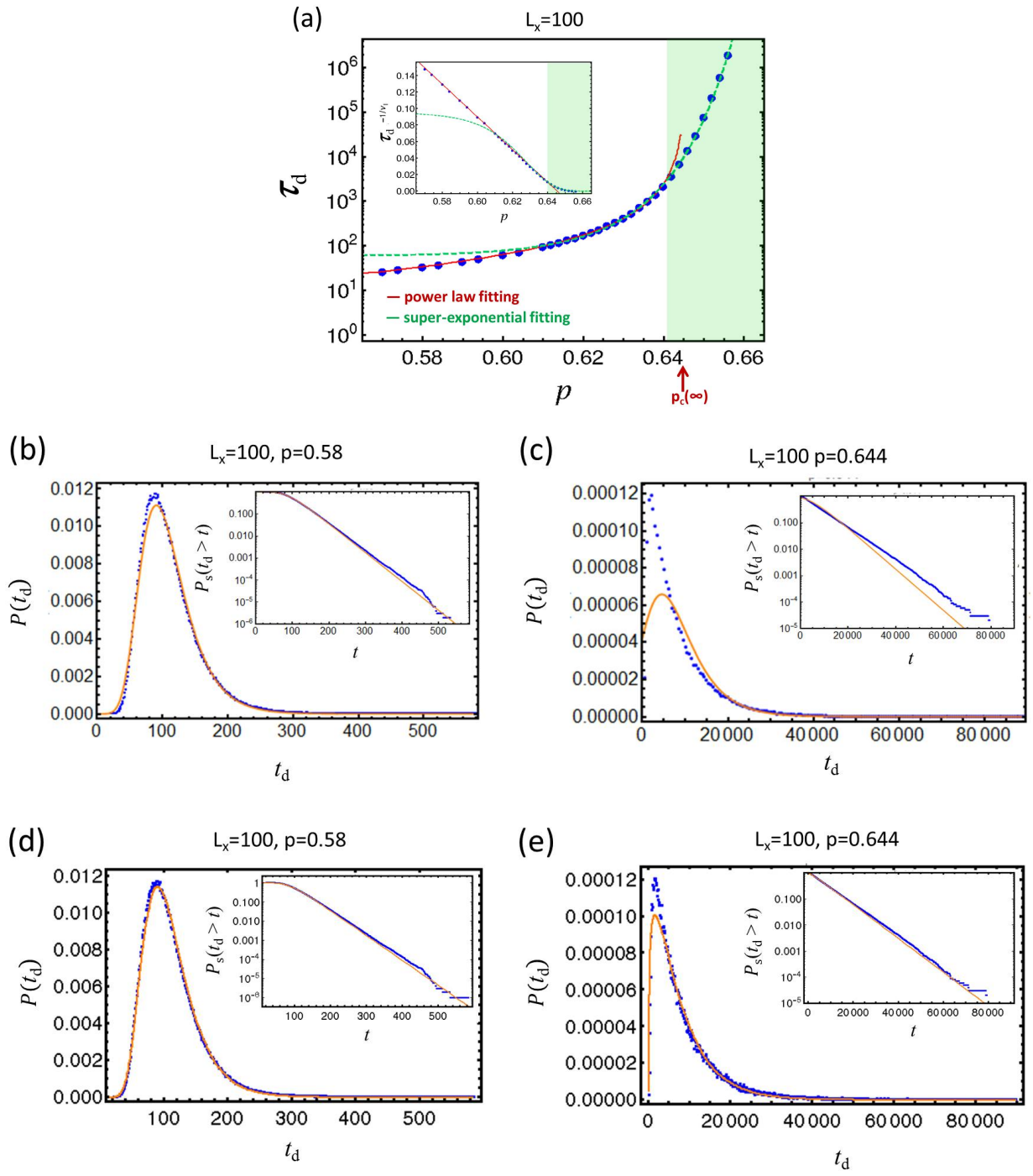

Figure 11.6: **(1+1)-dimensional directed percolation with L_x=100**. Contrary to Fig. 11.4 and Fig. 11.5, finite-size effect is strong for $L_x = 100$, and the decay rate $\tau_{\rm d}$ shows a longer range of super-exponential scaling. The fitted parameters are $N \approx 14$ and $\zeta = 33.4$ in (d) and $N = 1.24$ and $\zeta = 6.69 \times 10^3$ in (e).

11.6.3 Finite-size extreme value statistics

The form of extreme value statistics that we have been using up to now is actually the asymptotic form in the case of an infinite number of random variables. Let us see how this can be seen heuristically. We consider N independent and identically distributed random variable, $\{x_1, x_2, ..., _N\}$, whose parent distribution decays at least as fast as an exponential distribution, and for which the exponentially rare events are of interests. Each variable has a cumulative distribution given approximately by

$$Prob(x_i < y) = F(y) \sim \left(1 - e^{-y/\zeta}\right), \tag{11.7}$$

where ζ is a scale that is related to the correlation length. Now, when we consider the composite random variable $x_{\max}$, which is the largest among $\{x_i\}$, the cumulative distribution is just

$$F_N^{\max}(y) = F(y)^N = \left(1 - e^{-y/\zeta}\right)^N = \left(1 - \frac{e^{-y/\zeta + \ln N}}{N}\right)^N. \tag{11.8}$$

By changing the variable $z = \zeta(\ln N + y)$, in the limit of large N, using Cramér's method [277],

$$\lim_{N\to\infty} F_N^{\max}(y) = \lim_{N\to\infty} \mathcal{F}_N^{\max}(z) = e^{-e^{-z}}, \tag{11.9}$$

which is the form of the Type I Fisher-Tippett-Gumbel distribution in Eq. (11.2). In the context of lifetime statistics, the survival probability is the complementary cumulative distribution,

$$P_{\rm s}(t_{\rm d} > t) = 1 - F_N^{\max}(t) = 1 - \left(1 - \frac{e^{-t/\zeta + \ln N}}{N}\right)^N, \tag{11.10}$$

which we will refer as finite-size extreme value statistics, because we do not take the limit $n \to \infty$ in this expression.

When $p \to p_c$, $L_x/\xi_\perp \sim 1$, DP percolation paths are correlated, and thus the effective number of independent and identically distributed random variables, $N \sim L_x/\xi_\perp$, is generally small. This is why our previous fitting with Eq. (11.4) does not work appropriately. Instead, we tested our DP data with Eq. (11.10) and its derivative by fitting N and ζ, as shown in Fig. 11.4 (e)(f) and Fig. 11.5 (e)(f). It turns out that this finite-size extreme value statistics can capture the lifetime distribution even at $p \to p_c$ where the standard extreme value statistics fails, and the fitted value of N is consistently of order unity close to p_c (Fig. 11.4 (f) and Fig. 11.5 (f)).

11.7 Origin of super-exponential scaling very close to transition

From the above DP simulation experiments, we confirmed that the Fisher-Tippett-Gumbel extreme value distribution with super-exponential form for the survival probability is valid away from p_c, but near p_c the functional form is modified to the finite-size extreme value distribution in Eq. (11.10). However, the problem still remains: What causes the super-exponential scaling when $p \to p_c$?

To answer this question means that we need to calculate the functional form of decay rate τ_{d}. One method that we tried in order to derive the scaling form of the decay rate τ_{d} was by equating Eq. (11.5) and Eq. (11.10), taking the logarithm and expanding in the exponential terms. However, this is not satisfactory, because the coefficient ζ and N are unknown functions of p and should generally be related to τ_{d} itself. Moreover, it is not systematic.

Another way to derive τ_{d} is one that we already mentioned. It is based not on DP, but on the finding that there is an energy threshold, below which a puff cannot support itself, and thus goes into the laminar absorbing state [36]. This naturally relates to extreme value statistics [58], because the probability for decay of a puff is related to the probability that the total energy in a finite region of a puff is below some threshold, that is in general dependent on Re, as we have introduced in Section 9.3.6. However, this argument as written also uses the Fisher-Tippett-Gumbel extreme value distribution which should not be valid when $p \sim p_c$ due to correlations.

If all this were not enough, the dilemma seems especially acute when considering the lifetime measurements in pipe flow experiments [321], because it is not clear where the finite-size effect is imposed on the puffs in a long pipe. The pipe length is certainly much longer than the spatial extent of a puff, so if we think of a puff as being much longer than its diameter, effectively described by $1+1$ dimensional DP, the domain size L_x is much greater than the puff extent and should not be limiting the correlation length in the x direction until very close to the critical Re. This perspective assumes a particular relationship between turbulence and DP: we can discretize a puff into pixels or voxels (in three dimensions), and associate with each voxel a value 0 or 1 depending respectively on whether or not the turbulent kinetic energy is below or above the relaminarization threshold. This mapping associates a configuration of a turbulent puff with a configuration at that time of the DP cluster. The appropriate scale for the discretization is not unique of course, but should be larger than the Kolmogorov scale where viscous dissipation sets in, and of course smaller than the integral scale, i.e. the pipe diameter. Thus, to summarize, a pixel/voxel in DP is associated with a region of turbulence.

An alternative perspective that can be useful in some situations is to consider that the coarse-graining size for the DP pixels/voxels is simply one puff. In fact, this is essentially what Lemoult *et al.* used when

they mapped configurations of the turbulent patches in the Couette apparatus into space-time patterns that resembled DP clusters [308]. However, this is not appropriate for trying to understand the relationship between DP and turbulence lifetimes, because we want to understand the lifetime statistics and internal dynamics of a puff.

11.7.1 Spontaneous collapse of turbulence as a nucleation phenomenon

Fluctuations play crucial roles in turbulent flows, that constantly removing and dissipating energy. Near the transition, long-lived turbulent states are more susceptible to fluctuations. The turbulent state needs to maintain enough energy to sustain itself [289], otherwise it will decay to the laminar state, as we discussed in Section 9.3.6. Fig. 11.7 (a) shows an example of the turbulent kinetic energy of a turbulent puffs in DNS for pipe flow. At the tipping point of the decay, the flow suddenly has a substantial drop in energy within a relatively short duration, no matter how long it has lasted previously or what Re is. The abrupt collapse implies that some large fluctuations happen to push the system over some energy barrier, leading to the metastable turbulent state spontaneously decaying to laminar flow. Such a catastrophe can be thought of as nucleation, where the process of laminarization can be the analogy of the nucleation of laminar regions, except that in the present context, we are not dealing with fluctuations around an equilibrium state, but about a non-equilibrium steady state. Similar nucleation phenomenon were also noticed by Pomeau [54] and Manneville [322].

Similarly, in our $1+1$ dimensional DP simulation at $p < p_c$, the time series of the occupation fraction, defined as the fraction of sites at time t that are occupied, also show this nucleation-like phenomenon. In Fig. 11.7 (b), regardless of whether p is near or far from p_c, random fluctuations suddenly lead the whole cluster into the absorbing state.

The characteristics of these dangerous fluctuations should determine the spontaneous decay probability, using the argument presented in Section 9.3.6.

11.7.2 Finite-size effect in pipe flow

We now discuss how it could be that finite-size effects arise in the transitional pipe turbulence experiments [38, 41]. When Re increases, turbulent fluctuations start to aggregate and form into turbulent puffs. In particular, the characteristic time scale is in units of D/U, where D is the pipe diameter and U is the characteristic velocity scale. Thus, in order to measure lifetime statistics in pipe flow experiments, the diameter of the pipe was especially designed to be as small as possible, in order that the greatest range of timescales could be present in the experiment. In this situation, as the Re approaches Re_c, the radial

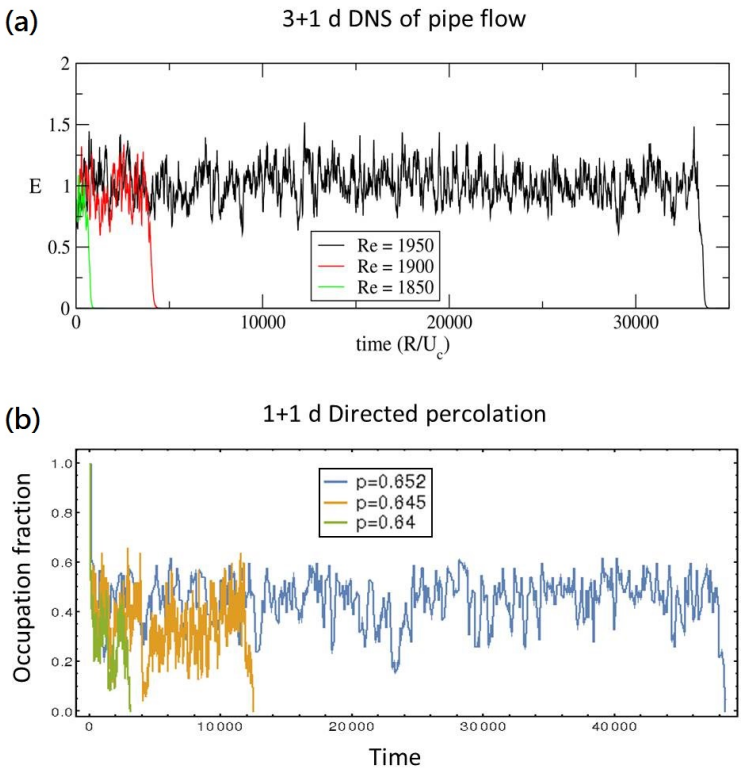

Figure 11.7: **Abrupt collapse of turbulence and directed percolation**. (a) Time series of energy from 3+1 dimensional directed numerical simulation in pipe flow at different Re. (b) Time series of occupation fraction in 1+1 dimensional directed percolation with L_x=100 at different percolation probability p. Figure (a) courtesy of Björn Hof (private communication).

correlation length of the puffs will become comparable to the diameter, while the finite-size effect in the transverse correlation length may not be apparent. As explicitly shown in the DP simulations in [56], this behavior of the correlation lengths means that the scaling laws will exhibit dimensional crossover, from (3+1)-dimensional DP when p is away from p_c, to (1+1)-dimensional DP at $p \sim p_c$ where the radial direction is highly correlated. In other words, transitional pipe turbulence is affected by finite size effect in both radial and longitudinal directions, and the experimentally observed lifetime statistics may already be affected by the finite-size effect in the radial direction even before the lifetime diverges.

11.7.3 Universal finite-size scaling of fluctuations near criticality

How does the finite-size effect influence the dangerous fluctuations that cause turbulent state to collapse? To answer this question, we appeal to a remarkable universality discovered twenty years ago for the distribution of fluctuations near the critical transition in finite-size systems. Bramwell, Holdsworth and Pinton (BHP) unexpectedly found that the fluctuations in the power to confine turbulence between two counter-rotating

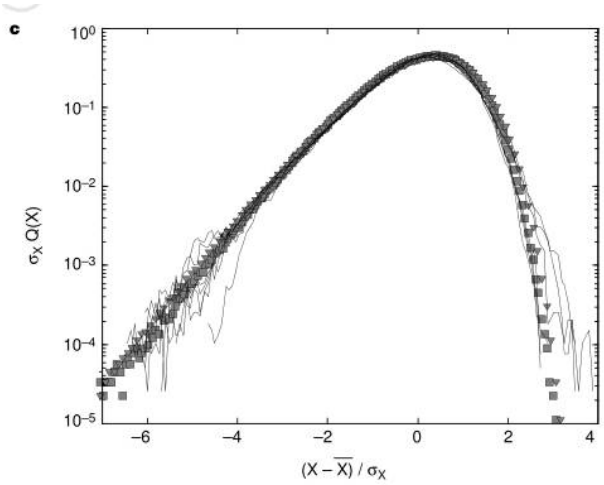

Figure 11.8: **Universal finite-size scaling of fluctuation distribution**. Data collapse of distribution of power fluctuations in confined turbulent flow between rotating plates at different frequencies (thin lines) and distribution of magnetic fluctuations in 2D XY model at low temperature with different system size in simulation (discrete data). $Q(X)$ denotes probability density function for variable X, rescaled by mean $\overline{X}$ and standard deviation σ_X. Figure is taken from [320].

plates have a universal function form that is shared by the distribution of instantaneous magnetic fluctuations in the finite-size two-dimensional XY model (in the spin wave approximation) in the low temperature regime near criticality [320]. In Fig. 11.8, we show the rescaled probability density (shifted by the mean and scaled by the standard deviation) for both the turbulent power fluctuations and the 2D XY model. The data are statistically indistinguishable, and form a distribution now known as the BHP distribution. A similar data collapse form was also found in turbulent power fluctuations in other closed flow systems [323], in Burgers turbulence [324] and in liquid crystal orientation fluctuations near the Freédericksz transition.

We wanted to see if a similar phenomenon occurred near the critical point of DP. In Fig. 11.9 (c) and (d) is shown the probability density for the $1+1$ dimensional DP occupation density for $p = 0.66$, slightly above the infinite system p_c, on a system whose spatial extent is $L_x = 100$. The distribution is clearly very close to the BHP distribution shown in Fig. 11.9 (a) and (b), indicating that the correlation length in the spatial direction has attained the system size. The presence of the universal finite-size scaling BHP distribution in DP near criticality suggests that a similar phenomenon would happen for the turbulent energy fluctuations.

11.7.4 Generalized extreme value statistics for sum of correlated variables

It is important to note that the BHP distribution describes the sum of a set of random variables, for example the spin contributions to the magnetization in the XY model case, and does not explicitly involve any maximum or minimum functions to have been taken.

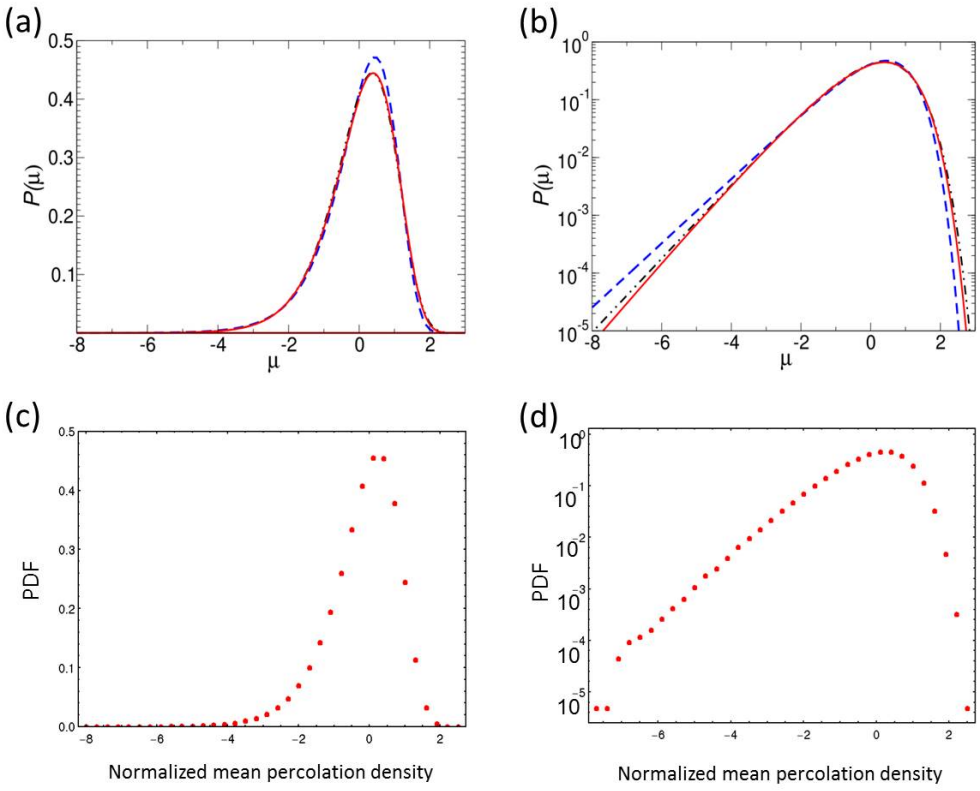

Figure 11.9: **Universal finite-size scaling of fluctuation distribution, distribution of DP occupation density and distribution of turbulent energy**. (a)(b) Comparison of standard Gumbel distribution (blue dash), generalized Gumbel distribution with parameter $a = 1.57$ (black dot dash) and BHP distribution (red) in linear scale and log scale respectively. The generalized Gumbel distribution as not been described in the text but is a heuristic approximation to the BHP distribution, namely plotting the Gumbel distribution raised to the power of a. (c)(d) Distribution of occupation fraction in 1+1 dimensional directed percolation with L_x=100 and $p = 0.66$ shown in linear scale and log scale respectively. Figure (a)(b) are taken from [325]

Remarkably, despite this fact, the functional form of the BHP universal finite-size scaling fluctuation distribution is very close to the extreme value distribution [326, 327, 325] for i.i.d. random variables. Thus, even though it applies to for non-identical and correlated random variables, and does not explicitly involve any max/min functions, the BHP distribution is close to the extreme value distribution [326, 327, 325].

The fundamental reasons for this are partially understood. The statement was proved by linking the extreme value of random variables to their sum. Following the description in Section 11.6, if we take N random variables which are independent and identically distributed and order them into $\{\tilde{x}_i\}$ where $\tilde{x}_1 \geq \tilde{x}_2 \geq ... \geq \tilde{x}_N$, a new set of variables describes the sequential difference can be defined as $\{\tilde{x}_1 - \tilde{x}_2, \tilde{x}_2 - \tilde{x}_3, ..., \tilde{x}_N\}$. Apparently the maximum value $x_{\max}$ is the sum of the gap list, and the distribution of the maximum value is automatically equivalent to the distribution of the sum of the gaps, even though the the gap variables are not identical and independently distributed. This relation was extended to a more

general case and it was found that even for arbitrary non-identical and dependent variables, their sum also is described by a generalized distribution of the maximum value $x_{\max}$ [326, 327, 325]. Moreover, this form is asymptotically similar as the standard extreme value distribution. This sheds light on the origin of universal distribution of fluctuation in critical physical systems where fluctuations are highly correlated.

11.7.5 The energy threshold for transitional turbulence in pipe flow, revisited

We now review again the argument for the super-exponential scaling of the decay rate $\tau_{\rm d}$, presented in Section 9.3.6 and originally given in [58]. The decay rate $\tau_{\rm d}$ is defined by the inverse slope of the tail of the survival probability:

$$P_{\rm s}(t_{\rm d} > t) \sim e^{-(t-t_0)/\tau_{\rm d}}, \tag{11.11}$$

where $t_{\rm d}$ is the decay time or lifetime of turbulent puffs measured in experiments. As introduced in Section 9.3.6, the survival probability for a puff to be sustained after a period of time $t - t_0$ can be calculated from the spontaneous decay probability within in a correlated time window τ_0, denoted by $\widetilde{p}$. Specifically,

$$P_{\rm s}(t_{\rm d} > t) = (1 - \widetilde{p})^{(t-t_0)/\tau_0}. \tag{11.12}$$

Therefore, the decay rate is

$$\tau_{\rm d} \sim \tau_0 \frac{1}{-\ln(1-\widetilde{p})} \sim \frac{\tau_0}{\widetilde{p}}. \tag{11.13}$$

In the original argument of [58], the probability for a turbulent puff to spontaneous decay is assumed to be proportional to the probability that the maximum energy of a set of pixels/voxels i in a puff fails to attain a Reynolds number dependent threshold, i.e. $E_{\max} = \max(\{E_i\}) < y$, where the energy threshold y depends on Re.

This argument neglects any possible laminar-turbulent phase transition but represents a general scenario for turbulence decay. The spontaneous decay probability $\widetilde{p}$ can be represented by

$$\widetilde{p} = Prob(E_{\max} < y) = e^{-e^{-(y-\mu_y)/\beta_y}}, \tag{11.14}$$

according to Eq. (11.2). Changing the variable by $z = (y - \mu_y)/\beta_y$, z is now the rescaled energy threshold

above which turbulence can be sustained, and thus z should be a decreasing function of Re i.e.

$$z = z_0 + z_1(\mathrm{Re} - \mathrm{Re}^*) + \mathcal{O}(\mathrm{Re}^2) + ..., \tag{11.15}$$

where Re^* is an expansion point, typically around 2000 and $z_1 < 0$. Therefore Eq. (11.13) becomes

$$\tau_\mathrm{d} \sim \tau_0 \exp\left(e^{a\mathrm{Re}+b+\mathcal{O}(\mathrm{Re}^2)}\right), \tag{11.16}$$

where $a = -z_1$ and $b = z_0 - z_1\mathrm{Re}^*$. Note that in this argument, we are entitled to perform a Taylor expansion because we assumed there to be no non-analytic critical behavior at the Reynolds number Re^*.

This argument may break down if there is an actual transition, and the turbulent energy at each site becomes highly correlated. Thus the above argument, based on the standard extremal distribution, is not generally valid. Instead, we modify the above argument according to the generalized extreme statistics in Section 11.7.4. The idea is that the total energy over the space, $E_\mathrm{tot} = \sum_i E_i$, which is the sum of correlated variables, determines the spontaneous decay of turbulent state within a particular time window. In fact, when E_tot is less than the energy threshold y, the turbulence undergoes relaminarization. Fortunately, from Section 11.7.4, the distribution of the sum of correlated variables is the BHP distribution which has asymptotically similar form as the standard extremal distribution. Thus the spontaneous decay probability within a time window in Eq. (11.14) is well-approximated by

$$\widetilde{p} = Prob(E_\mathrm{tot} < y) \sim e^{-e^{-(y-\mu_y)/\beta_y}}, \tag{11.17}$$

and the similarity of the functional form means that by following similar calculations as above when we neglected correlations, the same conclusion will be obtained for super-exponential scaling of the decay rate as a function of Re, as in Eq. (11.16).

11.8 Critical behavior at the predator-prey extinction transition

In previous chapters, we showed that the decay and splitting lifetimes derived from the survival probability of a predator-prey model near extinction replicated the extreme value statistics super-exponential scaling observed in transitional pipe turbulence [24]. We can re-analyze these data and extract the critical point and exponents, using the same procedure as for DP explained above.

The simulations were executed on a quasi-one dimensional strip with periodic boundary conditions in

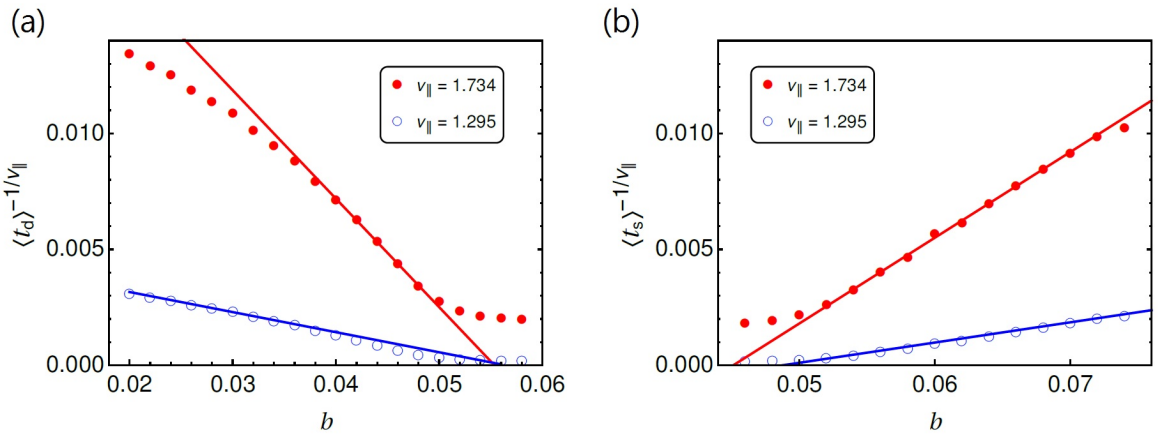

Figure 11.10: Power-law scaling in simulations of a predator-prey ecosystem in a two-dimensional strip, with finite size effect. (a) mean lifetime rescaled by the $1+1$ dimensional DP exponent (red) and the $2+1$ dimensional DP exponent (blue) versus prey birth rate. The red line is fitted for $0.038 \leq b \leq 0.048$, and the blue line is fitted for $b < 0.038$. (b) Similar to (a), but for the mean splitting time. The red line is fitted for $0.056 \leq b \leq 0.064$, and the blue line is fitted for $b > 0.064$.

the y-direction, with $L_x = 400$ and $L_y = 11$. Thus, we expect to see finite-size scaling crossover effects from $\xi_y < L_y$ to $\xi_y \; L_y$ when the control parameter, prey birth rate b, approaches the critical value b_c. Fig. 11.10 (a) shows that when $b < b_c$, $\xi_y < L_y$ the mean lifetime scales with b as a power law, with the $2+1$ dimensional DP exponent, and when $b \; b_c$ the mean lifetime scales with the $1+1$ dimensional DP exponent. The extrapolations of the two scaling functions converge to the estimated b_c in infinite system. Similar results are shown for the mean splitting time in Fig. 11.10 (b).

11.9 Conclusion

In conclusion, our results show that from lifetime and splitting statistics, it is possible to observe *both* super-exponential scaling and standard critical point power-law scaling. The super-exponential scaling does not seem to have a vertical asymptote at which the timescales diverge, unlike the critical point power-law scaling. The reason for the two apparently contrasting behaviors stems from crossover transition due to finite-size effects.

We have shown in analytic calculations and numerical simulations that the survival probability and non-splitting probability both follow the extreme value statistics functional form rather than the pure exponential form. The different functional forms are virtually indistinguishable. Near criticality the extreme value scaling breaks down due to finite-size effects, shown here in DP simulations, but these effects can be represented by the finite-size extension of the extreme value functions. Another corollary is that the decay and splitting

are, strictly speaking, not memoryless processes at all.

In addition, we argued that the statistics of the maximum hole size/empty sites for DP at $p > p_c$ corresponds to the splitting time statistics in transitional pipe flows and predator-prey systems, and we expect that the same super-exponential and power law scaling for the statistics of empty sites would also be exhibited in the Taylor-Couette experiment in [308].

The reason why the decay time and splitting time exhibit super-exponential variation with the control parameter is another story. In DP, when $\xi_\perp \ll L_x$, system is a set of weakly interacting clusters, and the lifetime statistics is determined by the longest path, with scale set by $\xi_\parallel$. When $\xi_\perp \sim L_x$, the fluctuations of the system are highly correlated and controlled by finite-size fluctuations. These surprisingly obey a universal finite-size scaling distribution (the BHP distribution), that happens to be close to the standard extreme value distribution. Computing the decay time dependence on p in DP or Re in turbulence will give a functional form that is obtained from an integral of the universal distribution function. In pipe flow experiments and simulation, we proposed that the finite-size constraint on the turbulent fluctuations arises from the radial correlation length to being comparable to the pipe diameter, an assumption that can be tested.

From these considerations, it seems that the super-exponential behavior of the puff decay/splitting times as a function of Re now has an explanation, consistent with the mapping between transitional turbulence, predator-prey dynamics and directed percolation.

Chapter 12

Conclusion

This thesis has tried to answer two sets of questions in evolutionary ecology and fluid mechanics. The first part concerns the interplay between evolutionary dynamics and ecological structure, as manifested in three different biological situations. The second part concerns the transition to turbulence in fluid dynamics, a problem that has remained unsolved for over 130 years. Surprisingly, the solution turned out to involve aspects of the biological physics uncovered in the first part of this thesis. The turbulence work probably represents the most important contribution of this thesis.

In Part I, the main question is what determines the rate of evolution, and how is it affected by the interplay between ecology and evolution? When the interactions between ecology and evolution are strong enough, such that the evolutionary timescale is comparable to the ecological timescale, there are qualitative changes in the structure of the ecosystem. New species can be induced as a response to environmental changes and create new links or forms of interaction to other species. This can result in significant changes in population dynamics and spatio-temporal patterns, and sometimes make the ecosystem more "turbulent". The changes in the ecosystem can also feedback to the environment and thus enhance the interplay between the ecology and evolution. We refer to this kind of scenarios as "rapid evolution", and Part I addresses three aspects of it, using stochastic individual-level models.

12.1 Anomalous population dynamics in rapid evolution

The first aspect focuses on the change in population dynamics due to rapid evolution. Anomalous phase relationships are a signature of phenotypic evolution and perhaps the underlying genetic variations, as a quick response to the intense environmental stress such as voracious predation. Similar to the inertial range in turbulent energy cascade, the nature of demographic stochasticity is manifested in the robust wide range of power-law scaling in the noise spectrum, reflecting a composition of different small timescales contributing to the fluctuating population dynamics. These effects are especially important near phase transitions such as extinction. The phase relationship characterized by a certain period is thus a function of frequency. Using

analytic and simulation calculations of a generic simple model that represents the trade-off between selection on reproduction and the metabolic cost of predator defense, we have shown that rapid evolution strongly renormalizes the timescale of the ecosystem. In such cases, sub-populations of prey can arise from mutations, and the characteristic anomaly in phase relationship in dynamics can emerge from demographic stochasticity. Our prediction of the coexistence region can help estimate the risk of extinction due to fluctuations and the impact of the rate of environmental changes, such as the dilution rate and nutrient concentration in a rotifer-algae system. The generic stochastic individual-level model can recapitulate rapid evolution phenomena, and shows that anomalous dynamics can arise without special assumptions or fine tuning, in sharp contrast to existing results in the ecology literature based on deterministic models. We expect the transition to rapid evolution from the normal cycles can be captured even better by considering spatiotemporal fluctuations, since before the transition the mutant prey have extremely low population numbers, and are highly localized. The study of the potentially interesting spatio-temporal patterns forming in rapid evolution is a topic for future work.

12.2 Phenotypic fluctuations in directed evolution

The second example of rapid evolution covered by this thesis includes multiple mutants and also spatio-temporal structures. The question addressed is how phenotypic fluctuations respond and adapt to selection processes, thus influencing how the evolutionary trajectory is shaped by the environment. This is motivated by collaborative experimental work on directed evolution of bacterial chemotaxis, where detailed measurements showed that phenotypic fluctuations can decrease under repeated selection. Again we approach this problem with an individual-level model, but in an abstract representation, where the multi-dimensional biological traits and genotype-phenotype mapping are projected to be one dimensional. We arrived at this simplified representation after realizing that the results of a more realistic individual-level model could be understood by abstracting the problem to one with a smaller number of degrees of freedom. Surprisingly, our simulations have shown that phenotypic fluctuations do not always decrease with round of selection. This is contrary to what would be expected by "purifying selection" in the context of conventional evolution theories such as population genetics, where selection on a Mount Fuji fitness landscape forces convergence to the optimal fitness. Nevertheless, our prediction shows that the form of selection can be significant not only in its direction and frequency but also its strength; phenotypic fluctuations can increase rather than decrease when there is strong selection. This prediction will be tested in chemotaxis experiments, where selection strength can be tuned through changing the selection range. Due to the simplicity of the abstract model,

more experiment-related features such as multiple traits and mother-daughter correlation can be included separately to determine the effect of any specific factor. Therefore the oversimplified abstract model can serve as a prototype that may help to predict interesting phenomena in future evolution experiments.

12.3 Collective coevolution of cyanobacteria and cyanophages mediated by horizontal gene transfer

The third aspect of Part I considers the richest and most complex problem, one which incorporates multiple mutations, spatio-temporal patterns, coevolution and horizontal gene transfer into predator-prey ecosystems. In this project we considered the stability of microbial-phage ecosystems by exploring the role of different evolutionary dynamics coupled to spatially-varying selection pressure. Such a situation arises in the case of the marine cyanobacteria *Prochlorococcus* whose phage predator, cyanophages, also were found to carry photosynthesis genes. Phylogenetic study also showed evidence of horizontal gene transfer between *Prochlorococcus* and cyanophages. To understand the role horizontal gene transfer plays in the coevolution of cyanobacteria and cyanophages, we developed a minimal individual-level model with horizontal gene transfer. From detailed analysis of simulations in a series of models, we discovered that collective mutualism can emerge even though it is mediated through antagonistic predator-prey interaction between bacteria and phages. We have shown that bacteria, which have a slow mutation rate compared to that of phage, can benefit, through horizontal gene transfer, from the phage high mutation rate which acts as a generator of new genes. Moreover, the slow bacterial mutation rate acts as a filter that preserves only beneficial genes, which when horizontally transferred back to the phage can insulate them from accumulation of deleterious mutations. Thus, through horizontal gene transfer, a collective state formed by bacteria and phages emerges. Through spatial-extended simulations, we also showed that other rich evolutionary characteristics of *Prochlorococcus*, such as range expansion and niche stratification, can arise from our over-simplified model. We also estimate the phase diagram as a function of horizontal gene transfer rate, showing that the collective state only exists when the horizontal gene transfer rate is neither too small nor too large. We propose that this type of mechanism can appear in other spatially-stratified systems, where genes that benefit the evolution of both host and parasite could be present.

12.4 Statistical mechanics of the laminar-turbulent transition

Part II was devoted to understanding the nature of the laminar-turbulent transition in pipe flow. The novel aspect was that we considered it to be a non-equilibrium phase transition problem, and as a result made predictions for the universality class governing the critical behavior. Some aspects of these predictions have been confirmed experimentally already, and others can in principle be tested in the future. This thesis work begins with experiments on transitional turbulence in pipe flow, which seem to show that turbulence is a transient metastable state. The measured mean lifetime and splitting of turbulence puffs does not diverge asymptotically at a critical Reynolds number, as would have been expected if there was a sharp transition. Yet measurements reveal that the lifetime scales with Reynolds number in a super-exponential way reminiscent of extreme value statistics. We performed direct numerical simulations to identify the important collective modes at the onset of turbulence. We found that a large-scale zonal flow and small-scale turbulent fluctuations interact antagonistically, essentially like predator and prey in an ecosystem. This finding allowed us to write down the simplest minimal stochastic model to account for these observations, a Landau theory for the laminar-turbulent transition. This model *predicts*, without using the Navier-Stokes equations, the puff lifetime and splitting behavior observed in experiment. This approach is a precise parallel to that used in the conventional theory of phase transitions, where one builds a Landau theory, a coarse-grained (or effective) theory from symmetry grounds. In our work, the Landau theory was developed from turbulent-mean flow interactions exposed by the numerical simulations, rather than being guessed by symmetry.

This universality class of the laminar-turbulent transition is determined by the interplay between the small-scale turbulence and large-scale collective zonal flow that exhibit predator-prey behavior. This predator-prey model can be mapped into Reggeon field theory and thence to directed percolation. Thus, the theory predicts that the dynamical interplay between zonal flow and turbulence leads to directed percolation critical phenomena. Why, then, is asymptotically divergent behavior not observed in the pipe flow experiments? Using directed percolation and a stochastic individual level model of predator-prey dynamics related to transitional turbulence, we investigated the relation between extreme value statistics and power law critical behavior, and showed that the paradox is resolved by considering correlated fluctuations near criticality. Surprisingly, critical fluctuations obey a universal finite-size scaling distribution (the BHP distribution), that happens to be close to the standard extreme value distribution from which the unusual super-exponential form of turbulence decay rate can be derived. To this end, it seems that the super-exponential behavior of the puff decay/splitting times as a function of Re now has an explanation, consistent with the mapping between transitional turbulence, predator-prey dynamics and directed percolation.

In experimental work, simulations and experiments in Taylor-Couette and channel flow were shown to exhibit directed percolation type scaling phenomena near a well-defined transition. It will be interesting to see if the super-exponential scaling phenomena can also be recapitulated in these experiments, confirming the connections that we have theoretically predicted in this thesis. This field has many fascinating and complex questions remaining open, and will be the subject of future and ongoing work.

References

[1] Stephen B Pope. *Turbulent Flows*. Cambridge University Press, 2000.

[2] D. Barkley. Theoretical perspective on the route to turbulence in a pipe. *Journal of Fluid Mechanics*, 803:P1, 2016.

[3] Bruno Eckhardt, Tobias M. Schneider, Bjorn Hof, and Jerry Westerweel. Turbulence transition in pipe flow. *Annual Review of Fluid Mechanics*, 39(1):447–468, 2007.

[4] Bruno Eckhardt. Introduction. Turbulence transition in pipe flow: 125th anniversary of the publication of Reynolds' paper. *Phil. Trans. Roy. Soc. A*, 367(1888):449–455, 2009.

[5] Paul Manneville. Transition to turbulence in wall-bounded flows: Where do we stand? *Mechanical Engineering Reviews*, 3(2):15–00684, 2016.

[6] Marten Scheffer, Jordi Bascompte, William A Brock, Victor Brovkin, Stephen R Carpenter, Vasilis Dakos, Hermann Held, Egbert H Van Nes, Max Rietkerk, and George Sugihara. Early-warning signals for critical transitions. *Nature*, 461(7260):53–59, 2009.

[7] Stephen P. Ellner. Rapid evolution: from genes to communities, and back again? *Functional Ecology*, 27(5):1087–1099, 2013.

[8] Philipp W Messer, Stephen P Ellner, and Nelson G Hairston. Can population genetics adapt to rapid evolution? *Trends in Genetics*, 32(7):408–418, 2016.

[9] F John Odling-Smee, Kevin N Laland, and Marcus W Feldman. *Niche construction: the neglected process in evolution*. Princeton University Press, 2003.

[10] Thomas Butler and Nigel Goldenfeld. Fluctuation-driven Turing patterns. *Physical Review E*, 84(1):011112, 2011.

[11] Alan J McKane, Tommaso Biancalani, and Tim Rogers. Stochastic pattern formation and spontaneous polarisation: the linear noise approximation and beyond. *Bulletin of mathematical biology*, 76(4):895–921, 2014.

[12] C Furusawa and K Kaneko. Global relationships in fluctuation and response in adaptive evolution. *Journal of the Royal Society, Interface*, 12(109):20150482–20150482, 2015.

[13] Steven J Franks and Ary A Hoffmann. Genetics of climate change adaptation. *Annual Review of Genetics*, 46:185–208, 2012.

[14] Avigdor Eldar and Michael B Elowitz. Functional roles for noise in genetic circuits. *Nature*, 467:167–173, 2010.

[15] David T Fraebel, Harry Mickalide, Diane Schnitkey, Jason Merritt, Thomas E Kuhlman, and Seppe Kuehn. Environment determines evolutionary trajectory in a constrained phenotypic space. *eLife*, 6, March 2017.

[16] Joshua S Weitz, Hyman Hartman, and Simon A Levin. Coevolutionary arms races between bacteria and bacteriophage. *Proceedings of the National Academy of Sciences of the United States of America*, 102(27):9535–9540, 2005.

[17] Joshua S Weitz. *Quantitative viral ecology: dynamics of viruses and their microbial hosts*. Princeton University Press, 2016.

[18] Nigel Goldenfeld and Carl Woese. Biology's next revolution. *Nature*, 445(7126):369–369, 2007.

[19] Nigel Goldenfeld and Carl Woese. Life is physics: evolution as a collective phenomenon far from equilibrium. *Annu. Rev. Condens. Matter Phys.*, 2(1):375–399, 2011.

[20] Nicholas Chia and Nigel Goldenfeld. Statistical mechanics of horizontal gene transfer in evolutionary ecology. *Journal of Statistical Physics*, 142(6):1287–1301, 2011.

[21] Steven J Biller, Paul M Berube, Debbie Lindell, and Sallie W Chisholm. Prochlorococcus: the structure and function of collective diversity. *Nature Reviews Microbiology*, 13(1):13–27, 2015.

[22] Lev Davidovich Landau. On the theory of phase transitions. i. *Zh. Eksp. Teor. Fiz.*, 11:19, 1937.

[23] Nigel Goldenfeld. *Lectures On Phase Transitions And The Renormalization Group*. Addison-Wesley Reading, MA, 1992.

[24] Hong-Yan Shih, Tsung-Lin Hsieh, and Nigel Goldenfeld. Ecological collapse and the emergence of travelling waves at the onset of shear turbulence. *Nature Physics*, 12:245–248, 2016.

[25] Haye Hinrichsen. Non-equilibrium critical phenomena and phase transitions into absorbing states. *Advances in Physics*, 49(7):815–958, 2000.

[26] Takehito Yoshida, Laura E Jones, Stephen P Ellner, Gregor F Fussmann, and Nelson G Hairston. Rapid evolution drives ecological dynamics in a predator-prey system. *Nature*, 424(6946):303–306, 2003.

[27] Brendan J. M. Bohannan and Richard E. Lenski. Effect of resource enrichment on a chemostat community of bacteria and bacteriophage. *Ecology*, 78(8):2303–2315, 1997.

[28] Brendan J. M. Bohannan and Richard E. Lenski. Effect of prey heterogeneity on the response of a model food chain to resource enrichment. *The American Naturalist*, 153(1):73–82, 1999.

[29] Takehito Yoshida, Stephen P Ellner, Laura E Jones, Brendan J. M Bohannan, Richard E Lenski, and Nelson G Hairston, Jr. Cryptic population dynamics: Rapid evolution masks trophic interactions. *PLoS Biol*, 5(9):e235 (12 pages), 2007.

[30] Hong-Yan Shih and Nigel Goldenfeld. Path-integral calculation for the emergence of rapid evolution from demographic stochasticity. *Physical Review E*, 90(5):050702, 2014.

[31] O. Reynolds. An experimental investigation of the circumstances which determine whether the motion of water shall be direct or sinuous, and of the law of resistance in parallel channels. *Phil. Trans. Roy. Soc. A*, 174:935–982, 1883.

[32] I. Wygnanski and F. H. Champagne. On transition in a pipe. Part 1: The origin of puffs and slugs and the flow in a turbulent slug. *Journal of Fluid Mechanics*, 59:281–335, 1973.

[33] Holger Faisst and Bruno Eckhardt. Sensitive dependence on initial conditions in transition to turbulence in pipe flow. *Journal of Fluid Mechanics*, 504(1):343–352, 2004.

[34] J Peixinho and T Mullin. Decay of turbulence in pipe flow. *Physical Review Letters*, 96(9):94501, 2006.

[35] B. Hof, J. Westerweel, T.M. Schneider, and B. Eckhardt. Finite lifetime of turbulence in shear flows. *Nature*, 443:59–62, 2006.

[36] Ashley P. Willis and Rich R. Kerswell. Critical behavior in the relaminarization of localized turbulence in pipe flow. *Phys. Rev. Lett.*, 98(1):014501, Jan 2007.

[37] Baofang Song and Björn Hof. Deterministic and stochastic aspects of the transition to turbulence. *Journal of Statistical Mechanics: Theory and Experiment*, 2014(2):P02001, 2014.

[38] Björn Hof, Alberto de Lozar, Dirk Jan Kuik, and Jerry Westerweel. Repeller or attractor? Selecting the dynamical model for the onset of turbulence in pipe flow. *Phys. Rev. Lett.*, 101(21):214501, Nov 2008.

[39] I. Wygnanski, M. Sokolov, and D. Friedman. On transition in a pipe. Part 2: The equilibrium puff. *Journal of Fluid Mechanics*, 59:283–304, 1975.

[40] David Moxey and Dwight Barkley. Distinct large-scale turbulent-laminar states in transitional pipe flow. *Proc. Natl. Acad. Sci. USA*, 107(18):8091–8096, 2010.

[41] Kerstin Avila, David Moxey, Alberto de Lozar, Marc Avila, Dwight Barkley, and Björn Hof. The onset of turbulence in pipe flow. *Science*, 333(6039):192–196, 2011.

[42] Mina Nishi, Bülent Ünsal, Franz Durst, and Gautam Biswas. Laminar-to-turbulent transition of pipe flows through puffs and slugs. *Journal of Fluid Mechanics*, 614:425–446, 2008.

[43] Grégoire Lemoult, Jean-Luc Aider, and José Eduardo Wesfreid. Turbulent spots in a channel: large-scale flow and self-sustainability. *Journal of Fluid Mechanics*, 731:R1, 2013.

[44] Grégoire Lemoult, Konrad Gumowski, Jean-Luc Aider, and José Eduardo Wesfreid. Turbulent spots in channel flow: an experimental study. *The European Physical Journal E*, 37(4):1–11, 2014.

[45] Daniel Borrero-Echeverry, Michael F. Schatz, and Randall Tagg. Transient turbulence in Taylor-Couette flow. *Phys. Rev. E*, 81(2):025301, Feb 2010.

[46] Ashley P Willis, P Cvitanović, and Marc Avila. Revealing the state space of turbulent pipe flow by symmetry reduction. *Journal of Fluid Mechanics*, 721:514–540, 2013.

[47] Predrag Cvitanović. Recurrent flows: the clockwork behind turbulence. *Journal of Fluid Mechanics*, 726:1–4, 2013.

[48] RR Kerswell. Recent progress in understanding the transition to turbulence in a pipe. *Nonlinearity*, 18(6):R17–R44, 2005.

[49] Genta Kawahara, Markus Uhlmann, and Lennaert van Veen. The significance of simple invariant solutions in turbulent flows. *Annual Review of Fluid Mechanics*, 44:203–225, 2012.

[50] Marc Avila, Fernando Mellibovsky, Nicolas Roland, and Björn Hof. Streamwise-localized solutions at the onset of turbulence in pipe flow. *Physical Review Letters*, 110(22):224502, 2013.

[51] Matthew Chantry, Ashley P Willis, and Rich R Kerswell. Genesis of streamwise-localized solutions from globally periodic traveling waves in pipe flow. *Physical Review Letters*, 112(16):164501, 2014.

[52] James P Crutchfield and Kunihiko Kaneko. Are attractors relevant to turbulence? *Physical Review Letters*, 60:2715–2718, 1988.

[53] Dwight Barkley. Simplifying the complexity of pipe flow. *Physical Review E*, 84(1):016309, 2011.

[54] Y. Pomeau. Front motion, metastability and subcritical bifurcations in hydrodynamics. *Physica*, 23D:3–11, 1986.

[55] H.K. Janssen. On the nonequilibrium phase transition in reaction-diffusion systems with an absorbing stationary state. *Zeitschrift für Physik B Condensed Matter*, 42(2):151–154, 1981.

[56] Maksim Sipos and Nigel Goldenfeld. Directed percolation describes lifetime and growth of turbulent puffs and slugs. *Physical Review E*, 84(3):035304, 2011.

[57] Jorge Peixinho and Tom Mullin. Finite-amplitude thresholds for transition in pipe flow. *Journal of Fluid Mechanics*, 582:169–178, 2007.

[58] Nigel Goldenfeld, Nicholas Guttenberg, and Gustavo Gioia. Extreme fluctuations and the finite lifetime of the turbulent state. *Phys. Rev. E*, 81(3):035304, Mar 2010.

[59] Mauro Mobilia, Ivan T. Georgiev, and Uwe C. Täuber. Phase transitions and spatio-temporal fluctuations in stochastic lattice Lotka-Volterra models. *Journal of Statistical Physics*, 128(1-2):447–483, 2007.

[60] E. P. Odum. *Fundamentals of ecology*. WB Saunders, Philadephia, 1953.

[61] D. A. Mac Lulich. Fluctuations in the numbers of varying hare (*Lepus americanus*). In *University of Toronto Studies Biological*, 43. The University of Toronto Press, Toronto, 1937.

[62] Laura E Jones, Lutz Becks, Stephen P Ellner, Nelson G Hairston, Takehito Yoshida, and Gregor F Fussmann. Rapid contemporary evolution and clonal food web dynamics. *Phil. Trans. R. Soc. B*, 364(1523):1579–1591, 2009.

[63] Alfred J Lotka. Analytical note on certain rhythmic relations in organic systems. *Proceedings of the National Academy of Sciences*, 6(7):410–415, 1920.

[64] Vito Volterra. *Variazioni e fluttuazioni del numero d'individui in specie animali conviventi*. C. Ferrari, 1927.

[65] Robert M May. Limit cycles in predator-prey communities. *Science*, 177(4052):900–902, 1972.

[66] Alfred J Lotka. *Elements of Physical Biology, reprinted 1956 as Elements of Mathematical Biology*. Dover Publishers, New York, 1924.

[67] Vito Volterra. Fluctuations in the abundance of a species considered mathematically. *Nature*, 118(2972):558–560, 1926.

[68] Vito Volterra. Variations and fluctuations of the number of individuals in animal species living together. *ICES Journal of Marine Science*, 3(1):3–51, 1928.

[69] Alfred J Lotka. Contribution to the theory of periodic reactions. *The Journal of Physical Chemistry*, 14(3):271–274, 1910.

[70] Michael L Rosenzweig and Robert H MacArthur. Graphical representation and stability conditions of predator-prey interactions. *The American Naturalist*, 97(895):209–223, 1963.

[71] Simon A. Levin. The problem of pattern and scale in ecology: The robert h. macarthur award lecture. *Ecology*, 73(6):pp. 1943–1967, 1992.

[72] Jordl Bascompte and Ricard V Solé. Rethinking complexity: modelling spatiotemporal dynamics in ecology. *Trends in Ecology & Evolution*, 10(9):361–366, 1995.

[73] Mercedes Pascual and Simon A Levin. From individuals to population densities: searching for the intermediate scale of nontrivial determinism. *Ecology*, 80(7):2225–2236, 1999.

[74] Mercedes Pascual, Pierre Mazzega, and Simon A. Levin. Oscillatory dynamics and spatial scale: The role of noise and unresolved pattern. *Ecology*, 82(8):pp. 2357–2369, 2001.

[75] Jérôme Chave. The problem of pattern and scale in ecology: what have we learned in 20 years? *Ecology Letters*, 16:4–16, 2013.

[76] Mario Pineda-Krch, Hendrik J. Blok, Ulf Dieckmann, and Michael Doebeli. A tale of two cycles distinguishing quasi-cycles and limit cycles in finite predatorprey populations. *Oikos*, 116(1):53–64, 2007.

[77] Juan A Bonachela, Miguel A Muñoz, and Simon A Levin. Patchiness and demographic noise in three ecological examples. *Journal of Statistical Physics*, 148(4):724–740, 2012.

[78] Michael B Bonsall and Alan Hastings. Demographic and environmental stochasticity in predator–prey metapopulation dynamics. *Journal of Animal Ecology*, 73(6):1043–1055, 2004.

[79] Ehud Meron. Pattern-formation approach to modelling spatially extended ecosystems. *Ecological Modelling*, 234:70–82, 2012.

[80] Andrew Liebhold, Walter D Koenig, and Ottar N Bjørnstad. Spatial synchrony in population dynamics. *Annual Review of Ecology, Evolution, and Systematics*, pages 467–490, 2004.

[81] Horst Malchow, Frank M Hilker, Ivo Siekmann, Sergei V Petrovskii, and Alexander B Medvinsky. Mathematical models of pattern formation in planktonic predation-diffusion systems: A review. In *Aspects of Mathematical Modelling*, pages 1–26. Springer, 2008.

[82] Reinier HilleRisLambers, Max Rietkerk, Frank van den Bosch, Herbert HT Prins, and Hans de Kroon. Vegetation pattern formation in semi-arid grazing systems. *Ecology*, 82(1):50–61, 2001.

[83] Bernd Blasius, Amit Huppert, and Lewi Stone. Complex dynamics and phase synchronization in spatially extended ecological systems. *Nature*, 399(6734):354–359, 1999.

[84] Simon Levin and Lee Segel. Hypothesis for origin of planktonic patchiness. *Nature*, 259:659, 1976.

[85] Shai Kinast, Yuval R Zelnik, Golan Bel, and Ehud Meron. Interplay between turing mechanisms can increase pattern diversity. *Physical review letters*, 112(7):078701, 2014.

[86] Thomas Butler and Nigel Goldenfeld. Robust ecological pattern formation induced by demographic noise. *Phys. Rev. E*, 80(3):030902, 2009.

[87] Jonathan A Sherratt, Mark A Lewis, and Andrew C Fowler. Ecological chaos in the wake of invasion. *Proceedings of the National Academy of Sciences*, 92(7):2524–2528, 1995.

[88] Quan-Xing Liu, Arjen Doelman, Vivi Rottschfer, Monique de Jager, Peter M. J. Herman, Max Rietkerk, and Johan van de Koppel. Phase separation explains a new class of self-organized spatial patterns in ecological systems. *Proceedings of the National Academy of Sciences*, 110(29):11905–11910, 2013.

[89] Alan J McKane and Timothy J Newman. Predator-prey cycles from resonant amplification of demographic stochasticity. *Physical Review Letters*, 94(21):218102, 2005.

[90] Satoru Morita, Yu Itoh, and Kei-Ichi Tainaka. Frequency of Stochastic Oscillations in Interacting Population Models. *Journal of the Physical Society of Japan*, 74(3):819–822, 2005.

[91] Andrew J Black and Alan J McKane. Stochastic formulation of ecological models and their applications. *Trends in ecology & evolution*, 27(6):337–345, 2012.

[92] Carlos A Lugo and Alan J McKane. Quasicycles in a spatial predator-prey model. *Physical Review E*, 78(5):051911, 2008.

[93] Thomas Butler and David Reynolds. Predator-prey quasicycles from a path-integral formalism. *Physical Review E*, 79:032901, 2009.

[94] NG van Kampen. A power series expansion of the master equation. *Canadian Journal of Physics*, 39(4):551–567, 1961.

[95] M Doi. Second quantization representation for classical many-particle system. *Journal of Physics A: Mathematical and General*, 9(9):1465–1477, 1976.

[96] Peter Grassberger and M Scheunert. Fock-space methods for identical classical objects. *Fortschritte der Physik*, 28(10):547–578, 1980.

[97] AS Mikhailov. Path integrals in chemical kinetics I. *Physics Letters A*, 85(4):214–216, 1981.

[98] N Goldenfeld. Kinetics of a model for nucleation-controlled polymer crystal growth. *Journal of Physics A Mathematical General*, 17:2807–2821, 1984.

[99] Daniel C Mattis and M Lawrence Glasser. The uses of quantum field theory in diffusion-limited reactions. *Reviews of Modern Physics*, 70:979–1001, 1998.

[100] Uwe C Täuber. Population oscillations in spatial stochastic Lotka–Volterra models: a field-theoretic perturbational analysis. *Journal of Physics A: Mathematical and Theoretical*, 45(40):405002, 2012.

[101] J L Cardy and R L Sugar. Directed percolation and Reggeon field theory. *Journal of Physics A: Mathematical and General*, 13(12):L423–L427, 1980.

[102] Hendrik Anthony Kramers. Brownian motion in a field of force and the diffusion model of chemical reactions. *Physica*, 7(4):284–304, 1940.

[103] JE Moyal. Stochastic processes and statistical physics. *Journal of the Royal Statistical Society. Series B (Methodological)*, 11(2):150–210, 1949.

[104] N. G. Van Kampen. *Stochastic Processes in Physics and Chemistry*. North Holland, Amsterdam, 3rd edition, 2007.

[105] MG Bulmer. The theory of prey-predator oscillations. *Theoretical population biology*, 9(2):137–150, 1976.

[106] RM Nisbet and WSC Gurney. A simple mechanism for population cycles. *Nature*, 263:319–320, 1976.

[107] Yoshiaki Itoh and Kei-ichi Tainaka. Stochastic limit cycle with power-law spectrum. *Physics Letters A*, 189(1-2):37–42, 1994.

[108] Veijo Kaitala, Esa Ranta, and Jan Lindstrom. Cyclic population dynamics and random perturbations. *Journal of Animal Ecology*, 65(2):249–251, 1996.

[109] Mercedes Pascual, Pierre Mazzega, and Simon A Levin. Oscillatory dynamics and spatial scale: the role of noise and unresolved pattern. *Ecology*, 82(8):2357–2369, 2001.

[110] Juan Pablo Aparicio and Hernán Gustavo Solari. Sustained oscillations in stochastic systems. *Mathematical biosciences*, 169(1):15–25, 2001.

[111] Mercedes Pascual and Pierre Mazzega. Quasicycles revisited: apparent sensitivity to initial conditions. *Theoretical Population Biology*, 64(3):385–395, 2003.

[112] Satoru Morita, Yu Itoh, and Kei-ichi Tainaka. Frequency of stochastic oscillations in interacting population models. *Journal of the Physical Society of Japan*, 74(3):819–822, 2005.

[113] Satoru Morita and Kei-ichi Tainaka. Undamped oscillations in prey–predator models on a finite size lattice. *Population Ecology*, 48(2):99–105, 2006.

[114] Jonathan A Sherratt, Barry T Eagan, and Mark A Lewis. Oscillations and chaos behind predator–prey invasion: mathematical artifact or ecological reality? *Philosophical Transactions of the Royal Society of London B: Biological Sciences*, 352(1349):21–38, 1997.

[115] Alan J McKane and Timothy J Newman. Stochastic models in population biology and their deterministic analogs. *Physical Review E*, 70(4):041902, 2004.

[116] E Dilos and A Marchand. Oscillations in population densities in the bacterial predator prey *Escherichia coli – Bdellovibrio bacteriovorus*: experimental study and theoretical model. *Annales de Microbiologie (Inst. Pasteur)*, A135(2):271–295, 1984.

[117] Ryuichi Sudo, Kobee Kobayashi, and Shuichi Aiba. Some experiments and analysis of a predator-prey model: Interaction between *Colpidium campylum* and *Alcaligenes faecalis* in continuous and mixed culture. *Biotechnology and Bioengineering*, 17(2):167–184, 1975.

[118] Alan A Berryman. The orgins and evolution of predator-prey theory. *Ecology*, 73(5):1530–1535, 1992.

[119] John N Thompson. Rapid evolution as an ecological process. *Trends in Ecology & Evolution*, 13(8):329 – 332, 1998.

[120] Gregor F. Fussmann, Stephen P. Ellner, Kyle W. Shertzer, and Nelson G. Hairston Jr. Crossing the hopf bifurcation in a live predator-prey system. *Science*, 290(5495):1358–1360, 2000.

[121] LauraE. Jones and StephenP. Ellner. Effects of rapid prey evolution on predatorprey cycles. *Journal of Mathematical Biology*, 55(4):541–573, 2007.

[122] Lutz Becks, Stephen P. Ellner, Laura E. Jones, and Nelson G. Hairston Jr. Reduction of adaptive genetic diversity radically alters eco-evolutionary community dynamics. *Ecology Letters*, 13(8):989–997, 2010.

[123] Lutz Becks, Stephen P. Ellner, Laura E. Jones, and Nelson G. Hairston. The functional genomics of an eco-evolutionary feedback loop: linking gene expression, trait evolution, and community dynamics. *Ecology Letters*, 15(5):492–501, 2012.

[124] Brendan JM Bohannan and Richard E Lenski. Linking genetic change to community evolution: insights from studies of bacteria and bacteriophage. *Ecology letters*, 3(4):362–377, 2000.

[125] Peter A Abrams and Hiroyuki Matsuda. Prey adaptation as a cause of predator-prey cycles. *Evolution*, 51(6):1742–1750, 1997.

[126] Kyle W. Shertzer, Stephen P. Ellner, Gregor F. Fussmann, and Nelson G. Hairston. Predatorprey cycles in an aquatic microcosm: testing hypotheses of mechanism. *Journal of Animal Ecology*, 71(5):802–815, 2002.

[127] Atsushi Yamauchi and Norio Yamamura. Effects of defense evolution and diet choice on population dynamics in a one-predator-two-prey system. *Ecology*, 86(9):2513–2524, 2005.

[128] Nelson G. Hairston, Stephen P. Ellner, Monica A. Geber, Takehito Yoshida, and Jennifer A. Fox. Rapid evolution and the convergence of ecological and evolutionary time. *Ecology Letters*, 8(10):1114–1127, 2005.

[129] Masato Yamamichi, Takehito Yoshida, and Akira Sasaki. Comparing the effects of rapid evolution and phenotypic plasticity on predator-prey dynamics. *The American Naturalist*, 178(3):287–304, 2011.

[130] Stephen P Ellner and Lutz Becks. Rapid prey evolution and the dynamics of two-predator food webs. *Theoretical Ecology*, 4(2):133–152, 2011.

[131] Peter A Abrams. Is predator-mediated coexistence possible in unstable systems? *Ecology*, 80(2):608–609, 1999.

[132] Peter A Abrams, Hiroyuki Matsuda, and Yasushi Harada. Evolutionarily unstable fitness maxima and stable fitness minima of continuous traits. *Evolutionary Ecology*, 7(5):465–487, 1993.

[133] Michael H. Cortez and Stephen P. Ellner. Understanding rapid evolution in predatorprey interactions using the theory of fastslow dynamical systems. *The American Naturalist*, 176(5):E109–E127, 2010.

[134] Akihiko Mougi. Predatorprey coevolution driven by size selective predation can cause anti-synchronized and cryptic population dynamics. *Theoretical Population Biology*, 81(2):113 – 118, 2012.

[135] Akihiko Mougi. Unusual predatorprey dynamics under reciprocal phenotypic plasticity. *Journal of Theoretical Biology*, 305(0):96 –102, 2012.

[136] Rebecca J Tien and Stephen P Ellner. Variable cost of prey defense and coevolution in predator–prey systems. *Ecological Monographs*, 82(4):491–504, 2012.

[137] Michael H Cortez and Joshua S Weitz. Coevolution can reverse predator–prey cycles. *Proceedings of the National Academy of Sciences*, 111(20):7486–7491, 2014.

[138] M Yamamichi and SP Ellner. Antagonistic coevolution between quantitative and mendelian traits. *Proceedings. Biological sciences*, 283(1827):20152926, 2016.

[139] Daniel T. Gillespie. Exact stochastic simulation of coupled chemical reactions. *The Journal of Physical Chemistry*, 81(25):2340–2361, 1977.

[140] L Peliti. Path integral approach to birth-death processes on a lattice. *Journal de Physique*, 46(9):1469–1483, 1985.

[141] Matt Parker and Alex Kamenev. Mean extinction time in predator-prey model. *Journal of Statistical Physics*, 141(2):201–216, 2010.

[142] PC Martin, ED Siggia, and HA Rose. Statistical dynamics of classical systems. *Physical Review A*, 8:423–437, 1973.

[143] Hans-Karl Janssen. On a lagrangean for classical field dynamics and renormalization group calculations of dynamical critical properties. *Zeitschrift für Physik B Condensed Matter*, 23(4):377–380, 1976.

[144] Markus F Weber and Erwin Frey. Master equations and the theory of stochastic path integrals. *Reports on Progress in Physics*, 80(4):046601, 2017.

[145] Ronald Aylmer Fisher. *The genetical theory of natural selection: a complete variorum edition*. Oxford University Press, 1930.

[146] SV Avery. Microbial cell individuality and the underlying sources of heterogeneity. *Nature reviews. Microbiology*, 4(8):577–587, 2006.

[147] Carla J Davidson and Michael G Surette. Individuality in bacteria. *Annual review of genetics*, 42:253–268, 2008.

[148] JL Spudich and DE Koshland Jr. Non-genetic individuality: chance in the single cell. *Nature*, 262(5568):467–471, 1976.

[149] V Sourjik and NS Wingreen. Responding to chemical gradients: bacterial chemotaxis. *Current opinion in cell biology*, 24(2):262–268, 2012.

[150] Sergei Maslov and Kim Sneppen. Well-temperate phage: optimal bet-hedging against local environmental collapses. *Scientific Reports (Nature Publisher Group)*, 5:10523, 2015.

[151] Kunihiko Kaneko. Phenotypic plasticity and robustness: evolutionary stability theory, gene expression dynamics model, and laboratory experiments. In *Evolutionary systems biology*, pages 249–278. Springer, 2012.

[152] Günter P Wagner and Lee Altenberg. Perspective: complex adaptations and the evolution of evolvability. *Evolution*, 50(3):967–976, 1996.

[153] Katsuhiko Sato, Yoichiro Ito, Tetsuya Yomo, and Kunihiko Kaneko. On the relation between fluctuation and response in biological systems. *Proceedings of the National Academy of Sciences of the United States of America*, pages 14086–14090, 2003.

[154] Kunihiko Kaneko and Chikara Furusawa. An evolutionary relationship between genetic variation and phenotypic fluctuation. *Journal of theoretical biology*, 240(1):78–86, 2006.

[155] Susan M Rosenberg. Evolving responsively: adaptive mutation. *Nature reviews. Genetics*, 2(7):504, 2001.

[156] Devon M Fitzgerald, PJ Hastings, and Susan M Rosenberg. Stress-induced mutagenesis: Implications in cancer and drug resistance. *Annual Review of Cancer Biology*, 1:119–140, 2017.

[157] SE Luria and M Delbrück. Mutations of bacteria from virus sensitivity to virus resistance. *Genetics*, 28(6):491–511, 1943.

[158] Russell Lande. Natural selection and random genetic drift in phenotypic evolution. *Evolution*, 30(2):314–334, 1976.

[159] Russell Lande. Quantitative genetic analysis of multivariate evolution, applied to brain: body size allometry. *Evolution*, 33(1Part2):402–416, 1979.

[160] William G Hill and Xu-sheng Zhang. Effects on phenotypic variability of directional selection arising through genetic differences in residual variability. *Genetics Research*, 83(2):121–132, 2004.

[161] Y Ito, H Toyota, K Kaneko, and T Yomo. How selection affects phenotypic fluctuation. *Molecular systems biology*, 5:264–264, 2009.

[162] Michael Eisenbach. *Bacterial Chemotaxis*, pages 2–17. John Wiley & Sons, Ltd, 2001.

[163] Herbert Levine and Wouter-Jan Rappel. The physics of eukaryotic chemotaxis. *Physics Today*, 66(2):24–30, 2013.

[164] George H Wadhams and Judith P Armitage. Making sense of it all: bacterial chemotaxis. *Nature Reviews Molecular Cell Biology*, 5(12):1024–1037, 2004.

[165] Linda Turner, William S Ryu, and Howard C Berg. Real-time imaging of fluorescent flagellar filaments. *Journal of bacteriology*, 182(10):2793–2801, 2000.

[166] Yuhai Tu. Biomolecular switches: Driven to peak. *Nature Physics*, 13:631–632, 2017.

[167] T. W. Engelmann. Neue methode zur untersuchung der sauerstoffausscheidung pflanzlicher und thierischer organismen. *Pflügers Archiv European Journal of Physiology*, 25(1):285–292, 1881.

[168] Wilhelm F. P. Pfeffer. Locomotorische richtungsbewegungen durch chemische reize. *Unters. Bot. Inst.Tbingen*, 1:363–482, 1884.

[169] Julius Adler. Chemotaxis in bacteria. *Annual review of biochemistry*, 44(1):341–356, 1975.

[170] Howard C Berg. *E. coli in Motion*. Springer Science & Business Media, 2004.

[171] Julius Adler. Chemotaxis in bacteria. *Science*, 153(3737):708–716, 1966.

[172] Julius Adler. Effect of amino acids and oxygen on chemotaxis in *Escherichia coli*. *Journal of bacteriology*, 92(1):121–129, 1966.

[173] Julius Adler. Chemoreceptors in bacteria. *Science*, 166(3913):1588–1597, 1969.

[174] Wung-Wai Tso and Julius Adler. Negative chemotaxis in *Escherichia coli*. *Journal of bacteriology*, 118(2):560–576, 1974.

[175] Howard C Berg, Douglas A Brown, et al. Chemotaxis in *Escherichia coli* analysed by three-dimensional tracking. *Nature*, 239(5374):500–504, 1972.

[176] Ekaterina Korobkova, Thierry Emonet, Jose MG Vilar, Thomas S Shimizu, and Philippe Cluzel. From molecular noise to behavioural variability in a single bacterium. *Nature*, 428(6982):574–578, 2004.

[177] G Ariel, A Rabani, S Benisty, JD Partridge, RM Harshey, and A Be'er. Swarming bacteria migrate by lévy walk. *Nature communications*, 6:8396–8396, 2015.

[178] V. Zaburdaev, S. Denisov, and J. Klafter. Lévy walks. *Rev. Mod. Phys.*, 87:483–530, Jun 2015.

[179] Yevgeniy V Kalinin, Lili Jiang, Yuhai Tu, and Mingming Wu. Logarithmic sensing in *Escherichia coli* bacterial chemotaxis. *Biophysical journal*, 96(6):2439–2448, 2009.

[180] Yuhai Tu, Thomas S Shimizu, and Howard C Berg. Modeling the chemotactic response of *Escherichia coli* to time-varying stimuli. *Proceedings of the National Academy of Sciences*, 105(39):14855–14860, 2008.

[181] Milena D Lazova, Tanvir Ahmed, Domenico Bellomo, Roman Stocker, and Thomas S Shimizu. Response rescaling in bacterial chemotaxis. *Proceedings of the National Academy of Sciences*, 108(33):13870–13875, 2011.

[182] Miri Adler, Avi Mayo, and Uri Alon. Logarithmic and power law input-output relations in sensory systems with fold-change detection. *PLoS computational biology*, 10(8):e1003781, 2014.

[183] Alan J Wolfe and Howard C Berg. Migration of bacteria in semisolid agar. *Proceedings of the National Academy of Sciences*, 86(18):6973–6977, 1989.

[184] Evelyn F Keller and Lee A Segel. Model for chemotaxis. *Journal of theoretical biology*, 30(2):225–234, 1971.

[185] James D Murray. *Mathematical biology. I, volume 17 of Interdisciplinary Applied Mathematics*. Springer-Verlag, New York,, 3 edition, 2001.

[186] Douglas A Brown and Howard C Berg. Temporal stimulation of chemotaxis in *Escherichia coli*. *Proceedings of the National Academy of Sciences*, 71(4):1388–1392, 1974.

[187] Howard C Berg and Edward M Purcell. Physics of chemoreception. *Biophysical journal*, 20(2):193–219, 1977.

[188] Ferdi L Hellweger, Robert J Clegg, James R Clark, Caroline M Plugge, and Jan-Ulrich Kreft. Advancing microbial sciences by individual-based modelling. *Nature Reviews Microbiology*, 14(7):461–471, 2016.

[189] Paul C Bressloff. Stochastic switching in biology: from genotype to phenotype. *Journal of Physics A: Mathematical and Theoretical*, 50(13):133001, 2017.

[190] Radek Erban and Hans G Othmer. From individual to collective behavior in bacterial chemotaxis. *SIAM Journal on Applied Mathematics*, 65(2):361–391, 2004.

[191] Dorine C Duives, Winnie Daamen, and Serge P Hoogendoorn. State-of-the-art crowd motion simulation models. *Transportation research part C: emerging technologies*, 37:193–209, 2013.

[192] Shugo Yasuda. Monte carlo simulation for kinetic chemotaxis model: An application to the traveling population wave. *Journal of Computational Physics*, 330:1022–1042, 2017.

[193] Daniel A Koster, Avraham Mayo, Anat Bren, and Uri Alon. Surface growth of a motile bacterial population resembles growth in a chemostat. *Journal of molecular biology*, 424(3):180–191, 2012.

[194] Mari Yoshida, Saburo Tsuru, Naoko Hirata, Shigeto Seno, Hideo Matsuda, Bei-Wen Ying, and Tetsuya Yomo. Directed evolution of cell size in escherichia coli. *BMC evolutionary biology*, 14(1):257, 2014.

[195] Jonathan M Raser and Erin K O'shea. Noise in gene expression: origins, consequences, and control. *Science*, 309(5743):2010–2013, 2005.

[196] Andrew P Feinberg and Rafael A Irizarry. Stochastic epigenetic variation as a driving force of development, evolutionary adaptation, and disease. *Proceedings of the National Academy of Sciences*, 107(suppl 1):1757–1764, 2010.

[197] Jerry L Jensen. *Statistics for petroleum engineers and geoscientists*, volume 2. Gulf Professional Publishing, 2000.

[198] Conrad H Waddington. Canalization of development and the inheritance of acquired characters. *Nature*, 150(3811):563–565, 1942.

[199] Zhenyu Wang and Nigel Goldenfeld. Fixed points and limit cycles in the population dynamics of lysogenic viruses and their hosts. *Physical Review E*, 82(1):011918, 2010.

[200] Silja Heilmann, Kim Sneppen, and Sandeep Krishna. Sustainability of virulence in a phage-bacterial ecosystem. *Journal of virology*, 84(6):3016–3022, 2010.

[201] Julian Davies and Dorothy Davies. Origins and evolution of antibiotic resistance. *Microbiology and molecular biology reviews*, 74(3):417–433, 2010.

[202] Anne E Clatworthy, Emily Pierson, and Deborah T Hung. Targeting virulence: a new paradigm for antimicrobial therapy. *Nature chemical biology*, 3(9):541–548, 2007.

[203] Britt Koskella and Michael A Brockhurst. Bacteria–phage coevolution as a driver of ecological and evolutionary processes in microbial communities. *FEMS microbiology reviews*, 38(5):916–931, 2014.

[204] Julie C Dunning Hotopp, Michael E Clark, Deodoro CSG Oliveira, Jeremy M Foster, Peter Fischer, Mónica C Muñoz Torres, Jonathan D Giebel, Nikhil Kumar, Nadeeza Ishmael, Shiliang Wang, et al. Widespread lateral gene transfer from intracellular bacteria to multicellular eukaryotes. *Science*, 317(5845):1753–1756, 2007.

[205] J. Lederberg and E. L. Tatum. Gene recombination in escherichia coli. *Nature*, 158(4016):558–558, 1946.

[206] Norton D Zinder and Joshua Lederberg. Genetic exchange in salmonella. *Journal of bacteriology*, 64(5):679–699, 1952.

[207] Michael Syvanen. Evolutionary implications of horizontal gene transfer. *Annual review of genetics*, 46:341–358, 2012.

[208] Michael Syvanen. The evolutionary implications of mobile genetic elements. *Annual review of genetics*, 18(1):271–293, 1984.

[209] Kalin Vetsigian, Carl Woese, and Nigel Goldenfeld. Collective evolution and the genetic code. *Proceedings of the National Academy of Sciences*, 103(28):10696–10701, 2006.

[210] Howard Ochman, Jeffrey G Lawrence, and Eduardo A Groisman. Lateral gene transfer and the nature of bacterial innovation. *Nature*, 405:299–304, 2000.

[211] Markus G Weinbauer and Fereidoun Rassoulzadegan. Are viruses driving microbial diversification and diversity? *Environmental microbiology*, 6(1):1–11, 2004.

[212] Kalin Vetsigian and Nigel Goldenfeld. Global divergence of microbial genome sequences mediated by propagating fronts. *Proceedings of the National Academy of Sciences of the United States of America*, 102(20):7332–7337, 2005.

[213] F Rodriguez-Valera, AB Martin-Cuadrado, B Rodriguez-Brito, L Pasić, TF Thingstad, F Rohwer, and A Mira. Explaining microbial population genomics through phage predation. *Nature reviews. Microbiology*, 7(11):828–836, 2009.

[214] Claire S Ting, Gabrielle Rocap, Jonathan King, and Sallie W Chisholm. Cyanobacterial photosynthesis in the oceans: the origins and significance of divergent light-harvesting strategies. *Trends in microbiology*, 10(3):134–142, 2002.

[215] MB Sullivan, D Lindell, JA Lee, LR Thompson, JP Bielawski, and SW Chisholm. Prevalence and evolution of core photosystem ii genes in marine cyanobacterial viruses and their hosts. *PLoS biology*, 4(8):e234–e234, 2006.

[216] Debbie Lindell, Matthew B Sullivan, Zackary I Johnson, Andrew C Tolonen, Forest Rohwer, and Sallie W Chisholm. Transfer of photosynthesis genes to and from prochlorococcus viruses. *Proceedings of the National Academy of Sciences of the United States of America*, 101(30):11013–11018, 2004.

[217] Debbie Lindell, Jacob D Jaffe, Zackary I Johnson, George M Church, and Sallie W Chisholm. Photosynthesis genes in marine viruses yield proteins during host infection. *Nature*, 438:86–89, 2005.

[218] Debbie Lindell, Jacob D Jaffe, Maureen L Coleman, Matthias E Futschik, Ilka M Axmann, Trent Rector, Gregory Kettler, Matthew B Sullivan, Robert Steen, Wolfgang R Hess, et al. Genome-wide expression dynamics of a marine virus and host reveal features of co-evolution. *Nature*, 449(7158):83–86, 2007.

[219] Michael Lynch and Wilfried Gabriel. Mutation load and the survival of small populations. *Evolution*, 44(7):1725–1737, 1990.

[220] Richard A Neher and Boris I Shraiman. Fluctuations of fitness distributions and the rate of mullers ratchet. *Genetics*, 191(4):1283–1293, 2012.

[221] Karthik Anantharaman, Melissa B Duhaime, John A Breier, Kathleen A Wendt, Brandy M Toner, and Gregory J Dick. Sulfur oxidation genes in diverse deep-sea viruses. *Science*, 344(6185):757–760, 2014.

[222] Ilnam Kang, Hyun-Myung Oh, Dongmin Kang, and Jang-Cheon Cho. Genome of a sar116 bacteriophage shows the prevalence of this phage type in the oceans. *Proceedings of the National Academy of Sciences*, 110(30):12343–12348, 2013.

[223] Jacek Wierzchos, Jocelyne DiRuggiero, Petr Vítek, Octavio Artieda, Virginia Souza-Egipsy, Pavel Skaloud, Michael Tisza, Alfonso F Davila, Carlos Vílchez, Inés Garbayo, et al. Adaptation strategies of endolithic chlorophototrophs to survive the hyperarid and extreme solar radiation environment of the atacama desert. *Frontiers in Microbiology*, 6:934, 2015.

[224] Rishiram Ramanan, Byung-Hyuk Kim, Dae-Hyun Cho, Hee-Mock Oh, and Hee-Sik Kim. Algae–bacteria interactions: evolution, ecology and emerging applications. *Biotechnology advances*, 34(1):14–29, 2016.

[225] Gerald Schönknecht, Wei-Hua Chen, Chad M Ternes, Guillaume G Barbier, Roshan P Shrestha, Mario Stanke, Andrea Bräutigam, Brett J Baker, Jillian F Banfield, R Michael Garavito, et al. Gene transfer from bacteria and archaea facilitated evolution of an extremophilic eukaryote. *Science*, 339(6124):1207–1210, 2013.

[226] Daniel D Joseph. *Stability of fluid motions I*. Springer, 1976.

[227] L.F. Richardson. *Weather Prediction by Numerical Process*. Cambridge University Press, Cambridge, UK, 1922.

[228] A N Kolmogorov. Local structure of turbulence in incompressible fluid at a very high reynolds number. *Dokl. Akad. Nauk. SSSR*, 30:299–302, 1941. [English translation in Proc. R. Soc. London Ser. A 434 (1991)].

[229] Grigory Isaakovich Barenblatt. *Scaling, self-similarity, and intermediate asymptotics: dimensional analysis and intermediate asymptotics*, volume 14. Cambridge University Press, 1996.

[230] K R Sreenivasan. The phenomenology of small-scale turbulence. *Annu. Rev. Fluid Mech.*, 29:435–472, 1997.

[231] George Keith Batchelor. *An introduction to fluid dynamics*. Cambridge university press, 1967.

[232] Robert D Moser. On the validity of the continuum approximation in high reynolds number turbulence. *Physics of Fluids*, 18(7):078105–078105, 2006.

[233] JJ Allen, MA Shockling, GJ Kunkel, and AJ Smits. Turbulent flow in smooth and rough pipes. *Philosophical Transactions of the Royal Society of London A: Mathematical, Physical and Engineering Sciences*, 365(1852):699–714, 2007.

[234] Øyvind Evju and Kent-Andre Mardal. On the assumption of laminar flow in physiological flows: Cerebral aneurysms as an illustrative example. In *Modeling the Heart and the Circulatory System*, pages 177–195. Springer, 2015.

[235] Masaki Sano and Keiichi Tamai. A universal transition to turbulence in channel flow. *Nature Physics*, 12:249–253, 2016.

[236] Siegfried Grossmann, Detlef Lohse, and Chao Sun. High–reynolds number taylor-couette turbulence. *Annual review of fluid mechanics*, 48:53–80, 2016.

[237] Daniel Borrero. *Subcritical transition to turbulence in Taylor-Couette flow*. PhD thesis, Georgia Institute of Technology, 2014.

[238] C David Andereck, SS Liu, and Harry L Swinney. Flow regimes in a circular couette system with independently rotating cylinders. *Journal of Fluid Mechanics*, 164:155–183, 1986.

[239] Nils Tillmark and P Henrik Alfredsson. Experiments on transition in plane couette flow. *Journal of Fluid Mechanics*, 235:89–102, 1992.

[240] F Daviaud, J Hegseth, and P Bergé. Subcritical transition to turbulence in plane couette flow. *Physical Review Letters*, 69(17):2511–2514, 1992.

[241] S. Bottin and H. Chaté. Statistical analysis of the transition to turbulence in plane Couette flow. *The European Physical Journal B-Condensed Matter*, 6(1):143–155, 1998.

[242] S. Bottin, F. Daviaud, P. Manneville, and O. Dauchot. Discontinuous transition to spatio-temporal intermittency in the plane couette flow. *Europhysics letters*, 43(2):171–176, 1998.

[243] Paul Manneville. On the transition to turbulence of wall-bounded flows in general, and plane Couette flow in particular. *European Journal of Mechanics-B/Fluids*, 49:345–362, 2015.

[244] Lukasz Klotz, Grégoire Lemoult, Idalia Frontczak, Laurette S Tuckerman, and José Eduardo Wesfreid. Couette-poiseuille flow experiment with zero mean advection velocity: Subcritical transition to turbulence. *Physical Review Fluids*, 2(4):043904, 2017.

[245] Donald Coles. Transition in circular couette flow. *Journal of Fluid Mechanics*, 21(3):385–425, 1965.

[246] C David Andereck, R Dickman, and Harry L Swinney. New flows in a circular couette system with co-rotating cylinders. *The Physics of Fluids*, 26(6):1395–1401, 1983.

[247] Rodolfo Ostilla-Mónico, Roberto Verzicco, and Detlef Lohse. Turbulent taylor–couette flow with stationary inner cylinder. *Journal of fluid mechanics*, 799, 2016.

[248] Leo P Kadanoff. Turbulent heat flow: Structures and scaling. *Physics Today*, 54(8):34–39, 2001.

[249] Eberhard Bodenschatz, Werner Pesch, and Guenter Ahlers. Recent developments in rayleigh-bénard convection. *Annual review of fluid mechanics*, 32(1):709–778, 2000.

[250] Guenter Ahlers and Jaechul Oh. Critical phenomena near bifurcations in nonequilibrium systems. *International Journal of Modern Physics B*, 17(22n24):3899–3907, 2003.

[251] Guenter Ahlers, Siegfried Grossmann, and Detlef Lohse. Heat transfer and large scale dynamics in turbulent rayleigh-bénard convection. *Reviews of Modern Physics*, 81:503–537, 2009.

[252] Detlef Lohse and Ke-Qing Xia. Small-scale properties of turbulent rayleigh-bénard convection. *Annual Review of Fluid Mechanics*, 42:335–364, 2010.

[253] Ke-Qing Xia. Current trends and future directions in turbulent thermal convection. *Theoretical and Applied Mechanics Letters*, 3(5), 2013.

[254] David Goluskin, Hans Johnston, Glenn R Flierl, and Edward A Spiegel. Convectively driven shear and decreased heat flux. *Journal of Fluid Mechanics*, 759:360–385, 2014.

[255] J von Hardenberg, D Goluskin, A Provenzale, and EA Spiegel. Generation of large-scale winds in horizontally anisotropic convection. *Physical review letters*, 115(13):134501, 2015.

[256] W. Pfenniger. Boundary layer suction experiments with laminar flow at high reynolds numbers in the inlet length of a tube by various suction methods. In G.V. Lachmann, editor, *Boundary Layer and Flow Control*, pages 961 – 980. Pergamon, 1961.

[257] A. Meseguer and L.N. Trefethen. Linearized pipe flow to Reynolds number 10^7. *Journal of Computational Physics*, 186(1):178 – 197, 2003.

[258] B. Hof, A. de Lozar, D. J. Kuik, and J. Westerweel. Repeller or attractor? selecting the dynamical model for the onset of turbulence in pipe flow. *Physical Review Letters*, 101:1–4, 2008.

[259] J. Peixinho and T. Mullin. Decay of turbulence in pipe flow. *Physical Review Letters*, 96(9):094501, 2006.

[260] J Nikuradze. Stromungsgesetze in rauhen Rohren. *VDI Forschungsheft*, 361(1), 1933. [English translation available as National Advisory Committee for Aeronautics, Tech. Memo. 1292 (1950). Online at: http://hdl.handle.net/2060/19930093938].

[261] G. Gioia and P. Chakraborty. Turbulent friction in rough pipes and the energy spectrum of the phenomenological theory. *Phys. Rev. Lett.*, 96:044502, 2006.

[262] Gustavo Gioia, Nicholas Guttenberg, Nigel Goldenfeld, and Pinaki Chakraborty. Spectral theory of the turbulent mean-velocity profile. *Physical Review Letters*, 105(18):184501, 2010.

[263] Dirk Jan Kuik, C Poelma, and Jerry Westerweel. Quantitative measurement of the lifetime of localized turbulence in pipe flow. *Journal of fluid mechanics*, 645:529–539, 2010.

[264] Lev D Landau. On the problem of turbulence. In *Dokl. Akad. Nauk SSSR*, volume 44, pages 339–349, 1944.

[265] EM Lifshitz and LD Landau. *Course of theoretical physics, volume 6, fluid mechanics*. Pergamon Press, Oxford UK, 1959.

[266] SR Broadbent and JM Hammersley. Percolation processes. i. crystals and mazes. In *Proceedings of the Cambridge Philosophical Society*, volume 53, pages 629–641, 1957.

[267] Peter Grassberger. On phase transitions in Schlögl's second model. *Zeitschrift für Physik B Condensed Matter*, 47(4):365–374, 1982.

[268] Kazumasa A. Takeuchi, Masafumi Kuroda, Hugues Chate, and Masaki Sano. Directed percolation criticality in turbulent liquid crystals. *Phys. Rev. Lett.*, 99:234503, 2007.

[269] Kunihiko Kaneko. Period-doubling of kink-antikink patterns, quasiperiodicity in antiferro-like structures and spatial intermittency in coupled logistic lattice: Towards a prelude of a "field theory of chaos". *Progress of Theoretical Physics*, 72(3):480–486, 1984.

[270] Kunihiko Kaneko. Spatiotemporal intermittency in coupled map lattices. *Progress of Theoretical Physics*, 74(5):1033–1044, 1985.

[271] Kunihiko Kaneko. Supertransients, spatiotemporal intermittency and stability of fully developed spatiotemporal chaos. *Physics Letters A*, 149(2-3):105–112, 1990.

[272] Hugues Chaté and Paul Manneville. Spatio-temporal intermittency in coupled map lattices. *Physica D: Nonlinear Phenomena*, 32(3):409–422, 1988.

[273] H Chaté and P Manneville. Continuous and discontinuous transition to spatio-temporal intermittency in two-dimensional coupled map lattices. *Europhysics letters*, 6(7):591–595, 1988.

[274] Peter Grassberger and Thomas Schreiber. Phase transitions in coupled map lattices. *Physica D: Nonlinear Phenomena*, 50(2):177–188, 1991.

[275] R. A. Fisher and L. H. C. Tippett. Limiting forms of the frequency distribution of the largest or smallest member of a sample. *Proc. Camb. Phil. Soc.*, 24(2):180–190, 1928.

[276] E. J. Gumbel. Les valeurs extrêmes des distributions statistiques. *Annales de l'institut Henri Poincaré*, 5(2):115–158, 1935.

[277] E. J. Gumbel. *Statistics of Extremes*. Columbia University Press, New York, NY, 1958.

[278] Martin Z. Bazant. Largest cluster in subcritical percolation. *Phys. Rev. E*, 62(2):1660–1669, Aug 2000.

[279] KR Sreenivasan and R. Ramshankar. Transition intermittency in open flows, and intermittency routes to chaos. *Physica D: Nonlinear Phenomena*, 23(1-3):246–258, 1986.

[280] A. de Lozar and B. Hof. Universality at the onset of turbulence in shear flows. *ArXiv e-prints*, January 2010.

[281] Joseph Polchinski. Renormalization and effective lagrangians. *Nuclear Physics B*, 231(2):269–295, 1984.

[282] Howard Georgi. Effective field theory. *Annual review of nuclear and particle science*, 43(1):209–252, 1993.

[283] D Barkley. Pipe flow as an excitable medium. *Revista Cubana de Fisica*, 29(1E):27–30, 2012.

[284] AG Darbyshire and T Mullin. Transition to turbulence in constant-mass-flux pipe flow. *Journal of Fluid Mechanics*, 289:83–114, 1995.

[285] Devranjan Samanta, Alberto De Lozar, and Björn Hof. Experimental investigation of laminar turbulent intermittency in pipe flow. *Journal of Fluid Mechanics*, 681:193–204, 2011.

[286] Yves Pomeau. The long and winding road. *Nature Physics*, 12:198–199, 2016.

[287] Matthew Chantry, Laurette S. Tuckerman, and Dwight Barkley. Universal continuous transition to turbulence in a planar shear flow. *Journal of Fluid Mechanics*, 824:R1, 2017.

[288] Nigel Goldenfeld and Hong-Yan Shih. Turbulence as a problem in non-equilibrium statistical mechanics. *Journal of Statistical Physics*, 167(3-4):575–594, 2017.

[289] A. P. Willis and R. R. Kerswell. Turbulent dynamics of pipe flow captured in a reduced model: puff relaminarisation and localised 'edge' states. *J. Fluid Mech.*, 619:213–233, 2009.

[290] Ashley P Willis. The openpipeflow. org navier–stokes solver. Technical report, Technical report, University of Sheffield, UK openpipeflow. org/index. php, 2015.

[291] Steven A Orszag. Numerical methods for the simulation of turbulence. *Physics of Fluids*, 12:II250–II257, 1969.

[292] Arnaud Prigent, Guillaume Grégoire, Hugues Chaté, Olivier Dauchot, and Wim van Saarloos. Large-scale finite-wavelength modulation within turbulent shear flows. *Physical Review Letters*, 89(1):014501, 2002.

[293] Yohann Duguet and Philipp Schlatter. Oblique laminar-turbulent interfaces in plane shear flows. *Phys. Rev. Lett.*, 110:034502, Jan 2013.

[294] P. H. Diamond, Y.-M. Liang, B. A. Carreras, and P. W. Terry. Self–regulating shear flow turbulence: A paradigm for the L-H transition. *Phys. Rev. Lett.*, 72:2565–2568, 1994.

[295] Eric Renshaw. *Modelling biological populations in space and time*, volume 11. Cambridge University Press, 1993.

[296] Géza Ódor. Universality classes in nonequilibrium lattice systems. *Reviews of Modern Physics*, 76(3):663, 2004.

[297] Korinna T Allhoff and Bruno Eckhardt. Directed percolation model for turbulence transition in shear flows. *Fluid Dynamics Research*, 44(3):031201, 2012.

[298] Liang Shi, Marc Avila, and Björn Hof. The universality class of the transition to turbulence. *arXiv preprint arXiv:1504.03304*, 2015.

[299] G Sivashinsky and V Yakhot. Negative viscosity effect in large-scale flows. *Physics of Fluids (1958-1988)*, 28(4):1040–1042, 1985.

[300] L Bardóczi, A Bencze, M Berta, and L Schmitz. Experimental confirmation of self-regulating turbulence paradigm in two-dimensional spectral condensation. *Physical Review E*, 90(6):063103, 2014.

[301] Jeffrey B Parker and John A Krommes. Generation of zonal flows through symmetry breaking of statistical homogeneity. *New Journal of Physics*, 16(3):035006, 2014.

[302] Tommaso Biancalani, Duccio Fanelli, and Francesca Di Patti. Stochastic Turing patterns in the Brusselator model. *Phys. Rev. E*, 81(4):046215, 2010.

[303] K. Itoh, S.-I. Itoh, P. H. Diamond, T. S. Hahm, A. Fujisawa, G. R. Tynan, M. Yagi, and Y. Nagashima. Physics of zonal flows. *Physics of Plasmas*, 13(5):055502 (11 pages), 2006.

[304] T. Estrada, T. Happel, C. Hidalgo, E. Ascasbar, and E. Blanco. Experimental observation of coupling between turbulence and sheared flows during L-H transitions in a toroidal plasma. *EPL*, 92(3):35001 (6 pages), 2010.

[305] Eun-jin Kim and P. H. Diamond. Zonal flows and transient dynamics of the L-H transition. *Phys. Rev. Lett.*, 90:185006 (4 pages), 2003.

[306] L. Schmitz, L. Zeng, T. L. Rhodes, J. C. Hillesheim, E. J. Doyle, R. J. Groebner, W. A. Peebles, K. H. Burrell, and G. Wang. Role of zonal flow predator-prey oscillations in triggering the transition to H-mode confinement. *Phys. Rev. Lett.*, 108:155002 (5 pages), 2012.

[307] PH Diamond, MN Rosenbluth, FL Hinton, M Malkov, J Fleischer, and A Smolyakov. Dynamics of zonal flows and self-regulating drift-wave turbulence. In *17th IAEA Fusion Energy Conference, Yokohama, Japan (International Atomics Energy Agency, Vienna)*, pages IAEA–CN–69/TH3/1 (8 pages), 1998.

[308] Grégoire Lemoult, Liang Shi, Kerstin Avila, Shreyas V Jalikop, Marc Avila, and Björn Hof. Directed percolation phase transition to sustained turbulence in Couette flow. *Nature Physics*, 12:254–258, 2016.

[309] Kazumasa A. Takeuchi, Masafumi Kuroda, Hugues Chate, and Masaki Sano. Experimental realization of directed percolation criticality in turbulent liquid crystals. *Phys. Rev. E*, 80:051116, 2009.

[310] Yohann Duguet, Philipp Schlatter, and Dan S Henningson. Formation of turbulent patterns near the onset of transition in plane couette flow. *Journal of Fluid Mechanics*, 650:119–129, 2010.

[311] Rory T Cerbus, Chien-chia Liu, Gustavo Gioia, and Pinaki Chakraborty. Kolmogorovian turbulence in transitional pipe flows. *arXiv preprint arXiv:1701.04048*, 2017.

[312] M Shimizu and S Kida. A driving mechanism of turbulent puff in pipe flow. *Advances in Turbulence XII*, pages 249–252, 2009.

[313] Fabian Waleffe. On a self-sustaining process in shear flows. *Physics of Fluids (1994-present)*, 9(4):883–900, 1997.

[314] B. Hof, C. W. H. van Doorne, J. Westerweel, F. T. M. Nieuwstadt, H. Faisst, B. Eckhardt, H. Wedin, R. R. Kerswell, and F. Waleffe. Experimental observation of nonlinear traveling waves in turbulent pipe flow. *Science*, 305(5690):1594–1598, 2004.

[315] Michael Tinkham. *Introduction to superconductivity*. Courier Corporation, 1996.

[316] Mitsukiyo Murakami and Kouji Kikuyama. Turbulent flow in axially rotating pipes. *Journal of Fluids Engineering*, 102(1):97–103, 1980.

[317] J. Kühnen, D. Scarselli, B. Hof, Nonlinear Dynamics, and Turbulence Group Team. Perturbing turbulence beyond collapse. In *APS Meeting Abstracts*, November 2016.

[318] Takahiro Ishida, Yohann Duguet, and Takahiro Tsukahara. Transitional structures in annular poiseuille flow depending on radius ratio. *Journal of Fluid Mechanics*, 794:R2, 2016.

[319] Takahiro Ishida, Yohann Duguet, and Takahiro Tsukahara. Turbulent bifurcations in intermittent shear flows: From puffs to oblique stripes. *Phys. Rev. Fluids*, 2:073902, Jul 2017.

[320] ST Bramwell, PCW Holdsworth, and J-F Pinton. Universality of rare fluctuations in turbulence and critical phenomena. *Nature*, 396:552–554, 1998.

[321] B. Hof, A. de Lozar, D.J. Kuik, and J. Westerweel. Repeller or attractor? selecting the dynamical model for the onset of turbulence in pipe flow. *Phys. Rev. Lett.*, 101:214501, 2008.

[322] Paul Manneville. Spatiotemporal perspective on the decay of turbulence in wall-bounded flows. *Physical Review E*, 79(2):025301, 2009.

[323] Vivek Aji and Nigel Goldenfeld. Fluctuations in finite critical and turbulent systems. *Physical review letters*, 86(6):1007, 2001.

[324] Alain Noullez and J-F Pinton. Global fluctuations in decaying burgers turbulence. *The European Physical Journal B-Condensed Matter and Complex Systems*, 28(2):231–241, 2002.

[325] Maxime Clusel and Eric Bertin. Global fluctuations in physical systems: a subtle interplay between sum and extreme value statistics. *International Journal of Modern Physics B*, 22(20):3311–3368, 2008.

[326] Eric Bertin. Global fluctuations and gumbel statistics. *Physical review letters*, 95(17):170601, 2005.

[327] Eric Bertin and Maxime Clusel. Generalized extreme value statistics and sum of correlated variables. *Journal of Physics. A, Mathematical and General*, 39(24):7607–7619, 2006.